

**Electrochemical and Spectroelectrochemical Studies of
Dipyrrolylquinoxaline, Porphyrins and Pyrazinoporphyrazines**

A Dissertation

Presented to

the Faculty of the Department of Chemistry

University of Houston

In Partial Fulfillment

of the Requirements for the Degree

Doctor of Philosophy

By

Zhen Fu

May 2012

**Electrochemical and Spectroelectrochemical Studies of
Dipyrrolylquinoxaline, Porphyrins and Pyrazinoporphyrazines**

Zhen Fu

Approved by

Dr. Karl M. Kadish, Chairman

Dr. Steven Baldelli

Dr. John L. Bear

Dr. James Briggs

Dr. Edwin Carrasquillo M.

Dean, College of Natural Sciences and Mathematics

Dedication

This Dissertation is dedicated to
my mother, Shuhua Guo,
my husband, Dr. Haitao Ji, my daughter, Grace.Ruiqi. Ji,
and
in memory of my father, Shunyi Fu.

Acknowledgement

First and foremost, I would like to offer my sincerest gratitude to my supervisor, Dr. Karl M. Kadish, who gave me the opportunity to study and work in his laboratory and supported me throughout my graduate study with his patience and knowledge while allowing me the room to work in my own way. Without his encouragement and effort, this Dissertation would not have been completed or written in its present form. One simply could not wish for a better or friendlier supervisor.

I also want to express my gratitude to Dr. Zhongping Ou, Dr. Jing Shen, Dr. Min Zhang and Dr. Xiaohui Cai for important discussions on the projects contained within this Dissertation. Special thanks go to Dr. Siyabonga Ngubane for sharing his knowledge in synthesis and different analytical techniques with me and for Dr. Ping Chen for sharing his valuable advice in electrochemistry and spectroelectrochemistry techniques.

In addition, I acknowledge and thank Dr. Shunichi Fukuzumi, Dr. Jonathan Sessler, Dr. Maxwell J. Crossley, Dr. Yohsuke Yamamoto and Dr. Claudio Ercolani for providing compounds and for their helpful suggestions. Financial support provided by the Robert A. Welch Foundation is also gratefully acknowledged.

Finally, I wish to express my deepest love and gratitude to my mother, Shuhua Guo, my husband, Dr. Haitao Ji and my daughter, Grace R. Ji, for their understanding, support, encouragement and endless love through the duration of my graduate studies.

**Electrochemical and Spectroelectrochemical Studies of
Dipyrrolylquinoxaline, Porphyrins and Pyrazinoporphyrazines**

A Dissertation
Presented to
the Faculty of the Department of Chemistry
University of Houston

In Partial Fulfillment
of the Requirements for the Degree
Doctor of Philosophy

by
Zhen Fu

May 2012

Abstract

In this Dissertation, the redox and UV-visible spectroscopic properties of a series of dipyrrolylquinoxalines, porphyrins and pyrazinoporphyrines are characterized in nonaqueous solvents. Electron-transfer reduction mechanisms and acid-base properties of dipyrrolylquinoxaline and its nitro-substituted derivatives are studied in PhCN and MeCN have been examined by means of cyclic voltammetry, UV-visible, NMR and ESR spectroscopy. Disproportionation reactions are coupled with the electron transfer reduction processes of the dipyrrolylquinoxalines to give the π -anion radical. Tris- and tetrakis-quinoxalinoporphyrins and metal complexes, i.e. $(PQ_3)M$ and $(PQ_4)M$, where $M = H_2^{II}, Cu^{II}, Pd^{II}, Ni^{II}, Zn^{II}$, or $Au^{III}PF_6$ were also investigated by cyclic voltammetry and thin-layer spectroelectrochemistry in CH_2Cl_2 , PhCN and pyridine. Stable antiaromatic $16\pi, 17\pi$ -electron porphyrinoid Cu^{II} and Zn^{II} complexes of tetraphenyltetrabenzoporphyrin (TPTBP) were also characterized in CH_2Cl_2 or PhCN. Finally, the electrochemical and spectroelectrochemical behavior of a new series of tetra-2,3-pyrazinoporphyrines were investigated in DMSO, DMF and pyridine. These compounds are represented as $[Th_8TPyzPzM]$ where $Th_8TPyzPz =$ the tetrakis-2,3-[5,6-di-(2-thienyl)-pyrazino]porphyrino anion and $M = Mg^{II}(H_2O), Co^{II}, Cu^{II}, Zn^{II}$ or H_2^I . The related pentametallic species having the formula $[(PtCl_2)_4Py_8TPyzPzM]$, $M = Pd^{II}, Pt^{II}, Cd^{II}, Cu^{II}, Zn^{II}, Mg^{II}$, were also investigated in DMSO, DMF and pyridine and described in this Dissertation.

Table of Contents

Title	Page
List of Abbreviations	xii
List of Figures	xiv
List of Tables	xxv
Chapter One Introduction	1
1.1 Outline of Research in this Dissertation	2
1.2 Use of Electrochemistry and Spectroelectrochemistry to Study Model Compounds	2
1.3 Dipyrrolylquinoxaline	4
1.4 Porphyrins and Metalloporphyrins	4
1.4.1 Quinoxalinoporphyrins	8
1.4.2 Tetrabenzoporphyrins	8
1.5 Porphyrazines and Phthalocyanines	10
1.6 References	14
Chapter Two Experimental Methods	21
2.1 Electrochemistry	22

2.1.1 Cyclic Voltammetry	22
2.2 UV-Visible Spectroelectrochemistry	24
2.3 Spectral Titration Methods for Determination of Equilibrium Constants	27
2.4 Other Experimental Methods	29
2.4.1 Degassing of the Solution	29
2.4.2 Temperature Control	29
2.5 Chemicals and Investigated Compounds	29
2.6 References	31
Chapter Three	
 Disproportionation of Dipyrrolylquinoxaline Radical	
 Anions via the Internal Protons of the Pyrrole	
 Moieties	32
3.1 Introduction	33
3.2 Results and Discussion	35
3.3 Conclusion	49
3.4 References	52
Chapter Four	
 Electroelectrochemistry and Acid-Base Properties of	
 Dipyrrolylquinoxalines	54
4.1 Introduction	55

5.2.8.1 Oxidation	110
5.2.8.2 Reduction	114
5.3 Conclusions	116
5.4 References	119
Chapter Six Electrochemistry and Electrosynthesis of Antiaromatic Benzofused Metalloporphyrin Species	121
6.1 Introduction	122
6.2 Results and Discussion	124
6.2.1 Solution UV-Visible Spectra	124
6.2.2 Electrochemistry and Electrosynthesis	126
6.3 Conclusions	134
6.4 References	135
Chapter Seven Tetra-2,3-pyrazinoporphyrazines with Externally Appended Thienyl Rings: UV-visible and Electrochemical Behaviours	137
7.1 Introduction	138
7.2 Results and Discussion	140
7.2.1 Solution UV-Visible Spectra	140

7.2.2 Pretreatment of Samples	145
7.2.3 Electrochemical Measurements	146
7.2.4 Spectroelectrochemistry	159
7.3 Conclusions	170
7.4 References	171
Chapter Eight	Electrochemistry and Spectroelectrochemistry of Metal	
	Complexes of Tetrakis-2,3-[5,6-di(2-pyridyl)pyrazino]	
	porphyrizine with Exocyclic (Pt^{II}) Metal Ion	
	Binding 173
8.1 Introduction	174
8.2 Results and Discussion	176
8.2.1 Electrochemistry	176
8.2.2 Spectroelectrochemistry	183
8.3 Conclusions	190
8.4 References	192

List of Abbreviations

Abbreviation	Meaning
Abs	absorbance
CH ₂ Cl ₂	dichloromethane
cpd	compound
CV	cyclic voltammetry
DMF	N, N-dimethylformamide
DMSO	dimethylsulfoxide
DPV	differential pulse voltammetry
DFT calculation	density functional theoretical calculation
$\Delta E_{1/2}$	difference in half-wave potential
$E_{1/2}$	half-wave potential (in volts)
E_p	peak potential (by cyclic voltammetry)
E_{pa}	anodic peak potential (by cyclic voltammetry)
E_{pc}	cathodic peak potential (by cyclic voltammetry)
ε	molar absorptivity
EPR	electron paramagnetic resonance
F _c	ferrocene
F _c ⁺	ferrocenium ion
HOMO	highest occupied molecular orbital
i_{pa}	anodic peak current (by cyclic voltammetry)
i_{pc}	cathodic peak current (by cyclic voltammetry)
LUMO	lowest unoccupied molecular orbital
Me	methyl
λ_{max}	wavelength at a specific selected peak maximum

Ph	phenyl
PhCN	benzonitrile
PQ _n	quinoxalinoporphyryns, n is the number of quinoxalines
py	pyridine
Py ₈ TPyPz	tetrakis-2,3-[5,6-di-(2-pyridyl)-pyrazino]porphyrine
SCE	saturated calomel electrode
TBAF	tetra- <i>n</i> -butylammonium fluoride trihydrate
TBAOAc	tetra- <i>n</i> -butylammonium acetate
TBAOH	tetra- <i>n</i> -butylammonium hydroxide
TBAP	tetra- <i>n</i> -butylammonium perchlorate
THF	tetrahydrofuran
Th ₈ TPyPz	tetrakis-2,3-[5,6-di-(2-thienyl)-pyrazino]porphyrine
TPTBP	tetraphenyltetrabenzoporphyrin
TPP	tetraphenylporphyrin

List of Figures

Figure		Page
Figure 1-1	Structures of dipyrrolylquinoxaline H ₂ DPQ, H ₂ DPQ(NO ₂) and H ₂ DPQ(NO ₂) ₂	5
Figure 1-2	Structures of (a) the free-base porphyrin macrocycle, (b) tetra-phenylporphyrin (TPP) and (c) tetrabenzoporphyrins (TBP).	6
Figure 1-3	Structures of investigated metalloporphyrins with 1 - 4 fused quinoxaline groups.	9
Figure 1-4	Working hypothesis for the stabilizing effect of the peripheral benzo-rings in the benzofused 16 π porphyrin.	11
Figure 1-5	Structures of (a) porphyrin, (b) porphyrazine, (c) phthalocyanine, and (d) pyrazinoporphyrazine.	12
Figure 2-1	(a) Cyclic voltammetry waveform showing reduction sweep between 0.00 to -2.00 V at a scan rate ($\Delta E/\Delta t$) of 0.1 V/s and (b) resulting cyclic voltammograms for compound which undergoes two one-electron reductions at $E_{1/2} = -0.71$ and -1.15 V.	23

Figure 2-2	Schematic illustration of the electrochemical cell. WE, CE and RE are the working, counter and reference electrodes, respectively.	25
Figure 2-3	Schematic illustration of the thin-layer UV-visible spectroelectrochemical cell. (a) platinum tipped bridge and (b) platinum net. WE, CE and RE are the working, counter and reference electrodes, respectively.	26
Figure 3-1	Cyclic voltammograms of 1H₂ – 3H₂ and 4 – 6 in deaerated MeCN containing TBAP (0.10 M) at 298 K.	36
Figure 3-2	Cyclic voltammogram and differential pulse voltammogram of 1H₂ in MeCN containing TBAP (0.10 M) at 298 K; scan rate: 0.1 V s ⁻¹ . Dashed lines are the initial first and second reductions.	37
Figure 3-3	(a) Absorption spectral changes observed upon electron transfer from CoCp ₂ (5.0 × 10 ⁻⁵ M) to 1H₂ (5.0 × 10 ⁻⁵ M) in MeCN at 303 K. (b) Time courses at 325 and 553 nm.	40
Figure 3-4	Second-order plots for disproportionation of 1H₂^{•-} produced in electron transfer from CoCp ₂ (2.5 × 10 ⁻⁵ M) to 1H₂ (2.5 × 10 ⁻⁵ M) in MeCN at various temperatures (273-333 K).	41
Figure 3-5	¹ H NMR spectra of (a) 1H₂ , (b) 1H⁻ and 1H₃⁻ produced by	

	electron-transfer reduction of $\mathbf{1H}_2$ (5.0 mM) with CoCp_2 (5.0 mM) and (c) $\mathbf{1H}^-$ produced by deprotonation of $\mathbf{1H}_2$ (5.0 mM) with Bu_4NOH (5.0 mM) in deaerated CD_3CN	42
Figure 3-6	^1H NMR spectra of (a) $\mathbf{1H}_2$, (b) $\mathbf{1H}^-$ and $\mathbf{1H}_3^-$ produced by electron-transfer reduction of $\mathbf{1H}_2$ (5.0 mM) with CoCp_2 (5.0 mM) and (c) $\mathbf{1H}^-$ produced by deprotonation of $\mathbf{1H}_2$ (5.0 mM) with Bu_4NOH (5.0 mM) in deaerated $\text{DMSO}-d_6$	43
Figure 3-7	Optimized structures of $\mathbf{1H}_3^-$ isomers as determined via DFT calculations carried out at the B3LYP/6-31G(d) level. Relative energies are given in parentheses.	45
Figure 3-8	(a) EPR spectra of $\mathbf{1H}_2^{\bullet-}$ produced via electron transfer from CoCp_2 (1.0×10^{-3} M) to $\mathbf{1H}_2$ (1.0×10^{-3} M) in MeCN at various temperatures. (b) Simulated spectrum of $\mathbf{1H}_2^{\bullet-}$ using hyperfine coupling constants and those predicted by DFT calculations. (c) DFT optimized structure of $\mathbf{1H}_2^{\bullet-}$ with <i>hfc</i> values together with the calculated values given in parentheses.	46
Figure 3-9	Van't Hoff plot of the disproportionation equilibrium constant (<i>K</i>) of $\mathbf{1H}_2^{\bullet-}$ in MeCN.	47
Figure 3-10	Eyring plot of the disproportionation of $\mathbf{1H}_2^{\bullet-}$ in MeCN.	48
Figure 3-11	UV-vis absorption spectral changes in electrolysis of (a) $\mathbf{1H}_2$ (3.3	

	$\times 10^{-4}$ M), (b) $2H_2$ (3.1×10^{-4} M) and (c) $3H_2$ (9.2×10^{-4} M) in the presence of TBAP (0.20 M) in MeCN at applied potentials of -0.80 V (vs SCE) for 347 s, -0.96 V for 310 s and -1.70 V for 180 s, respectively.	50
Figure 3-12	UV-vis absorption spectral change of (a) $1H_2$ (1.8×10^{-5} M) (b) $2H_2$ (1.7×10^{-5} M) and (c) $3H_2$ (2.0×10^{-5} M) in MeCN titrated with TBAOH (1.0×10^{-2} M).	51
Figure 4-1	Cyclic voltammograms of (a) $Q(NO_2)_n$ (4-6) and (b) $H_2DPQ(NO_2)_n$ ($1H_2$ - $3H_2$) where $n = 0, 1$ or 2 in PhCN, 0.1 M TBAP.	61
Figure 4-2	UV-vis spectra of the singly reduced compounds $Q(NO_2)_n$ at the indicated applied potentials.	62
Figure 4-3	Cyclic voltammograms of (a) $H_2DPQ(NO_2)$ $2H_2$ and (b) $H_2DPQ(NO_2)_2$ $1H_2$ in PhCN, 0.1 M TBAP. First scan (solid line); second scan (dotted line). The same current-voltage curve was obtained for the 2 nd , 3 rd and 4 th potential sweeps.	66
Figure 4-4	Thin-layer cyclic voltammograms of $H_2(NO_2)DPQ$ $2H_2$ in PhCN, 0.2 M TBAP. Scan rate = 10 mV/s. Dash line is the initial reversible reduction.	69
Figure 4-5	UV-vis spectral changes observed during the course of	

	controlled potential reduction of $\text{H}_2\text{DPQ}(\text{NO}_2)$ (2H_2) in PhCN, 0.2 M TBAP at -1.05 V and -1.35 V. See Figure 4-4 for the corresponding cyclic voltammogram.	71
Figure 4-6	Absorbance-time curves for controlled potential reductions of $\text{H}_2\text{DPQ}(\text{NO}_2)$ in PhCN at -1.05 V.	72
Figure 4-7	UV-vis spectral changes observed during the course of controlled potential reduction of $\text{H}_2\text{DPQ}(\text{NO}_2)_2$ (1H_2) in PhCN, 0.2 M TBAP at -0.90 V and -1.20 V. See Figure 4-1 for the corresponding cyclic voltammogram.	73
Figure 4-8	UV-vis spectral changes of $\text{H}_2\text{DPQ}(\text{NO}_2)$ at concentration of 10^{-3} M titrated by 0 to 5 equiva. TBAOH in PhCN.	75
Figure 4-9	(a) Cyclic voltammograms of $\text{H}_2\text{DPQ}(\text{NO}_2)$ (2×10^{-3} M) titrated by TBAOH at certain equivalent in PhCN, 0.1 M TBAP; (b) Corresponding equivalent-current curve.	76
Figure 4-10	UV-vis spectral changes during controlled potential reduction of 0.71×10^{-3} M $\text{H}_2\text{DPQ}(\text{NO}_2)$ (a) in PhCN, 0.2 M TBAP at -1.35 V and the same solvent after addition of (b) 1.2 equiv. TBAOH and (c) 5.0 equiv. TBAOH. The potential applied is shown by arrow in the figure insert.	78
Figure 4-11	UV-vis spectral changes of $\text{H}_2\text{DPQ}(\text{NO}_2)$ (10^{-5} - 10^{-6} M) titrating	

	with TBAOH, TBAF and TBAOAc in PhCN.	81
Figure 4-12	UV-vis spectral changes of $H_2DPQ(NO_2)_n$ ($n=0-2$) ($10^{-5}-10^{-6}$ M) titrating with TBAOH, TBAF and TBAOAc in PhCN.	82
Figure 4-13	Cyclic voltammograms of $H_2DPQ(NO_2)$ titrated by TFA at certain equivalent in PhCN, 0.1 M TBAP.	83
Figure 4-14	Pure TFA in PhCN, 0.1 M TBAP. Scan rate = 0.1 V/s.	84
Figure 4-15	UV-vis spectral changes of H_2DPQ , $H_2DPQ(NO_2)$, $H_2DPQ(NO_2)_2$ ($10^{-5}-10^{-6}$ M) titrating with TBAOH in PhCN.	87
Figure 5-1	Cyclic voltammograms of $(PQ_3)M$ ($M = 2H, Cu, Pd, Ni, Zn$) in pyridine, 0.1 M TBAP. Scan rate = 0.1 V/s.	94
Figure 5-2	Cyclic voltammograms of $(PQ_3)M$ ($M = Cu, Pd, Ni, Zn$) in PhCN, 0.1 M TBAP. Scan rate = 0.1 V/s.	95
Figure 5-3	Cyclic voltammograms of $(PQ_4)M$ ($M = Cu, Ni, Pd, Zn$) in CH_2Cl_2 , 0.1 M TBAP.	100
Figure 5-4	Cyclic voltammograms of $(PQ_n)Cu^{II}$ ($n = 1-4$) in PhCN, 0.1 M TBAP.	104
Figure 5-5	Plot of half-wave potentials of $(PQ_3)M$ vs half-wave potentials of $(PQ_4)M$ upon the first reduction in CH_2Cl_2 (above) and pyridine (below), 0.1 M TBAP.	105

Figure 5-6	Cyclic voltammograms of $(PQ_n)AuPF_6$ ($n = 3-4$) in pyridine, 0.1 M TBAP.	107
Figure 5-7	Cyclic voltammograms of (a) $(PQ_4)Cu$, (b) $(PQ_4)Ni$ and (c) $(PQ_4)AuPF_6$ in CH_2Cl_2 containing 0.1 M TBAP.	109
Figure 5-8	Two-step UV-visible spectral changes during oxidation of $(PQ_3)Cu$ in PhCN, 0.2 M TBAP.	113
Figure 5-9	Thin-layer UV-visible spectral changes for the first reduction of (a) $(PQ_3)Au^{III}PF_6$ and (b) $(PQ_4)Au^{III}PF_6$, and UV-vis spectra of the neutral porphyrins, (c) $(PQ_3)Cu^{II}$ and (d) $(PQ_4)Cu^{II}$ in PhCN containing 0.2 M TBAP.	115
Figure 5-10	Thin-layer UV-visible spectral changes for the second reduction of (a) $(PQ_3)Au^{III}PF_6$ and (b) $(PQ_4)Au^{III}PF_6$ in PhCN containing 0.2 M TBAP, and first reductions of (c) $(PQ_3)Cu^{II}$ and (d) $(PQ_4)Cu^{II}$ in PhCN for comparison.	117
Figure 6-1	The UV-vis spectra of TPTBP copper(II) and zinc(II) complexes: (a) copper(II) complexes 1 ($c = 11.0 \mu M$; dotted line), 3 ($c = 16.7 \mu M$; solid line) and 2 ($c = 82.8 \mu M$; broken line) in CH_2Cl_2 . (b) zinc(II) complexes 4 ($c = 8.40 \mu M$; dotted line) and 5 ($c = 43.3 \mu M$; solid line) in CH_2Cl_2 . Data are taken from ref. 16.	125

- Figure 6-2** Cyclic voltammograms and corresponding UV-vis spectral changes for **1-3** in CH₂Cl₂, 0.2 M TBAP during (a) the 16π/17π electron conversions and (b) the 17 π/18 π electron conversions at the indicated potentials where ③ gives a 16π electron species, ② gives a 17π electron species and ① gives an 18π electron species. 127
- Figure 6-3** Cyclic voltammograms and corresponding UV-vis spectral changes during controlled potential reduction and oxidation of Zn(II) compounds **4** and **5** in CH₂Cl₂, 0.1 M TBAP at the indicated potentials where ③ gives a 16π electron species, ② gives a 17π electron species and ① gives an 18π electron species. The peak marked with an asterisk in the CV of **5** is due to a surface reaction involving oxidation of H₂O from the compound. 128
- Figure 6-4** Cyclic voltammograms and corresponding UV-vis spectral changes for **4** and **5** in PhCN, 0.2 M TBAP where ③ gives a 16π-electron species, ② gives a 17π-electron species and ① gives an 18π-electron species. 132
- Figure 7-1** UV-visible solution spectra in DMF of [Th₈PyzPzH₂] (solid line) and [Th₈PyzPzMg(H₂O)] (dash line). 144

Figure 7-2	First scan (---) and second scan (—) thin-layer cyclic voltammograms of [Th ₈ TPyzPzZn] in DMSO and DMF, 0.2 M TBAP.	147
Figure 7-3	Second scan thin-layer cyclic voltammograms of [Th ₈ TPyzPzZn] in pyridine, 0.2 M TBAP.	148
Figure 7-4	Thin-layer cyclic voltammograms obtained on second scan for reduction of [Th ₈ TPyzPzM] (M = Mg ^{II} (H ₂ O), Zn ^{II} , Cu ^{II} , Co ^{II}) in pyridine containing 0.2 M TBAP. Peaks for reduction of unknown trace impurity in the Mg ^{II} sample is indicated by an asterisk (*).	152
Figure 7-5	Thin-layer cyclic voltammograms of [Th ₈ TPyzPzCo] in DMSO and pyridine, 0.2 M TBAP.	153
Figure 7-6	UV-visible spectral changes during first and second one-electron reductions of (a) [Th ₈ TPyzPzZn] and (b) [Th ₈ TPyzPzMg(H ₂ O)] in DMSO containing 0.2 M TBAP.	160
Figure 7-7	UV-visible spectral changes obtained during first and second reductions of (a) [Th ₈ TPyzPzCo] (b) [Th ₈ TPyzPzZn] in DMSO containing 0.2 M TBAP.	163
Figure 7-8	UV-visible spectral changes obtained during stepwise reductions of [Th ₈ TPyzPzCo ^{II}] in pyridine containing 0.2 M TBAP.	164

Figure 7-9	UV-visible spectral changes obtained during metal centered $\text{Co}^{\text{II}} \rightarrow \text{Co}^{\text{III}}$ oxidation of (a) $[\text{Th}_8\text{TPyzPzCo}]$ and (b) $[\text{Py}_8\text{TPyzPzCo}]$ in DMSO containing 0.2 M TBAP.	165
Figure 7-10	Cyclic voltammograms of $[\text{Th}_8\text{TPyzPzH}_2]$ in pyridine, DMSO and DMF, all containing 0.1 M TBAP. Scan rate = 0.1 V/s.	167
Figure 7-11	Cyclic voltammograms of $[\text{Th}_8\text{TPyzPz}]^{2-}$ in pyridine, 0.1 M TBAP and 0.12 M TBAOH.	168
Figure 7-12	UV-vis spectral changes of $[\text{Th}_8\text{TPyzPzH}_2]$ in pyridine containing 0.2 M TBAP during controlled-potential electrolysis.	169
Figure 8-1	Thin-layer cyclic voltammograms of $[\text{Py}_8\text{TPyzPzM}]$ where M = Pt, Cd and Cu in DMSO, 0.2 M TBAP. Scan rate = 20 mV/s.	178
Figure 8-2	Cyclic voltammograms of PtCl_2 (reproduced from ref 3), $[\text{LZn}]$ (reproduced from ref 15) and $[(\text{PtCl}_2)_4\text{LZn}]$ (L = Py_8TPyzPz) in DMSO, 0.1 M TBAP. The peak marked by an asterisk is associated with reduction of bound PtCl_2 . Scan rate = 0.1 V/s. ...	180
Figure 8-3	Thin-layer cyclic voltammograms of $[(\text{PtCl}_2)_4\text{LPt}]$ and $[\text{LPt}]$ (L = Py_8TPyzPz) in DMSO, 0.2 M TBAP.	182
Figure 8-4	Thin-layer cyclic voltammograms with added $E_{1/2}$ values (V vs	

	SCE) of $[(PtCl_2)_4Py_8TPyzPzM]$ in DMSO containing 0.2 M TBAP. Scan rate = 20 mV/s.	184
Figure 8-5	UV-visible spectral changes during first reduction of $[LPd]$, $[(PdCl_2)_4LPd]$ (reproduced from ref 3) and $[(PtCl_2)_4LPd]$ (L = $Py_8TPyzPz$) in DMSO containing 0.2 M TBAP.	186
Figure 8-6	UV-visible spectral changes obtained during the first and second reductions of (a) $[(PtCl_2)_4LZn]$ and (b) $[(PtCl_2)_4LMg]$ (L = $Py_8TPyzPz$) in DMSO containing 0.2 M TBAP.	188
Figure 8-7	UV-visible spectral changes obtained during the first and second reductions of (a) $[(PtCl_2)_4LZn]$ and (b) $[(PtCl_2)_4LMg]$ (L = $Py_8TPyzPz$) in DMSO containing 0.2 M TBAP.	189
Figure 8-8	UV-visible spectral changes obtained during the first to fourth reductions $[(PtCl_2)_4Py_8TPyzPzZn]$ in DMSO containing 0.2 M TBAP.	190

List of Tables

Table		Page
Table 4-1	Equilibrium Constants for the Reactions of Bases and Acid with $H_2DPQ(NO_2)_n$ where $n = 0, 1$ or 2 in PhCN.	85
Table 5-1	Half-wave Potentials (V vs SCE) of $(PQ_n)M$ in CH_2Cl_2 Containing 0.1 M TBAP.	96
Table 5-2	Half-wave Potentials (V vs SCE) of $(PQ_n)M$ in PhCN Containing 0.1 M TBAP.	97
Table 5-3	Half-wave Potentials (V vs Ag/AgCl) of $(PQ_3)M$ in THF Containing 0.1 M TBAP.	98
Table 5-4	Shifts in $E_{1/2}$ (V vs SCE) upon Going from $(PQ_2)M$ to $(PQ_3)M$, $(QPQ)M$ to $(PQ_3)M$ and $(PQ_3)M$ to $(PQ_4)M$ Macrocycle in Nonaqueous Solvents Containing 0.1 M TBAP.	102
Table 5-5	Half-wave Potentials (V vs SCE) of Gold Derivatives in Different Solvents Containing 0.1 M TBAP.	108
Table 5-6	UV-visible Spectral Data of $(PQ_3)M$ in PhCN and Pyridine Containing 0.1 M TBAP.	111
Table 5-7	UV-visible Spectral Data of $(PQ_n)M$ ($n = 3$ and 4) in CH_2Cl_2 Containing 0.1 M TBAP.	112

Table 7-1	UV-visible Solution Spectra in Pyridine, DMSO and DMF of the Thienyl Compounds $[\text{Th}_8\text{TPyzPzM}] \cdot x\text{H}_2\text{O}$ ($\text{M} = \text{Mg}^{\text{II}}(\text{H}_2\text{O}), \text{Zn}^{\text{II}}, \text{Cu}^{\text{II}}, \text{Co}^{\text{II}}, 2\text{H}^{\text{I}}$) and Related Octapyridino Analogues $[\text{Py}_8\text{TPyzPzM}]$	142
Table 7-2	Half-wave Potentials ($E_{1/2}$, V vs SCE and vs Fc/Fc^+) for Reduction of $[\text{Th}_8\text{TPyzPzM}]$ ($\text{M} = \text{Zn}^{\text{II}}, \text{Mg}^{\text{II}}(\text{H}_2\text{O}), \text{Cu}^{\text{II}}, \text{Co}^{\text{II}}$) in DMSO, DMF and Pyridine, 0.2 M TBAP.	150
Table 7-3	Half-wave Potentials Measured by Regular Cyclic Voltammetry ($E_{1/2}$, V vs SCE) for Reductions of $[\text{Th}_8\text{TPyzPzM}]$ ($\text{M} = \text{Mg}^{\text{II}}, \text{Zn}^{\text{II}}, \text{Cu}^{\text{II}}, \text{Co}^{\text{II}}, 2\text{H}^{\text{I}}$) and Analogues in Pyridine, DMSO and DMF, 0.1 M TBAP (scan rate = 100 mV/s).	154
Table 8-1	Half-wave Potential ($E_{1/2}$, V vs SCE) of the LM, $[(\text{PtCl}_2)_4\text{LM}]$ and $[(\text{PdCl}_2)_4\text{LM}]$ ($\text{L} = \text{Py}_8\text{TPyzPz}$; $\text{M} = \text{Zn}^{\text{II}}, \text{Mg}^{\text{II}}, \text{Cu}^{\text{II}}, \text{Cd}^{\text{II}}, \text{Pd}^{\text{II}}, \text{Pt}^{\text{II}}$) and Analogues in DMSO, 0.1 M TBAP.	179
Table 8-2	UV-visible Solution Spectra of the $[(\text{PtCl}_2)\text{LM}]$ ($\text{L} = \text{Py}_8\text{TPyzPz}$; $\text{M} = \text{Zn}^{\text{II}}, \text{Mg}^{\text{II}}, \text{Cd}^{\text{II}}, \text{Pd}^{\text{II}}, \text{Pt}^{\text{II}}$) in DMSO, DMF and Py (0.2 M TBAP).	185

Chapter One

Introduction

1.1 Outline of Research in This Dissertation

The starting point of this Dissertation, Chapter One, gives a general introduction to the compounds investigated and techniques utilized in this work. Chapter Two describes the Experimental Techniques in more detail. The research described in the following six chapters is divided into three parts. The first involves the electron-transfer reduction and acid/base properties of dipyrrolylquinoxaline and its nitro-substituted derivatives (Chapters Three and Four). This is then followed by a description of the electrochemical and spectroelectrochemical properties of substituted porphyrins and metalloporphyrins, including tris- and tetrakis-quinoxalinoporphyrins (Chapter Five) and tetraphenyltetrabenzoporphyrins (Chapter Six). The third part of this Dissertation focuses mainly on the electrochemical and spectroelectrochemical characterization of pyrazinoporphyrazines, which includes tetrakis-2,3-[5,6-di-(2-thienyl)-pyrazino]-porphyrazine and its metallated complexes (Chapter Seven) as well as metal derivatives of tetrakis-2,3-[5,6-di(2-pyridyl)pyrazino]porphyrazine with exocyclic (Pt^{II}) metal ion binding (Chapter Eight).

1.2 Use of Electrochemistry and Spectroelectrochemistry to Study Model Compounds

Electrochemical studies of model synthetic compounds can provide valuable information on potentials and electron transfer mechanisms under a variety of experimental conditions, while also UV-visible, ESR and/or FTIR spectroelectrochemistry can be utilized to characterize the spectral products of electrooxidation/reduction. The data obtained by electrochemistry and

spectroelectrochemistry are generally analyzed as a function of solution conditions, metal oxidation state in the metallomacrocycle, type and number of axial ligands and nature of the π -ring systems in order to ascertain the site of electron transfer and to monitor the degree of interaction, if any, between different redox active centers on the molecules. The data can also be analyzed in terms of available structural information in the solid state to better understand, predict and “tune” chemical reactivity of the investigated compounds.

Spectroelectrochemistry is a technique which combines electrochemistry with *in situ* spectroscopic measurements such as UV-visible, FTIR and ESR. Studies of the spectral changes which occur as a function of time or applied potential during a given redox process have often been used to distinguish metal-centered reactions from ring-centered ones in metalloporphyrins. Generally, a porphyrin metal-centered oxidation or reduction will lead to red or blue shifts in the most intense UV-visible band located between 350 and 450 nm (called the Soret band), but with little loss of molar absorptivity of this band. In contrast, when an electron transfer process occurs at the conjugated π -ring system of a porphyrin, or porphyrin-like molecule, there is often a significant decrease in intensity of the Soret band along with the appearance of new, broad visible or near-IR bands located between 600 - 900 nm. These types of spectral changes indicate the probable formation of a porphyrin π -anion or π -cation radical.¹⁻³

By using combined electrochemistry and spectroelectrochemistry techniques, we are able to better understand how the electron transfer sites will vary with the specific macrocycle substituents, central metal ion, coordinated axial ligands, properties of the solvent, type of the supporting electrolyte and temperature of the measurement. Many

examples are given in the present Dissertation.

1.3 Dipyrrolylquinoxaline

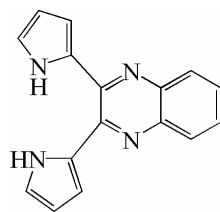
Dipyrrolylquinoxaline, represented as H₂DPQ, and its nitro-substituted derivatives whose structures are shown in Figure 1-1, are synthetic receptors capable of recognizing, sensing, and transporting anions^{4, 5} and thus have importance not only in supramolecular systems but also in terms of their potential clinical applications.⁶ These types of compounds have also been shown to have applications in the synthesis of precursors for porphyrins and related macrocycles,⁷⁻⁹ where incorporating these fragments into a larger “expanded” macrocyclic framework will lead to novel porphyrinoids that could act as potential “molecular cages” for anionic, cationic, or neutral substrates.⁸

Studies on the fate of the chemically and electrochemically reduced dipyrrolylquinoxalines in Figure 1-1 as well as their acid and base properties are described in Chapters Three and Four. A Communication¹⁰ on part of this work was published in 2011 and was based in large part on the data in Chapter Three.

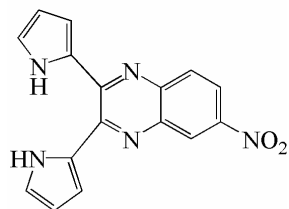
1.4 Porphyrins and Metalloporphyrins

Porphyrins are a ubiquitous class of naturally occurring molecules involved in a wide variety of important biological processes ranging from oxygen transport to photosynthesis, from catalysis to pigmentation changes.¹¹⁻¹³

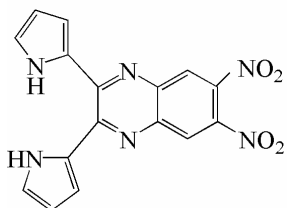
The porphyrin macrocycle (see Figure 1-2a) is an aromatic system containing 22 π -electrons, 18 of which are delocalized according to Hückel’s rule of aromaticity ($4n+2$) delocalized π -electrons, where $n = 4$. The size of the macrocycle is perfect to bind



H₂DPQ

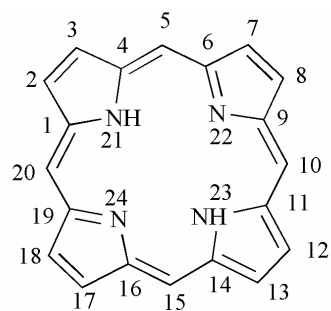


H₂DPQ(NO₂)

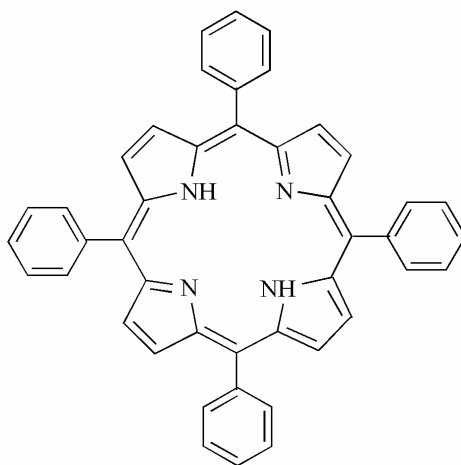


H₂DPQ(NO₂)₂

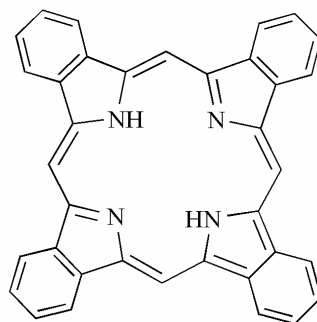
Figure 1-1. Structures of dipyrrolylquinoxalines H₂DPQ, H₂DPQ(NO₂) and H₂DPQ(NO₂)₂.



(a) porphyrin



(b) TPP



(c) TBP

Figure 1-2. Structures of (a) the free-base porphyrin macrocycle, (b) tetraphenylporphyrin (TPP) and (c) tetrabenzoporphyrins (TBP).

almost all metal ions, and indeed a number of metals (e.g. Zn, Cu, Ni, Fe, and Co) can be inserted in the center of the macrocycle forming metalloporphyrins.¹¹⁻¹³

The peripheral positions of a porphyrin macrocycle may be substituted by electron-donating or electron-withdrawing groups to form porphyrin derivatives with a larger range of basicities. There are two positions available for substitution on a porphyrin macrocycle as shown in Figure 1-2a, which are four meso positions numbered as 5, 10, 15 and 20, and eight β -pyrrole positions as 2, 3, 7, 8, 12, 13, 17 and 18.¹¹ Free-base tetraphenylporphyrin (TPP) has four phenyl groups at the meso-positions while tetrabenzoporphyrin (TBP) has four fused ring systems which occurs on β -pyrrole positions. The structures of these compounds are also shown in Figure 1-2.

The porphyrin macrocycle possesses a highly conjugated π ring system, which can easily accommodate the addition or abstraction of electrons. In nonaqueous media, two stepwise ring-centered oxidations and two stepwise ring-centered reductions are generally observed over a potential range of -2.0 to +2.0 V vs SCE, leading to the formation of π -anion radicals and dianions upon reduction and π -cation radicals and dications upon oxidation.^{14, 15} The addition of electron-withdrawing or electron-donating substituents at the meso or β -pyrrole position of macrocycle will affect the electron density of the π -ring system, and all four of the above mentioned macrocycle-centered redox processes will not be seen in every case. Moreover, the electron transfer site may be in some cases located at the central metal ion (such as for Fe, Mn, Co compounds), at the axial ligands if they are redox active or at electroactive substituent on the macrocycle in some cases. The exact redox behavior of a given compound will also

depend on the properties of the utilized electrochemical solvent and supporting electrolyte as described in the several chapters of this Dissertation.

1.4.1 Quinoxalinoporphyrins

Quinoxalinoporphyrins, shown in Figure 1-3 and denoted as PQ_n ($n = 1 - 4$), are a class of laterally-extended porphyrins with aromatic rings fused to the β, β' -positions of a pyrrolic ring of the macrocycle. They are building blocks for coplanar laterally-extended oligoporphyrins with possible applications in molecular electronics.¹⁶⁻²⁰ An expansion of the π -system of the porphyrin offers a means to modulate the redox and photophysical properties of these macrocycles.²¹ The work described in Chapter Five expands upon results from our past electrochemical and spectroelectrochemical studies of mono- and bis-quinoxalinoporphyrins $(PQ)M$,²²⁻²⁵ $(PQ_2)M$ ²⁶ and $(QPQ)M$ ²⁶ (see Figure 1-3) to examine how the fusion of three and four quinoxaline groups to give derivatives of $(PQ_3)M$ and $(PQ_4)M$ (see Figures 1-3d and 1-3e) will affect the compound's properties.

1.4.2 Tetrabenzoporphyrins

Tetrabenzoporphyrins (TBP) (see Figure 1-2c) are another intriguing class of extended porphyrins whose unique photophysical²⁷⁻²⁹ and physicochemical properties³⁰⁻³² have found uses in many areas, two examples being as agents for photodynamic therapy^{33, 34} and optical limiters.³⁵⁻³⁷ Porphyrins typically exhibit $4n+2$ aromaticity and their structures and properties are usually primarily derived from the heteroaromatic nature of the ligand π -system. In recent years, there have been a number

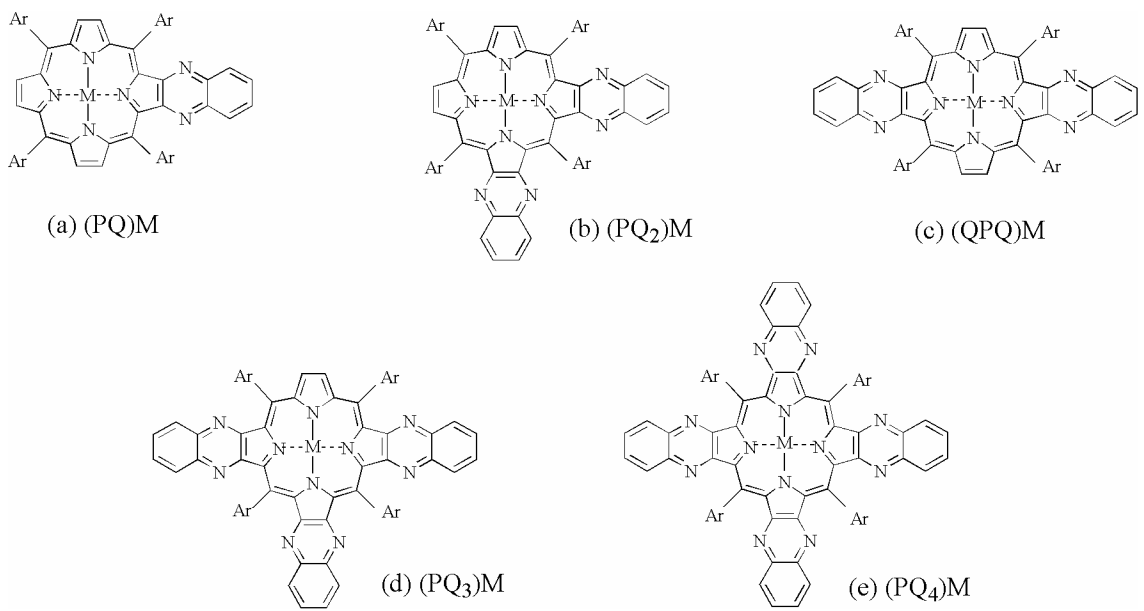


Figure 1-3. Structures of investigated metalloporphyrins with 1 - 4 fused quinoxaline groups.

of reports of novel antiaromatic porphyrins and ring-expanded porphyrinoid analogs with $4n$ inner ring electron counts.³⁸⁻⁴³

In a recent study, tetraphenyltetrabenzoporphyrins (TPTBP) were chosen by our collaborators in Japan as a suitable skeleton to synthesize further examples of stable antiaromatic 16π and 17π -electron porphyrinoid.⁴⁴ The 16π porphyrins could be chemically generated from the 18π porphyrins (Figure 1-4) and were electronically stabilized by the presence of the four 6π benzo-rings around the porphyrin core. The 16π derivatives were also generated by electrochemical means as described in this Dissertation. The electrochemical and spectroelectrochemical interconversions between 16π , 17π and 18π electron forms of the tetraphenyltetrabenzoporphyrins were investigated.

1.5 Porphyrazines and Phthalocyanines

The electrochemistry and spectroelectrochemistry of porphyrazines (see Figure 1-5b for structures) are described in Chapters Seven and Eight. These compounds have a symmetrical 18π -electron aromatic core and are structurally related to porphyrins.^{45, 46} Both types of macrocycles contain a central C_8N_8 ring surrounded by four pyrrole groups, but the porphyrazines differ from the porphyrins by having four meso-nitrogen atoms instead of four methane bridges in the central ring.

Phthalocyanine (Pc) (Figure 1-5c) is a classic ring substituted “porphyrazine”. It consists of four isoindole units, which are linked angularly by four meso-nitrogen bridges, leading to a macrocyclic aromatic molecule.⁴⁷ Phthalocyanines and their derivatives have been widely employed as various advanced materials, such as dyes for

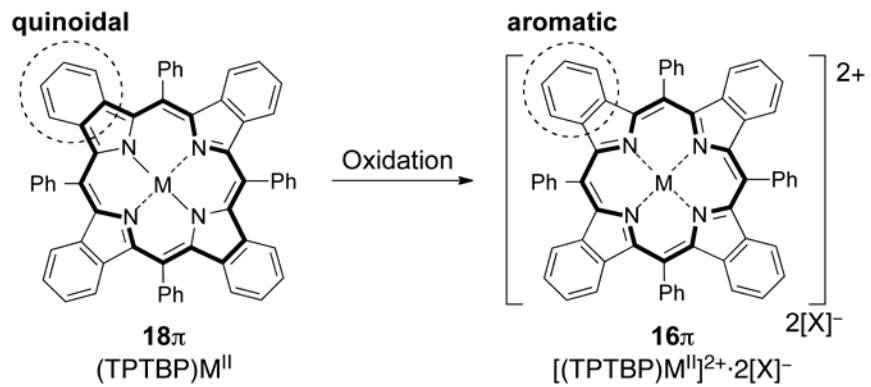
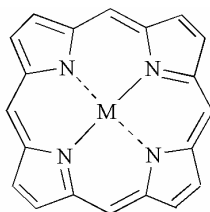
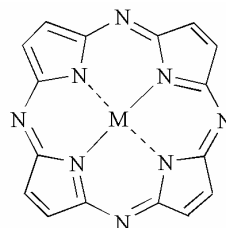


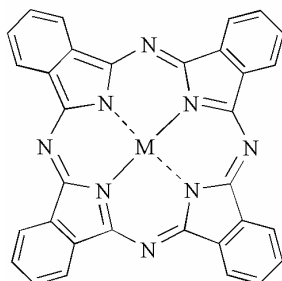
Figure 1-4. Working hypothesis for the stabilizing effect of the peripheral benzo-rings in the benzofused 16π porphyrin.⁴⁴



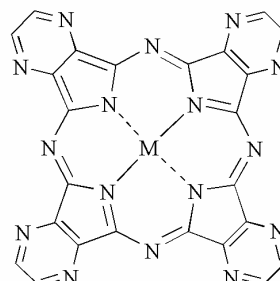
(a) porphyrin



(b) porphyrazine



(c) phthalocyanine



(d) pyrazinoporphyrazine

Figure 1-5. Structures of (a) porphyrin, (b) porphyrazine, (c) phthalocyanine, and (d) pyrazinoporphyrazine.

read-write optical media, photosensitizers for photodynamic therapy (PDT), photovoltaic devices, and so forth.^{12, 48-56} These sophisticated molecular functionalities are ascribed to the versatile electronic structures of phthalocyanines. As a consequence, phthalocyanines have today established themselves in a firm position as high-tech materials.⁴⁷

Porphyrazines and phthalocyanines have been characterized as electron-deficient macrocycles on the basis of their UV-visible spectral features and electrochemical behavior.^{19, 57-70} In Chapter Seven, a related series of pyrazinoporphyrazines (see Figure 1-5d) carrying externally thienyl rings, $[\text{Th}_8\text{TPyzPzM}]$,⁷¹ will be discussed. The role played by exocyclic pendant vicinal thienyl rings in the electronic distribution within the entire molecular framework of molecules is one target of the present investigation, mainly conducted by UV-visible spectral and electrochemical measurements. The electrochemical and spectroelectrochemical properties of a series of heteropentametallic porphyrazine macrocycles, $[(\text{PtCl}_2)_4\text{Py}_8\text{TPyzPzM}]$,⁷² having four PtCl_2 units coordinated to the pyridine N atoms of the external dipyridinopyrazine fragments were examined and the results of this study are described in Chapter Eight.

1.5 References

1. Fuhrhop, J.-H., *Struct. Bonding* **1974**, *18*, 1.
2. Derrin, M. H.; Gouterman, M.; Derrin, C. L., *J. Chem. Phys.* **1969**, *5*, 4137.
3. Gouterman, M., *J. Mol. Spectrosc.* **1961**, *6*, 138.
4. Dietrich, B.; Hosseini, M. W., In *Supramolecular Chemistry of Anions*, Bianchi, A.; Bowman-James, K.; Garcís-España, E., Eds. Wiley-VCH: New York, **1997**; p 45.
5. Mizuno, T.; Wei, W.; Eller, L. R.; Sessler, J. L., *J. Am. Chem. Soc.* **2002**, *124*, (7), 1134.
6. Black, C. B.; Andrioletti, B.; Try, A. C.; Ruiperez, C.; Sessler, J. L., *J. Am. Chem. Soc.* **1999**, *121*, 10438.
7. Sessler, J. L.; Seidel, D., *Angew. Chem., Int. Ed.* **2003**, *42*, 5134.
8. Sessler, J. L.; Maeda, H.; Mizuno, T.; Lynch, V.; Furuta, H., *J. Am. Chem. Soc.* **2002**, *124*, 13474.
9. Sessler, J. L.; Weghorn, S. J., *Expanded, Contracted and Isomeric Porphyrins*. Elsevier: Oxford, UK, **1997**.
10. Fukuzumi, S.; Mase, K.; Ohkubo, K.; Fu, Z.; Karnas, E.; Sessler, J. L.; Kadish, K. M., *J. Am. Chem. Soc.* **2011**, *133*, 7284.
11. Smith, K. M., *Porphyrin and Metalloporphyrins*. Elsevier: New York, **1975**.
12. Kadish, K. M.; Smith, K. M.; Guillard, R., *The Porphyrin Handbook*. Academic Press: San Diego, **2000**; Vol. 1-20.

13. Kadish, K. M.; Smith, K. M.; Gilliland, R., *Handbook of Porphyrin Science*. World Scientific: Singapore, **2010**; Vol. 1-20.
14. Kadish, K. M.; Van Caemelbecke, E.; Royal, G., In *The Porphyrin Handbook*, Kadish, K. M.; Smith, K. M.; Guillard, R., Eds. Academic Press: New York, **2000**; Vol. 8, p 1.
15. Kadish, K. M., *Inorg. Chem.* **1986**, *34*, 435.
16. Holten, D.; Bocian, D. F.; Lindsey, J. S., *Acc. Chem. Res.* **2002**, *35*, 57.
17. Jiao, J.; Anariba, F.; Tiznado, H.; Schmidt, I.; Lindsey, J. S.; Zeaera, F.; Bocian, D. F., *J. Am. Chem. Soc.* **2006**, *128*, 6965.
18. Kelley, R. F.; Shin, W. S.; Rybtchinski, B.; Sinks, L. E.; Wasielewski, M. R., *J. Am. Chem. Soc.* **2007**, *129*, 3173.
19. Kim, D.; Osuka, A., *Acc. Chem. Res.* **2004**, *37*, 735.
20. Reimers, J. R.; Hush, N. S.; Crossley, M. J., *J. Porphyrins Phthalocyanines* **2002**, *6*, 795.
21. Khoury, T.; Crossley, M. J., *New J. Chem.* **2009**, *33*, 1076.
22. Kadish, K. M.; E, W.; Ou, Z.; Shao, J.; Sintic, P. J.; Ohkubo, K.; Fukuzumi, S.; Crossley, M. J., *Chem. Comm.* **2002**, 356.
23. Ou, Z.; E, W.; Shao, J.; Burn, P. L.; Sheehan, C. S.; Walton, R.; Kadish, K. M.; Crossley, M. J., *J. Porphyrins Phthalocyanines* **2005**, *9*, 142.
24. Ou, Z.; E, W.; Zhu, W.; Thordarson, P.; Sintic, P. J.; Crossley, M. J.; Kadish, K. M.,

- Inorg. Chem.* **2007**, *46*, 10840.
25. Ou, Z.; Kadish, K. M.; E, W.; Shao, J.; Sentic, P. J.; Ohkubo, K.; Fukuzumi, S.; Crossley, M. J., *Inorg. Chem.* **2004**, *43*, 2078.
26. E, W.; Kadish, K. M.; Sentic, P. J.; Khoury, T.; Govenlock, L. J.; Ou, Z.; Shao, J.; Ohkubo, K.; Reimers, J. R.; Fukuzumi, S.; Crossley, M. J., *J. Phys.Chem. A* **2008**, *112*, 556.
27. Nguyen, K. A.; Pachter, R., *J. Chem. Phys.* **2001**, *114*, 17490.
28. Shkirman, S. F.; Gladkov, L. L.; Konstantinova, V. K.; Solovyov, K. N., *Spectrosc. Lett.* **1998**, *31*, 1749.
29. Vancott, T. C.; Koralewski, M.; Metcalf, D. H.; Schatz, P. N.; Willizmson, B. E., *J. Phys.Chem.* **1993**, *97*, 7417.
30. Carlson, J. B.; Vouros, P., *J. Mass Spectrosc.* **1996**, *31*, 1403.
31. Finikova, O. S.; Cheprakov, A. V.; Carroll, P. J.; Dalosto, S.; A., V. S., *Inorg. Chem.* **2002**, *41*, 6944.
32. Hanack, M.; Zipplies, T., *J. Am. Chem. Soc.* **1985**, *107*, 6127.
33. Friedberg, J. S.; Skema, C.; Baum, E. D.; Burdick, J.; Vinogradov, S. A.; Wilson, D. F.; Horan, A. D.; Nachamkin, I., *J. Antimicrob. Chemother.* **2001**, *48*, 105.
34. Yasuike, M.; Yamaoka, T.; Ohno, O.; Sakuragi, M.; Ichimura, K., *Inorg. Chim. Acta* **1991**, *184*, 191.
35. Ambrose, W. P.; Moerner, W. E., *Chem. Phys.* **1990**, *144*, 71.

36. Chen, P. L.; Tomov, I. V.; Dvornikov, A. S.; Nakashima, M.; Roach, J. F.; Alabran, D. M.; Rentzepis, P. M., *J. Phys. Chem.* **1996**, *100*, 17507.
37. Ono, N.; Ito, S.; Wu, C. H.; Chen, C. H.; Wen, T. C., *Chem. Phys.* **2000**, *262*, 467.
38. Vogel, E.; Grigat, I.; Köcher, M.; Lex, J., *Angew. Chem.* **1989**, *101*, 1687.
39. Setsune, J.; Kashihara, K.; Wada, K.; Shiozaki, H., *Chem. Lett.* **1999**, 847.
40. Cissell, J. A.; Vaid, T. P.; Yap, G. P. A., *Org. Lett.* **2006**, *8*, 2401.
41. Weiss, A.; Hodgson, M. C.; Boyd, P. D. W.; Siebert, W.; Brothers, P. J., *Chem. Eur. J.* **2007**, *13*, 5982.
42. Chen, X.-G.; Liu, C.; Shen, D.-M.; Chen, Q.-Y., *Synthesis* **2009**, 3860.
43. Yamamoto, Y.; Hirata, Y.; Kodama, M.; Yamaguchi, T.; Matsukawa, S.; Akiba, K.; Hashizume, D.; Iwasaki, F.; Muranaka, A.; Uchimar, T.; Chen, P.; Kadish, K. M.; Kobayashi, N., *J. Am. Chem. Soc.* **2010**, *132*, 12627.
44. Sugawara, S.; Hirata, Y.; Kojima, S.; Yamamoto, Y.; Miyazaki, E.; Takimiya, K.; Matsukawa, S.; Hashizume, D.; Mack, J.; Kobayashi, N.; Fu, Z.; Kadish, K. M.; Sung, Y. M.; Kim, K. S.; Kim, D., *Chem. Eur. J.* **2012**, *18*, 3566.
45. Leznoff, C. C.; Lever, A. B. P., *Phthalocyanines: Properties and Applications*. VCH Publishers: New York, **1993**; Vol. 3.
46. L'Her, M.; Pondaven, A., In *The Porphyrin Handbook*, Kadish, K. M.; Smith, K. M.; Guillard, R., Eds. Academic Press: New York, **2003**; Vol. 16, p 117.
47. Fukuda, T.; Kobayashi, N., In *Handbook of Porphyrin Science*, Kadish, K. M.;

- Smith, K. M.; Guillard, R., Eds. World Scientific: Singapore, **2010**; Vol. 9, p 3.
48. Leznoff, C. C.; Lever, A. B. P., *Phthalocyanines: Properties and Applications*. VCH: New York, **1989**; Vol. 1.
49. McKeown, N. B., *Phthalocyanine Materials: Synthesis, Structure, and Function*. Cambridge University Press: Cambridge, **1998**.
50. Hanack, M.; Schneider, T.; Barthel, M.; Shirk, J. S.; Flom, S. R.; Pong, R. G. S., *Coord. Chem. Rev.* **2001**, 219, 235.
51. Cook, M. J., *Chem. Rec.* **2002**, 2, 225.
52. O'Flaherty, S. M.; Hold, S. V.; Cook, M. J.; Torres, T.; Chen, Y.; Hanack, M.; Blau, W. J., *Adv. Mater.* **2003**, 15, 19.
53. Chen, Y.; Hanack, M.; Araki, Y.; Ito, O., *Chem. Soc. Rev.* **2005**, 34, 517.
54. Inabe, T., *Chem. Soc. Jpn* **2005**, 78, 1373.
55. de la Torre, G.; Claessens, C. G.; Torres, T., *Chem. Comm.* **2007**, 2000.
56. Nyokong, T., *Coord. Chem. Rev.* **2007**, 251, 1707.
57. Kudrevich, S. V.; van Lier, J. E., *Coord. Chem. Rev.* **1996**, 156, 163.
58. Donzello, M. P.; Ercolani, C.; Stuzhin, P. A.; Chiesi-Villa, A.; Rizzoli, C., *Inorg. Chem.* **1999**, 2075.
59. Michel S, L. J.; Hoffman, B. M.; Baum, S. M.; Barrett A, G. M., *Progress in Inorganic Chemistry*. J. Wiley & Sons: **2001**; p 473.
60. Donzello, M. P. D., D.; D'Arcangelo, G.; Zhan, R.; Ou, Z.; Ercolani, C.; Stuzhin, P.A.;

- Kadish, K. M., *J. Am. Chem. Soc.* **2003**, *125*, 14190.
61. Stuzhin, P. A.; Ercolani, C., The Porphyrin Handbook. In Kadish, K. M.; Smith, K. M.; Guillard, R., Eds. Academic Press: New York, **2003**; Vol. 15, p 263.
62. Donzello, M. P.; Ou, Z.; Dini, D.; Meneghetti, M.; Ercolani, C.; Kadish, K. M., *Inorg. Chem.* **2004**, *43*, 8637.
63. Donzello, M. P.; Ou, Z.; Monacelli, F.; Ricciardi, G.; Rizzoli, C.; Ercolani, C.; Kadish, K. M., *Inorg. Chem.* **2004**, *43*, 8626.
64. Donzello, M. P.; Ercolani, C.; Stuzhin, P. A., *Coord. Chem. Rev.* **2006**, *250*, 1530.
65. Donzello, M. P.; Ercolani, C.; Kadish, K. M.; Ricciardi, G.; Rosa, A.; Stuzhin, P. A., *Inorg. Chem.* **2007**, *46*, 4145.
66. Donzello, M. P.; Ercolani, C.; Mannina, L.; Viola, E.; Bubnova, A.; Khelevina, O. G.; Stuzhin, P. A., *Aus. J. Chem.* **2008**, *61*, 262.
67. Donzello, M. P.; Viola, E.; Cai, X.; Mannina, L.; Rizzoli, C.; Ricciardi, G.; Ercolani, C.; Kadish, K. M.; Rosa, A., *Inorg. Chem.* **2008**, *47*, 3903.
68. Donzello, M. P.; Ercolani, C.; Kadish, K. M.; Ricciardi, G.; Rosa, A., *Inorg. Chem.* **2009**, *48*, 9890.
69. Viola, E.; Donzello, M. P.; Ciattini, S.; Portalone, G.; Ercolani, C., *Eur. J. Inorg. Chem.* **2009**, 1600.
70. Donzello, M. P.; Fujimori, M.; Miyoshi, Y.; Yoshikawa, H.; Viola, E.; Awaga, K.; Ercolani, C., *J. Porphyrins Phthalocyanines* **2010**, *14*, 343.

71. Mori, G. D.; Fu, Z.; Viola, E.; Cai, X.; Ercolani, C.; Donzello, M. P.; Kadish, K. M.,
Inorg. Chem. **2011**, *50*, 8225.
72. Donzello, M. P.; Viola, E.; Fu, Z.; Ercolani, C., *J. Porphyrins Phthalocyanines* **2011**,
15, 984.

Chapter Two
Experimental Methods

2.1 Electrochemistry

2.1.1 Cyclic Voltammetry

Cyclic voltammetry is a powerful technique to rapidly measure redox potentials and determine the stability of the electroreduced and electrooxidized species in solution.¹ In the cyclic voltammetric experiment, a potential is applied to a working electrode and linearly varied in a positive or negative direction between an initial and a pre-defined limiting value, after which the potential sweep is reversed, and scanned in the opposite direction¹⁻³ as shown in Figure 2-1a for the case of a compound which undergoes two one-electron reductions over the investigated potential range. Current flowing at the working electrode is measured and plotted versus the applied voltage to give the cyclic voltammogram in Figure 2-1b. The peak current for reduction is given by i_{pc} , while that for oxidation is given by i_{pa} . At 25 °C, the magnitude of the peak current is defined by the Randles-Sevcik equation¹ given in Equation 2-1,

$$i_p = (2.69 \times 10^5) n^{3/2} A C D^{1/2} v^{1/2} \quad (2-1)$$

where i_p is the peak current in μA , n is number of electrons transferred, A is the electrode area in cm^2 , D is the diffusion coefficient of the species in cm^2/s , C is the bulk concentration of the species in mol/cm^3 , and v is the scan rate in V/s . For the example shown in Figure 2-1, the potential is scanned between 0.00 and -2.00 V in 20 sec on the forward scan and between -2.00 and 0.00 V in 20 sec on the reverse scan, and the scan rate is 0.1 V/s.

For a reversible electron transfer process, the half-wave potential, $E_{1/2}$, is defined by the average values of the anodic and cathodic peak potentials (Equation 2-2).

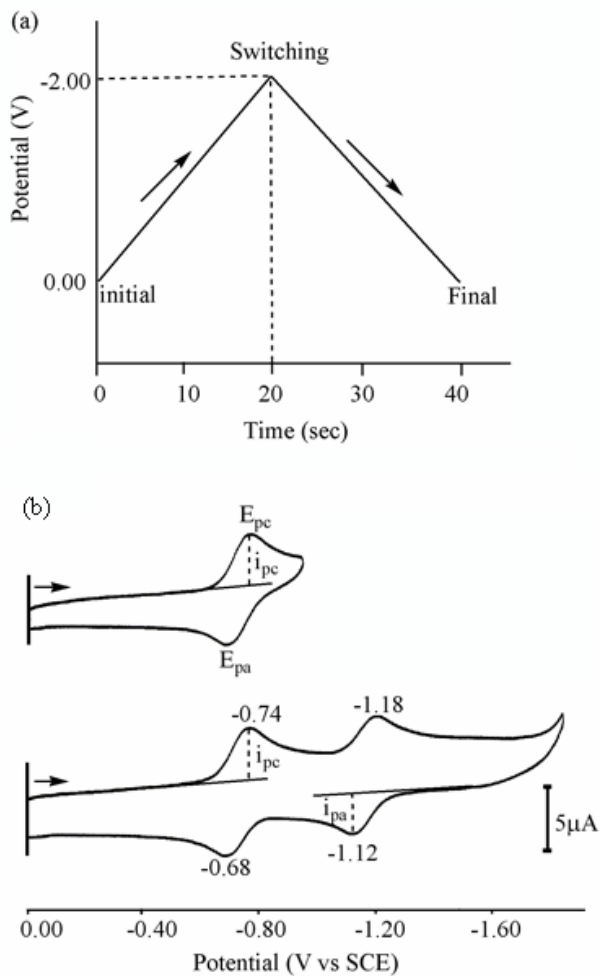


Figure 2-1. (a) Cyclic voltammetry waveform showing reduction sweep between 0.00 to -2.00 V at a scan rate ($\Delta E/\Delta t$) of 0.1 V/s and (b) resulting cyclic voltammograms for compound which undergoes two one-electron reductions at $E_{1/2} = -0.71$ and -1.15 V.

$$E_{1/2} = \frac{E_{pa} + E_{pc}}{2} \quad (2-2)$$

For the specific example in Figure 2-1b, the measured $E_{1/2} = -0.71$ and -1.15 V vs SCE, ie, the average of $\frac{1}{2}[-0.74 + (-0.68)]$ and $\frac{1}{2}[-1.12 + (-1.18)]$, respectively. The cathodic and anodic peak currents for the process in Figure 2-1b are about equal, which indicates stable electrogenerated species in solution.

All cyclic voltammograms in this Dissertation were obtained with an EG&G Princeton Applied Research (PAR) 173 potentiostat. A homemade three-electrode cell (see Figure 2-2) was used and consisted of a platinum button or glassy carbon working electrode (WE), a platinum counter electrode (CE) and a homemade saturated calomel reference electrode (SCE). The SCE was separated from the bulk of the solution by a fritted glass bridge of low porosity which contained the solvent/supporting electrolyte mixture. The saturated KCl solution in the SCE was changed periodically for maintaining the correct potential. Ferrocene was utilized to be an internal reference to check the potentials.

2.2 UV-Visible Spectroelectrochemistry

UV-visible spectroelectrochemical experiments were performed with an optically transparent platinum thin-layer working electrode (Figure 2-3),⁴ which enabled electrochemical and the spectroscopic measurements to be carried out simultaneously. Potentials were applied and monitored with an EG&G PAR Model 173 Potentiostat. Time-resolved UV-visible spectra were recorded with a Hewlett-Packard Model 8453

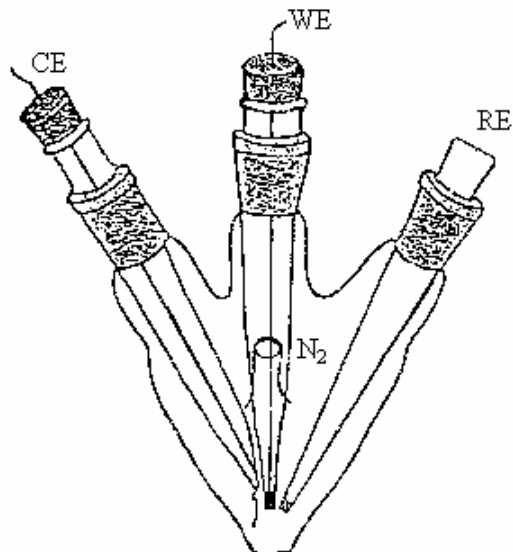


Figure 2-2. Schematic illustration of the electrochemical cell. WE, CE and RE are the working, counter and reference electrodes, respectively.

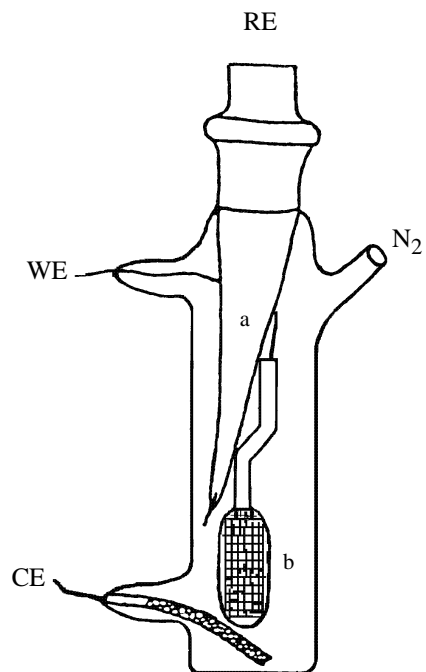


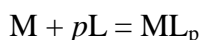
Figure 2-3. Schematic illustration of the thin-layer UV-visible spectroelectrochemical cell. a) platinum tipped bridge and b) platinum net. WE, CE and RE are the working, counter and reference electrodes, respectively.

diode array rapid-scanning spectrophotometer.

2.3 Spectral Titration Methods for Determination of Equilibrium Constants⁵

Equilibrium constants for the binding of an axial ligand to the central metal ion of a metallomacrocycle or the loss/addition of protons to the dipyrrolylquinoxalines were determined using both spectral and electrochemical titration methods. Stock solutions were prepared for each specific ligand (and H⁺ or OH⁻ in the case of acid or base titration) and measurements were made after each aliquot was quantitatively added to solutions containing the investigated compound. UV-visible absorbance changes and/or reduction potentials were then plotted vs free ligand, H⁺ or OH⁻ concentration in solution.

The spectral titration method described below, was used to obtain the logK or logβ values and the number of added or lost axial ligands during the electron transfer processes. For ligand binding reaction:



the relationship between the concentrations of M and ML_p in solution and the equilibrium constant, log K, is given by Equation 2-3.

$$\log([ML_p]/[M]) = \log K + p \log [L] \quad (2-3)$$

where [M] and [ML_p] are the concentrations of the unligated and ligated species and [L] is the free-ligand concentration in solution. A wavelength is selected where M and ML_p have different UV-visible spectra and the absorbance is then proportional to concentration as shown below,

$$A_0 = \epsilon_M b C_M$$

$$A_f = \varepsilon_{ML_p} b C_{ML_p}$$

$$A_i = \varepsilon_M b [M] + \varepsilon_{ML_p} b [ML_p]$$

where C_M and C_{ML_p} are the total concentration of M or ML_p , ε is the molar absorptivity, b is the path length, A_0 and A_f are the initial and final absorbances at a given wavelength (λ_{max}) for the species M and ML_p , respectively, and A_i is the absorbance at λ_{max} at a given point in the titration.

According to the mass balance equation: $C_M = C_{ML_p} = [M] + [ML_p]$, and then can write:

$$\begin{aligned} A_i &= \varepsilon_M b [M] + \varepsilon_{ML_p} b [ML_p] \\ &= \varepsilon_M b (C_M - [ML_p]) + \varepsilon_{ML_p} b [ML_p] \\ &= \varepsilon_M b C_M - \varepsilon_M b [ML_p] + \varepsilon_{ML_p} b [ML_p] \\ &= A_0 + (\varepsilon_{ML_p} - \varepsilon_M) b [ML_p] \\ [ML_p] &= (A_i - A_0) / [(\varepsilon_{ML_p} - \varepsilon_M) b] \\ \text{or } A_i &= \varepsilon_M b [M] + \varepsilon_{ML_p} b [ML_p] \\ &= \varepsilon_M b [M] + \varepsilon_{ML_p} b (C_{ML_p} - [M]) \\ &= \varepsilon_M b [M] + \varepsilon_{ML_p} b C_{ML_p} - \varepsilon_{ML_p} b [M] \\ [M] &= (A_f - A_i) / [(\varepsilon_{ML_p} - \varepsilon_M) b] \end{aligned}$$

Substituting the values of $[M]$ and $[ML_p]$ into Equation 2-3 gives a relevant equation used to calculate $\log K$ and the number of ligand gained or lost (p):

$$\log((A_i - A_0)/(A_f - A_i)) = \log K + p \log [L] \quad (2-4)$$

A graph of $\log((A_i - A_0)/(A_f - A_i))$ versus $\log [L]$ should be a straight line whose slope corresponds to the number of ligands (p) axially bound to the compound and intercept

gives formation constant (log K). Examples are given in Figure 4-12 in this Dissertation.

2.4 Other Experimental Methods

2.4.1 Degassing of the Solution

High purity nitrogen was used to deoxygenate the solutions for 5 -10 minutes before each electrochemical experiment and a positive nitrogen pressure was maintained above the solution throughout the experiment.

2.4.2 Temperature Control

All electrochemical experiments were performed at room temperature ($22 \pm 1^\circ\text{C}$) unless otherwise noted. A dry ice/acetone mixture was used to obtain variable temperatures that varied from 22 to -75°C . The exact temperature was monitored using a mercury thermometer and the cell was centered in a slush bath containing the dry ice and acetone mixture.

2.5 Chemicals and Investigated Compounds

Benzonitrile (PhCN) obtained from Fluka Chemicals was distilled over phosphorous pentoxide (P_2O_5) under vacuum prior to use. Absolute dichloromethane (CH_2Cl_2) was purchased from EMD Chemicals. Pyridine (99.9+%), dimethyl sulfoxide (DMSO, 99.9+%), N,N-dimethylformamide (DMF, 99.8+%) and acetonitrile (MeCN) were purchased from Sigma-Aldrich Co. and used without further purification. High purity N_2 from Matheson-Trigas was used to deoxygenate the solution before each electrochemical experiment. Tetra-*n*-butylammonium perchlorate (TBAP) and

tetra-*n*-butylammonium hexafluoro-phosphate (TBAPF₆) were purchased from Sigma Aldrich and used without further purification. Trifluoroacetic acid (TFA), tetra-*n*-butylammonium hydroxide (TBAOH), tetra-*n*-butylammonium fluoride (TBAF) and tetra-*n*-butylammonium acetate (TBAOAc) were also purchased from Sigma Aldrich and used without further purification.

All compounds investigated as part of this dissertation were obtained from our collaborators in the U.S., Japan, Australia and Italy and their purity verified by spectral methods in our laboratory. The specific compounds provided to us and references as to their synthesis are given below.

Compounds in the dipyrrolylquinoxaline series were obtained from Prof. Jonathan L. Sessler at University of Texas in Austin and were synthesized in his laboratory according to published procedures.^{6, 7} The tris- and tetrakis-quinoxalinoporphyrins and their metal complexes were obtained from Prof. Maxwell J. Crossley at the University of Sydney in Australia and were synthesized in his lab according to published procedures.⁸ Tetraphenyltetrabenzoporphyrin copper and zinc complexes together with their oxidized forms were obtained from Prof. Yohsuke Yamamoto at Hiroshima University in Japan. Synthetic methods for preparation of these complexes have also been reported in the literature.⁹ Tetrakis-2,3-[5,6-di(2-thiophenyl)pyrazino]porphyrine and its metal complexes together with the tetrakis-2,3-[5,6-di(2-pyridyl)pyrazino]porphyrine with exocyclic (Pt^{II}) metal ion binding were provided by Prof. Claudio Ercolani at Università degli Studi di Roma, Italy. The synthetic methods for these compounds are reported in the literature.^{10, 11}

2.6 References

1. Bard, A. J.; Faulkner, L. R., *Electrochemical Methods: Fundamentals and Applications*. 2 ed.; Wiley: New York, **2000**.
2. Nicholson, R. S.; Irving, S., *Anal. Chem.* **1964**, *36*, (4), 706.
3. Heinze, J., *Angew. Chem., Int. Ed.* **1984**, *23*, (11), 831.
4. Lin, X. Q.; Kadish, K. M., *Anal. Chem.* **1985**, *57*, 1498.
5. Bronilt, D.; Rougee, M., *Biochemistry* **1974**, *13*, 4519.
6. Black, C. B.; Andrioletti, B.; Try, A. C.; Ruiperez, C.; Sessler, J. L., *J. Am. Chem. Soc.* **1999**, *121*, 10438.
7. Mizuno, T.; Wei, W.; Eller, L. R.; Sessler, J. L., *J. Am. Chem. Soc.* **2002**, *124*, (7), 1134.
8. Khoury, T.; Crossley, M. J., *New J. Chem.* **2009**, *33*, 1076.
9. Sugawara, S.; Hirata, Y.; Kojima, S.; Yamamoto, Y.; Miyazaki, E.; Takimiya, K.; Matsukawa, S.; Hashizume, D.; Mack, J.; Kobayashi, N.; Fu, Z.; Kadish, K. M.; Sung, Y. M.; Kim, K. S.; Kim, D., *Chem. Eur. J.* **2012**, *18*, 3566.
10. Mori, G. D.; Fu, Z.; Viola, E.; Cai, X.; Ercolani, C.; Donzello, M. P.; Kadish, K. M., *Inorg. Chem.* **2011**, *50*, 8225.
11. Donzello, M. P.; Viola, E.; Fu, Z.; Ercolani, C., *J. Porphyrins Phthalocyanines* **2011**, *15*, 984.

Chapter Three

Disproportionation of Dipyrrolylquinoxaline Radical Anions via the Internal Protons of the Pyrrole Moieties

3.1 Introduction

Disproportionation of one-electron reduced species plays an important role in converting one-electron processes to two-electron processes in a variety of chemical and biological redox reactions.¹⁻⁶ Notable examples are the disproportionation (dismutation) of superoxide anion and the disproportionation of semiquinone radical anions in photosynthesis.⁷⁻¹² In both cases, external protons are required for the disproportionation to occur.¹³⁻¹⁶ Furthermore, to the best of our knowledge there are no examples in the literature, chemical or biological, where disproportionation of radical anions is mediated by internal protons, i.e., those present within the compounds that are reduced.

We report herein the first example of such a transformation. Specifically, we describe the chemical fate of dipyrrolylquinoxaline-derived radical anions, and show that the internal pyrrole protons are involved in the disproportionation of these radical anions. The electron-transfer reduction of the dipyrrolylquinoxalines of this study is compared with that of the same quinoxaline units without pyrrole moieties, and detailed below dramatic differences are seen. In particular, the radical anions of simple quinoxalines lacking appended pyrrole subunits are stable, with disproportionation only occurring in the presence of external protons.

In this study, the redox properties of the three dipyrrolylquinoxaline derivatives shown in Chart 3-1, namely, 2,3-dipyrrol-2'-yl-6,7-dinitroquinoxaline (**1H₂**), 2,3-dipyrrol-2'-yl-6-nitroquinoxaline (**2H₂**) and 2,3-dipyrrol-2'-ylquinoxaline (**3H₂**),¹⁷⁻¹⁹ were examined. Also studied were the corresponding quinoxalines bearing the same number of electron-withdrawing nitro groups but without the two hydrogen-containing pyrrole substituents (compounds **4-6**).

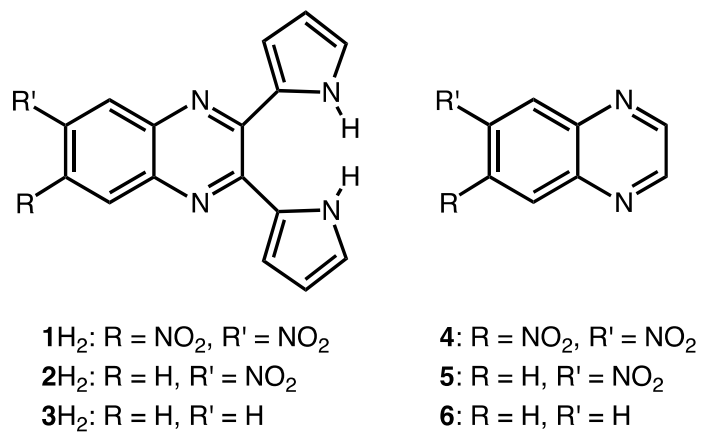


Chart 3-1. Structures of Investigated Dipyrrolylquinoxalines.

3.2 Results and Discussion

Figure 3-1 shows cyclic voltammograms of **1H₂**-**3H₂** and **4-6** in acetonitrile (CH₃CN). In the case of **1H₂** and **2H₂**, the first reduction is reversible when the negative potential scan is reversed just after the first cathodic peak (broken line in Figure 3-1). After the second and third cathodic peaks are observed, however, the corresponding anodic peak of the first reduction disappears (solid line in Figure 3-1).

In the case of **4** and **5**, which have the same quinoxaline units as **1H₂** and **2H₂** but lack the pyrrole moieties, the first and second reductions are both reversible and lead stepwise to formation of the corresponding radical anion and dianion. The differential pulse voltammetry (DPV) current of the first reduction of **1H₂** is twice as large as the current for the second and third reductions, as shown in Figure 3-2.

The data from the DPV analysis of **1H₂** are self-consistent with the results from cyclic voltammetry results and lead us to suggest that the first reduction is followed by a disproportionation of **1H₂^{•-}** to produce **1H⁻** and **1H₃⁻** (Scheme 3-1). The generated **1H₃⁻** is already reduced by two electron, but the anion **1H⁻** has an unreduced π ring system, and further undergoes two stepwise one-electron reductions at $E_{pc} = -1.06$ and $E_{1/2} = -1.27$ V (Figure 3-1). Because the concentration of **1H₂^{•-}** is half that of the initial compound, the DPV current for the first reduction of **1H₂** is twice that measured for the reduction of **1H⁻** and **1H²⁻** because **1H₃⁻** is not reduced (Figure 3-2). Similar results are seen for **2H₂** and **3H₂**.

The three reductions of **1H₂** and **2H₂** occur at more positive potentials than that of **3H₂**, which lacks the electron-withdrawing NO₂ groups (Figure 3-1). In addition, the single reduction observed for **3H₂** (within the solvent negative potential range) is

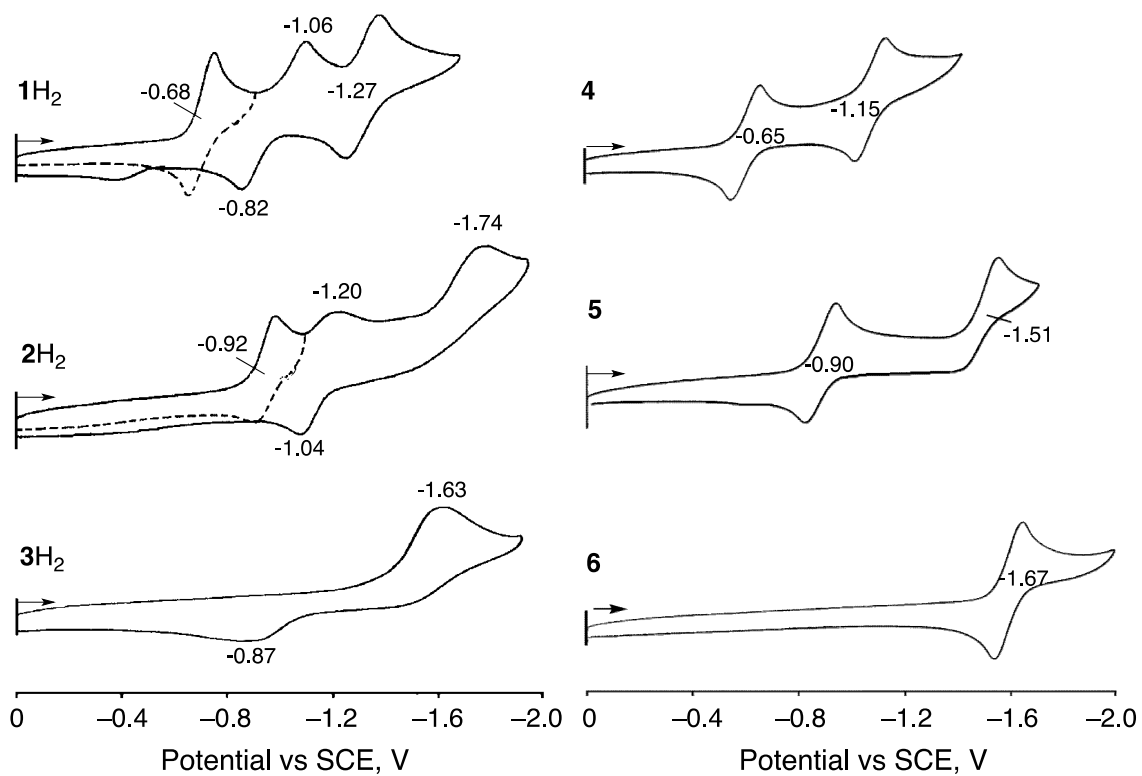


Figure 3-1. Cyclic voltammograms of $1H_2$ - $3H_2$ and **4-6** in deaerated CH_3CN containing TBAP (0.10 M) at 298 K.

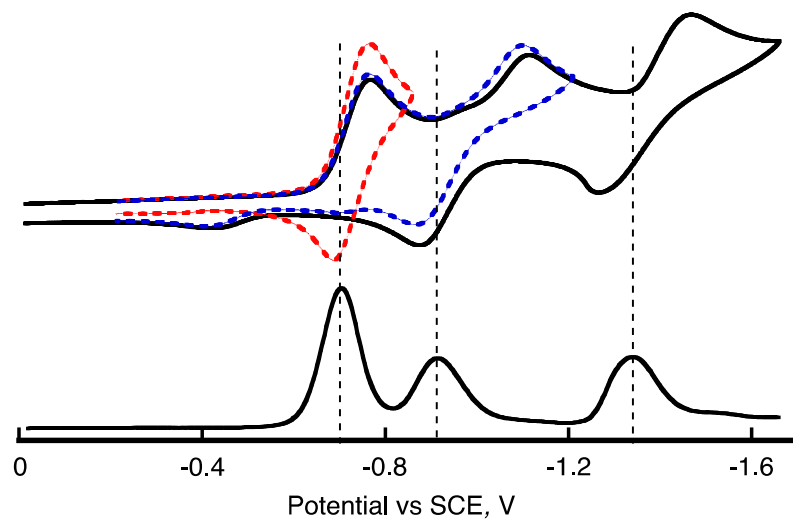
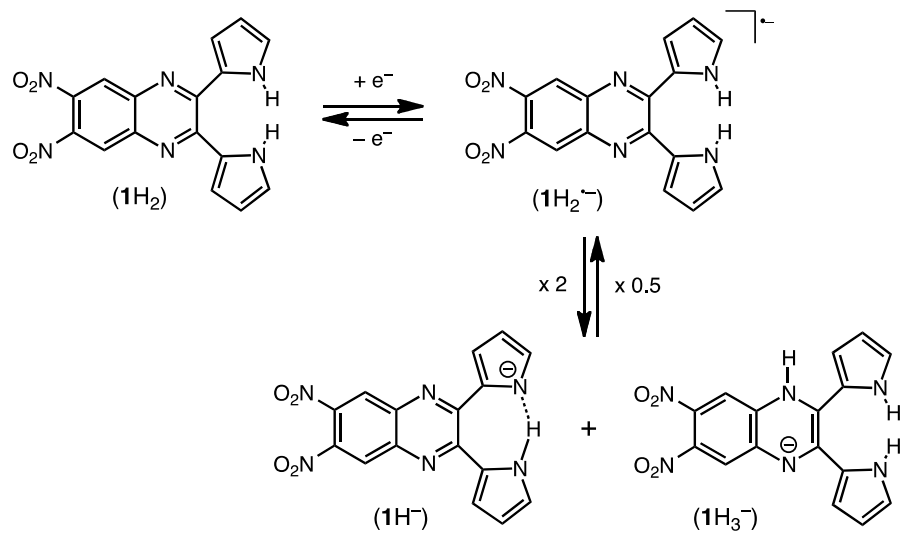


Figure 3-2. Cyclic voltammogram and differential pulse voltammogram of $1H_2$ in CH_3CN containing TBAP (0.10 M) at 298 K; scan rate: 0.1 V s^{-1} . Dashed lines are the initial first and second reductions.²⁰



Scheme 3-1. First steps in reduction of **1H₂** in CH_3CN .

irreversible and remains irreversible at all scan rates and temperatures. Such a finding is consistent with the disproportionation of $3\mathbf{H}_2^{\bullet-}$ being significantly faster than that of either $1\mathbf{H}_2^{\bullet-}$ or $2\mathbf{H}_2^{\bullet-}$.

In order to identify the processes that occur following the first reduction of $1\mathbf{H}_2$, a chemical reduction of $1\mathbf{H}_2$ by cobaltocene (CoCp_2) to $1\mathbf{H}_2$ was examined in Osaka.²⁰ The UV-vis spectral changes that occur during this reaction are shown in Figure 3-3a and gave similar results as observed for the electrochemical reduction carried out in Houston. The absorption changes at 325 and 553 nm were both found obey second-order kinetics, as illustrated in Figure 3-3b (for the second-order plot, cf. Figure 3-4). This leads us to suggest that rapid electron transfer takes place from CoCp_2 to $1\mathbf{H}_2$ to afford the radical anion ($1\mathbf{H}_2^{\bullet-}$, $\lambda_{\text{max}} = 325$ nm) and CoCp_2^+ ($\lambda_{\text{max}} = 260$ nm), a process that is followed by the disproportionation of $1\mathbf{H}_2^{\bullet-}$ via a hydrogen-atom transfer or a concerted proton-coupled electron-transfer (not stepwise) process, as shown in Scheme 3-1. The products of the disproportionation were examined in Osaka by ^1H NMR spectroscopy and confirmed to be $1\mathbf{H}^-$ and $1\mathbf{H}_3^-$ (see Figures 3-5 and 3-6).

The same mono-deprotonated product ($1\mathbf{H}^-$) could also be obtained by the reaction of $1\mathbf{H}_2$ with tetra-*n*-butylammonium hydroxide (TBAOH) as described in the literature;²¹ this species is characterized by an absorption band at $\lambda_{\text{max}} = 553$ nm as seen in Figure 3-3. The titration of $1\mathbf{H}_2$ with TBAOH indicate that $1\mathbf{H}^-$ and 1^{2-} are formed respectively by the reaction of $1\mathbf{H}_2$ with 1 and 2 equiv. of TBAOH, the exact product being dependent upon the concentrations (dissociation) of $1\mathbf{H}_2$ in solution. Additional details for this reaction are discussed in Chapter Four.

Our assignment of a strong N-H-N hydrogen bond in the mono-deprotonated product

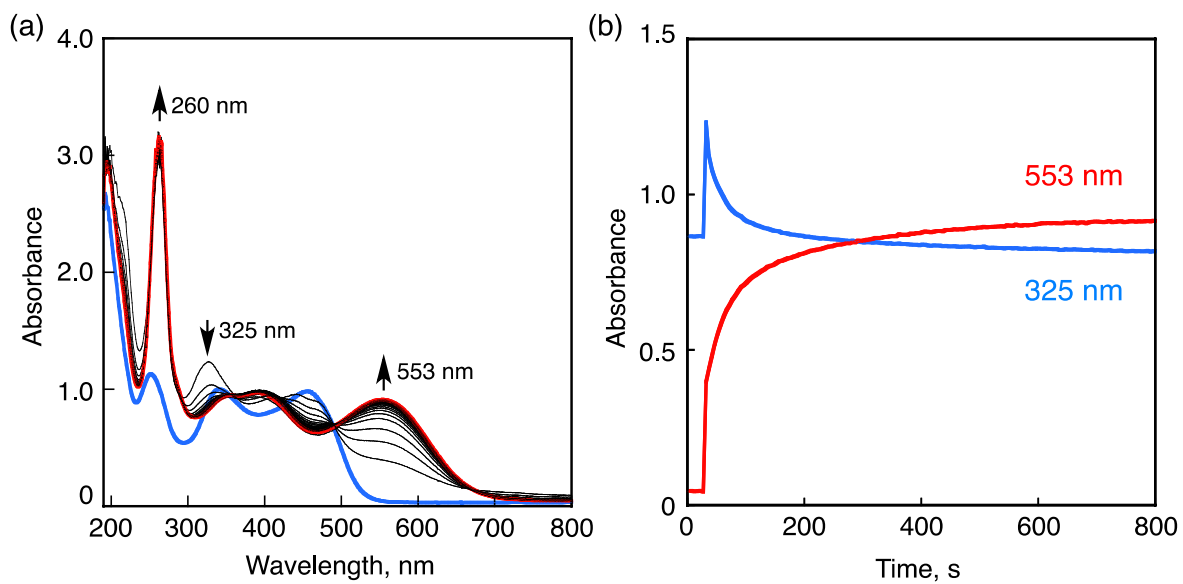


Figure 3-3. (a) Absorption spectral changes observed upon electron transfer from CoCp_2 (5.0×10^{-5} M) to 1H_2 (5.0×10^{-5} M) in CH_3CN at 303 K. (b) Time courses at 325 and 553 nm.²⁰

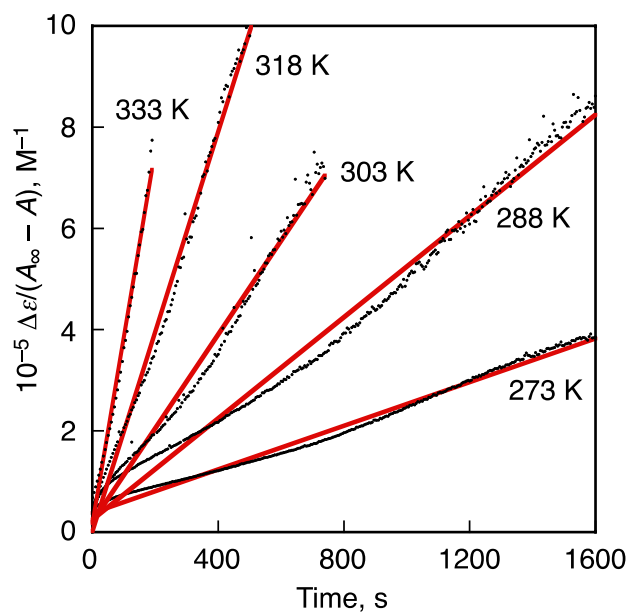


Figure 3-4. Second-order plots for disproportionation of $1\text{H}_2^{\bullet-}$ produced in electron transfer from CoCp_2 ($2.5 \times 10^{-5} \text{ M}$) to 1H_2 ($2.5 \times 10^{-5} \text{ M}$) in CH_3CN at various temperatures (273-333 K).²⁰

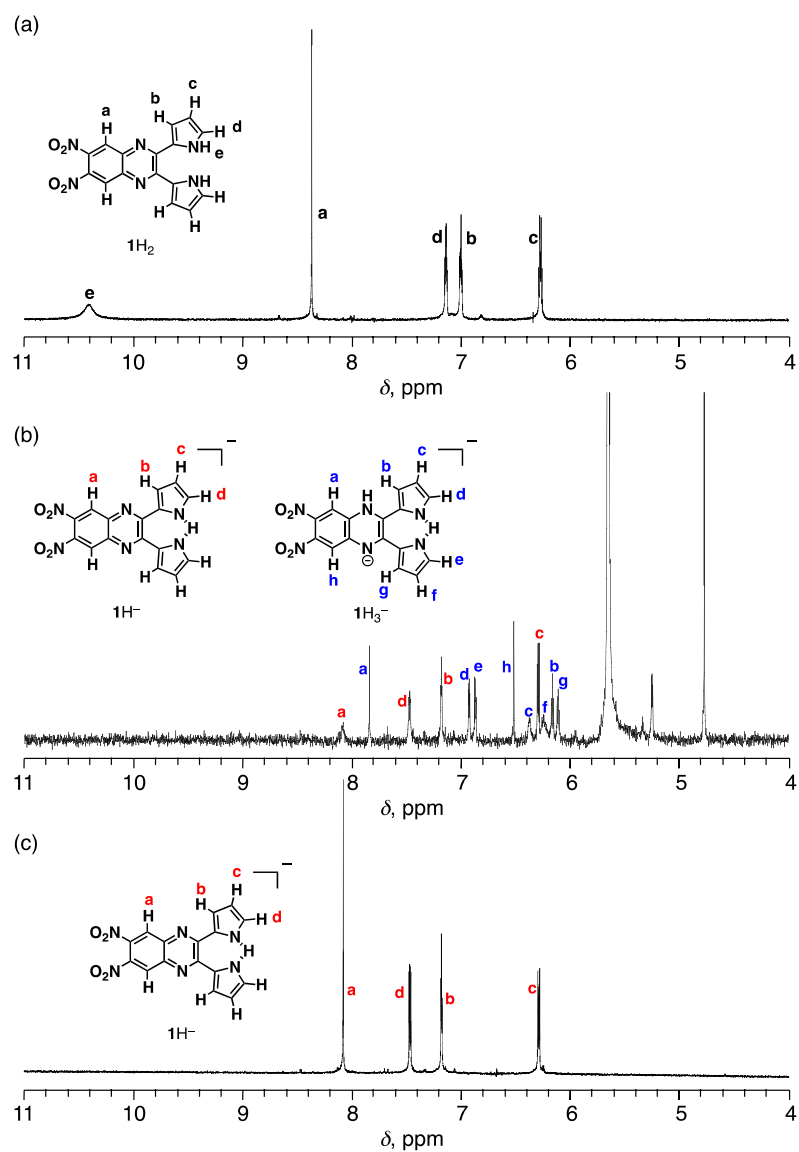


Figure 3-5. ^1H NMR spectra of (a) 1H_2 , (b) 1H^- and 1H_3^- produced by electron-transfer reduction of 1H_2 (5.0 mM) with CoCp_2 (5.0 mM) and (c) 1H^- produced by deprotonation of 1H_2 (5.0 mM) with Bu_4NOH (5.0 mM) in deaerated CD_3CN .²⁰

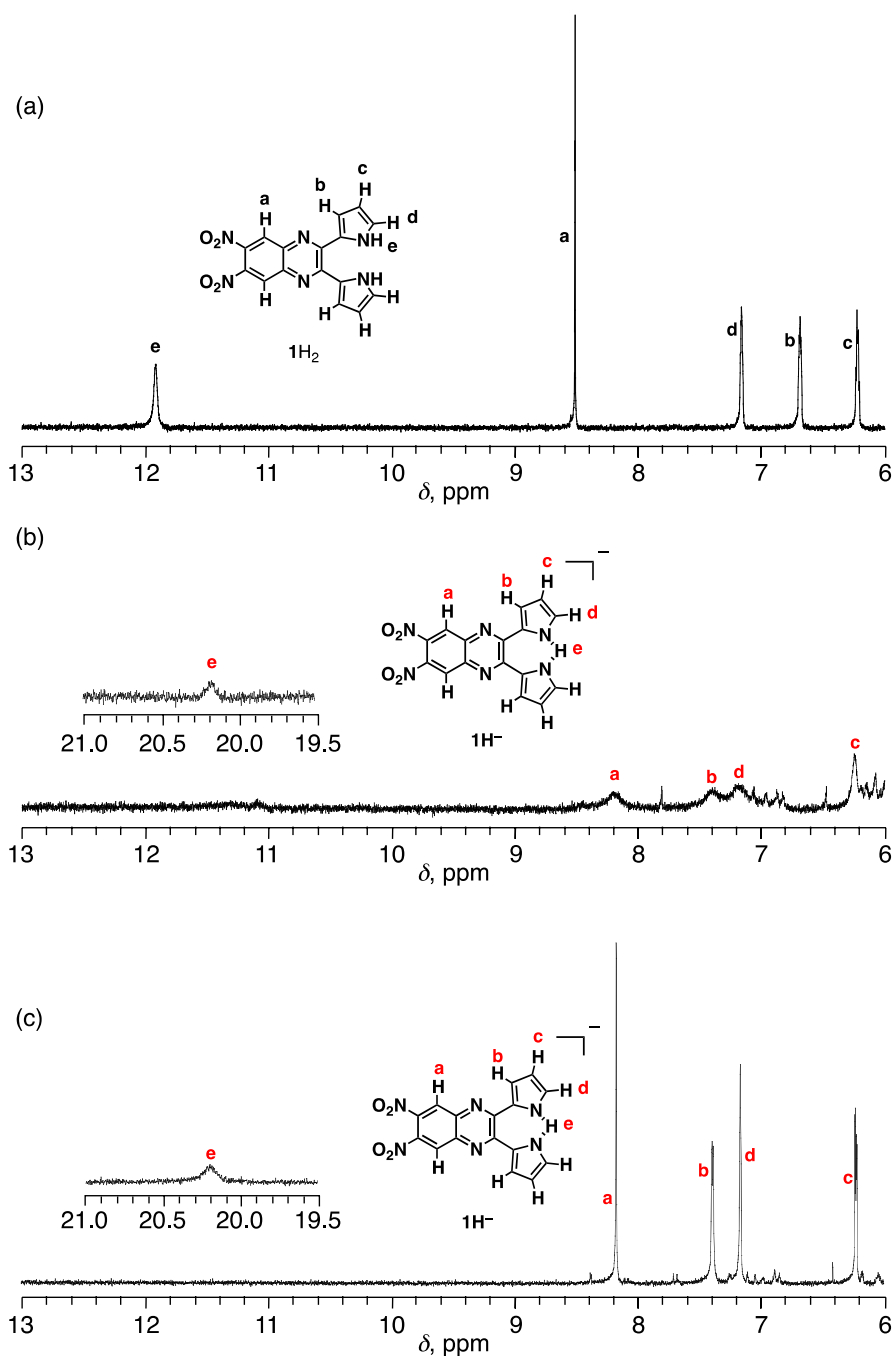


Figure 3-6. ^1H NMR spectra of (a) $\mathbf{1H}_2$, (b) $\mathbf{1H}^-$ and $\mathbf{1H}_3^-$ produced by electron-transfer reduction of $\mathbf{1H}_2$ (5.0 mM) with CoCp_2 (5.0 mM) and (c) $\mathbf{1H}^-$ produced by deprotonation of $\mathbf{1H}_2$ (5.0 mM) with Bu_4NOH (5.0 mM) in deaerated $\text{DMSO-}d_6$.²⁰

from $\mathbf{1H}_2^{\bullet-}$ (Scheme 3-1) is based on the observation that the ^1H NMR spectral features are analogous to what was previously for the same compound under similar experimental conditions.²¹ The anion $\mathbf{1H}_3^-$ was also estimated from DFT calculations performed by our collaborators in Osaka (Figure 3-7a). The result of these calculations indicate that protonation at the quinoxaline unit is more favorable rather than that at the nitro group based on a comparison of the energies of the $\mathbf{1H}_3^-$ isomers.

The disproportionation equilibrium of $\mathbf{1H}_2^{\bullet-}$ was examined by measuring the EPR spectrum of $\mathbf{1H}_2^{\bullet-}$ produced by electron transfer from CoCp_2 to $\mathbf{1H}_2$ at various temperatures (Figure 3-8a). The simulated hyperfine coupling constants of $\mathbf{1H}_2^{\bullet-}$ agree well with the values estimated by DFT calculations (Figure 3-8b), providing support for spin delocalization on the quinoxaline moiety.

The disproportionation equilibrium constant (K) for $\mathbf{1H}_2^{\bullet-}$ was determined using the observed concentration of $\mathbf{1H}_2^{\bullet-}$, a value that was determined by comparing the value of the double integration of the EPR signal with that of diphenylpicryl-hydrazyl (DPPH), a stable radical reference, and plotted against temperature to give a Van't Hoff plot, shown in Figure 3-9. From the linear plot, ΔH and ΔS values were obtained from slope and intercept, as 18 kcal mol^{-1} and $68 \text{ cal mol}^{-1} \text{ K}^{-1}$, respectively. The positive ΔH value obtained in this way indicates that the disproportionation of $\mathbf{1H}_2^{\bullet-}$ is endothermic.

The activation enthalpy (ΔH^\ddagger) and entropy (ΔS^\ddagger) were calculated to be 33 kcal mol^{-1} and $-20 \text{ cal mol}^{-1} \text{ K}^{-1}$, respectively, from the Eyring plot of the disproportionation rate constants determined from the second-order decay of $\mathbf{1H}_2^{\bullet-}$ at various temperatures (see Figure 3-10).

The disproportionation of $\mathbf{1H}_2^{\bullet-}$, $\mathbf{2H}_2^{\bullet-}$ and $\mathbf{3H}_2^{\bullet-}$ to produce the three mono-

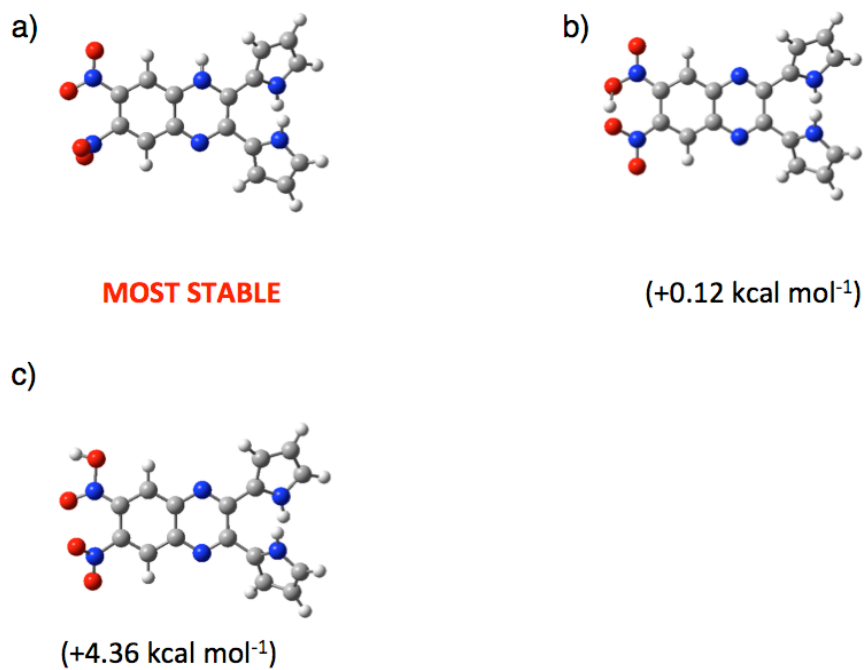


Figure 3-7. Optimized structures of 1H_3^- isomers as determined via DFT calculations carried out at the B3LYP/6-31G(d) level. Relative energies are given in parentheses.²⁰

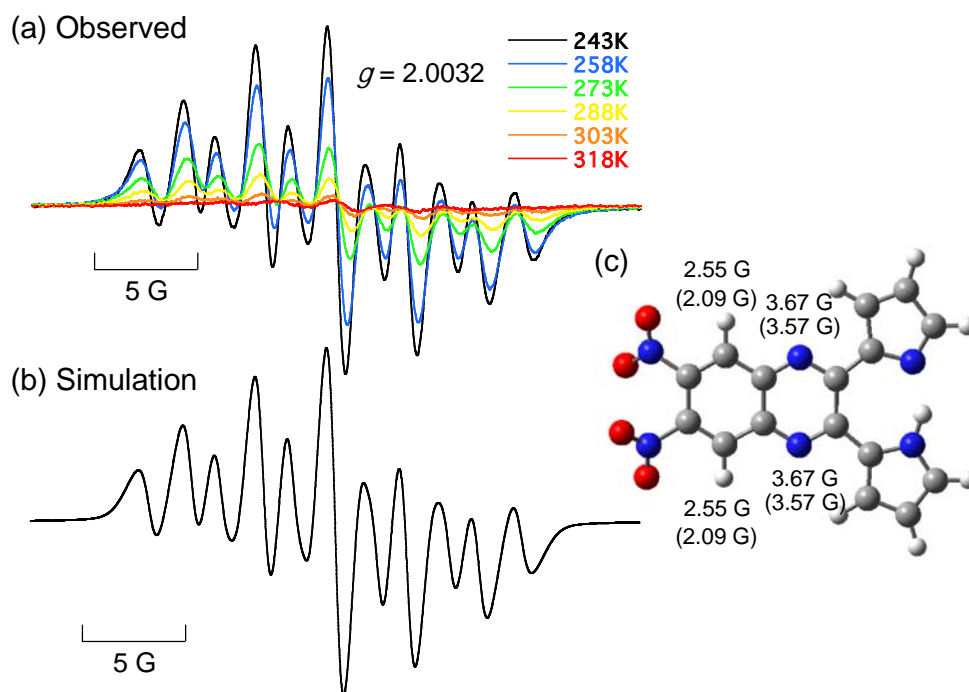


Figure 3-8. (a) EPR spectra of $1\text{H}_2^{\bullet-}$ produced via electron transfer from CoCp_2 (1.0×10^{-3} M) to 1H_2 (1.0×10^{-3} M) in CH_3CN at various temperatures. (b) Simulated spectrum of $1\text{H}_2^{\bullet-}$ using hyperfine coupling constants and those predicted by DFT calculations. (c) DFT optimized structure of $1\text{H}_2^{\bullet-}$ with *hfc* values together with the calculated values given in parentheses.²⁰

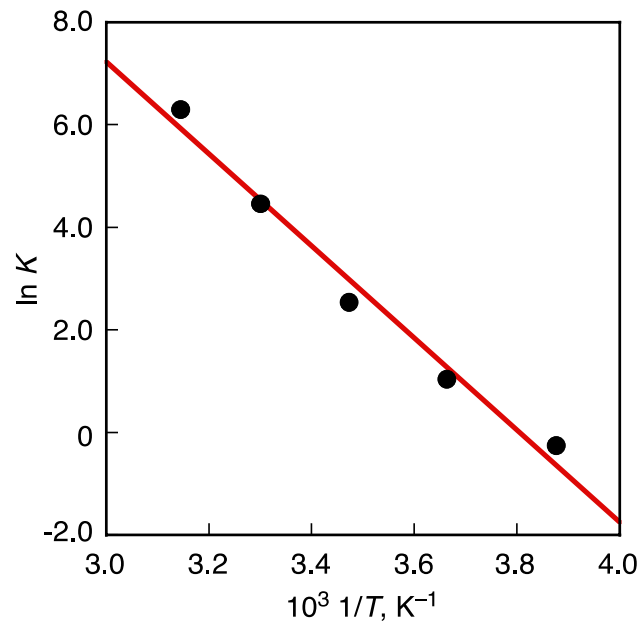


Figure 3-9. Van't Hoff plot of the disproportionation equilibrium constant (K) of $\mathbf{1H_2^{\bullet-}}$ in CH_3CN .²⁰

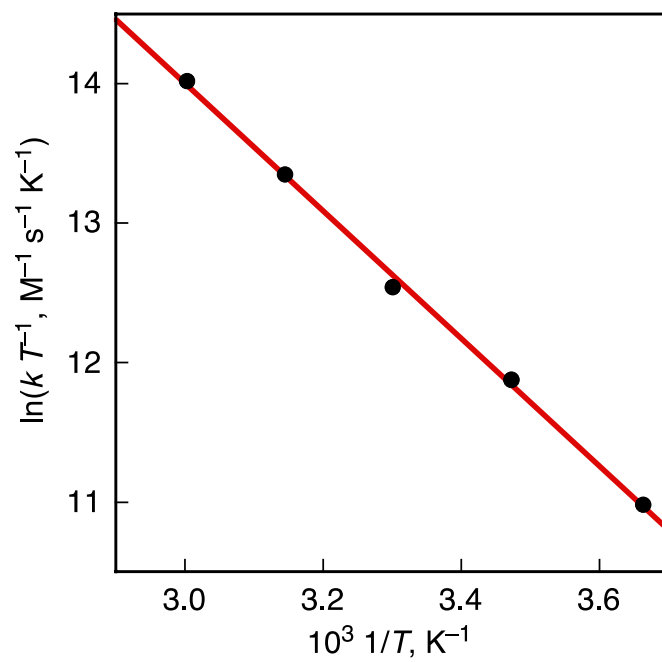


Figure 3-10. Eyring plot of the disproportionation of 1H_2^* in CH_3CN .²⁰

deprotonated dipyrrolylquinoxaline anions ($1H^-$, $2H^-$ and $3H^-$) and three mono-hydrodipyrrolylquinoxaline anions ($1H_3^-$, $2H_3^-$ and $3H_3^-$) was confirmed by spectroelectrochemical measurements of the type shown in Figure 3-11. The visible absorption spectra of the disproportionation products match those of mono-deprotonated dipyrrolylquinoxaline anions ($1H^-$, $2H^-$ and $3H^-$), because the monohydrodipyrrolylquinoxaline anions ($1H_3^-$, $2H_3^-$, and $3H_3^-$) absorb only minimally in the visible region. The absorption spectra of mono-deprotonated dipyrrolylquinoxalines ($2H^-$ and $3H^-$) produced by the reactions of $2H_2$ and $3H_2$ with TBAOH are shown in Figure 3-12 for comparison. More details will be discussed in Chapter Four.

3.3 Conclusion

In summary, the disproportionation of dipyrrolylquinoxaline radical anions produced by electron-transfer reduction of dipyrrolylquinoxaline occurs via hydrogen atom transfer from the pyrrole moiety to the quinoxaline moiety to produce mono-deprotonated dipyrrolylquinoxalines and mono-protonated dihydrodipyrrolylquinoxaline. In contrast, the same quinoxaline radical anions without the pyrrole moieties are stable in aprotic solvents. The present study furthers our understanding of disproportionation processes and provides a unique way to convert a one-electron reduction to a two-electron process without the need for external protons.

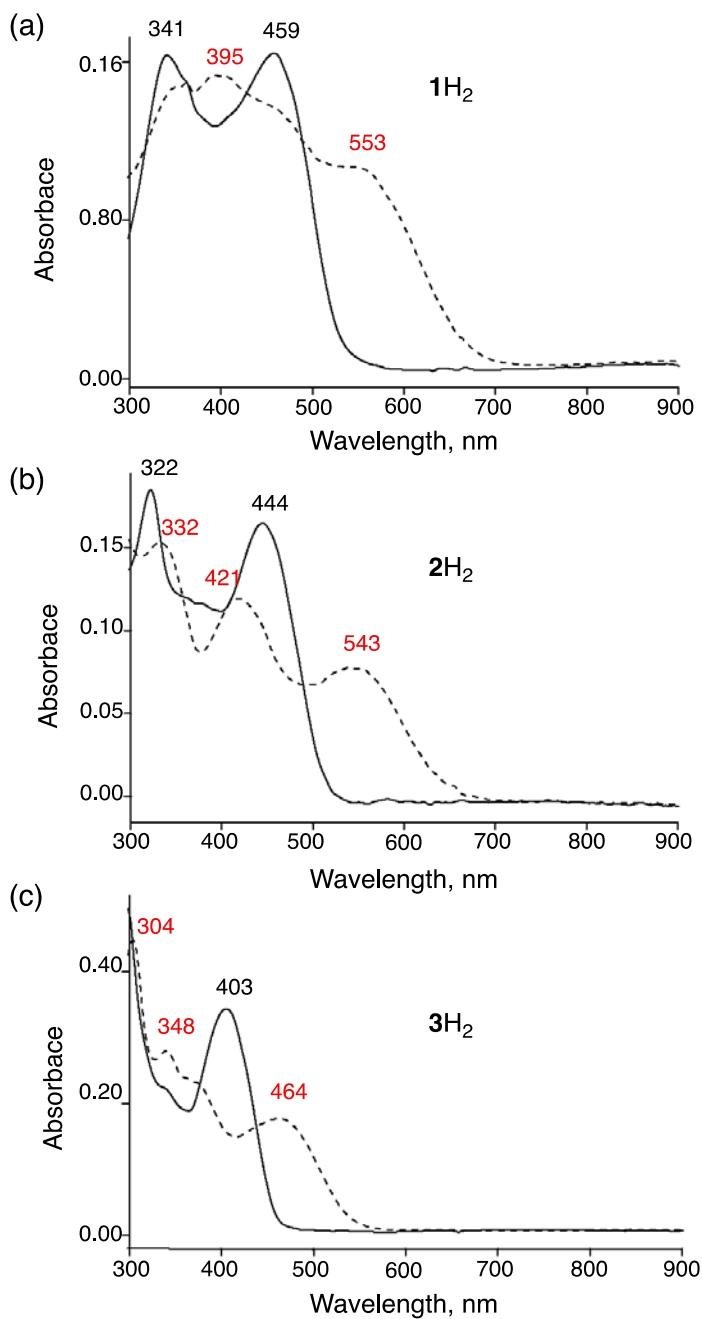


Figure 3-11. UV-vis absorption spectral changes in electrolysis of (a) 1H_2 (3.3×10^{-4} M), (b) 2H_2 (3.1×10^{-4} M) and (c) 3H_2 (9.2×10^{-4} M) in the presence of TBAP (0.20 M) in CH_3CN at applied potentials of -0.80 V (vs SCE) for 347 s, -0.96 V for 310 s and -1.70 V for 180 s, respectively.

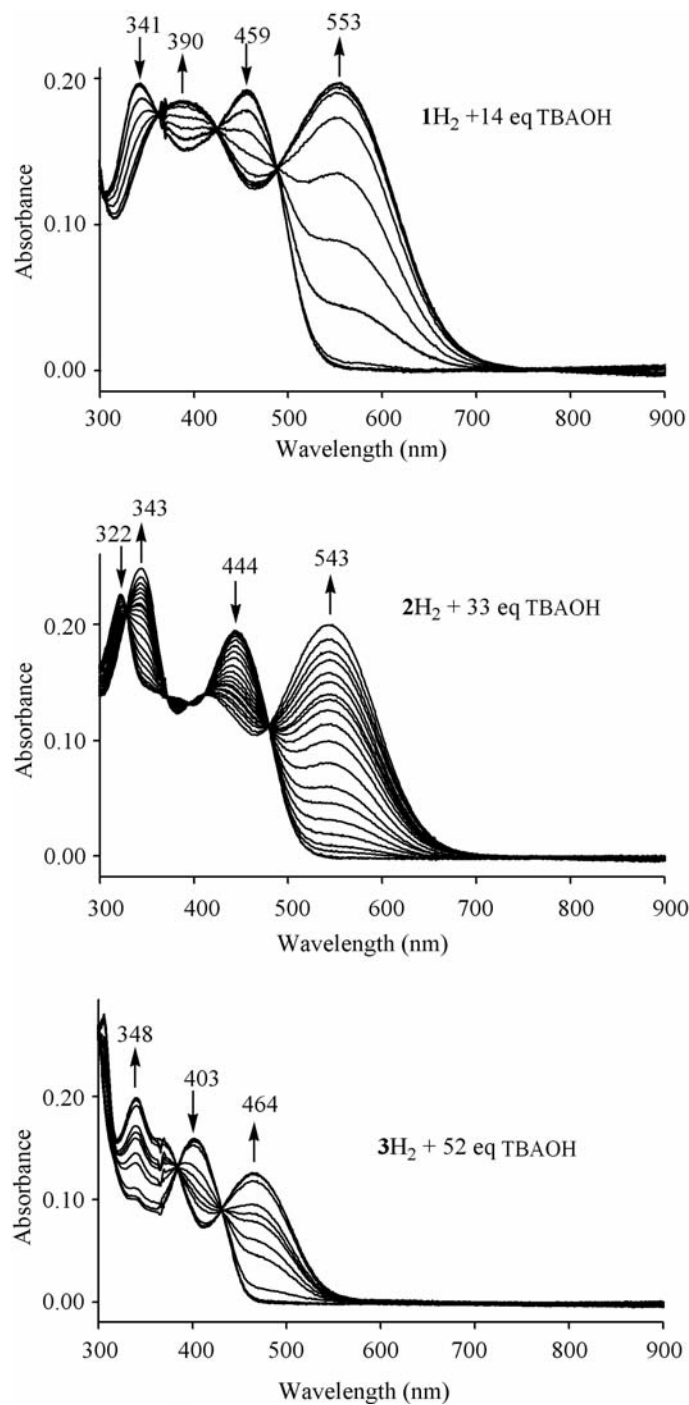


Figure 3-12. UV-vis absorption spectral change of (a) $1H_2$ (1.8×10^{-5} M) (b) $2H_2$ (1.7×10^{-5} M) and (c) $3H_2$ (2.0×10^{-5} M) in CH_3CN titrated with TBAOH (1.0×10^{-2} M).

3.4 References

1. Cukier, R. I.; Nocera, D. G. *Annu. Rev. Phys. Chem.* **1998**, *49*, 337.
2. Mayer, J. M. *Annu. Rev. Phys. Chem.* **2004**, *55*, 363.
3. Warren, J. J.; Tronic, T. A.; Mayer, J. M. *Chem. Rev.* **2010**, *110*, 6961.
4. Fukuzumi, S.; Fujioka, N.; Kotani, H.; Ohkubo, K.; Lee, Y.-M.; Nam, W. *J. Am. Chem. Soc.* **2009**, *131*, 17127.
5. Fukuzumi, S.; Kishi, T.; Kotani, H.; Lee, Y.-M.; Nam, W. *Nature Chem.* **2011**, *3*, 38.
6. Fukuzumi, S.; Kobayashi, T.; Suenobu, T. *Angew. Chem., Int. Ed.* **2011**, *50*, 728.
7. Cabelli, D. E.; Riley, D.; Rodriguez, J. A.; Valentine, J. S.; Zhu, H. In *Biomimetic Oxidations Catalyzed by Transition Metal Complexes*; Meunier, B., Ed.; Imperial College Press: London, **2000**.
8. Ellerby, L. M.; Cabelli, D. E.; Graden, J. A.; Valentine, J. S. *J. Am. Chem. Soc.* **1996**, *118*, 6556.
9. Okado-Matsumoto, A.; Fridovich, I. *J. Biol. Chem.* **2001**, *276*, 38388. (c) Smirnov, V. V.; Roth, J. P. *J. Am. Chem. Soc.* **2006**, *128*, 16424.
10. Smirnov, V.V.; Roth, J. P.; *J. Am. Chem. Soc.* **2006**, *128*, 16043.
11. Aguilar-Martínez, M.; Macías-Ruvalcaba, N. A.; Bautista-Martínez, J. A.; Gómez, M.; González, F. J.; González, I. *Curr. Org. Chem.* **2004**, *8*, 1721.
12. Macías-Ruvalcaba, N. A.; Okumura, N.; Evans, D. H. *J. Phys. Chem. B* **2006**, *110*, 22043.
13. Costeintin, C. *Chem. Rev.* **2008**, *108*, 2145.
14. Jaworski, J. S.; Kosson, A.; Filipek, S.; Kolinski, M.; Kuck, D. *J. Phys. Chem. C* **2009**, *113*, 7436.

15. Yuasa, J.; Fukuzumi, S. *J. Am. Chem. Soc.* **2007**, *129*, 12912.
16. Warren, J. J.; Mayer, J. M. *J. Am. Chem. Soc.* **2010**, *132*, 7784.
17. Mizuno, T.; Wei, W.-H.; Eller, L. R.; Sessler, J. L. *J. Am. Chem. Soc.* **2002**, *124*, 1134.
18. Black, C. B.; Andrioletti, B.; Try, A. C.; Ruiperez, C.; Sessler, J. L. *J. Am. Chem. Soc.* **1999**, *121*, 10438.
19. Anzenbacher, P. Jr., Try, A. C.; Miyaji, H.; Jursíková, K.; Lynch, V. M.; Marquez, M.; Sessler, J. L. *J. Am. Chem. Soc.* **2000**, *122*, 10268.
20. Fukuzumi, S.; Mase, K.; Ohkubo, K.; Fu, Z.; Karnas, E.; Sessler, J. L.; Kadish, K.M. *J. Am. Chem. Soc.* **2011**, *133*, 7284.
21. Pietrzak, M.; Try, A. C.; Andrioletti, B.; Sessler, J. L.; Anzenbacher, P. Jr., Limbach, H.-H. *Angew. Chem. Int. Ed.* **2008**, *47*, 1123.

Chapter Four

Electroreduction and Acid-Base Properties of

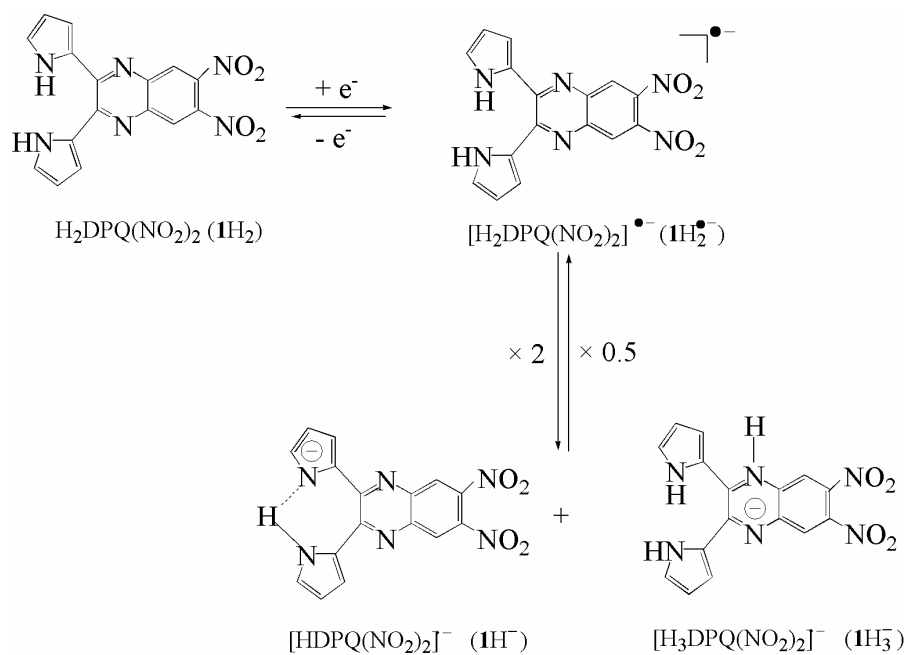
Dipyrrolylquinoxalines

4.1 Introduction

Over the past decades, considerable effort has been devoted to exploring receptors capable of recognizing neutral and anionic species.^{1,2} This effort has been stimulated by the fact that these types of receptors are capable of recognizing, sensing, and transporting anions not only in supramolecular compounds but also in systems which may have potential clinical applications.³ One such receptor is 2,3-dipyrrol-2'-ylquinoxaline H₂DPQ, which has the advantage of possessing a built-in chromophore and is also readily synthesized in two steps from commercially available materials,^{2,3} as first reported by Oddo in 1911⁴ and later refined by Behr et al. in 1973.⁵ The DPQ entity was not considered as a possible colorimetric anion sensor until three decades later when Sessler and coworkers reported the synthesis and anion binding properties of two related compounds, 2,3-dipyrrol-2'-yl-6-nitroquinoxaline, H₂DPQ(NO₂)³ and 2,3-dipyrrol-2'-yl-6,7-dinitroquinoxaline, H₂DPQ(NO₂)₂.²

In a recent Communication we examined the fate of chemically and electrochemically generated dipyrrolylquinoxaline-derived radical anions and showed that the internal pyrrole protons of the molecule were involved in a disproportionation of the product generated after a one-electron reduction in acetonitrile (CH₃CN).⁶ The relevant electrochemical and chemical reactions are shown in Scheme 4-1 for the case of H₂DPQ(NO₂)₂.

The initial one-electron reduction of these neutral compounds and following disproportionation reaction leads to an unreduced mono-deprotonated species having a single proton shared by the two pyrrole groups,⁷ [HDPQ(NO₂)₂]⁻ (labeled as **1H** in Scheme 4-1) and a doubly reduced tri-protonated species having one protons on each



Scheme 4-1 Published Mechanism for the First Reduction of $\text{H}_2\text{DPQ}(\text{NO}_2)_2$ in Nonaqueous Media⁶

pyrrole and a third proton bound to one of the two quinoxaline nitrogens, $[\text{H}_3\text{DPQ}(\text{NO}_2)_2]^-$ ($\mathbf{1H}_3^-$).

This work described in the present Chapter expands upon our initial Communication⁶ (covered in Chapter Three) and focuses on elucidating the complete electrochemistry, spectroelectrochemistry and acid-base properties of H_2DPQ , $\text{H}_2\text{DPQ}(\text{NO}_2)$ and $\text{H}_2\text{DPQ}(\text{NO}_2)_2$ in benzonitrile (PhCN) before and after the addition of acid or base in the form of trifluoroacetic acid (TFA), tetrabutylammonium hydroxide (TBAOH), tetrabutylammonium fluoride (TBAF) or tetrabutylammonium acetate (TBAOAc). The structures of the neutral dipyrrolylquinoxalines are shown in Chart 4-1 along with their abbreviated notations, given as $\mathbf{1H}_2$, $\mathbf{2H}_2$ and $\mathbf{3H}_2$. The totally protonated and totally deprotonated forms of $\mathbf{1H}_2$, $\mathbf{2H}_2$ and $\mathbf{3H}_2$, formulated as $[\text{H}_4\text{DPQ}(\text{NO}_2)_n]^{2+}$ and $[\text{DPQ}(\text{NO}_2)_n]^{2-}$, respectively, where $n = 0, 1$ or 2 , are also shown in Chart 4-1 along with the abbreviated notations of $\mathbf{1H}_4^{2+}$, $\mathbf{2H}_4^{2+}$ and $\mathbf{3H}_4^{2+}$ for the three dications in acidic media and $\mathbf{1}^{2-}$, $\mathbf{2}^{2-}$ and $\mathbf{3}^{2-}$ for the three dianions in basic media.

Cyclic voltammetry was used to measure redox potentials of each electrode reaction, while thin-layer spectroelectrochemistry was employed to record the UV-visible spectra of each electrogenerated product. Equilibrium constants for deprotonation of the two pyrrole protons or protonation of the two quinoxaline nitrogens were monitored by UV-visible spectroscopy during a titration with acid or base and comparisons are made between the redox behavior of $\text{H}_2\text{DPQ}(\text{NO}_2)_n$ and their totally protonated or totally deprotonated analogues, i.e., $[\text{H}_4\text{DPQ}(\text{NO}_2)_n]^{2+}$ and $[\text{DPQ}(\text{NO}_2)_n]^{2-}$ where $n = 0, 1$ or 2 .

Comparisons are also made between the redox behavior of $\text{H}_2\text{DPQ}(\text{NO}_2)_n$ and quinoxalines which lack the linked pyrrole units. One group of comparison quinoxaline

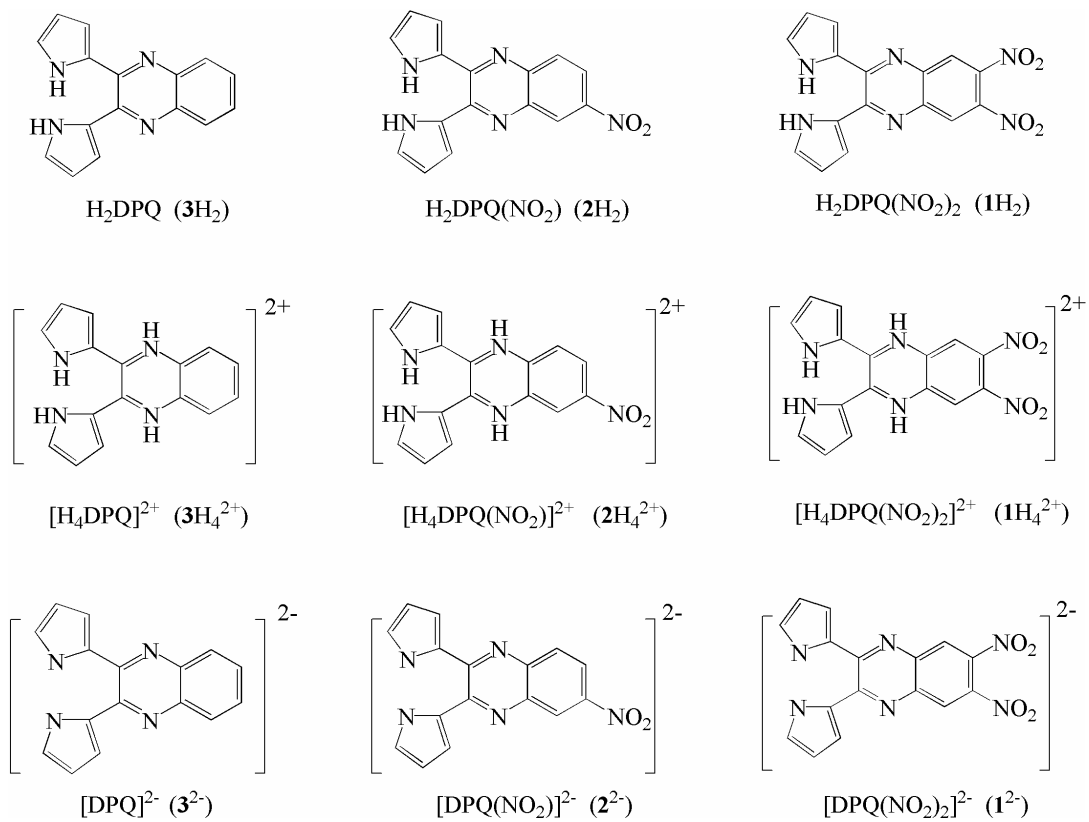


Chart 4-1. Structures of investigated dipyrrolylquinoxalines in neutral, acidic and basic forms.

compounds is represented as $Q(NO_2)_n$ where $n = 0, 1$ or 2 and the other as R_2Q where R is a methyl, thienyl or furyl group.

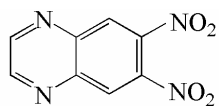
4.2 Results and Discussion

4.2.1 Electroreduction of $Q(NO_2)_n$ where $n = 0, 1$ or 2

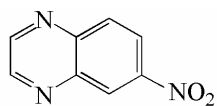
In order to better understand the chemical reactions following electron addition to $H_2DPQ(NO_2)_n$, measurements were first carried out under the same solution conditions on two groups of quinoxalines lacking a pyrrole unit. One group of comparison molecules is represented as $Q(NO_2)_n$ where $n = 2, 1$ or 0 (compounds **4-6**) and the others as R_2Q (compounds **7-9**) whose structures are shown in Chart 4-2. The first group of compounds were previously examined by cyclic voltammetry in CH_2Cl_2 ,⁸ and the second were electrochemically characterized in CH_3CN .⁹

The quinoxaline moiety without the electron-withdrawing nitro groups undergoes a single one-electron addition at $E_{1/2} = -1.67$ V in PhCN, 0.1 M TBAP, as compared to an irreversible one-electron reduction in CH_2Cl_2 which is located at $E_{pc} = -1.63$ V for a scan rate of 0.1 V/s.⁸ The reversible reduction of Q **6** in PhCN generates the quinoxaline anion radical, $Q^{\bullet-}$, which is stable on the electrochemical and spectroelectrochemical timescales. A stable anion radical is also generated upon the reversible one-electron addition to $Q(NO_2)$ **5** ($E_{1/2} = -0.90$ V) and $Q(NO_2)_2$ **4** ($E_{1/2} = -0.64$ V). Cyclic voltammograms of **4-6** in PhCN, 0.1 M TBAP are shown in Figure 4-1a and UV-visible spectral changes during the formation of $[Q(NO_2)_n]^{\bullet-}$ under the same solution conditions are shown in Figure 4-2.

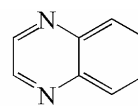
As seen in Figure 4-1a, the half-wave potential values for conversion of $Q(NO_2)_n$ to



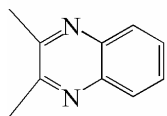
Q(NO₂)₂ (4)



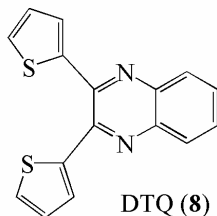
Q(NO₂) (5)



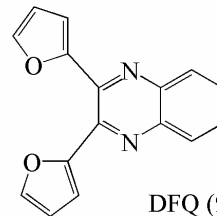
Q (6)



DMQ (7)



DTQ (8)



DFQ (9)

Chart 4-2. Structures of different substituted quinoxalines.

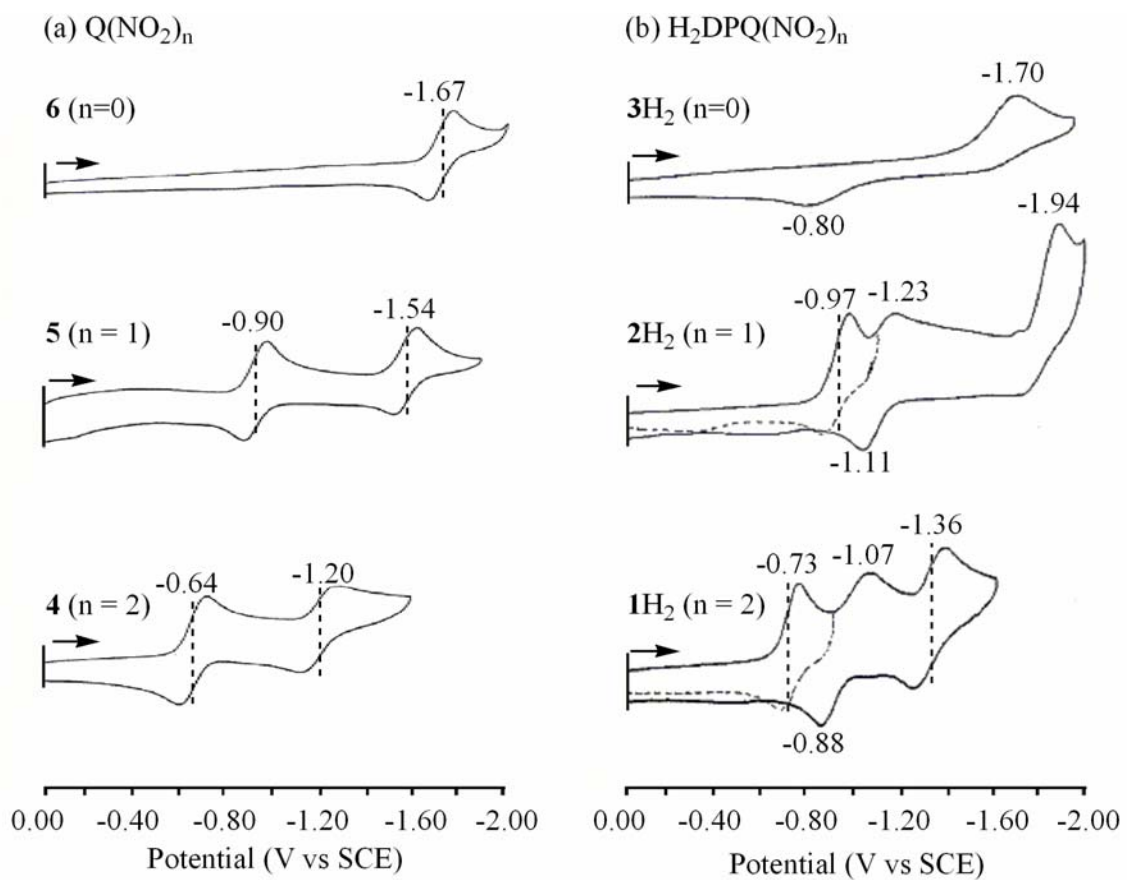


Figure 4-1. Cyclic voltammograms of (a) $Q(NO_2)_n$ (**4-6**) and (b) $H_2DPQ(NO_2)_n$ (**1H₂-3H₂**) where n = 2, 1 or 0 in PhCN, 0.1 M TBAP. Scan rate = 0.1 V/s.

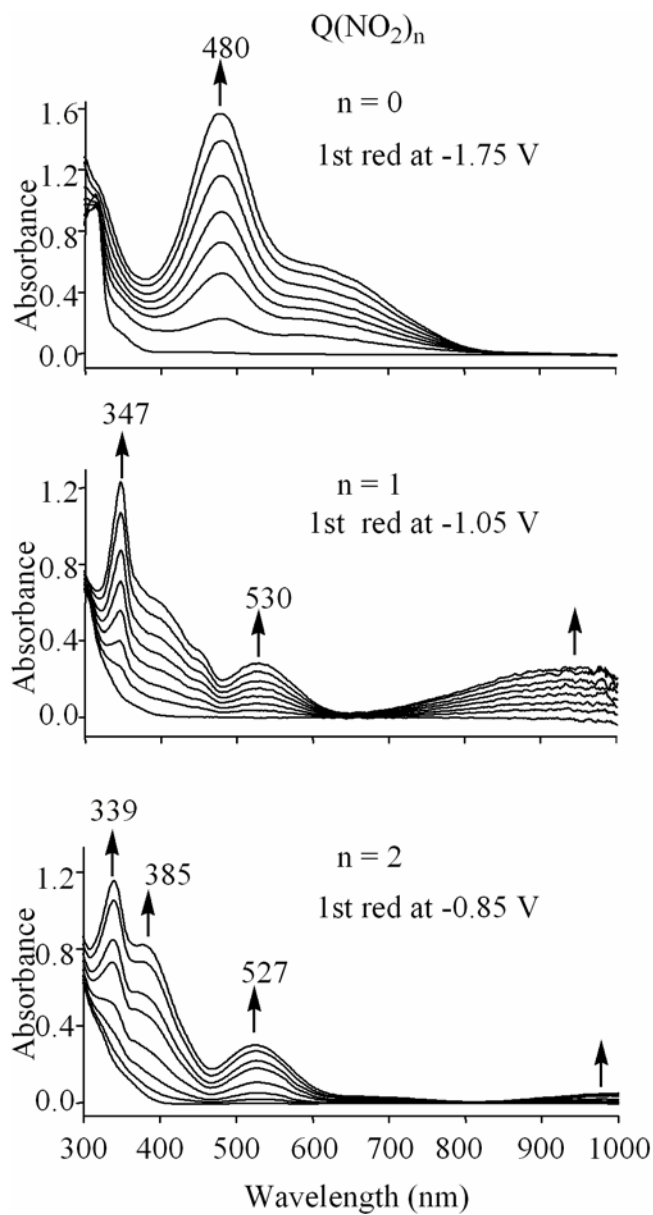


Figure 4-2. UV-visible spectral changes of singly reduced Q(NO₂)_n in PhCN, 0.2 M TBAP at the indicated applied potentials (see cyclic voltammograms of compounds in Figure 4-1).

$Q(NO_2)_n \bullet^-$ are shifted positively with each added electron-withdrawing NO_2 substituent. The addition of one NO_2 group to **Q** leads to a 770 mV positive shift in $E_{1/2}$ for the first reversible one-electron reduction (-1.67 V to -0.90 V), but a smaller substituent effect is seen upon addition of the second nitro group where $E_{1/2}$ shifts from -0.90 V for reduction of **Q** to -0.64 V for reduction of $Q(NO_2)_2$ (Figure 4-1a).

$Q(NO_2)$ (**5**) and $Q(NO_2)_2$ (**6**) are both reversibly reduced in a second one-electron transfer step, with $E_{1/2}$ values located at -1.54 and -1.20, respectively in PhCN, 0.1 M TBAP. The absolute difference in $E_{1/2}$ values between formation of the anion radical and dianion in these two compounds amounts to 640 and 560 mV, respectively.

Reversible one-electron reductions were earlier reported for the structurally related comparison compounds, dimethylquinoxaline (**7**), dithienylquinoxaline (**8**) and difurylquinoxaline (**9**), with $E_{1/2}$ values ranging between -1.94 and -2.28 V vs Fc/Fc⁺ in CH_3CN .⁹ ($E_{1/2}$ values, when corrected vs SCE, would range from about -1.54 to -1.78 V for a Fc/Fc⁺ couple located at 0.40 V vs SCE in this solvent).

One key point which emerges from the data involving reduction of the six comparison compounds, **4-9** in PhCN and also CH_3CN is that the *in-situ* generated radical anion is in all cases stable. This is clearly due to the lack of disproportionation reaction which requires the pyrrole protons on the molecule in the case of $H_2DPQ(NO_2)_2$, $H_2DPQ(NO_2)$ and H_2DPQ (**1H₂-3H₂**).⁶ Another key point is that the mono- and dinitro-substituted quinoxaline moieties, **5** and **4**, are both more easily reducible than the related compounds **7-9** due to the electron-withdrawing effect of the nitro groups and a second reversible one-electron reduction can then be accessed for **5** and **4** at -1.54 V or -1.20 V, respectively. Additional reductions beyond the monoanion radical are also seen

for the nitro-substituted dipyrrolylquinoxalines, **2H₂** and **3H₂**, whose electrochemistry is described in more detail on the following pages.

4.2.2 Electroreduction of H₂DPQ(NO₂)_n where n = 0, 1 or 2

As seen in Figure 4-1b, dipyrrolylquinoxaline, H₂DPQ (**3H₂**), exhibits a single irreversible reduction at $E_{pc} = -1.70$ V which is coupled with an irreversible oxidation peak at $E_p = -0.80$ V for a scan rate of 0.1 V/s. The return oxidation peak is present if the scan is terminated before the first reduction and the overall shape of the current-voltage curve in Figure 4-1b is consistent with a chemical reaction following electron transfer (an ED mechanism where D is the disproportionation step).¹⁰

It should be noted that the peak potential for the irreversible one-electron reduction of H₂DPQ (**3H₂**) is almost identical to that for the reversible one-electron reduction of Q at $E_{1/2} = -1.67$ V (Figure 4-1a). In addition, the effect of NO₂ substituents on the redox reactions of compounds **1H₂-3H₂** is quite similar to that of compounds **4-6**. For example, the difference in $E_{1/2}$ between reduction of Q and Q(NO₂) is 770 mV, and almost the same difference in potential (~700 mV) is seen for the related dipyrrolequinoxalines where H₂DPQ is reduced at $E_{pc} = -1.70$ V as compared to $E_{pc} = -1.00$ V for H₂DPQ(NO₂) at a scan rate of 0.1 V/s (Figure 4-1b). Like in the case of Q(NO₂) and Q(NO₂)₂, a smaller substituent effect is seen upon addition of the second nitro group to the dipyrrolylquinoxaline compounds where $E_{1/2}$ shifts from -0.97 V for the first reduction of H₂DPQ(NO₂) to -0.73 V for the first reduction of H₂DPQ(NO₂)₂. This similarity in reduction potentials and substituent effect for compounds in the series of **1H₂-3H₂** and **4-6** implies a similar site of electron transfer in all cases.

As indicated above, the potentials for the reversible first one-electron reduction of H₂DPQ(NO₂) (**2H₂**) and H₂DPQ(NO₂)₂ (**1H₂**) are both positively shifted with respect to potentials for the irreversible one-electron reduction of H₂DPQ (**3H₂**). The potentials for reduction of H₂DPQ(NO₂) and H₂DPQ(NO₂)₂ are also slightly more difficult than $E_{1/2}$ values of the one-electron reduction of the comparison nitroquinoxalines Q(NO₂) (**5**) and Q(NO₂)₂ (**4**), and this is consistent with a small electron-donating effect from the two pyrrole groups in the dipyrrolylquinoxalines.

Similar electrochemical behavior is exhibited by H₂DPQ(NO₂) and H₂DPQ(NO₂)₂ in PhCN. As seen in Figure 4-1b, an initial reversible one-electron transfer is seen for both neutral compounds, at $E_{1/2} = -0.97$ V (**2H₂**) or -0.73 V (**1H₂**), and this is followed at more negative potentials by a second irreversible one-electron addition at $E_p = -1.23$ V (**2H₂**) or -1.07 V (**1H₂**) for a scan rate of 0.1 V/s.

It should be noted that the first one-electron reduction of H₂DPQ(NO₂) **2H₂** and H₂DPQ(NO₂)₂ **1H₂** are reversible at all scan rates when the negative sweep is reversed at a potential prior to the second reduction (Figure 4-1). In contrast, the first reduction becomes irreversible only when the scan is extended to potentials beyond the second reduction, i.e., to values greater than -1.23 V in the case of **2H₂** and -1.07 V in the case of **1H₂**, at which point the initial reduction and reoxidation peaks then totally disappear on a second sweep and on all subsequent potential sweeps. This is illustrated by the dashed line in Figure 4-3 and is consistent with the formation of a new electroactive species in solution which is reduced in two steps, the first of which is reversible and located at $E_{1/2} = -1.13$ V (**2H₂**) or -0.90 V (**1H₂**).

This second reduction peak of H₂DPQ(NO₂) and H₂DPQ(NO₂)₂ are both coupled to

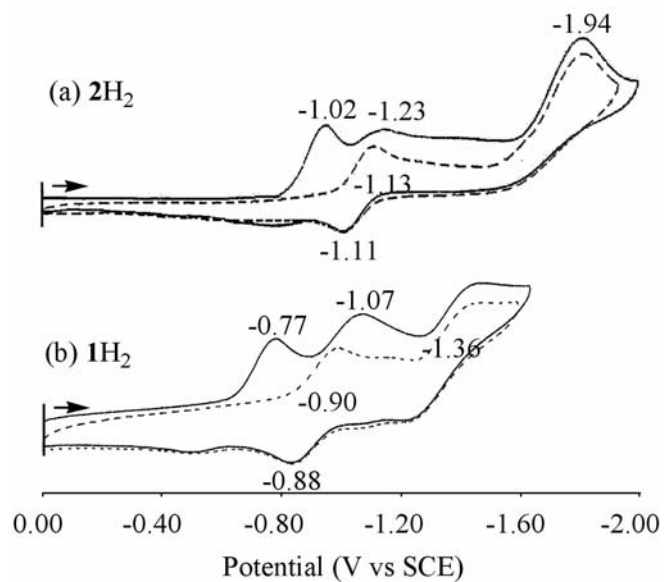


Figure 4-3. Cyclic voltammograms of (a) $\text{H}_2\text{DPQ}(\text{NO}_2)_2 \cdot 2\text{H}_2\text{O}$ and (b) $\text{H}_2\text{DPQ}(\text{NO}_2)_2 \cdot \text{H}_2\text{O}$ in PhCN, 0.1 M TBAP. First scan (solid line); second scan (dotted line). The same current-voltage curves were obtained for the 2nd, 3rd and 4th potential sweeps. Scan rate = 0.1 V/s.

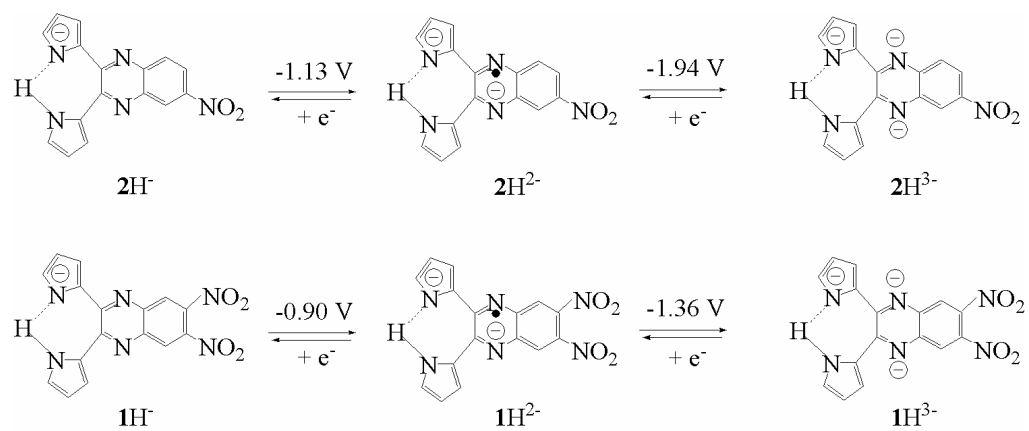
well-defined reoxidation peaks which appears at $E_{pa} = -1.11$ V (**2H₂**) or -0.88 V (**1H₂**) on the first and all subsequent sweeps for a scan rate of 0.1 V/s (see Figure 4-3). However, as will be demonstrated, the second cathodic (reduction) and first anodic (reoxidation) peaks are not associated with the same electrochemical process and are actually two separate redox couples separated by one or more intervening chemical reactions. The product of the chemical reactions is also electroactive and a third reduction is observed at $E_{pc} = -1.94$ V for **2H₂** and $E_{1/2} = -1.36$ V for **1H₂**.

The product generated after the first reduction and disproportionation of the mono- and dinitro DPQ derivatives was earlier assigned⁶ as $[\text{HDPQ}(\text{NO}_2)]^-$ and $[\text{HDPQ}(\text{NO}_2)_2]^-$ on the basis of ¹H NMR.⁷ These *in-situ* generated monoanions have a single proton shared between two pyrrole groups and undergo two one-electron additions as drawn in Scheme 4-2.

Additional evidence for the conversion of $\text{H}_2\text{DPQ}(\text{NO}_2)_n$ to $[\text{HDPQ}(\text{NO}_2)_n]^-$ prior to the redox reactions shown in Scheme 4-2 is given by thin-layer electrochemistry and spectroelectrochemistry, examples of which are shown in Figures 4-4 and 4-5 for the case of $\text{H}_2\text{DPQ}(\text{NO}_2)$ (**2H₂**). The two reduction of $\text{H}_2\text{DPQ}(\text{NO}_2)$ in the thin-layer cell upon scanning from 0.00 to -1.50 V (Figure 4-4) resembles what is observed in the first two steps by routine cyclic voltammetry at a scan rate of 0.1 V/s (Figure 4-1). The initial reversible reduction in the thin-layer cell at $E_{1/2} = -0.96$ V (dashed line in Figure 4-4a) is followed by a second irreversible reduction at $E_{pc} = -1.22$ V, but only one return anodic peak is seen on the reverse scan. This process is located at $E_{pa} = -1.09$ V for a scan rate of 10 mV/s (Figure 4-4a).

The peak current for the reduction at $E_{pc} = -1.22$ V is less than that of the first

Scheme 4-2



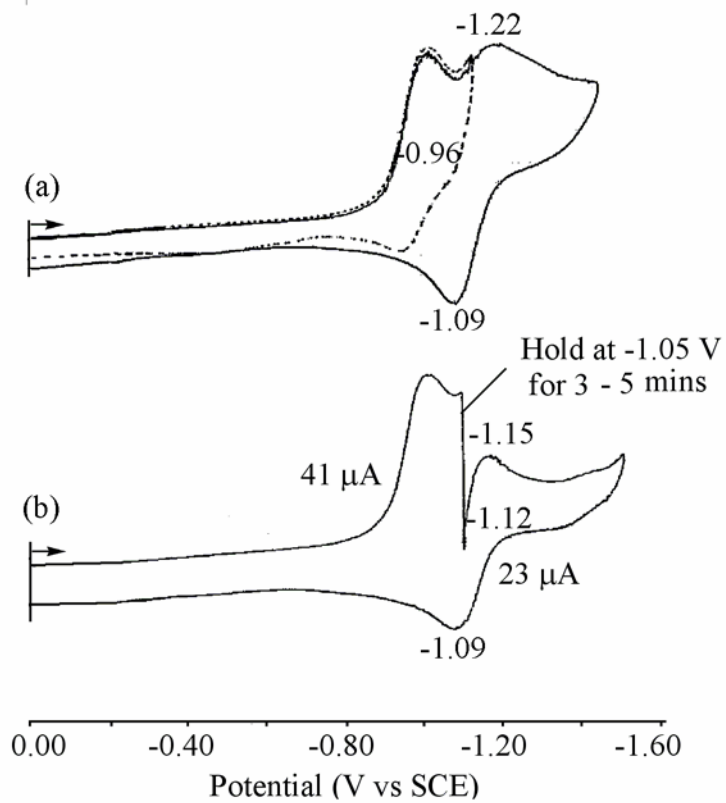


Figure 4-4. Thin-layer cyclic voltammograms of $\text{H}_2(\text{NO}_2)\text{DPQ} \cdot 2\text{H}_2$ in PhCN , 0.2 M TBAP. Scan rate = 10 mV/s . Dashed line is the initial reversible reduction.

reduction at $E_{1/2} = -0.96$ V, as is also observed by “regular” CV for the same compounds in Figures 4-3. Furthermore, the reduction peak at $E_p = -1.22$ V totally disappears in the thin-layer cyclic voltammogram when the potential is scanned from 0.00 to -1.05 V and then held for three minutes before continuing to -1.40 V and being reversed (Figure 4-4b). Under these conditions, the disproportionation shown in Scheme 4-1 has proceeded to completion and a new cathodic peak is seen at $E_{pc} = -1.15$ V (Figure 4-4b). This new reduction process at $E_{pc} = -1.15$ V is coupled to the original anodic peak at $E_{pa} = -1.09$ V to give $E_{1/2} = -1.12$ V in the thin-layer cell (Figure 4-4b). This half wave potential is virtually identical to the $E_{1/2} = -1.13$ V measured from the “regular” cyclic voltammogram in Figure 4-3a.

Finally, it should also be noted that the current for reoxidation of $\text{H}_2\text{DPQ}(\text{NO}_2)$ in Figure 4-4b (23 μA) is about half of that observed for reduction (41 μA), consistent with the mechanism shown in Scheme 4-1 for $\text{H}_2\text{DPQ}(\text{NO}_2)_2$.

4.2.3 Spectroelectrochemistry of $\text{H}_2\text{DPQ}(\text{NO}_2)_n$ where $n = 0, 1$ or 2

The conversion of $\text{H}_2\text{DPQ}(\text{NO}_2)_n$ to $[\text{HDPQ}(\text{NO}_2)_n]^-$ proceeds in two steps, both of which could be followed as a function of time by measuring changes in the UV-visible spectra during controlled potential reduction in the thin-layer cell. These spectral changes are shown in Figures 4-5 and 4-6 for $\text{H}_2\text{DPQ}(\text{NO}_2)$ (2H_2) and in Figure 4-7 for $\text{H}_2\text{DPQ}(\text{NO}_2)_2$ (1H_2). For both compounds, only small differences in the overall morphology of the UV-visible spectra are observed after the initial application of an applied potential (up to 94 s in the case of 2H_2 and up to 45 s in the case of 1H_2), but quite substantial changes then occur at longer times of up to 173 s for 1H_2 and 335 s for

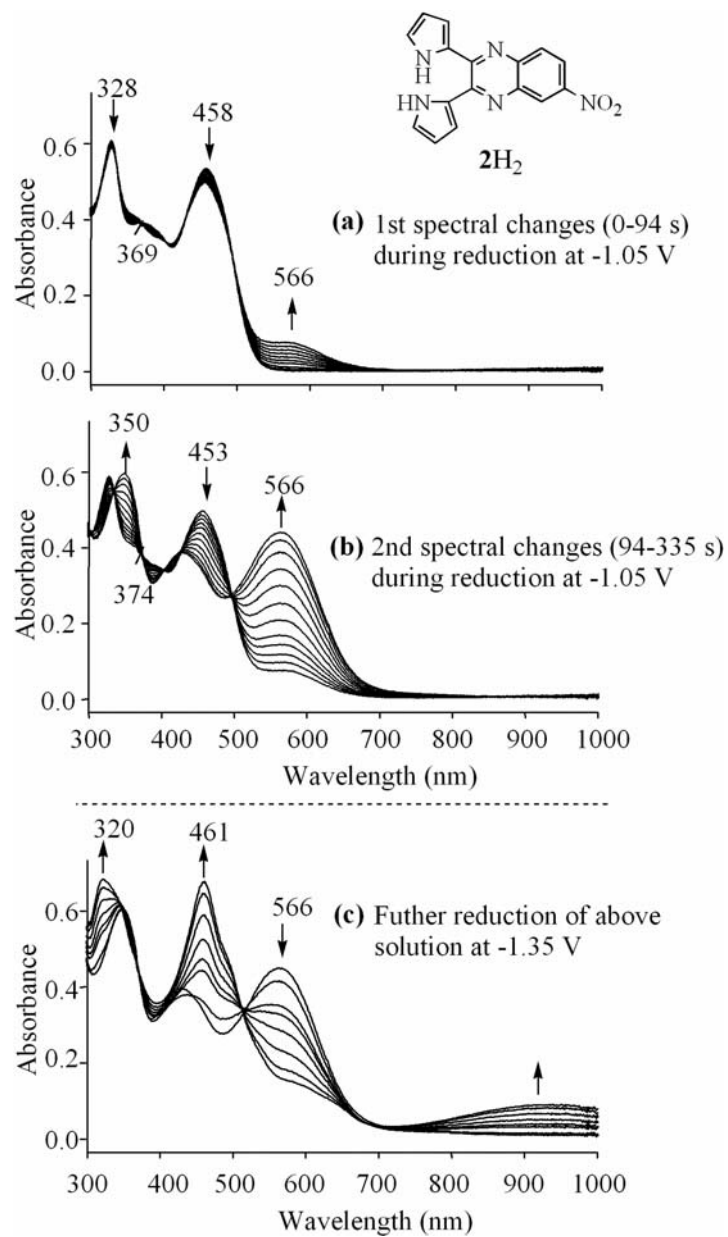


Figure 4-5. UV-vis spectral changes observed during the course of controlled potential reduction of H₂DPQ(NO₂) (2H₂) in PhCN, 0.2 M TBAP at -1.05 V and -1.35 V. See Figure 4-4 for the corresponding cyclic voltammogram.

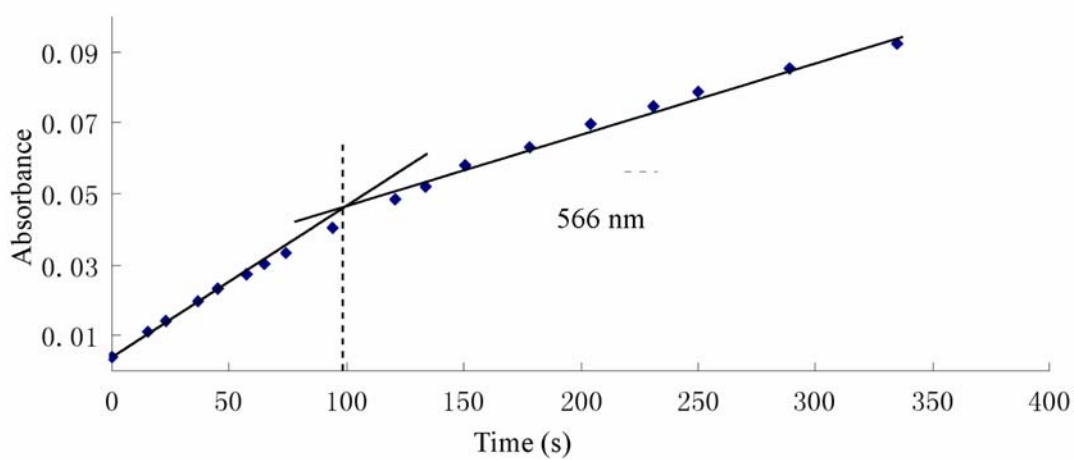
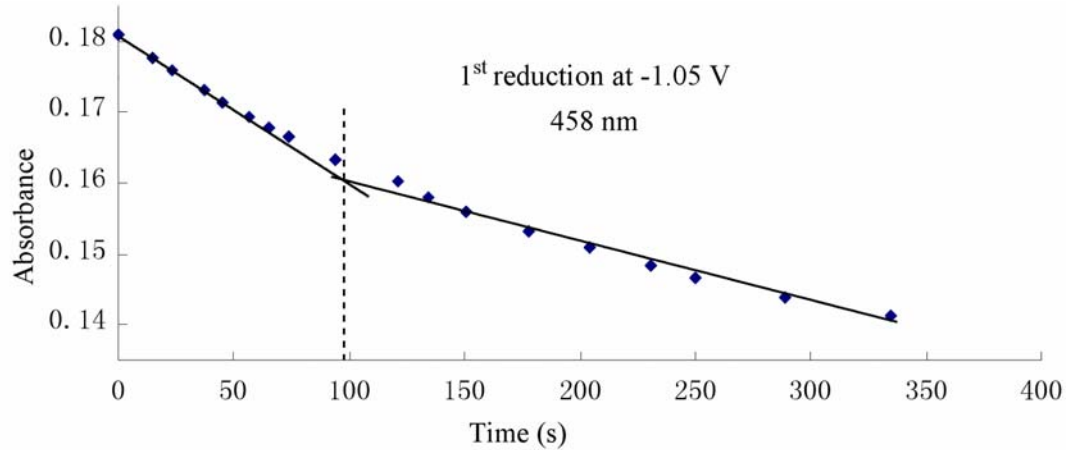


Figure 4-6. Absorbance-time curves for controlled potential reductions of H₂DPQ(NO₂) in PhCN at -1.05 V.

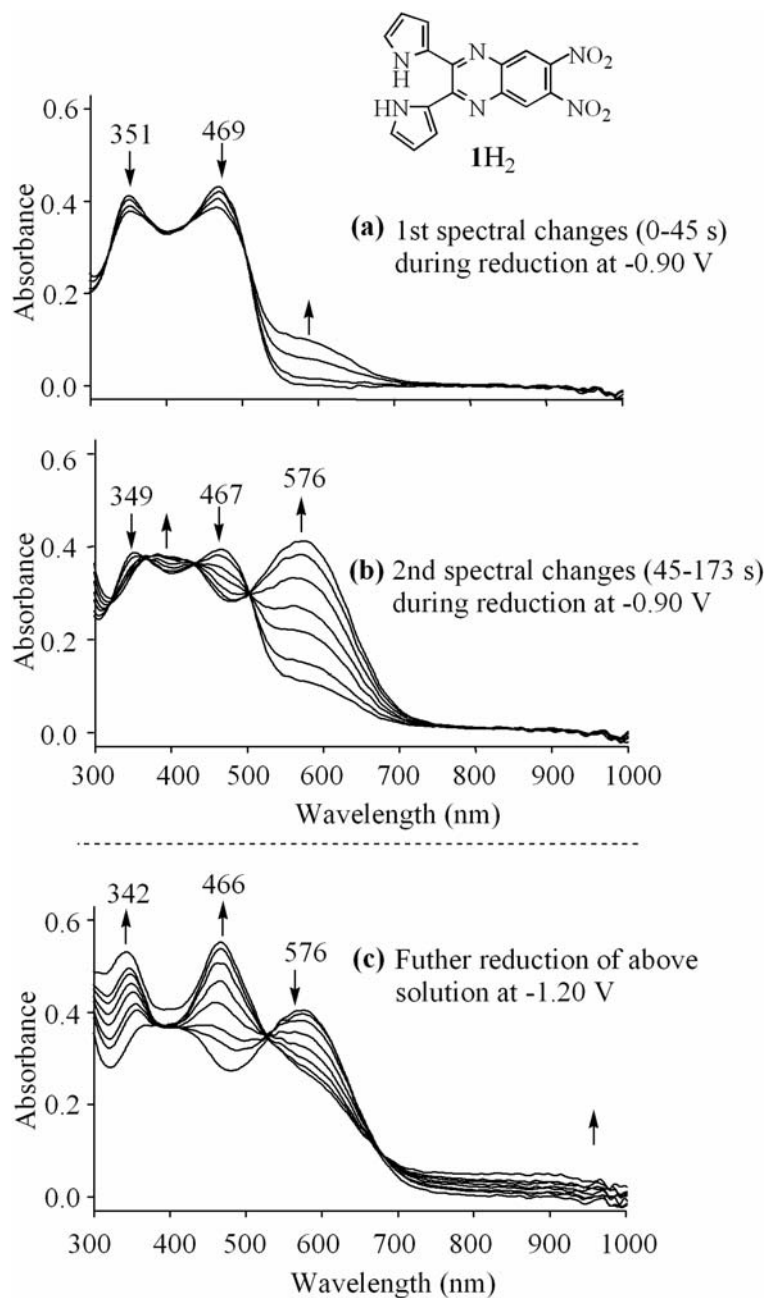


Figure 4-7. UV-vis spectral changes observed during the course of controlled potential reduction of $H_2DPQ(NO_2)_2$ ($1H_2$) in PhCN, 0.2 M TBAP at -0.90 V and -1.20 V. See Figure 4-1 for the corresponding cyclic voltammogram.

2H₂.

The spectral pattern after controlled potential reduction of **2H₂** at -1.35 V (Figure 4-5c) or **1H₂** at -1.20 V (Figure 4-7c) are similar between 300 and 700 nm to the spectra of the related unreduced compounds. The neutral compound **2H₂** has bands at 328 and 458 nm (Figure 4-5a) and the anion radical generated after reduction at -1.35 V (**2H⁻**) has bands at 320 and 461 nm in addition to a broad IR band between 700 and 1000 nm (Figure 4-5c). Likewise, the neutral **1H₂** has bands at 351 and 469 nm (Figure 4-7a) and the anion radical generated after reduction at -1.20 V (**1H⁻**) has bands at 342 and 466 nm in addition to a broad IR band between 700 and 1000 nm (Figure 4-7c).

The first reduction product of H₂DPQ(NO₂) in PhCN, 0.1 M TBAP when subjected to an applied potential of -1.05 V for 335 s is characterized by absorption bands at 350, 430 and 566 nm (Figure 4-5b) and the same set of absorbance bands are seen upon addition of TBAOH to neutral solution of H₂DPQ(NO₂). The ratio of the 566 nm band of the reduction product over the 458 nm band of the initial compound, $A_{566}(\text{final})/A_{458}(\text{initial})$ is 0.80 under the electrochemical conditions shown in Figure 4-5, and a similar ratio of 0.72 is obtained for a 10⁻³ M solution of H₂DPQ(NO₂) in PhCN containing 1 equiv. TBAOH (see Figure 4-8). This result suggests that the same mono-deprotonated form of the compound is in solution after the addition of 1.0 equiv. TBAOH as after the first reduction at an applied potential of -1.05 V.

Further evidence for the assignment of one proton being lost in the electroreduction is obtained from cyclic voltammograms measured in PhCN during a titration with TBAOH (Figure 4-9a). The peak current for the first reduction at $E_{1/2} = -0.97$ V linearly decreases as TBAOH is added to solution. A plot of the maximum peak current vs the

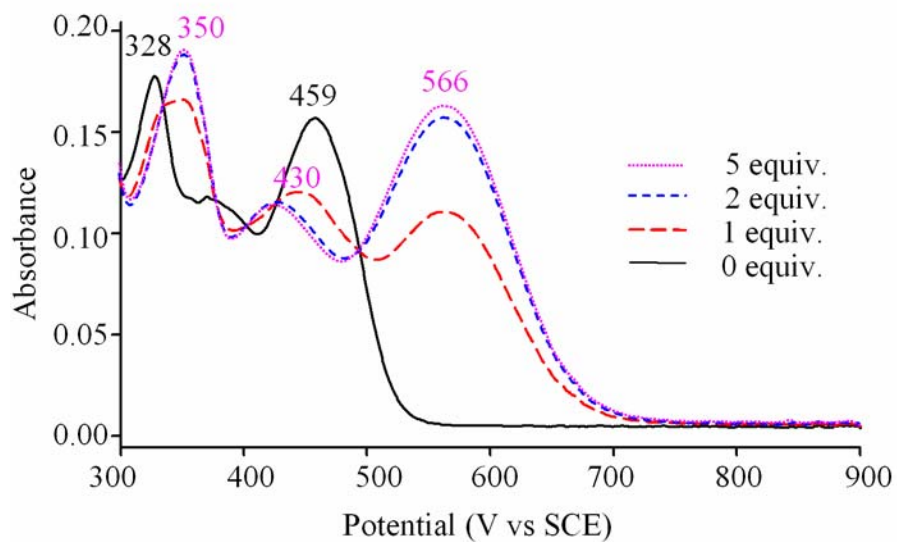


Figure 4-8. UV-vis spectral changes of H₂DPQ(NO₂) at concentration of 10⁻³ M titrated by 0 to 5 equiv. TBAOH in PhCN.

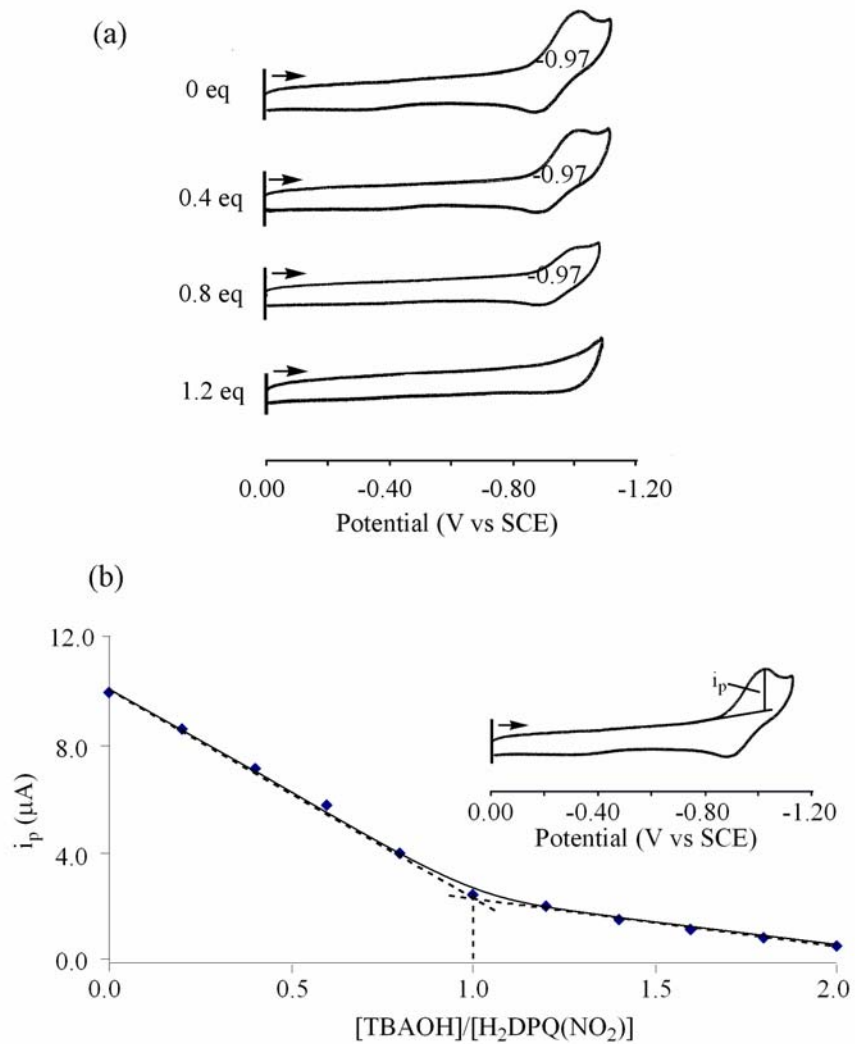


Figure 4-9. (a) Cyclic voltammograms of $\text{H}_2\text{DPQ}(\text{NO}_2)$ ($2 \times 10^{-3} \text{ M}$) in PhCN, 0.1 M TBAP with added TBAOH and (b) peak current for the first reduction as a function of the $[\text{TBAOH}]/[\text{H}_2\text{DPQ}(\text{NO}_2)]$ ratio.

[TBAOH]/[H₂DPQ(NO₂)] ratio is presented in Figure 4-9b and consists of two straight line segments with an intersection at 1.0, thus indicating that the addition of 1.0 equiv. TBAOH to solutions of H₂DPQ(NO₂) is sufficient for the first reduction process to totally disappear.

Under both solution conditions, the UV-visible spectra of the neutral and reduced derivatives are also investigated in PhCN containing between 2.0 and 5.0 equiv. TBAOH. At 2 equiv. TBAOH, the ratio increases to 1.01 and at 5.0 equiv., it increases slightly to 1.07 as seen in Figure 4-8. The UV-visible spectra obtained during the second reduction of H₂DPQ(NO₂) in PhCN, 0.2 M TBAP at $E_{app} = -1.35$ V (Figures 4-5c) are characterized by two visible bands at 320 and 461 nm and a broad absorption feature at 950 nm. Virtually the same spectrum is obtained when the reduction is carried out in PhCN containing 1.2, 5 equiv. TBAOH (Figure 4-10) suggesting that the same reduction product in each case.

In summary, the overall electrochemistry and spectroelectrochemistry of H₂DPQ derivative at higher concentrations (10⁻³ M) is consistent with the conclusion that a mono-deprotonated anion is obtained after disproportionation of a dipyrrolylquinoxaline radical anion which is formed as the initial reduction product. Again, this is in accordance with the mechanism proposed in our initial publication.⁶ The overall mechanism for the reduction of H₂DPQ(NO₂) is present in Scheme 4-3.

4.2.4 Deprotonation at Lower Concentrations and Effects of Protonation

UV-visible spectral changes obtained from the spectroscopic titration of H₂DPQ(NO₂) (10⁻⁵-10⁻⁶ M) with TBAOH, TBAF and TBAOAc in PhCN are shown in

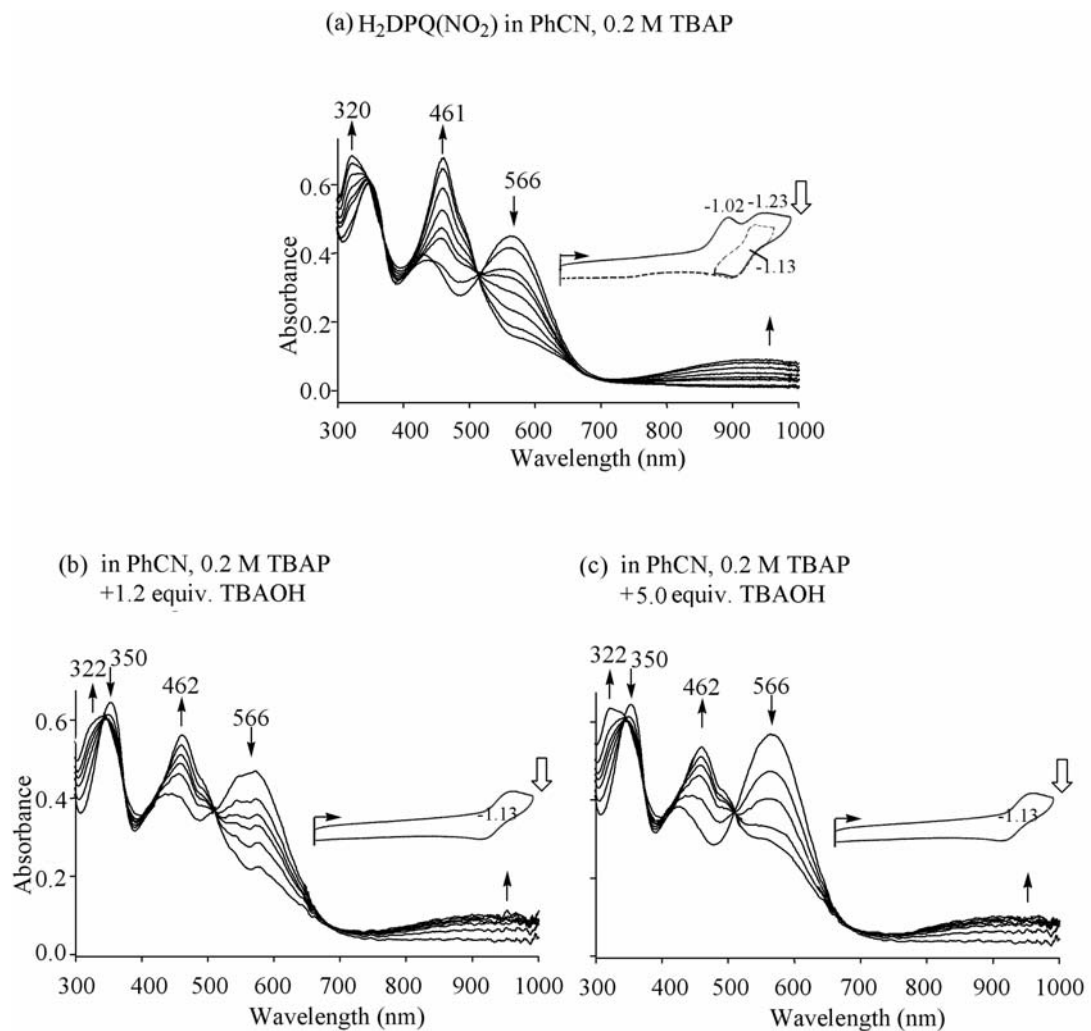


Figure 4-10. UV-vis spectral changes during controlled potential reduction of 0.71×10^{-3} M $\text{H}_2\text{DPQ}(\text{NO}_2)$ (a) in PhCN, 0.2 M TBAP at -1.35 V and the same solvent after addition of (b) 1.2 equiv. TBAOH and (c) 5.0 equiv. TBAOH. The potential applied is shown by arrow in the figure insert.

Scheme 4-3.

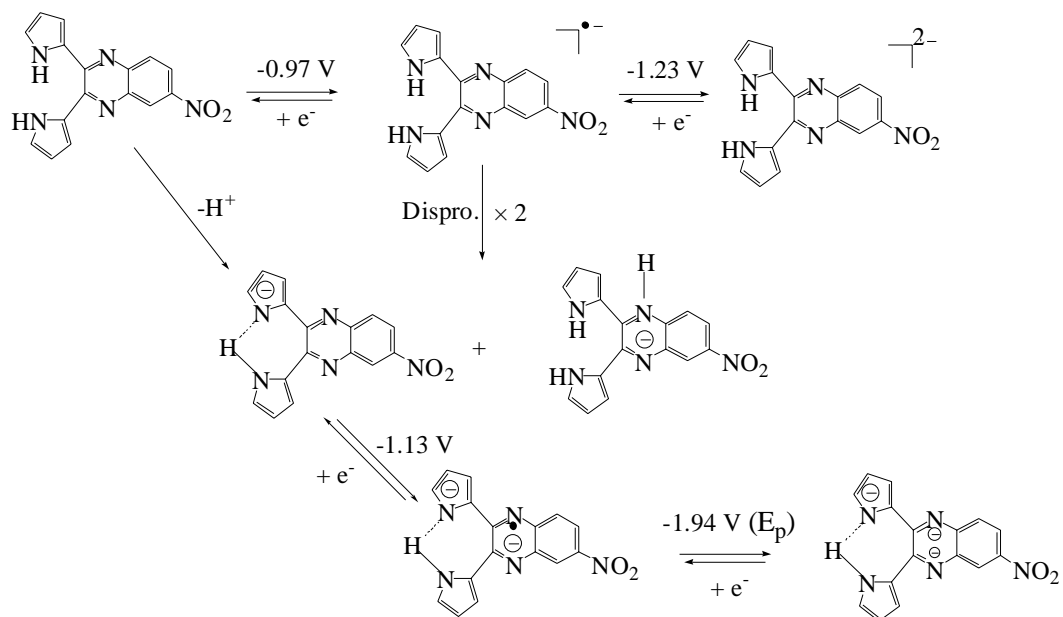


Figure 4-11. Corresponding Hill-plots indicate that two protons are removed from the core at the same time or that an anion binds to the compound. This differs from the result shown in Figure 4-9 which involves one proton is because the lower molar concentration leads to a larger dissociation constant in this case,¹¹ so that two protons can be easily removed or bound.

Figure 4-12 illustrates the UV-vis spectral changes of $\text{H}_2\text{DPQ}(\text{NO}_2)_n$ ($n = 0 - 2$) (10^{-5} - 10^{-6} M) observed upon titration with trifluoroacetic (TFA) in PhCN. The Hill-plot curve indicates that two protons are added to the two nitrogen atoms of quinoxaline group, leading to the formation of $[\text{H}_4\text{DPQ}(\text{NO}_2)_n]^{2+}$ ($n = 0-2$) in PhCN.

Figure 4-13 shows the cyclic voltammograms of $\text{H}_2\text{DPQ}(\text{NO}_2)_n$ at concentration of 10^{-3} M observed upon titrating with trifluoroacetic acid (TFA) in PhCN, 0.1 M TBAP, where two peaks appear upon addition of acid to the solution. These two peaks can be attributed to the reductions of the acid protons, and can be compared to the cyclic voltammogram of pure TFA in PhCN, 0.1 M TBAP (see Figure 4-14). The equivalence-current curve in Figure 4-13b also indicates that the acid titrations of $\text{H}_2\text{DPQ}(\text{NO}_2)_n$ ($n = 0 - 2$) at higher concentration also involve the addition of two protons to the quinoxaline moiety.

Table 4-1 shows the equilibrium constants for the reaction of both bases and acid with $\text{H}_2\text{DPQ}(\text{NO}_2)_n$, where $n = 0, 1$ or 2 in PhCN. Because of the presence of the electron withdrawing group, the acidity of the pyrrole NH proton increases as n goes from 0 to 2. Consistent with this proposition, $\log\beta_2$ for deprotonation of the two pyrrole protons on the compounds ranged from 7.1 to 8.8 in PhCN, while $\log\beta_2$ for addition of two protons to the two quinoxaline nitrogen atoms ranged from 0.7 to 4.6 in PhCN, the exact value varying as a function of the number of NO_2 substituents.

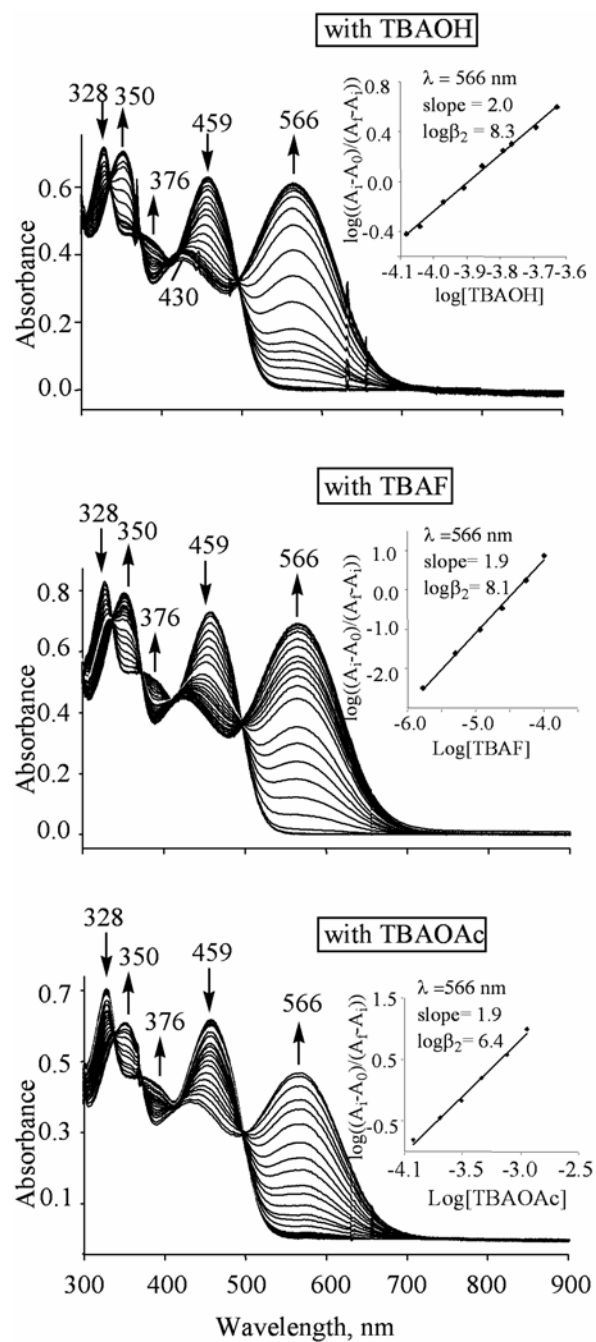


Figure 4-11. UV-vis spectral changes of $H_2DPQ(NO_2)$ (10^{-5} - 10^{-6} M) titrating with TBAOH, TBAF and TBAOAc in PhCN.

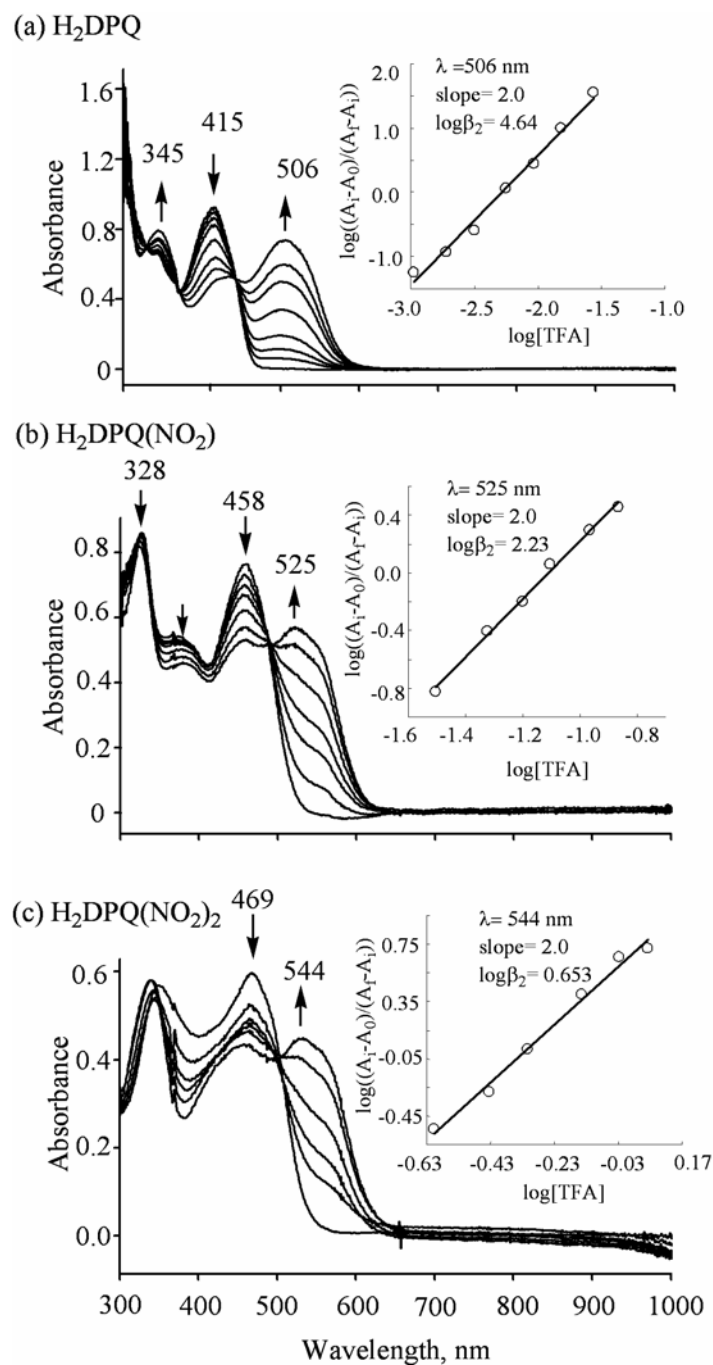


Figure 4-12. UV-vis spectral changes of $\text{H}_2\text{DPQ}(\text{NO}_2)_n$ ($n = 0-2$) (10^{-5} - 10^{-6} M) titrating with TBAOH, TBAF and TBAOAc in PhCN.

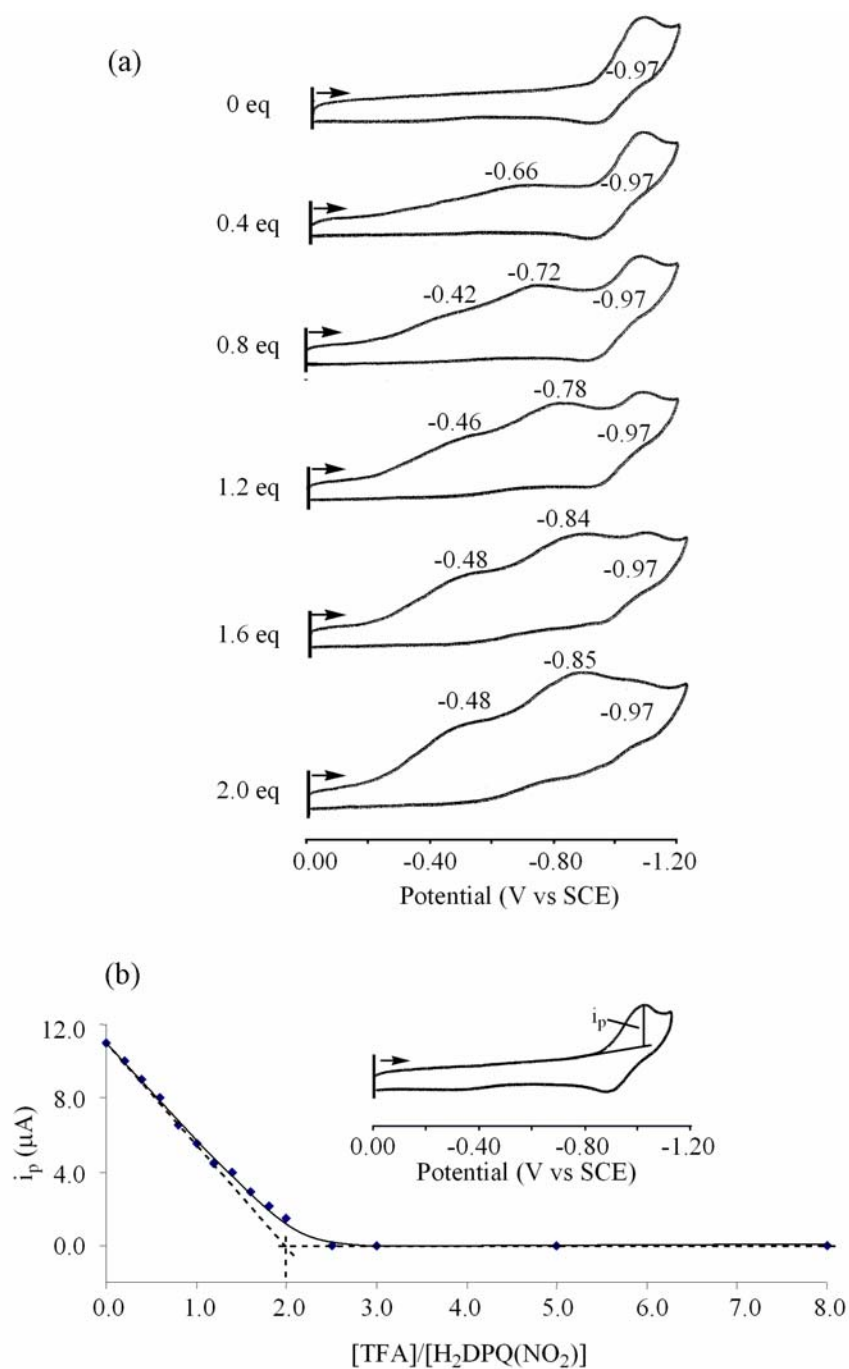


Figure 4-13. Cyclic voltammograms of H₂DPQ(NO₂) titrated by TFA at certain equivalent in PhCN, 0.1 M TBAP.

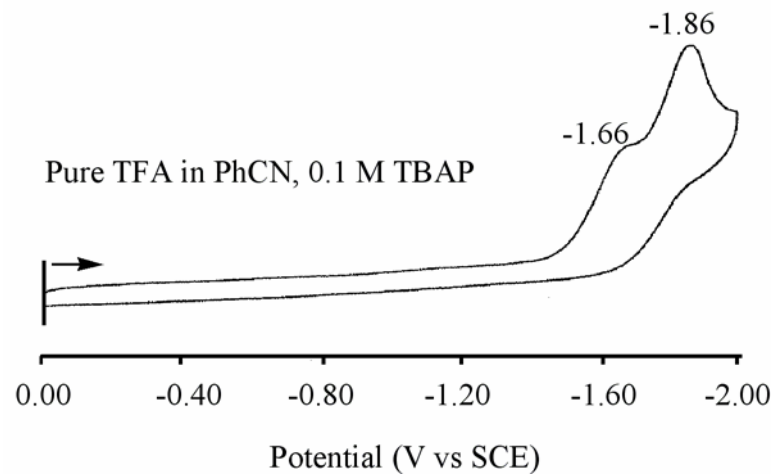


Figure 4-14. Pure TFA in PhCN, 0.1 M TBAP. Scan rate = 0.1 V/s.

Table 4-1. Equilibrium Constants for the Reactions of Bases and Acid with $\text{H}_2\text{DPQ}(\text{NO}_2)_n$ where $n = 0, 1$ or 2 in PhCN.

Cpd	Deprotonation- $\log \beta_2^a$			Protonation- $\log \beta_2^b$
	OH^-	F^-	OAc^-	TFA
H_2DPQ	7.1	7.0	5.3	4.6
$\text{H}_2\text{DPQ}(\text{NO}_2)$	8.3	8.1	6.4	2.2
$\text{H}_2\text{DPQ}(\text{NO}_2)_2$	8.8	8.7	6.9	0.7

^a $\text{H}_2\text{DPQ}(\text{NO}_2)_n + 2\text{A}^- \rightleftharpoons [\text{DPQ}(\text{NO}_2)_n]^{2-} + 2\text{HA}$ where $n = 0, 1$ or 2 .

^b $\text{H}_2\text{DPQ}(\text{NO}_2)_n + 2\text{H}^+ \rightleftharpoons [\text{H}_4\text{DPQ}(\text{NO}_2)_n]^{2+}$ where $n = 0, 1$ or 2 .

As might be expected, the formation constants vary for each $\text{H}_2\text{DPQ}(\text{NO}_2)_n$ derivative when subject to titration with different basic anions in the same solvents. Without exception, the trend $\text{TBAOH} > \text{TBAF} > \text{TBAOAc}$ was maintained. However, in all cases, two protons on the pyrrole rings were involved, as inferred from the spectral changes (see Figure 4-15). These changes were similar for all three $\text{H}_2\text{DPQ}(\text{NO}_2)_n$ derivatives studied. Generally, a decrease in the band at 414-469 nm and the growth of a new band at 479-576 nm is seen in Figure 4-15.

4.3 Conclusions

The overall electrochemistry and spectroelectrochemistry data at a relatively high concentration (10^{-3} M) of the DPQ derivatives investigated supports for the conclusion that a monodeprotonated anion is obtained after disproportionation of an initially formed dipyrrolylquinoxaline radical anion. This is in accord with the mechanism put forward in our recent publication.⁶

Electrochemical titrations of $\text{H}_2\text{DPQ}(\text{NO}_2)$ at concentration of 10^{-3} M in the presence of base also gave rise to the mono-deprotonated anion, as inferred from the observed spectral changes. Moreover, titrations of H_2DPQ , $\text{H}_2\text{DPQ}(\text{NO}_2)$ and $\text{H}_2\text{DPQ}(\text{NO}_2)_2$ with base at concentration of 10^{-5} - 10^{-6} M indicate that two protons are removed from the core or that an anion binds to the compound.

On the other hand, the spectroscopic titration of H_2DPQ , $\text{H}_2\text{DPQ}(\text{NO}_2)$ and $\text{H}_2\text{DPQ}(\text{NO}_2)_2$ with acid lead to the formation of the protonated forms, $[\text{H}_4\text{DPQ}(\text{NO}_2)_n]^{2+}$ ($n = 0 - 2$), in a manner that was straightforward and independent of DPQ concentration.

As the result of the present investigation, it has become possible to control and

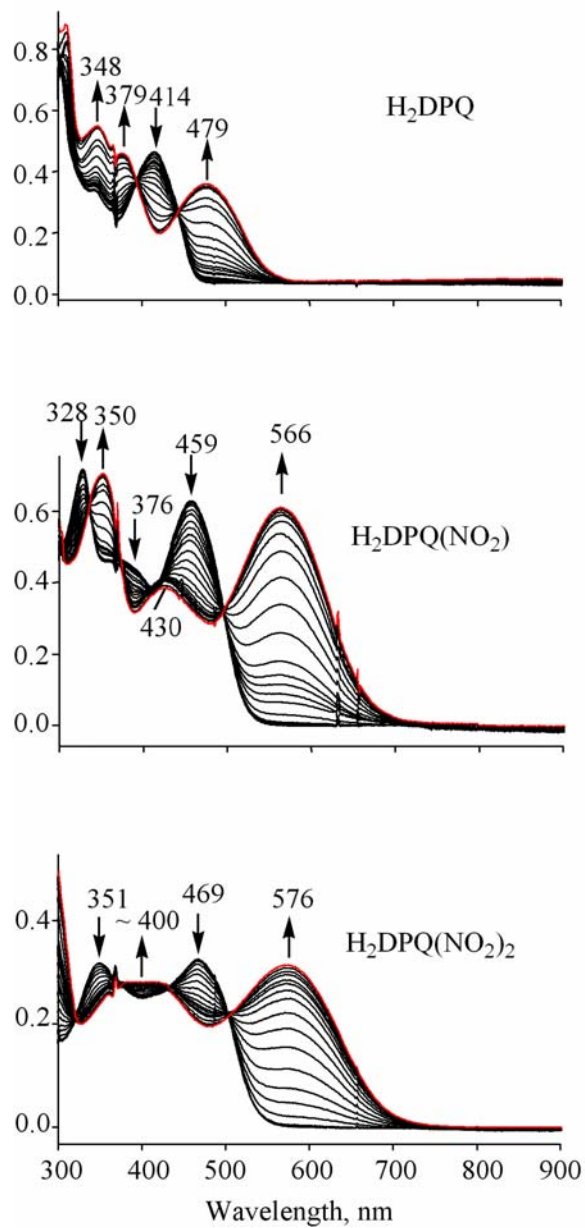


Figure 4-15. UV-vis spectral changes of H₂DPQ, H₂DPQ(NO₂), H₂DPQ(NO₂)₂ (10^{-5} - 10^{-6} M) upon titrating with TBAOH in PhCN.

identify the species obtained, as well as their relative ease of formation, when a congeneric series of DPQ derivatives, $\text{H}_2\text{DPQ}(\text{NO}_2)_n$ ($n = 0 - 2$), is analyzed under well-defined chemical and electrochemical conditions. This knowledge is expected to allow for a more detailed analysis of these kinds of quinoxaline derivatives as they are applied, e.g., in the design of new colorimetric anion or cation sensors.

4.4 References

1. Dietrich, B.; Hosseini, M. W., In *Supramolecular Chemistry of Anions*, Bianchi, A.; Bowman-James, K.; Garcís-España, E., Eds. Wiley-VCH: New York, **1997**; p 45.
2. Mizuno, T.; Wei, W.; Eller, L. R.; Sessler, J. L., *J. Am. Chem. Soc.* **2002**, *124*, (7), 1134.
3. Black, C. B.; Andrioletti, B.; Try, A. C.; Ruiperez, C.; Sessler, J. L., *J. Am. Chem. Soc.* **1999**, *121*, 10438.
4. Oddo, B. G., *Chim. Ital.* **1911**, *41*, 248.
5. Behr, D.; Brandange, S.; Lindstrom, B., *Acta Chem. Scand.* **1973**, *27*, 2411.
6. Fukuzumi, S.; Mase, K.; Ohkubo, K.; Fu, Z.; Karnas, E.; Sessler, J. L.; Kadish, K. M., *J. Am. Chem. Soc.* **2011**, *133*, 7284.
7. Pietrzak, M.; Try, A. C.; Andrioletti, B.; Sessler, J. L.; Anzenbacher, P. J.; Limbach, H.-H., *Angew. Chem. Int. Ed.* **2008**, *47*, 1123.
8. Kadish, K. M.; E, W.; Sintic, P. J.; Ou, Z.; Shao, J.; Ohkubo, K.; Fukuzumi, S.; Govenlock, L. J.; McDonald, J. A.; Try, A. C.; Cai, Z.; Reimers, J. R.; Crossley, M. J., *J. Phys. Chem. B* **2007**, *111*, 8762.
9. Angulo, G.; Dobkowski, J.; Kapturkiewicz, A.; Maciolek, K., *J. Photochem. Photobiol. A: Chemistry* **2010**, *213*, 101.
10. Bard, A. J.; Faulkner, L. R., *Electrochemical Methods: Fundamentals and Applications.* **2000**.
11. Skoog, D. A.; West, D. M.; Holler, F. J.; Crouch, S. R., In *Fundamentals of Analytical Chemistry*, Brooks/Cole/Thomson-learning: Belmont, **2004**; p 243.

Chapter Five

Electrochemistry and Spectroelectrochemistry of Tris- and Tetrakis-quinoxalinoporphyrins and Metal Complexes

5.1 Introduction

Porphyrinoid macrocycles appear in many naturally occurring redox systems and have many functional properties that make them attractive for use in emerging technologies.^{1,2} Quinoxalinoporphyrins are a class of laterally-extended porphyrins with aromatic ring systems fused to the β, β' -positions of a pyrrolic ring of the macrocycle. These compounds may be considered as building blocks for coplanar laterally-extended oligoporphyrins with applications in molecular electronics.³⁻⁸ Up to four quinoxaline groups have been fused to a porphyrin macrocycle and this expansion of the π -system offers a means to modulate the redox potentials and photophysical properties of the compounds.⁸

Previous work from our laboratory on the mono- and bis-quinoxalinoporphyrins **1**, **2**, **3** in Chart 5-1 have focused on the electrochemistry and spectroelectrochemistry of derivatives containing M^{II} , M^{III} or M^{IV} central metal ions as well as the free-base derivatives.⁹⁻¹⁵ The work described in the present Chapter expands upon our past electrochemical and spectroelectrochemical studies of quinoxalinoporphyrins⁹⁻¹⁵ to examine how the fusion of three and four quinoxaline groups will further affect the compound's redox properties and UV-visible spectra of the neutral, electroreduced and electrooxidized species. The investigated tris- and tetrakis-quinoxalinoporphyrins are given the notation $(PQ_3)M$ **4** and $(PQ_4)M$ **5** and have the structures shown in Chart 5-1.

Quinoxaline (Q) itself is an electroactive aromatic compound which is reversibly reduced at $E_{1/2} = -1.62$ V in CH_3CN ¹⁶ or -1.80 V in DMF¹⁷ giving a π -anion radical.⁴ The first reduction of the fused Q unit in the quinoxalinoporphyrins

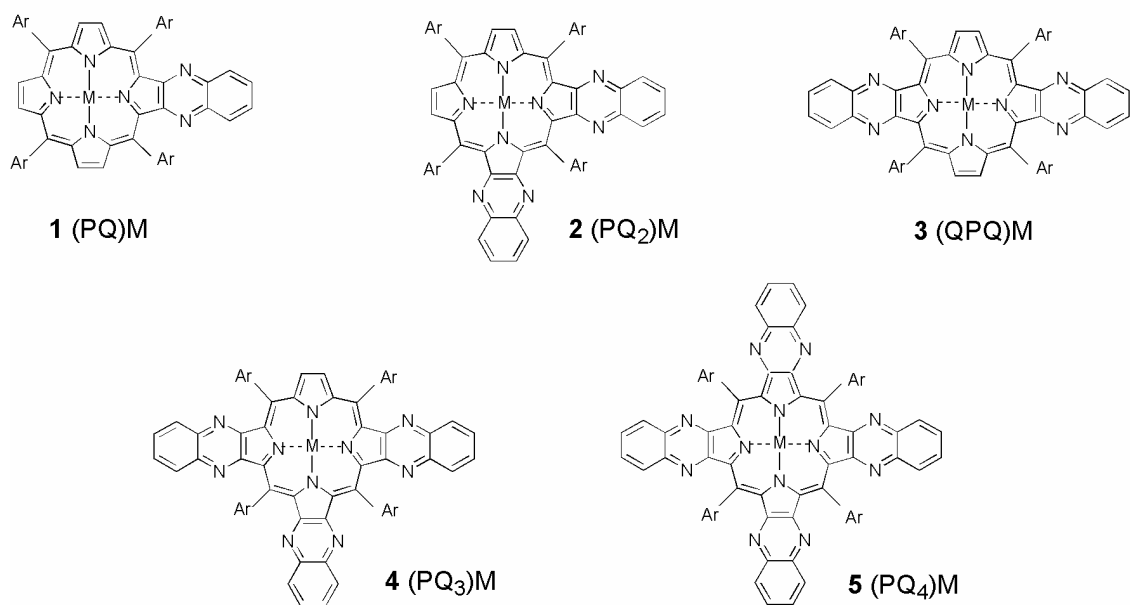


Chart 5-1. Structures of investigated metalloporphyrins with 1-4 fused quinoxaline groups.

1-3, however, is more difficult by almost 600 mV as compared to Q itself in the absence of the porphyrin and this electrode reaction cannot be observed in most electrochemical solvents having a negative potential window less than -2.0 V vs SCE. The one exception is in THF which has a wider potential range up to -3.0 V vs SCE where electron addition to this fused electroactive group can be monitored.

A summary of redox behavior for the previously investigated derivatives of **1** to **3** is briefly described on the following pages while discussing the behavior of the newly investigated compounds in the series of (PQ₃)M **4** and (PQ₄)M **5**.

5.2 Results and Discussion

5.2.1 Electrochemistry of (PQ₃)M and (PQ₄)M

Cyclic voltammograms showing the reduction of (PQ₃)M (M = 2H, Cu, Pd, Ni and Zn) in pyridine are illustrated in Figure 5-1 while Figure 5-2 shows both reductions and oxidations of the same series of compounds in PhCN. No oxidations of (PQ₃)M can be observed in pyridine because of the limited anodic potential range of this solvent. The electrochemical data of (PQ₃)M **4** and (PQ₄)M **5** together with that of **1-3** are summarized in Tables 5-1, 5-2 and 5-3 in CH₂Cl₂, PhCN, and THF, respectively, .

The first two reversible reductions of (PQ₃)M are localized on the conjugated π -ring system of the macrocycle and generate the porphyrin π -anion radical and dianion, respectively. The potential difference between the first and second one-electron reductions of the metalated complexes (PQ₃)M amounts 0.36 to 0.41 V in pyridine (Figure 5-1) and this value is comparable with the $\Delta E_{1/2} = 0.42 \pm 0.05$ V

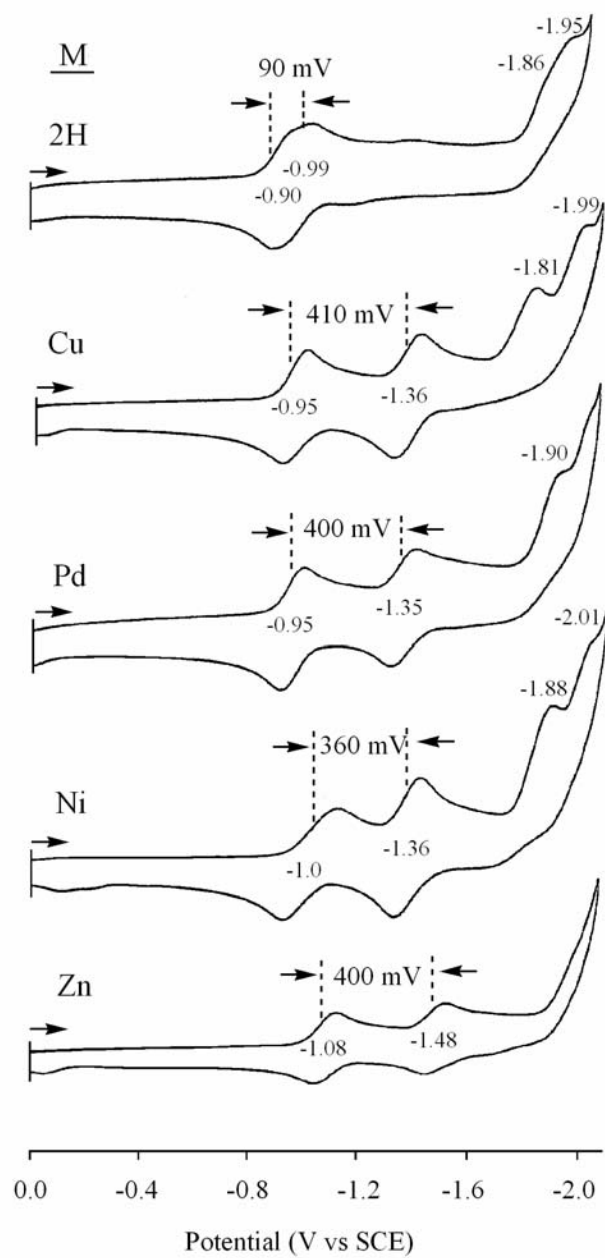


Figure 5-1. Cyclic voltammograms of $(PQ_3)M$ ($M = 2H, Cu, Pd, Ni, Zn$) in pyridine, 0.1 M TBAP. Scan rate = 0.1 V/s.

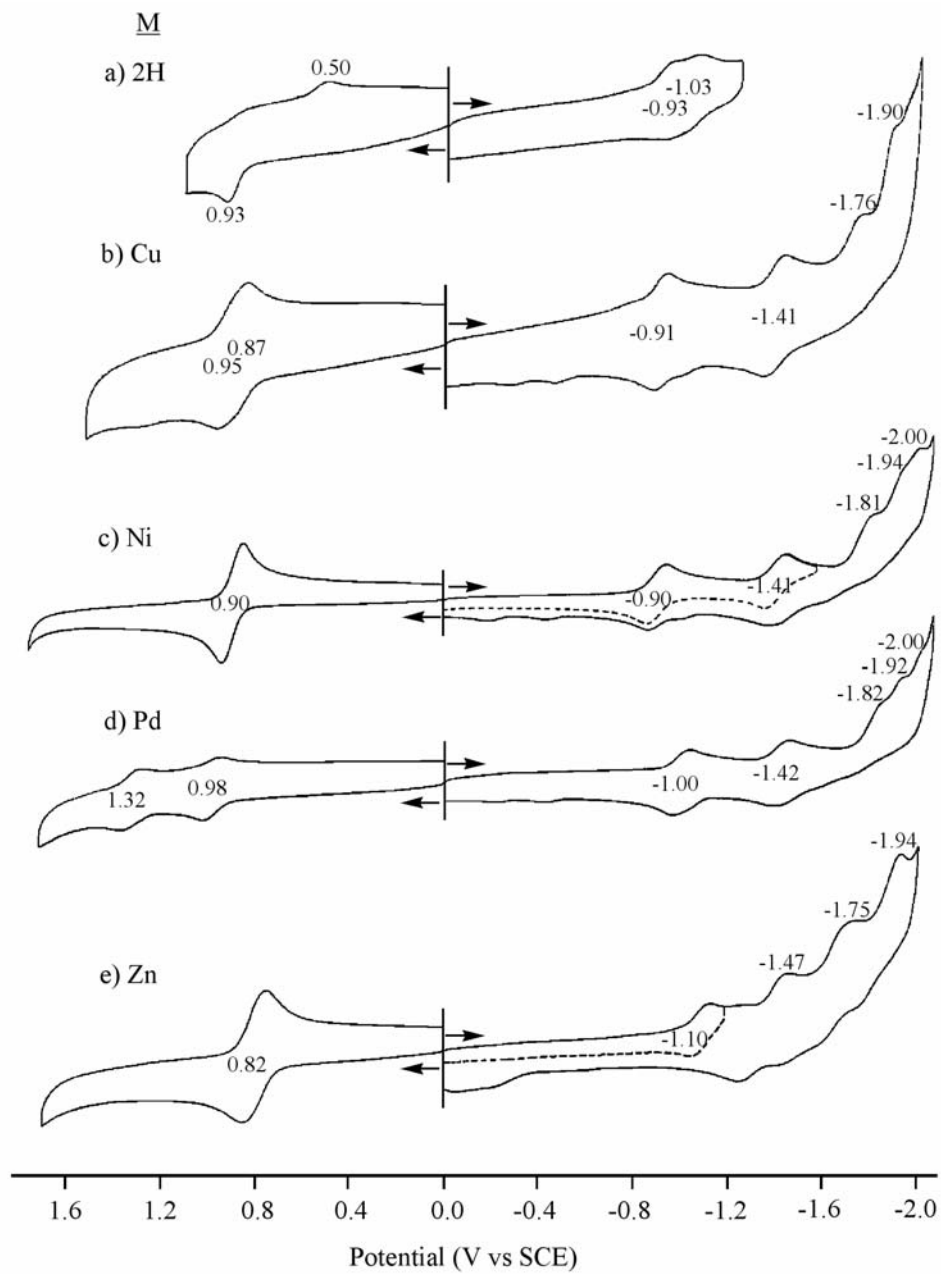


Figure 5-2. Cyclic voltammograms of $(PQ_3)M$ ($M = 2H, Cu, Pd, Ni, Zn$) in PhCN, 0.1 M TBAP. Scan rate = 0.1 V/s.

Table 5-1. Half-wave Potentials (V vs SCE) of (PQ_n)M in CH₂Cl₂ Containing 0.1 M TBAP

M	Macro-cycle	oxidation		reduction		HOMO-LUMO gap(V)	ref
		2 nd	1 st	1 st	2 nd		
2H	P	--	0.95	-1.22	-1.55	2.17	11
	PQ	0.99 ^b	0.99 ^b	-1.13	-1.33	2.12	11
	PQ ₂	1.00 ^{a,b}	1.00	-0.97	-1.23	1.97	15
	QPQ	1.23	0.94	-1.03	-1.32 ^a	1.97	15
	PQ ₃	--	0.97 ^a	-1.01	--	--	tw
	PQ ₄	--	0.83 ^a	-0.77 ^a	--	--	tw
Zn	P	1.06	0.72	-1.42	--	2.14	11
	PQ	1.10 ^a	0.72	-1.31	-1.75 ^a	2.03	11
	PQ ₂	1.08 ^a	0.77	-1.29	--	2.06	15
	QPQ	0.93	0.76	-1.14	-1.42	1.90	15
	PQ ₃	0.80	0.67	-1.12	-1.37	1.79	tw
	PQ ₄	0.67 ^b	0.67 ^b	-1.16 ^a	-1.37	--	tw
Cu	P	1.28 ^a	0.92	-1.36	-1.92 ^a	2.28	11
	PQ	1.30 ^a	0.97	-1.19	-1.72 ^a	2.16	11
	PQ ₂	1.03	0.92	-1.13	-1.41	2.05	15
	QPQ	1.04	0.91	-0.99	-1.40	1.90	15
	PQ ₃	0.95	0.85	-0.95	-1.41	1.80	tw
	PQ ₄	0.93	0.76	-0.86	-1.38	1.62	tw
Ni	P	0.93 ^b	0.93 ^b	-1.31	--	2.24	11
	PQ	0.95 ^b	0.95 ^b	-1.12	-1.59 ^a	2.07	11
	PQ ₂	0.93 ^b	0.93 ^b	-1.07	--	2.00	15
	QPQ	0.92 ^b	0.92 ^b	-1.00	-1.40	1.92	15
	PQ ₃	0.89 ^b	0.89 ^b	-0.97	-1.56 ^a	1.86	tw
	PQ ₄	0.81 ^b	0.81 ^b	-0.89	-1.38	1.70	tw
Pd	P	1.52 ^a	1.05	-1.32	-1.95 ^a	2.37	11
	PQ	1.46 ^a	1.06	-1.16	-1.62 ^a	2.22	11
	PQ ₂	1.38	0.99	-1.14	--	2.13	15
	QPQ	1.41	1.01	-1.00	-1.43	2.01	15
	PQ ₃	1.38	0.95	-1.06	-1.56 ^a	2.01	tw
	PQ ₄	1.29	0.89	-1.05	-1.50 ^a	1.94	tw

^a Peak potentials at a scan rate of 0.1 V/s.^b Overlapping two one-electron processes.

tw = this work.

Table 5-2. Half-wave Potentials (V vs SCE) of (PQ_n)M in PhCN Containing 0.1 M TBAP

M	Macro cycle	oxidation		reduction		HOMO-LUMO gap(V)	ref
		2 nd	1 st	1 st	2 nd		
2H	P	1.25	0.99	-1.19	-1.56	2.18	11
	PQ	1.06 ^b	1.06 ^b	-1.08	-1.31	2.14	11
	PQ ₂	--	1.04 ^a	-0.95	-1.26	--	15
	PQ ₃	--	0.93 ^a	-0.93	-1.03	--	tw
Zn	P	1.09	0.77	-1.34	-1.73	2.11	11
	PQ	1.04	0.84	-1.19	-1.58 ^a	2.03	11
	PQ ₂	0.94	0.82	-1.21	-1.62 ^a	2.03	15
	PQ ₃	0.82 ^b	0.82 ^b	-1.10	-1.47 ^a	1.92	tw
Cu	P	1.26	0.96	-1.28	-1.75	2.24	11
	PQ	1.14	0.98	-1.09	-1.55	2.07	11
	PQ ₂	1.06	0.95	-1.06	-1.59	2.01	15
	PQ ₃	0.95	0.87	-0.91	-1.41	1.78	tw
	PQ ₄	0.76 ^b	0.76 ^b	-0.83	-1.44	1.59	tw
Ni	P	1.08 ^b	1.08 ^b	-1.26	-1.81	2.34	11
	PQ	1.03 ^b	1.03 ^b	-1.08	-1.56	2.11	11
	PQ ₂	0.97 ^b	0.97 ^b	-1.01	-1.59	1.98	15
	PQ ₃	0.90 ^b	0.90 ^b	-0.90	-1.41	1.80	tw
Pd	P	1.46	1.12	-1.25	-1.75	2.37	11
	PQ	--	1.11	-1.09	-1.56	2.20	11
	PQ ₂	--	1.07	-1.09	-1.53	2.16	15
	PQ ₃	1.32	0.98	-1.00	-1.42	1.98	tw
	PQ ₄	1.27	0.89	-1.03	-1.43	1.92	tw

^a Peak potentials at a scan rate of 0.1 V/s.

^b Overlapping two one-electron processes.

tw = this work.

Table 5-3. Half-wave Potentials (V vs Ag/AgCl) of (PQ₃)M in THF Containing 0.1 M TBAP*

macro	M	ox			red		
		P1	P1	P2	Q1 ^a	Q2 ^a	Q3 ^a
PQ	2H	1.26 ^a	-1.03	-1.25	-2.24		
	Pd	1.38	-1.04	-1.45	-2.14		
	Cu	1.20	-1.07	-1.46	-2.15		
	Ni	1.10	-1.04	-1.44	-2.18		
	Zn	1.02	-1.18	-1.55	-2.27		
QPQ	2H	1.17	-0.91	-1.14	-1.97	-2.18	
	Pd	1.29	-0.90	-1.32	-2.08	-2.25	
	Cu	1.16 ^b	-0.89	-1.27	-2.06	-2.26	
	Ni	1.04	-0.88	-1.27	-2.06	-2.28	
	Zn	1.07	-1.02	-1.43	-2.10	-2.27	
PQ ₂	2H	1.31 ^a	-0.89	-1.17	-2.07	-2.22	
	Pd	1.29	-1.05	-1.46	-2.00	-2.25	
	Cu	1.12	-1.01	-1.46	-1.98	-2.28	
	Ni	1.03	-0.93	-1.48	-2.00	-2.26	
	Zn	1.03	-1.17	-1.65 ^a	-1.86	-2.29	
PQ ₃	2H	1.27 ^a					
	Pd	1.24	-0.91	-1.28	-1.92	-2.04	-2.25
	Cu	1.09	-0.81	-1.27	-1.85	-2.00	-2.23
	Ni	0.97	-0.81	-1.31	-1.91	-2.05	-2.27
	Zn	1.01	-1.04	-1.45	-1.90	-2.09	-2.28

* data collected by our Australian collaborator.

^a Peak potentials at a scan rate of 0.1 V/sec.

^b peak distorted due to absorption.

given by Fuhrhop et al.¹⁸ as one diagnostic criterion for ring-centered reduction of metalloporphyrins. A smaller separation in half-wave potentials between formation of the free-base porphyrin π -anion radical and the dianion is seen for $(PQ_3)H_2$ where $\Delta E_{1/2} = 90$ mV. Smaller values of $\Delta E_{1/2}$ have previously been observed for a number of related free-base porphyrins with TPP-like structures.¹⁹

Two additional reductions of doubly reduced $(PQ_3)M$ and $(PQ_3)H_2$ are seen at $E_{1/2}$ values are close to the negative potential limit of the solvent as shown in Figures 5-1 and 5-2 and these reactions can be assigned to electron additions involving the fused quinoxaline groups, as discussed in more detail below.

The reductive behavior for $(PQ_3)M$ in PhCN is quite similar to that which is seen in pyridine. The main difference between the two solvents is that PhCN has a longer positive potential limit so two oxidations at the π -ring system of the macrocycle can be detected in PhCN to give a π -cation radical and dication. These processes, which give the porphyrin π -cation radical and dication, are well-separated from each other for the Pd and Cu derivatives, but are overlapped in the case of $(PQ_3)Ni$ and $(PQ_3)Zn$, to give a single two-electron transfer process with the double peak current as shown in Figure 5-2.

Cyclic voltammograms for $(PQ_4)M$ complexes ($M = Cu, Pd, Ni$ and Zn) in CH_2Cl_2 are shown in Figure 5-3. Two well-separated one-electron reversible reductions are observed only for $(PQ_4)Cu$, $(PQ_4)Ni$, while $(PQ_4)Pd$ and $(PQ_4)Zn$ both exhibit a second reduction which is overlapped with a following process. Similarly to the case of $(PQ_3)M$, there are two oxidations to stepwise give a π -cation radical

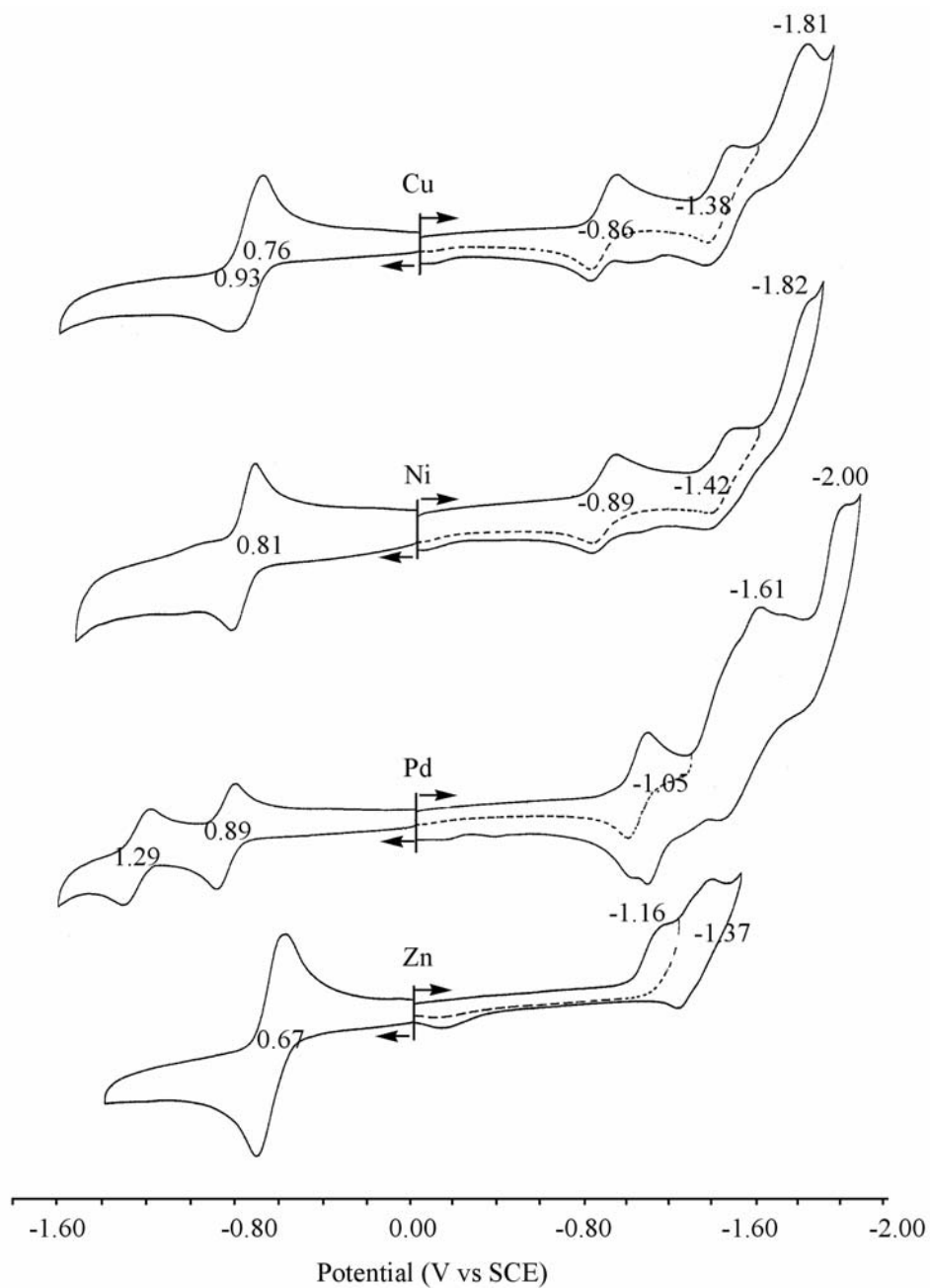


Figure 5-3. Cyclic voltammograms of (PQ₄)M (M = Cu, Ni, Pd, Zn) in CH₂Cl₂, 0.1 M TBAP.

and dication. The $\Delta E_{1/2}$ between these electrode reactions vary with the metal ion as shown in Figure 5-3. Again, the two oxidations of (PQ₄)Ni and (PQ₄)Zn are overlapped to give a single two-electron transfer process.

5.2.2 (PQ₃)M vs (PQ₂)M and (QPQ)M

Table 5-3 illustrates the shifts in $E_{1/2}$ (V vs SCE) upon going from (PQ₂)M to (PQ₃)M, (QPQ)M to (PQ₃)M and (PQ₃)M to (PQ₄)M in nonaqueous solvents containing 0.1 M TBAP. In all cases, the (PQ₃)M compounds are easier to reduce and oxidize than the (PQ₂)M and (QPQ)M. As seen in Table 5-4, half-wave potentials for the first reductions of (PQ₃)M are all positively shifted from $E_{1/2}$ for the same reactions of corner (PQ₂)M by 80-170 mV in CH₂Cl₂, 70-130 mV in pyridine, 90-150 mV in PhCN, 130-200 mV in THF. Half-wave potentials for the second reductions of (PQ₃)M are also positively shifted from the corner (PQ₂)M potentials by 140-270 mV in pyridine, 110-230 mV in PhCN, and 170-190 mV in THF. In contrast, $E_{1/2}$ for the Pd, Cu, Ni, Zn derivatives of (PQ₃)M shift only slightly with respect to the half-wave potential of their (QPQ)M counterparts, which indicates that the fusion of the third quinoxaline group at the pyrrolic group to the linear (QPQ)M has little effect on the first two one-electron reductions of these porphyrins.

As for oxidation, the same (PQ₃)M derivatives are slightly easier to oxidize compared to (PQ₂)M and (QPQ)M. The differences in half-wave potentials in this case amount to 40-100 mV in CH₂Cl₂ and 20-60 mV in THF from (PQ₃)M to (PQ₂)M. This observation indicates that the fusion of the third quinoxaline group to

the porphyrin macrocycle has an equal effect on the oxidations (the HOMO orbitals).

5.2.3 (PQ₄)M vs (PQ₃)M

The $E_{1/2}$ for the first reduction shifts by 10-90 mV upon going from (PQ₄)M to (PQ₃)M in CH₂Cl₂, and by 10-80 mV is seen in pyridine. The only exception is (PQ₄)Pd where the first reduction is harder by 30 mV in PhCN as compared to (PQ₃)Pd. As for the oxidation, the difference in potential between $E_{1/2}$ for the oxidation of the (PQ₄)M and (PQ₃)M is 60-90 mV in CH₂Cl₂, 90 mV in PhCN as shown in Table 5-4.

5.2.4 (PQ_n)M (n = 0 – 4)

Cyclic voltammograms of (PQ_n)Cu (n = 0 - 4) in PhCN are illustrated in Figure 5-4. The HOMO-LUMO gaps range from 2.24 to 1.69 V depending on the solvent and number of Q groups as seen in Tables 5-1 and 5-2. The HOMO-LUMO gap decreases in the following order: (P)M > (PQ)M > (PQ₂)M > (PQ₃)M > (PQ₄)M for compounds with the same central metal ion, and this is graphically shown in Figure 5-4 for the case of the five Cu(II) complexes.

5.2.5 Metalation for (PQ₃)M and (PQ₄)M

A linear relationship (correlation coefficient = 0.99) can be seen between the first reduction potentials of the (PQ₃)M and (PQ₄)M complexes in CH₂Cl₂ (Figure 5-5). The slope of the plot in this Figure is 1.09 which indicates that metalation has almost the same effect on the $E_{1/2}$ for the first reduction of the (PQ₃)M and (PQ₄)M

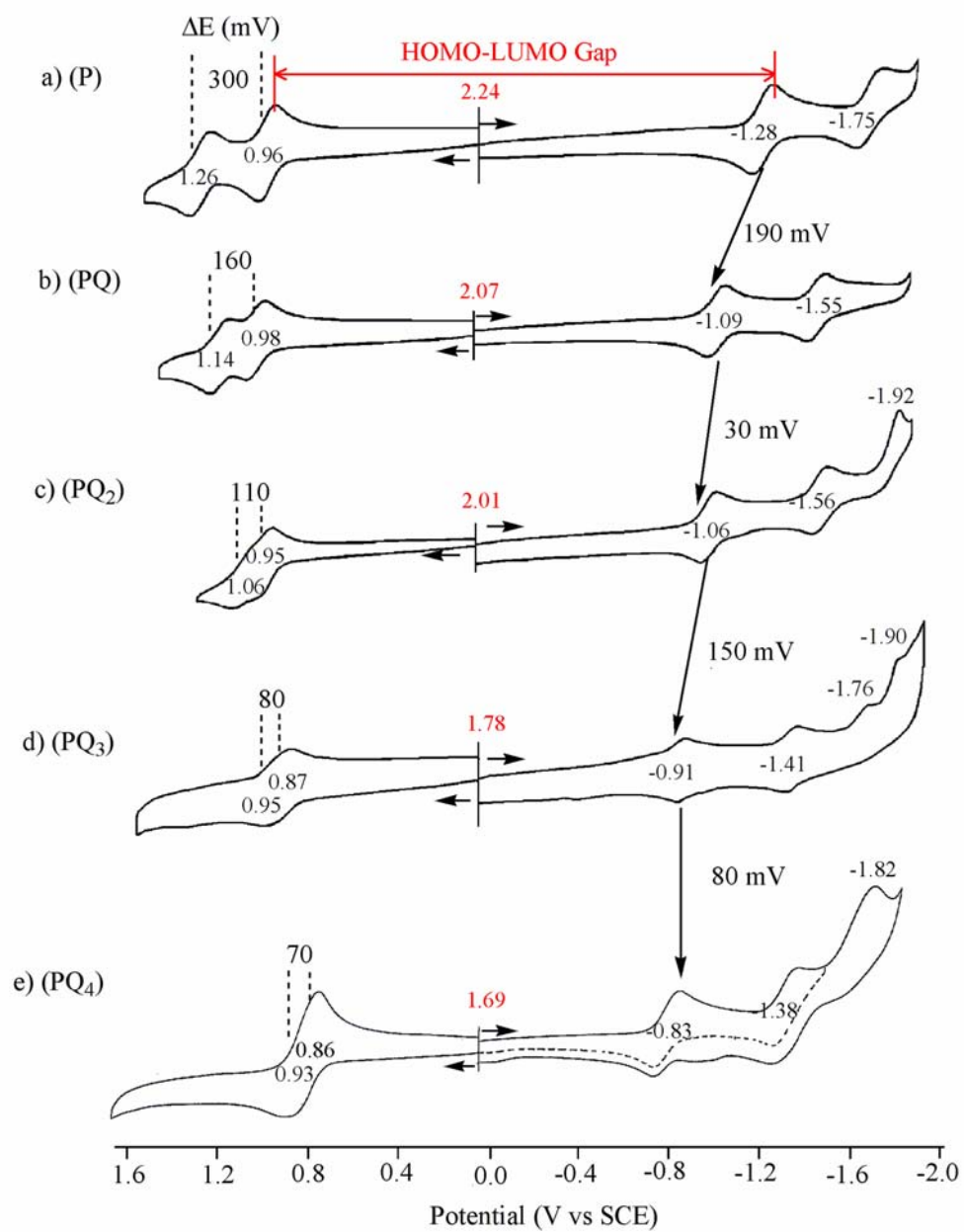


Figure 5-4. Cyclic voltammograms of $(PQ_n)Cu^{II}$ ($n = 1-4$) in PhCN, 0.1 M TBAP.

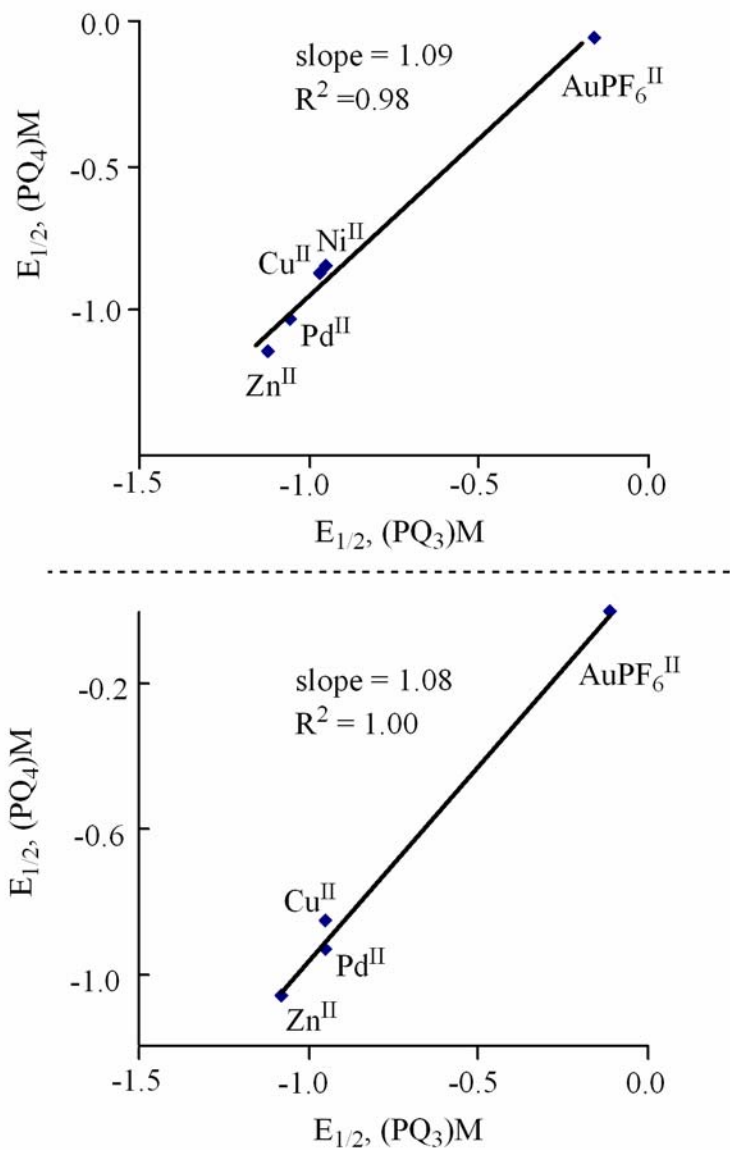


Figure 5-5. Plot of half-wave potentials of (PQ₃)M vs half-wave potentials of (PQ₄)M upon the first reduction in CH₂Cl₂ (above) and pyridine (below), 0.1 M TBAP.

complexes in CH_2Cl_2 , 0.1 M TBAP. A similar result is obtained in PhCN (slope =1.08, correlation coefficient =1.00).

5.2.6 Gold Complexes

Cyclic voltammograms of $(\text{PQ}_3)\text{AuPF}_6$ and $(\text{PQ}_4)\text{AuPF}_6$ in pyridine are shown in Figure 5-6. Table 5-5 lists half-wave potentials for reduction of the different Au(III) in four solvents, PhCN, CH_2Cl_2 , pyridine and THF.

Three reversible one-electron reductions for these two compounds are seen in a variety of nonaqueous solvents. The first electrode reaction involves the central metal ion and the next two, the conjugated π -ring system as reported in the case of $(\text{PQ})\text{Au}^{\text{III}}\text{PF}_6$.⁹ Evidence for assignment of a Au(III)/Au(II) process in the first reduction is given in this chapter on the basis of electrochemistry coupled with UV-visible spectroscopy.

Cyclic voltammograms of $(\text{PQ}_4)\text{Au}^{\text{III}}\text{PF}_6$ and $(\text{PQ}_4)\text{Cu}^{\text{II}}$ and $(\text{PQ}_4)\text{Ni}^{\text{II}}$ in CH_2Cl_2 are illustrated in Figure 5-7. Two one-electron reductions are expected and observed for $(\text{PQ}_4)\text{Cu}^{\text{II}}$ and $(\text{PQ}_4)\text{Ni}^{\text{II}}$, consistent with the stepwise formation of a porphyrin π -anion radical and dianion. This contrast with $(\text{PQ}_4)\text{Au}^{\text{III}}\text{PF}_6$ where one of three processes involves the central ion. As described in a later section, this reaction occurs prior to formation of a Au(II) porphyrin π -anion radical and dianion at more positive potentials.

5.2.7 Intramolecular Communication

$(\text{PQ}_3)\text{Cu}$ undergoes five reductions at -0.81, -1.27, -1.85, -2.00 and -2.23 V vs

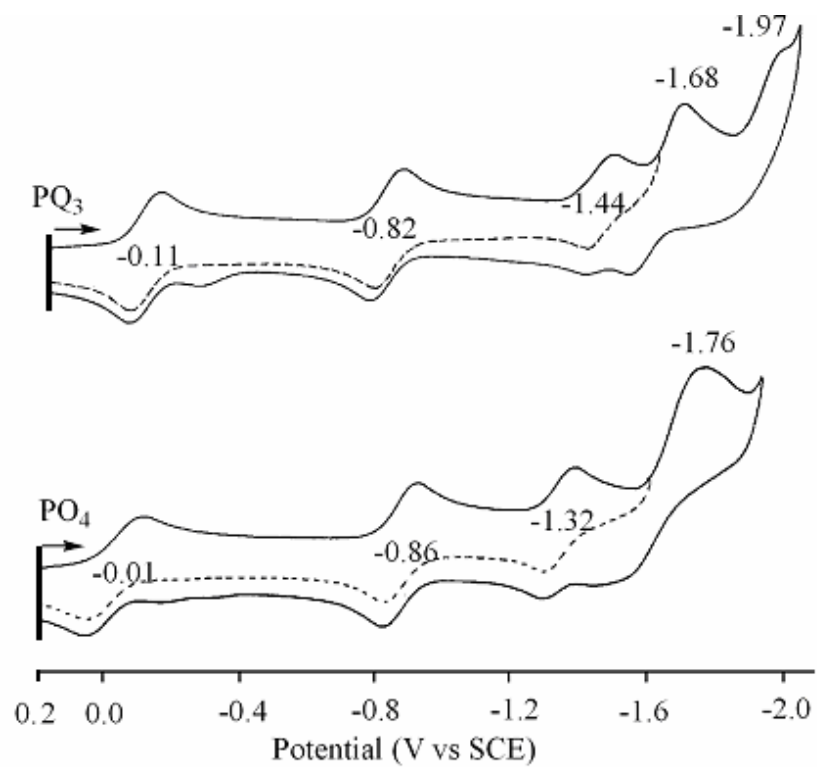


Figure 5-6. Cyclic voltammograms of $(PQ_n)AuPF_6$ ($n = 3 - 4$) in pyridine, 0.1 M TBAP.

Table 5-5. Half-wave Potentials (V vs SCE) of Gold Derivatives in Different Solvents Containing 0.1 M TBAP

macrocycle	solvent	ox		red				
		P1	Au ^{III/II}	P1	P2	Q1 ^a	Q2 ^a	Q3 ^a
P	PhCN	1.66	-0.56	-1.09	-1.81			
PQ		1.63	-0.39	-0.88	-1.81			
PQ ₂		1.53	-0.29	-1.00	-1.53	-1.98 ^a		
PQ₃		1.42	-0.13	-0.84	-1.46^b	-1.90^a	-1.98^a	
P	CH ₂ Cl ₂	1.59	-0.64	-1.15				
PQ		1.54	-0.47	-0.97	-1.80			
QPQ		1.48	-0.28	-0.82	-1.66			
PQ ₂		1.48	-0.31	-0.15	-1.55			
PQ₃		1.36	-0.16	-0.89	-1.47	-1.68^a		
PQ₄		1.24	-0.07	-0.94	-1.38	-1.55^a	-1.70^a	-1.98^a
P	pyridine		-0.52	-1.08	-1.76			
PQ			-0.35	-0.87	-1.69			
QPQ			-0.17	-0.71	-1.56			
PQ ₂			-0.24	-0.97	-1.48	-1.85 ^a		
PQ₃			-0.11	-0.82	-1.44	-1.68^a	-1.97^a	
PQ₄			-0.01	-0.86	-1.32		-1.76^a	
P	THF ^b		-0.40	-1.10	-1.77			
PQ			-0.20	-0.88	-1.65	-2.22 ^a		
QPQ			-0.02	-0.70	-1.53	-2.04 ^a	-2.22 ^a	
PQ ₂		1.53	-0.07	-0.95	-1.45	-1.97 ^a	-2.26 ^a	
PQ₃		1.45	0.09	-0.76	-1.37	-1.85^a	-2.05^a	-2.25^a

^a Peak potentials at a scan rate of 0.1 V/s.

^b data collected by our Australian collaborator. Potential was references against Ag/AgCl.

This work in bold print.

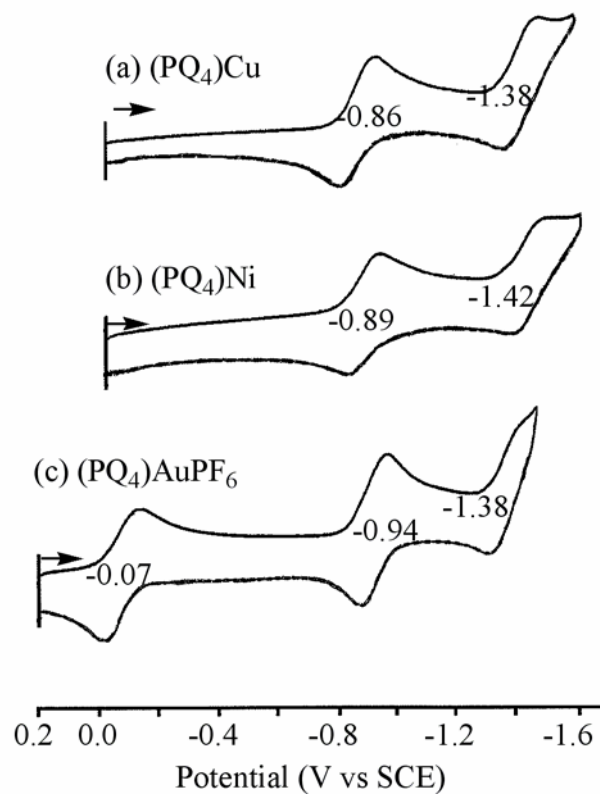


Figure 5-7. Cyclic voltammograms of (a) (PQ₄)Cu, (b) (PQ₄)Ni and (c) (PQ₄)AuPF₆ in CH₂Cl₂ containing 0.1 M TBAP.

Ag/AgCl in THF (see Table 5-3). The first two reductions are reversible and are ring-centered reactions yielding π -anion radical and dianion. The last three reductions are irreversible and are assigned as quinoxaline-centered reactions.^{2,8,9} Each quinoxaline group gains one electron at different anodic peak potential which means that the fused quinoxaline already has received some electron density from the previous reductions making a harder reduction for itself.

5.2.8 UV-visible Spectroelectrochemistry

The UV-visible spectra of each neutral trisquinoxalinoporphyrin derivatives (PQ₃)M with different central metal ion in PhCN and pyridine are listed in Table 5-6. The neutral spectra of trisquinoxalinoporphyrins (PQ₃)M and tetrakisquinoxalinoporphyrins (PQ₄)M in CH₂Cl₂ are summarized in Table 5-7. The spectroelectrochemistry of tris- and tetrakis-quinoxalinoporphyrins was carried in a thin-layer cell to demonstrate the site of electron transfer.

5.2.8.1 Oxidation

The first oxidation of (PQ₃)M and (PQ₄)M leads to dramatic changes in both the Soret and visible bands. An example of the thin-layer spectral changes during the oxidation of (PQ₃)Cu at a controlled potential of 1.20 V in PhCN is shown in Figure 5-8. Two sets of UV-visible spectral changes were observed as a function of time based on different sets of isosbestic points as shown in Figures 5-8a and 5-8b. The first process generates the porphyrins π cation radical and the second give the dication.

The neutral compound has three Soret bands at 348, 442, 501 nm and two

Table 5-6. UV-visible Spectral Data of (PQ₃)M in PhCN and Pyridine Containing 0.1 M TBAP

Solvent	M	$\lambda(\text{nm}, \epsilon \times 10^{-4} \text{ M}^{-1} \text{ cm}^{-1})$								
		Soret bands				visible bands				
PhCN	2H	346(1.0)		420(1.7)	470(1.7) ^{sh}	495(2.1)	579(0.7)	610(0.8)	642(0.7)	690(0.5)
	Pd	350(3.1)		433(3.3)	487(3.5)		569(0.6) ^{sh}	605(1.0)	614(1.1)	648(2.2)
	Cu	348(2.1)		442(3.0)	501(3.0)			630(0.8)		675(1.1)
	Ni	361(7.4)		448(6.6)	502(6.6)			641(1.5)		678(2.3)
	Zn	347(3.6)	410(5.7)	431(6.2)	491(5.3) ^{sh}	512(6.5)	621(1.7) ^{sh}	634(2.0)		678(2.5)
pyridine	2H	346(2.6)		420(4.7)	469(4.4)	493(5.7)	577(1.2)	608(1.3)	633(1.0)	690(0.4)
	Pd	350(3.2)		432(3.5)	487(3.6)		567(0.7) ^{sh}	605(1.2)	615(1.2)	647(2.4)
	Cu	350(7.4)	408(6.6) ^{sh}	443(8.7)	507(9.3)			632(2.2)		678(2.9)
	Ni	351(6.4)	416(8.5) ^{sh}	433(9.0)	491(7.3) ^{sh}	512(8.3)		628(2.9)		668(2.7)
	Zn	348(3.3)	410(4.7)	432(5.5)	490(4.6) ^{sh}	513(6.2)	621(1.7) ^{sh}	635(2.0)		676(1.8)

sh = shoulder peak.

Table 5-7. UV-visible Spectral Data of (PQ_n)M (n = 3 and 4) in CH₂Cl₂ Containing 0.1 M TBAP

		$\lambda(\text{nm}, \epsilon \times 10^{-4} \text{ M}^{-1} \text{ cm}^{-1})$							
	M	Soret bands				visible bands			
(PQ ₃)	2H	344(3.2)	419(5.9)	466(5.4)	491(6.8)	576(1.3)	607(1.3)	636(1.0)	688(0.3)
	Pd	348(7.1)	430(7.4)		483(7.6)		604(1.9)		646(4.5)
	Cu	346(6.4)	436(9.0)		496(8.6)		627(2.1)		672(3.0)
	Ni	358(7.3)	445(6.1)		501(6.0)		633(1.1)		677(2.4)
	Zn	346(4.2)	433(6.3)		501(7.0)		629(1.7)		673(2.7)
(PQ ₄)	2H	349(1.8)	425(3.7)	469(5.4)	523 (4.4)	589 (0.7)	626(1.1)	647(1.7)	699(0.5)
	Pd	350(10.0)	428(9.6)		496(10.6)		618(1.9)		669(9.5)
	Cu	349(6.0)	436(8.5)		510(7.0)		647(1.3)		698(4.4)
	Ni	358(4.0)	444(3.4)		516(3.7)		648(0.6)		702(2.1)
	Zn	348(5.5)	435(9.6)		522(10.2)		649(1.2)		696(5.1)

sh = shoulder peak.

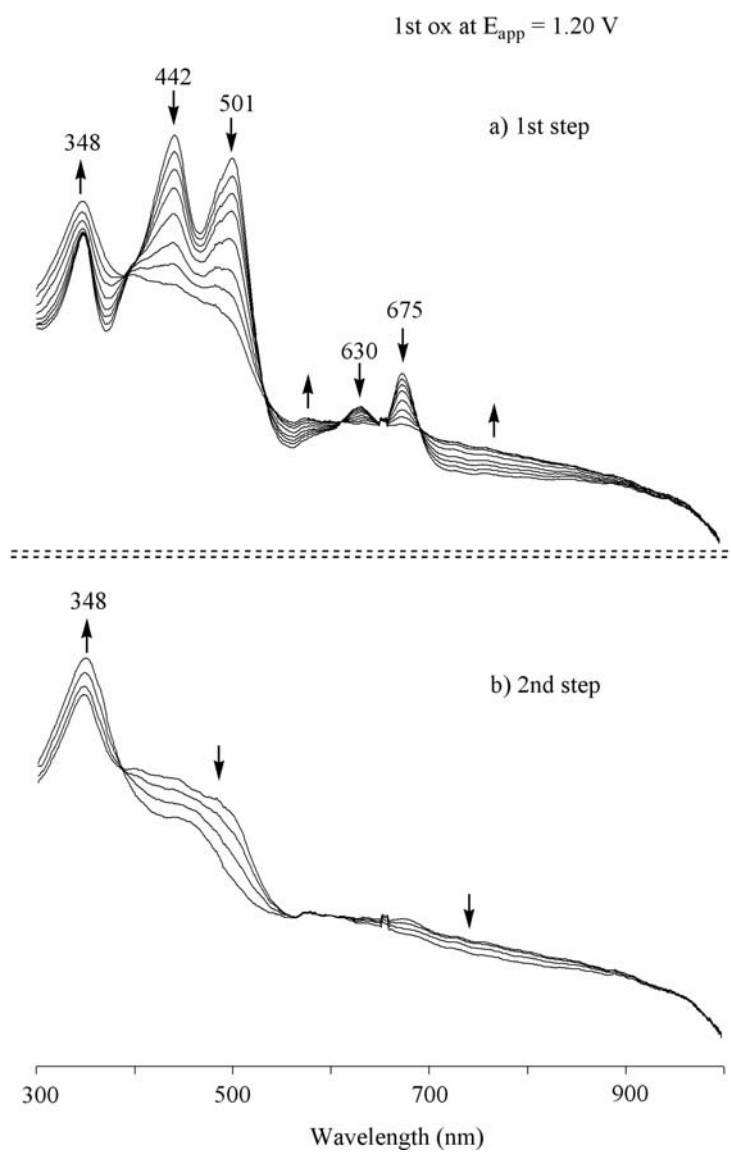


Figure 5-9. Two-step UV-visible spectral changes during oxidation of $(PQ_3)Cu$ in PhCN, 0.2 M TBAP.

visible bands at 630 and 675 nm in PhCN (see Table 5-6). Most of those bands decrease in intensity during the first step at an applied potential of 1.20 V except for the 348 nm band. At the same time, a broad visible band appears at the region between 700 and 900 nm (Figure 5-8a) which indicates that the first one-electron was abstracted from the porphyrin macrocycle giving a π -cation radical, $[(\text{PQ}_3)\text{Cu}]^+$. The 348 nm band continued increasing in intensity instead of decreasing when the potential was kept held at 1.20 V, the characteristic radical band disappeared at the same time as seen in Figure 5-8b which indicates the porphyrin macrocycle loses a second electron yielding a dianion, $[(\text{PQ}_3)\text{Cu}]^{2+}$, respectively.

5.2.8.2 Reduction

Thin-layer UV-visible spectra taken during the first electroreduction of $(\text{PQ}_3)\text{AuPF}_6$ and $(\text{PQ}_4)\text{AuPF}_6$ in PhCN are shown in Figures 5-9a and 5-9b, respectively. For comparison, the spectra of unreduced $(\text{PQ}_3)\text{Cu}$ and $(\text{PQ}_4)\text{Cu}$ in the same solvent are also shown in this figure. A metal-centered reduction is proposed for both $(\text{PQ}_3)\text{AuPF}_6$ and $(\text{PQ}_4)\text{AuPF}_6$, leading to formation of an Au(II) porphyrin with an uncharged macrocyclic ring. This mechanism was proposed by our group for $(\text{P})\text{AuPF}_6$ ⁹ and $(\text{PQ})\text{AuPF}_6$.¹¹

$(\text{PQ}_3)\text{AuPF}_6$, for example, has bands at 341, 425, 473, 617 and 658 nm in PhCN (see Figure 5-9a). All three Soret bands increase in intensity during the first reduction at an applied potential of -0.40 V, and the 658 nm band disappears along with appearing two new visible bands at 601 and 642 nm. The first electron addition product of $(\text{PQ}_3)\text{AuPF}_6$ has bands at 343, 430, 484, 601 and 642 nm in PhCN, which

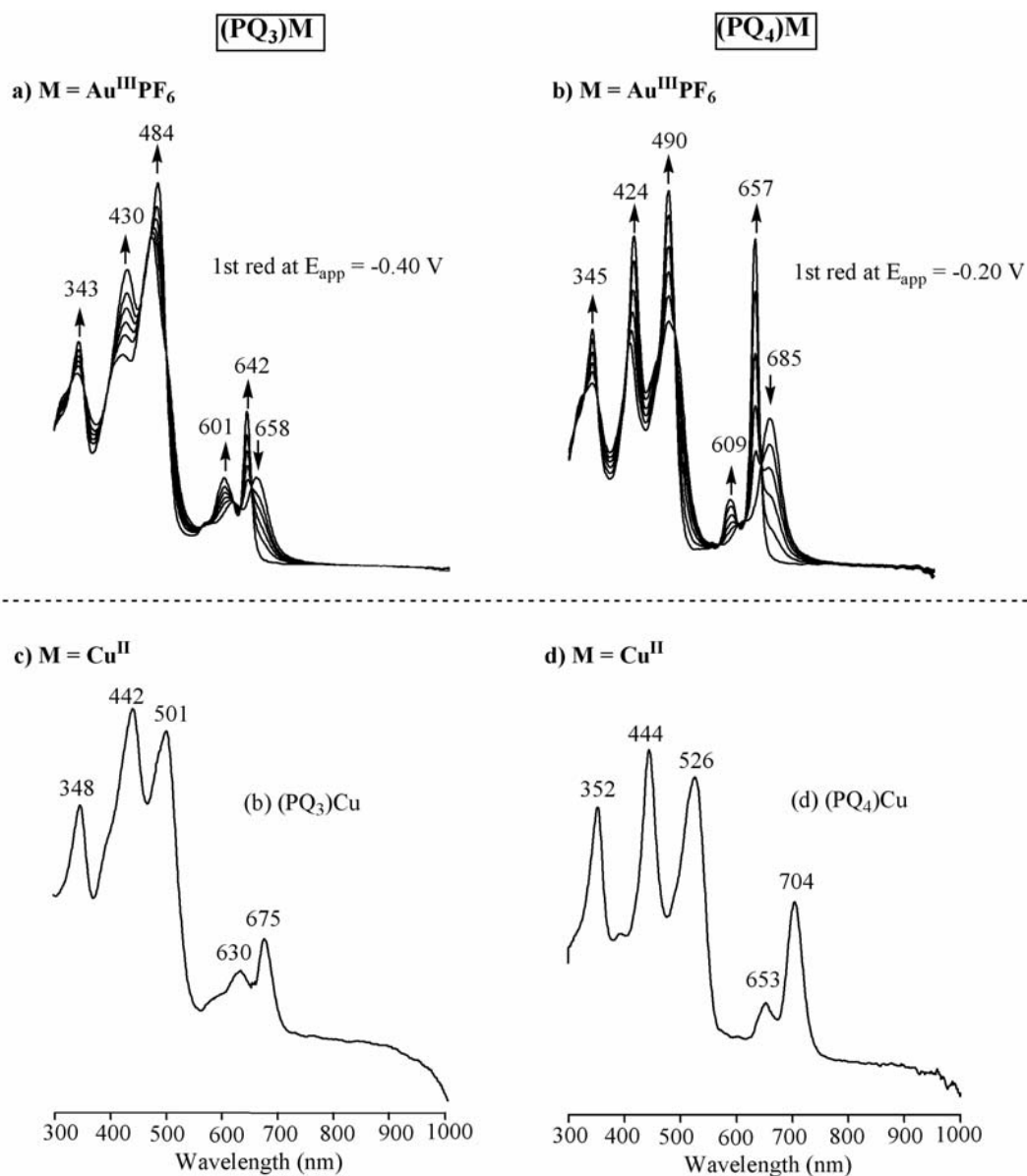


Figure 5-9. Thin-layer UV-visible spectral changes for the first reduction of (a) $(PQ_3)Au^{III}PF_6$ and (b) $(PQ_4)Au^{III}PF_6$, and UV-vis spectra of the neutral porphyrins, (c) $(PQ_3)Cu^{II}$ and (d) $(PQ_4)Cu^{II}$ in PhCN containing 0.2 M TBAP.

are similar to (PQ₃)Cu which has bands at 348, 442, 501, 630 and 675 nm band in PhCN as shown in Figure 5-9c, which indicates that the singly reduced Au(III) species shows some M(II) character. This is the same case is as for (PQ₄)AuPF₆, as shown in Figure 5-9b and 5-9d. Identical spectroelectrochemical changes are also seen upon the second reduction of (PQ₃)AuPF₆ and the first reduction of (PQ₃)Cu^{II} to its porphyrin π -anion radical form (see Figure 5-10). These observations indicate that singly reduced (PQ₃)AuPF₆ and (PQ₄)AuPF₆ are characteristic of neutral (PQ₃)M^{II} rather than a porphyrin π -anion radical and first one-electron reaction for (PQ_n)M occurred on the metal center giving a Au(II) form of the compound.

When a potential of -1.00 V was applied after the complete electrolysis at -0.40 V, the split 430, 484 nm Soret band and 601, 642 nm visible bands assigned to a Au(II) form decreases in intensity as shown in Figure 5-10a. The final product of the second reduction has two Soret bands at 339, 440 nm and a diagnostic radical visible band around 950 nm in PhCN which may indicate that this second electron was added to the porphyrin macrocycle instead of the metal center.

5.3 Conclusions

(PQ₃)M and (PQ₄)M where M = 2H, Pd, Cu or Ni both could form π -anion radicals and dianions by reduction and π -cation radicals and dications by oxidation. The (PQ_n)M compounds are easier to reduce or oxidize upon increasing the number of quinoxaline groups. (PQ₃)AuPF₆ and (PQ₄)AuPF₆ both undergoes a metal centered reduction prior to two ring-centered reactions in all solvents, as verified by electrochemical and spectroelectrochemical methods.

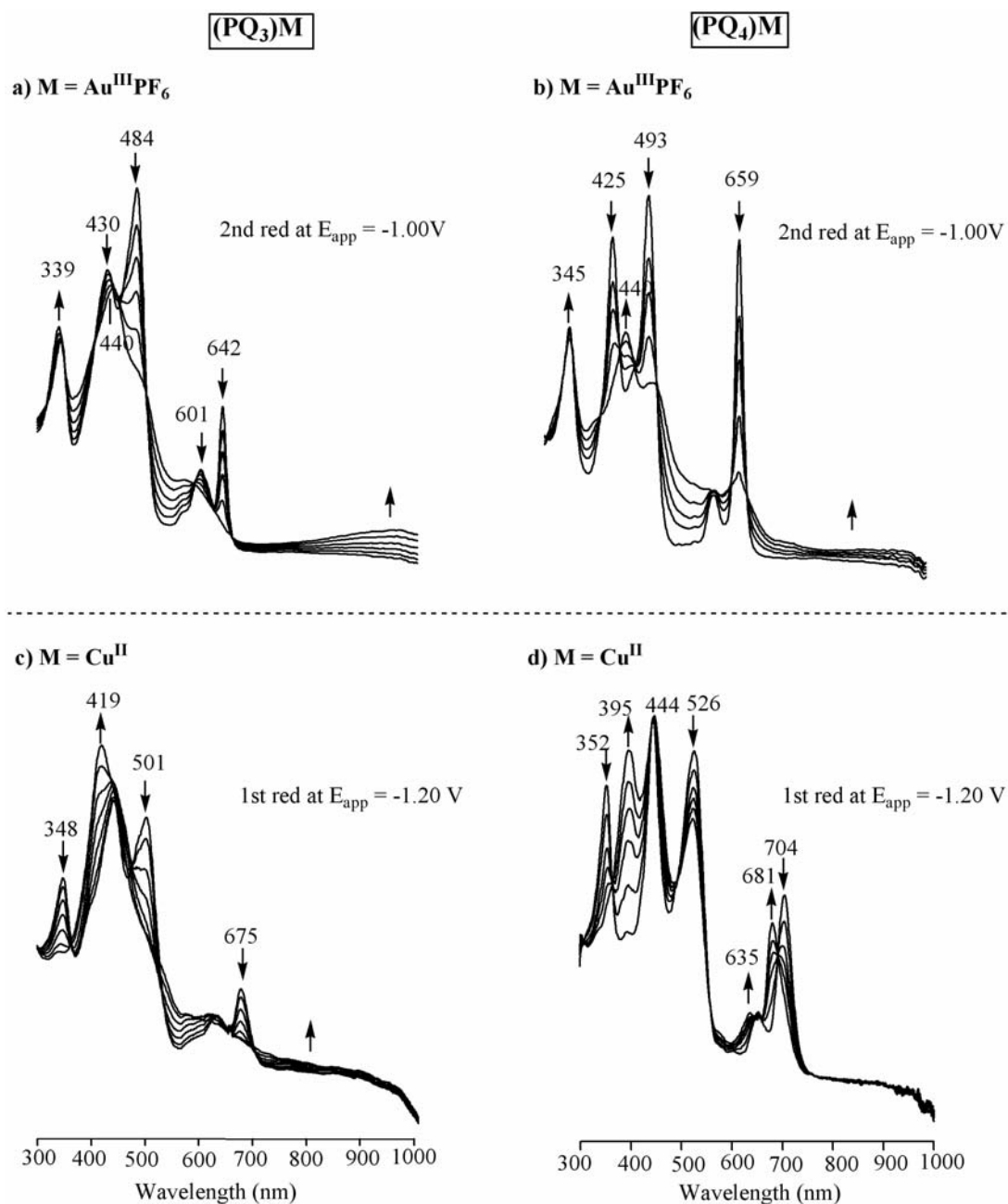


Figure 5-10. Thin-layer UV-visible spectral changes for the second reduction of (a) $(PQ_3)Au^{III}PF_6$ and (b) $(PQ_4)Au^{III}PF_6$ in PhCN containing 0.2 M TBAP, and first reductions of (c) $(PQ_3)Cu^{II}$ and (d) $(PQ_4)Cu^{II}$ in PhCN for comparison.

The fusion of a third and fourth electroactive quinoxaline group to the porphyrin macrocycle results in (1) an easier reduction (2) an easier oxidation. (3) a smaller HOMO-LUMO gap (mainly due to the effect on the LUMOs).

5.4 References

1. Kadish, K. M.; Smith, K. M.; Gilliland, R. *Handbook of Porphyrin Science*; World Scientific: Singapore, **2010**; Vol. 1-20.
2. Kadish, K. M.; Smith, K. M.; Guillard, R. *The Porphyrin Handbook*; Academic Press: San Diego, **2000**; Vol. 1-20.
3. Kim, D.; Osuka, A. *Acc. Chem. Res.* **2004**, *37*, 735.
4. Holten, D.; Bocian, D. F.; Lindsey, J. S. *Acc. Chem. Res.* **2002**, *35*, 57.
5. Jiao, J.; Anariba, F.; Tiznado, H.; Schmidt, I.; Lindsey, J. S.; Zaera, F.; Bocian, D. *F. J. Am. Chem. Soc.* **2006**, *128*, 6965.
6. Kelley, R. F.; Shin, W. S.; Rybtchinski, B.; Sinks, L. E.; Wasielewski, M. R. *J. Am. Chem. Soc.* **2007**, *129*, 3173.
7. Reimers, J. R.; Hush, N. S.; Crossley, M. J. *Journal of Porphyrins and Phthalocyanines* **2002**, *6*, 795.
8. Khoury, T.; Crossley, M. J. *New J. Chem.* **2009**, *33*, 1076.
9. Kadish, K. M.; Wenbo, E.; Ou, Z. P.; Shao, J. G.; Santic, P. J.; Ohkubo, K.; Fukuzumi, S.; Crossley, M. J. *Chem. Commun.* **2002**, 356.
10. Fukuzumi, S.; Ohkubo, K.; E, W. B.; Ou, Z. P.; Shao, J. G.; Kadish, K. M.; Hutchison, J. A.; Ghiggino, K. P.; Santic, P. J.; Crossley, M. J. *J. Am. Chem. Soc.* **2003**, *125*, 14984.
11. Ou, Z.; Kadish, K. M.; E, W.; Shao, J.; Santic, P. J.; Ohkubo, K.; Fukuzumi, S.; Crossley, M. J. *Inorg. Chem.* **2004**, *43*, 2078.
12. Ou, Z.; E, W.; Shao, J.; Burn, P. L.; Sheehan, C. S.; Walton, R.; Kadish, K. M.; Crossley, M. J. *Journal of Porphyrins and Phthalocyanines* **2005**, *9*, 142.

13. Kadish, K. M.; Wenbo, E.; Santic, P. J.; Ou, Z. P.; Shao, J. G.; Ohkubo, K.; Fukuzumi, S.; Govenlock, L. J.; McDonald, J. A.; Try, A. C.; Cai, Z. L.; Reimers, J. R.; Crossley, M. J. *J. Phys. Chem. B* **2007**, *111*, 8762.
14. Ou, Z.; E, W.; Zhu, W.; Thordarson, P.; Santic, P. J.; Crossley, M. J.; Kadish, K. M. *Inorg. Chem.* **2007**, *46*, 10840.
15. E, W.; Kadish, K. M.; Santic, P. J.; Khoury, T.; Govenlock, L. J.; Ou, Z.; Shao, J.; Ohkubo, K.; Reimers, J. R.; Fukuzumi, S.; Crossley, M. J. *J. Phys. Chem. B* **2008**, *112*, 556.
16. Barqawi, K. R. A., M. A. *Electrochim. Acta* **1987**, *32*, 597.
17. Ames, J. R.; Houghtaling, M. A.; Terrian, D. L. *Electrochim. Acta* **1992**, *37*, 1433.
18. Fuhrhop, J.-H.; Kadish, K. M.; Davis, D. G. *J. Am. Chem. Soc.* **1973**, *95*, 5140.
19. Kadish, K. M.; Van Caemelbecke, E.; Royal, G. In *The Porphyrin Handbook*; Kadish, K. M., Smith, K. M., Guillard, R., Eds.; Academic Press: New York, **2000**; Vol. 8, p 1.

Chapter Six

**Electrochemistry and Electrosynthesis of Antiaromatic
Benzofused Metalloporphyrin Species**

6.1 Introduction

Porphyrins typically exhibit Hückel rule $4n+2$ aromaticity and their structures and properties are usually primarily derived from the heteroaromatic nature of the ligand π -system. In recent years there have been a number of reports of novel antiaromatic porphyrins and ring-expanded porphyrinoid analogs with $4n$ inner ring electron counts. Osuka and coworkers have carried out intensive studies on ring-expanded porphyrinoids and have successfully isolated strongly antiaromatic compounds, such as gold(III) hexaphyrins.¹⁻⁴ Conventional tetrapyrrole porphyrins with $4n$ π -electron systems, including both 16π - and 20π -electron porphyrins, are rare, however. Since the late 1980s, there have been several examples reported of doubly reduced 20 π -electron species. Vogel et al. initially reported the structural characterization of a metal-free N-alkylated reduced porphyrin,⁵ while Setsune et al.⁶ subsequently carried out spectroscopic descriptions of their analogs and Chen and coworkers recently reported a metal-free non-N-alkylated species.^{7, 8} Vaid et al.^{9, 10} and Brothers et al.¹¹ have also recently reported the synthesis and isolation of reduced metalloporphyrins. Until recently there were no examples of oxidized 16 -electron porphyrins. Our Japanese collaborators Yamamoto and coworkers at Hiroshima University reported the first example in 2005¹²⁻¹⁴ and further work was subsequently reported by Cissell and Vaid¹⁵.

In a recent study, Yamamoto and coworkers developed and synthesized further examples of stable antiaromatic 16π -electron porphyrinoid π -systems.¹⁶ The two-electron oxidation of the Cu^{II} (**1**) and Zn^{II} (**4**) complexes of tetraphenyltetrabenzoporphyrin (TPTBP) (structures see Chart 6-1) results in the formation of stable antiaromatic porphyrins $[(\text{TPTBP})\text{Cu}^{\text{II}}(\text{H}_2\text{O})]^{2+} \cdot 2[\text{SbF}_6]^-$ (**3**) and

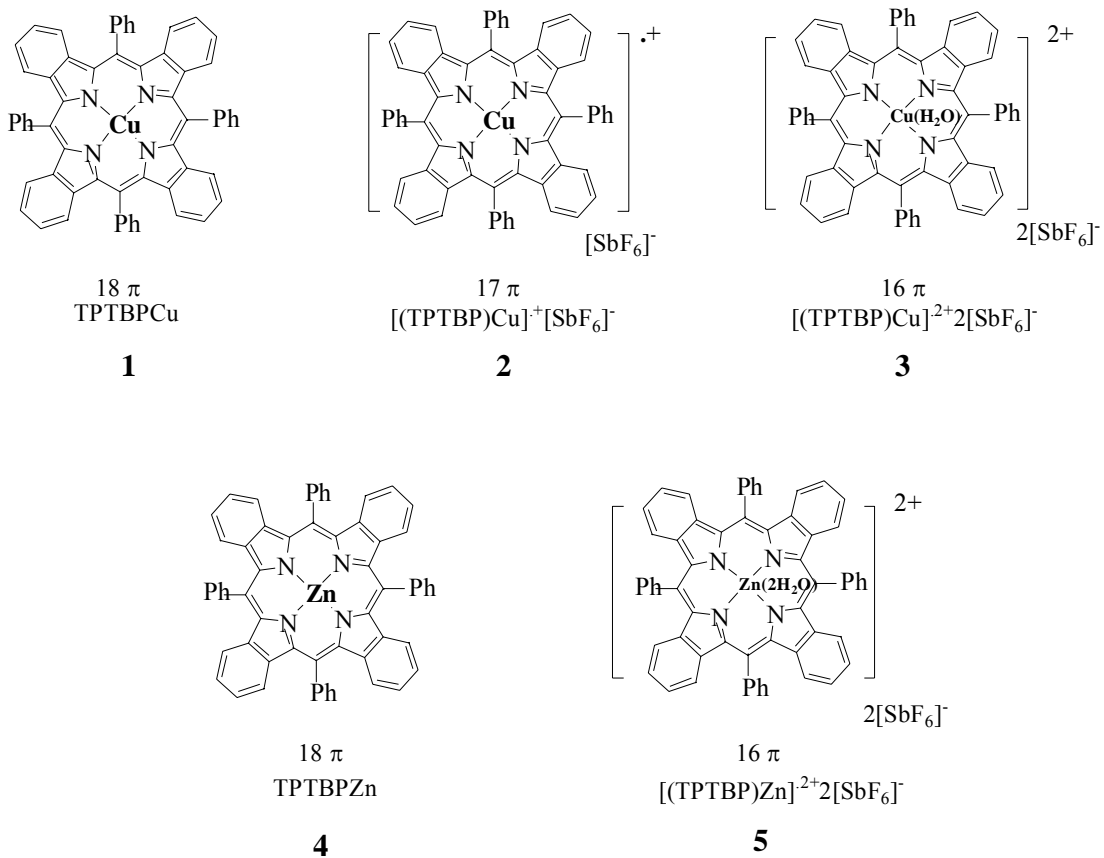


Chart 6-1. Structures of the investigated porphyrins.

$[(\text{TPTBP})\text{Zn}^{\text{II}}(\text{H}_2\text{O})_2]^{2+} \cdot 2[\text{SbF}_6]^-$ (**5**) species with 16π -electrons on the inner ligand perimeter. X-ray structures of the parent TPTBP complexes, the dications and a singly oxidized $[(\text{TPTBP})\text{Cu}^{\text{II}}]^{+\bullet}[\text{SbF}_6]^-$ (**2**) species, reveal that the use of a TPTBP macrocycle rather than a simple porphyrin ligand such as TPP reduces the degree of non-planarity in the 16π -electron species relative to the parent 18π complex.¹⁶ Significant high field shifts of the ^1H NMR signals of the outer ring protons and large positive values in nucleus-independent chemical shifts (NICS) calculations in the central cavity of the porphyrin ring provide unambiguous evidence for the antiaromatic character of the 16π Zn^{II} species.¹⁶

In this chapter, half-wave potentials of the stepwise electrochemical conversions between 16π Cu^{II} **3** or 16π Zn^{II} **5**, and their 18π forms, Cu^{II} **1** and Zn^{II} **4**, were measured in CH_2Cl_2 and PhCN utilizing cyclic voltammetry at a glassy carbon electrode. The reversibility and progress of the reactions upon reducing the 16π M^{II} derivatives to their 18π forms or upon oxidizing the 18π M^{II} species to their 16π forms was monitored by UV-visible spectroscopy in a thin-layer cell and resulting spectra for the electrogenerated 16, 17 and 18π compounds are compared to UV-vis spectra for the same species obtained by chemical oxidation/reduction methods.

6.2 Results and Discussion

6.2.1 Solution UV-visible Spectra

The electronic absorption spectrum of **3** in CH_2Cl_2 contains bands at 328, 410 and 540 nm (Figure 6-1), which are shifted to the blue relative to the corresponding bands in

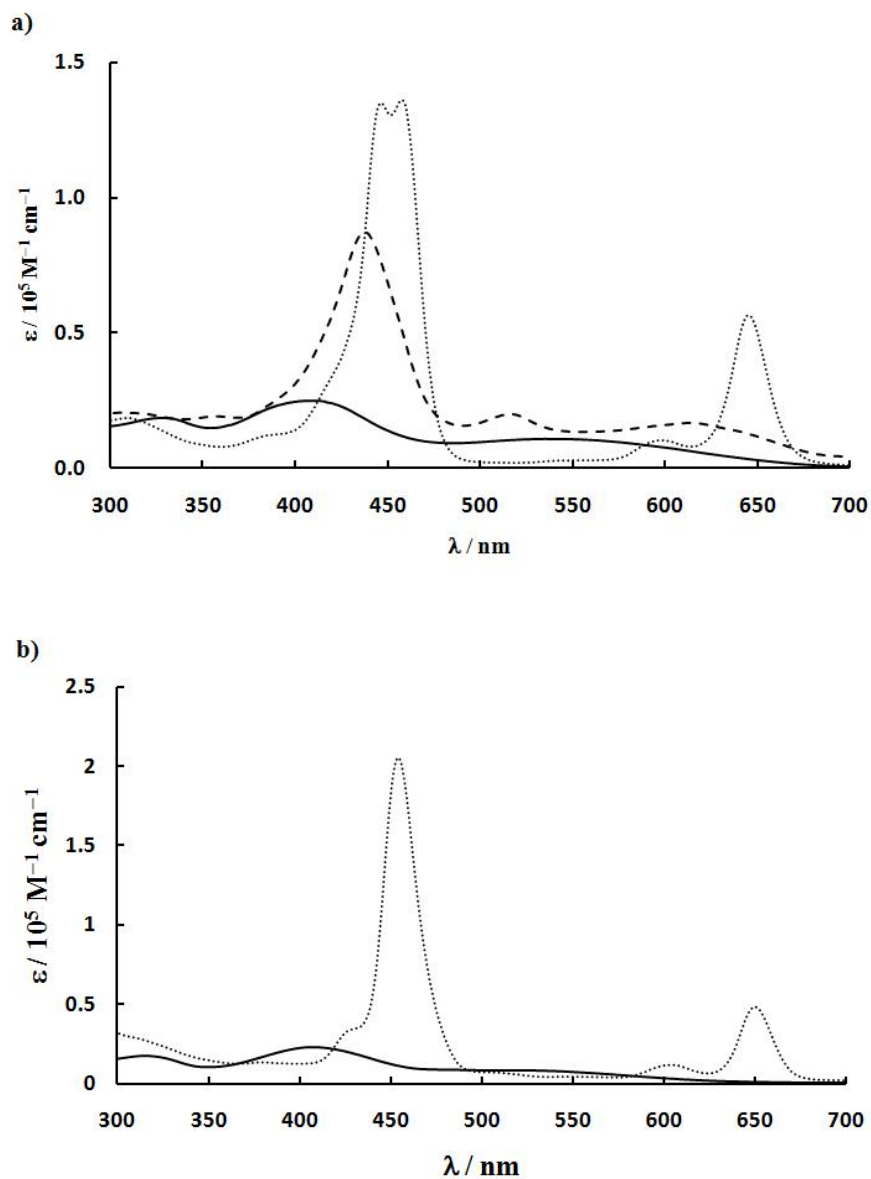


Figure 6-1. The UV-vis spectra of TPTBP copper(II) and zinc(II) complexes: a) copper(II) complexes **1** ($c = 11.0 \mu\text{M}$; dotted line), **3** ($c = 16.7 \mu\text{M}$; solid line) and **2** ($c = 82.8 \mu\text{M}$; broken line) in CH_2Cl_2 . b) zinc(II) complexes **4** ($c = 8.40 \mu\text{M}$; dotted line) and **5** ($c = 43.3 \mu\text{M}$; solid line) in CH_2Cl_2 . Data are taken from Ref. 16.

the spectrum of **1** whose bands lie at 447, 457 and 646 nm. Similar absorption bands are obtained in CH₂Cl₂ containing 0.1 M TBAP as the supporting electrolyte (See spectra in Figures 6-2 and 6-3). The peak in the Q band region at 540 nm is characteristic of the 16 π [(TPTBP)Cu^{II}(H₂O)]²⁺•2[SbF₆]⁻ (**3**). Complex **3** slowly decomposes in solution to another species in a nearly quantitative manner, with the 17 π species being the obvious candidate, despite the relatively high stability of this product in the solid state.¹⁶

The electronic absorption spectrum of **2** contains bands slightly blue-shifted to 437 and 517 nm relative to those of **1** (Figure 6-1a), which correspond closely with those of the decomposition product of the copper(II) 16 π porphyrin complex (The electrogenerated 17 π species has bands at 438 and 517 nm; see later discussion). The electronic absorption spectrum of **5** contains bands at 316, 407 and 510 nm (Figure 6-1b), which are blue-shifted relative to bands in the spectrum of the parent 18 π complex **4** at 454, 604 and 650 nm (Figure 6-1b). Although the 16 π zinc(II) complex (**5**) gradually decomposes in solution in a manner similar to the 16 π copper(II) complex (**3**), different final products are obtained. While the copper(II) species decomposes to form a 17 π radical cation, the decomposition product of the zinc(II) species has a characteristic absorption band at 493 nm, which was not observed in the spectrum of the 17 π [(TPTBP)Cu^{II}]^{•+} radical species generated by electrochemical oxidation.¹⁷

6.2.2 Electrochemistry and Electrosynthesis

Redox properties of the 16 π , 17 π and 18 π electron forms of (TPTBP)Cu^{II} and the 16 π and 18 π electron forms of (TPTBP)Zn^{II} were examined in CH₂Cl₂ and PhCN

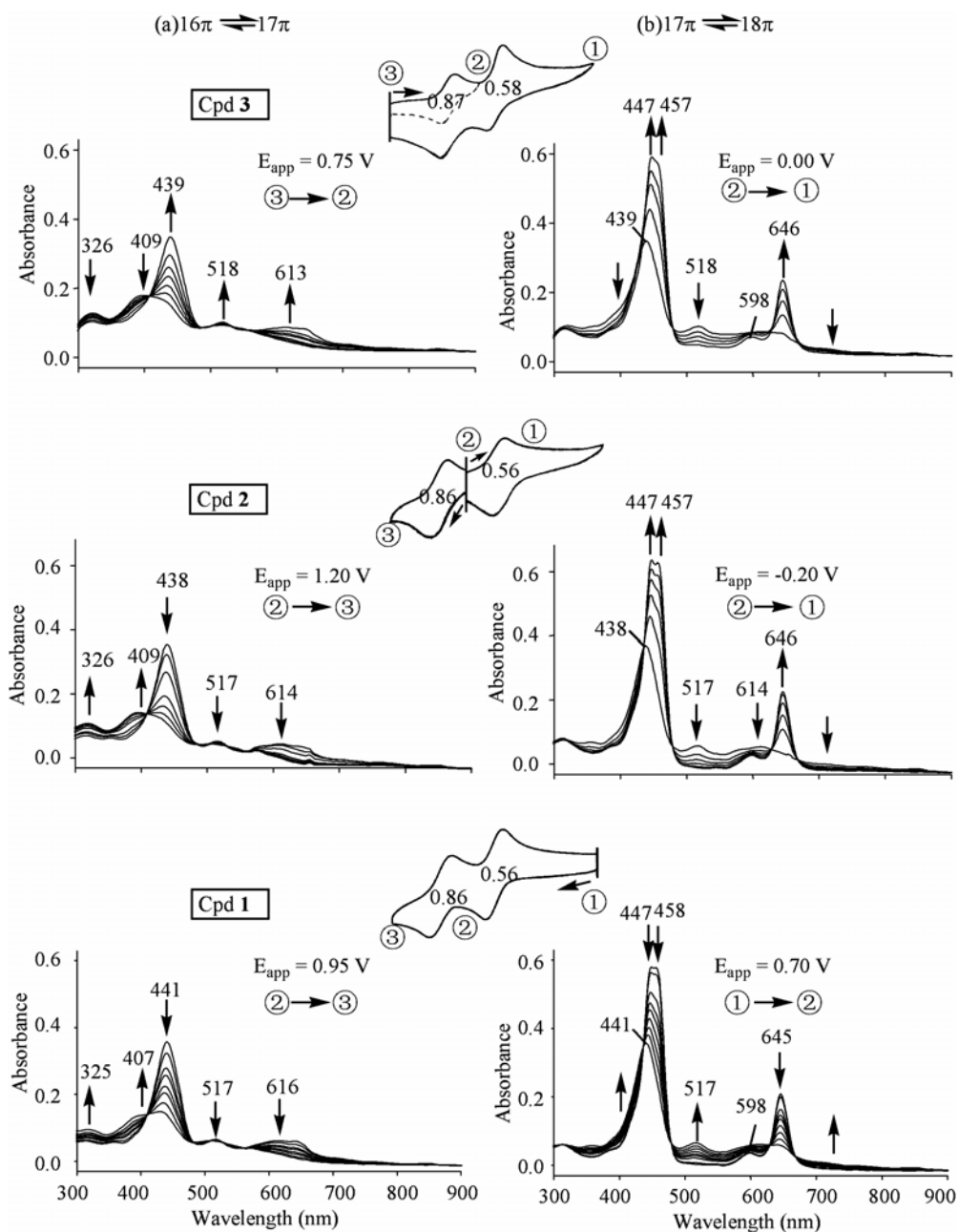


Figure 6-2. Cyclic voltammograms and corresponding UV-vis spectral changes for **1-3** in CH_2Cl_2 , 0.2 M TBAP during (a) the $16\pi/17\pi$ electron conversions and (b) the $17\pi/18\pi$ electron conversions at the indicated potentials where ③ gives a 16π electron species, ② gives a 17π electron species and ① gives an 18π electron species.

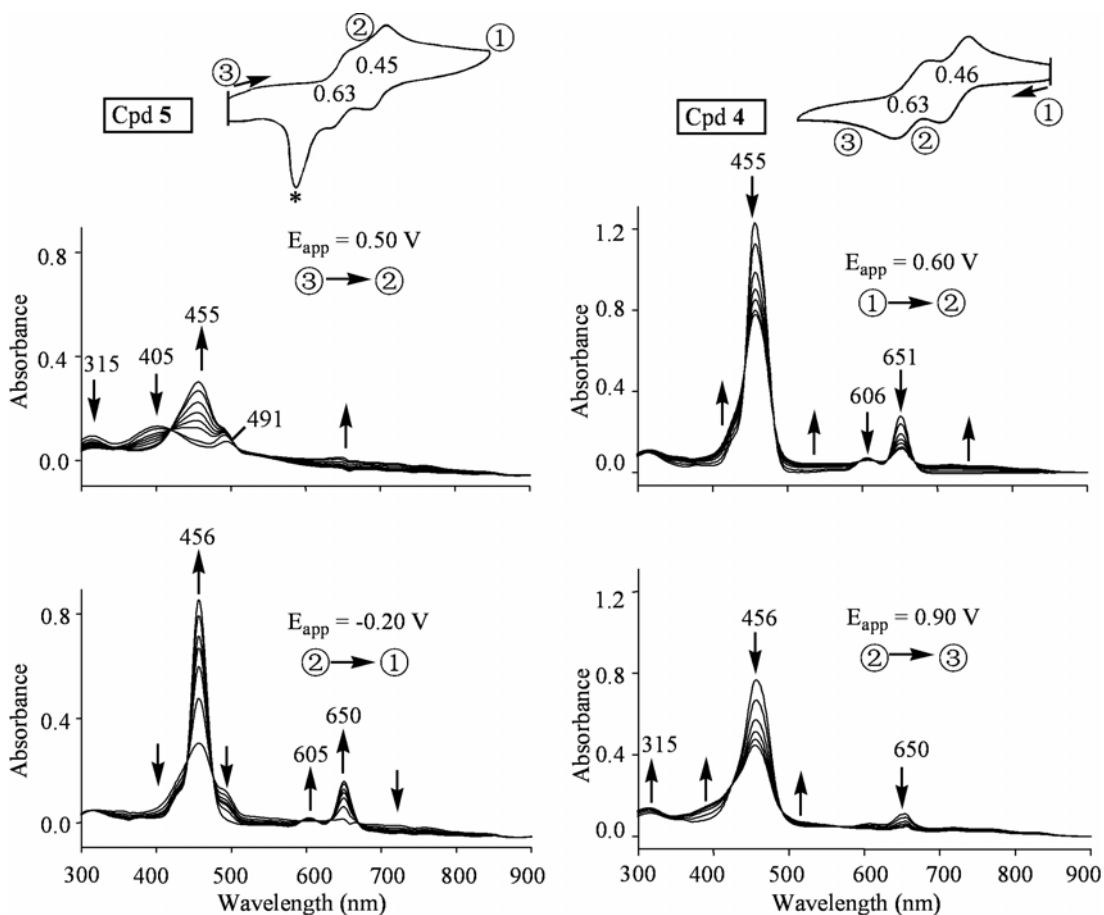


Figure 6-3. Cyclic voltammograms and corresponding UV-vis spectral changes during controlled potential reduction and oxidation of Zn(II) compounds **4** and **5** in CH₂Cl₂, 0.2 M TBAP at the indicated potentials where ③ gives a 16 π electron species, ② gives a 17 π electron species and ① gives an 18 π electron species. The peak marked with an asterisk in the CV of **5** is due to a surface reaction involving oxidation of H₂O from the compound.

containing 0.1 M TBAP with the goal of characterizing the electrochemistry and electrosynthesis of these species in nonaqueous media. UV-visible spectra of the products formed in each stepwise one-electron addition or abstraction were also elucidated as a function of applied potential in a thin-layer spectroelectrochemical cell. Examples of cyclic voltammograms for the three related Cu(II) derivatives in CH₂Cl₂, 0.1 M TBAP are illustrated in Figure 6-2 which also shows the spectral changes obtained under the application of a fixed oxidizing or reducing potential to give the desired species.

(TPTBP)Cu^{II} (**1**) in CH₂Cl₂, 0.1 M TBAP undergoes two reversible one-electron oxidations at $E_{1/2} = 0.56$ and 0.86 V and two reversible one-electron reductions at $E_{1/2} = -1.18$ and -1.78 V, leading to a π -cation radical (17π), dication (16π), π -anion radical (19π) and dianion (20π), respectively. The two oxidations at positive potentials generate the 17π and 16π electron forms of the porphyrin, transitions which are reversible and rapid under the electrochemical conditions as judged by the well-defined cyclic voltammogram illustrated in the lower part of Figure 6-2.

The doubly oxidized 16π electron [(TPTBP)Cu^{II}(H₂O)]²⁺•2[SbF₆]⁻ (**3**) exhibits three reversible one-electron reductions in CH₂Cl₂, the first two of which are located at $E_{1/2} = 0.87$ and 0.58 to give the 17π and 18π electron forms of the compound (see CV at top of Figure 6-2) while the singly oxidized 17π electron [(TPTBP)Cu^{II}]⁺[SbF₆]⁻ (**2**) undergoes a reversible one-electron oxidation at $E_{1/2} = 0.86$ V and a reversible one-electron reduction at $E_{1/2} = 0.56$ V. The fact that potentials for the three related Cu(II) porphyrins are identical within experimental error suggests the absence of

coupled chemical reactions in the stepwise electrochemical conversion between (TPTBP)Cu^{II} (**1**), [(TPTBP)Cu^{II}]⁺[SbF₆]⁻ (**2**) and [(TPTBP)Cu^{II}(H₂O)]²⁺•2[SbF₆]⁻ (**3**) under the given solution conditions. This is also suggested by the thin-layer spectroelectrochemical data described below.

A CH₂Cl₂ solution of chemically generated [(TPTBP)Cu^{II}]⁺[SbF₆]⁻ (**2**) exhibits absorptions at 438, 517 and 614 nm (see Figure 6-1a) and virtually the same spectral pattern is observed under conditions of the electrochemical experiments, i.e., in solutions containing 0.1 or 0.2 M TBAP (Figure 6-2, center). The same UV-visible spectrum is also seen after the one-electron controlled potential reduction of [(TPTBP)Cu^{II}(H₂O)]²⁺•2[SbF₆]⁻ (**3**) at 0.75 V (③ to ② in Figure 6-2, top left) or after the one-electron controlled potential oxidation of (TPTBP)Cu^{II} (**1**) at 0.70 V in the thin-layer cell (① to ② in Figure 6-2, bottom right). 17π/18π electron conversions at the indicated potentials where ③ gives a 16π-electron species, ② gives a 17π-electron species and ① gives an 18π-electron species.

Electrochemical generation of the 16π electron porphyrin from its 17π or 18π electron form, [(TPTBP)Cu^{II}]⁺[SbF₆]⁻ (**2**) and (TPTBP)Cu^{II} (**1**), in CH₂Cl₂, 0.2 M TBAP (② to ③ or ① to ② to ③ in Figure 6-2) also gives virtually the same UV-visible spectrum as the chemically generated [(TPTBP)Cu^{II}(H₂O)]²⁺•2[SbF₆]⁻ (**3**) in CH₂Cl₂ without TBAP although the doubly oxidized compound under the electrochemical conditions would contain one or two associated ClO₄⁻ counterions rather than just SbF₆⁻. Thus, the potential driven conversion between the three forms of the Cu(II) porphyrins is rapid and easily accomplished on the electrochemical timescale in

CH₂Cl₂ and there is no obvious effect of supporting electrolyte on UV-visible spectra of the electrogenerated species in a given oxidation state.

An electrochemical conversion between 16 π and 18 π Zn(II) porphyrins was also examined. Cyclic voltammetric measurements of (TPTBP)Zn^{II} (**4**) and 16 π [(TPTBP)Zn^{II}(H₂O)₂]²⁺•2[SbF₆]⁻ (**5**) show no obvious effect of solvent or compound oxidation state on the measured half wave potentials. For example, in CH₂Cl₂ containing 0.1 M TBAP, [(TPTBP)Zn^{II}(H₂O)₂]²⁺•2[SbF₆]⁻ (**5**) is reduced stepwise at $E_{1/2} = 0.63$ and 0.45 V to give (TPTBP)Zn^{II} (**4**) as a final product while **4** is stepwise oxidized at $E_{1/2} = 0.46$ and 0.63 V as shown in Figure 6-3 to give [(TPTBP)Zn^{II}]²⁺ which contains one or two associated ClO₄⁻ counterions and no H₂O. Both sets of half wave potentials are shifted positively by about 100 mV upon changing the solvent from CH₂Cl₂ to PhCN, but again there is no difference between the measured $E_{1/2}$ values for reduction of the 16 π electron porphyrin ($E_{1/2} = 0.73$ and 0.52 V) or oxidation of the 18 π electron porphyrin ($E_{1/2} = 0.52$ and 0.73 V) in this solvent (see CV in Figure 6-4, inset).

Although identical redox potentials are obtained in both solvents starting from the oxidized or reduced forms of the Zn(II) porphyrins, this is not the case for the UV-visible spectra. As described earlier in the chapter, [(TPTBP)Zn^{II}(H₂O)₂]²⁺•2[SbF₆]⁻ (**5**) reacts with the CH₂Cl₂ solvent to give a side product, possibly the singly reduced 17 π -electron form of the porphyrin, having an absorption band at 489-491 nm. A spontaneous reduction of **5** also occurs in PhCN, 0.2 M TBAP but in this solvent the electrochemically examined species in solutions to which [(TPTBP)Zn^{II}(H₂O)₂]²⁺•2[SbF₆]⁻ (**5**) has been added is actually a mixture of the single

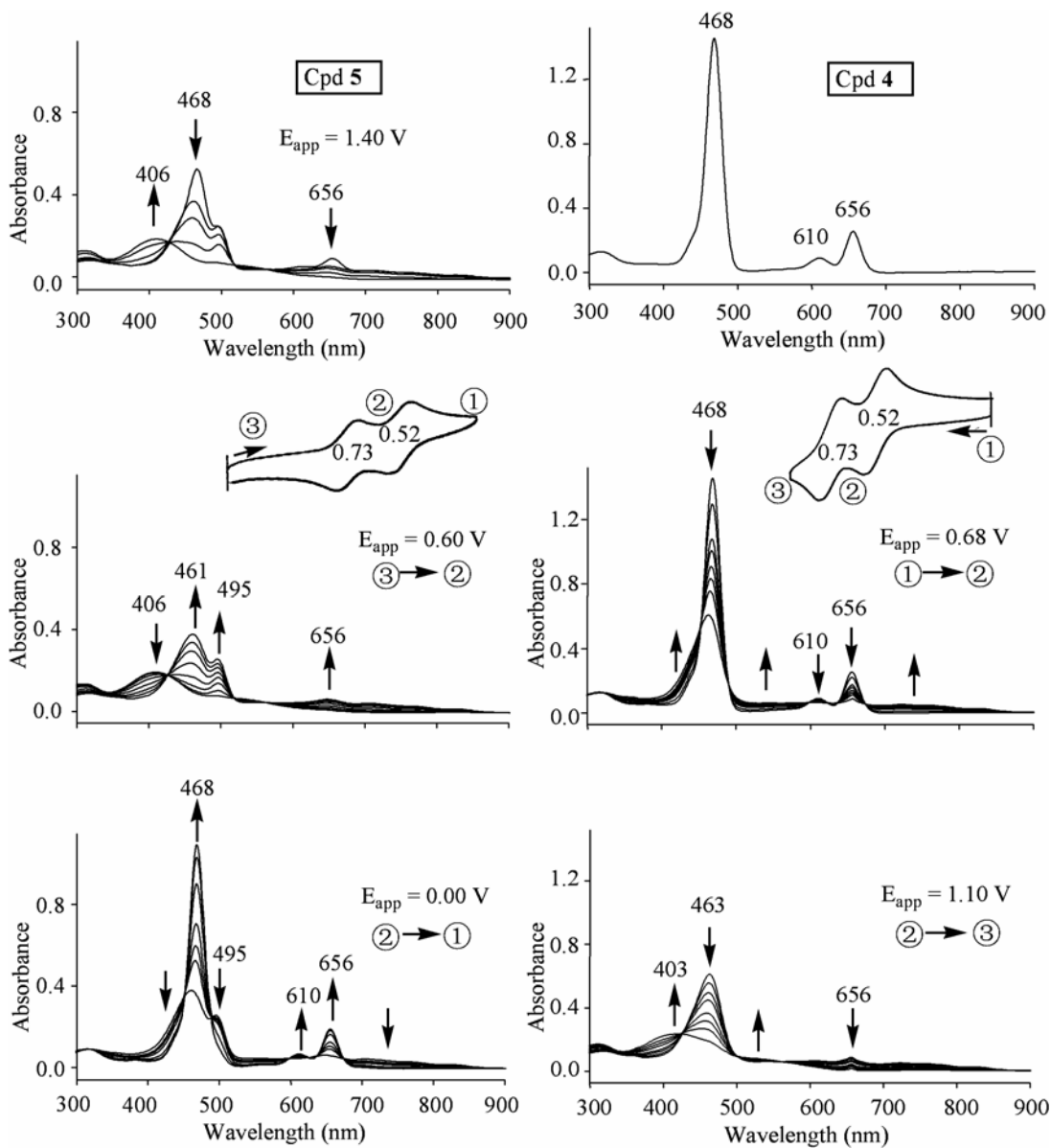


Figure 6-4. Cyclic voltammograms and corresponding UV-vis spectral changes for **4** and **5** in PhCN, 0.2 M TBAP where ③ gives a 16 π -electron species, ② gives a 17 π -electron species and ① gives an 18 π -electron species.

and doubly reduced forms of the compound which would formally be the 17 and 18 π electron porphyrins. The lack of stability of **5** in PhCN is illustrated in the top of Figure 6-4 where UV-vis bands for the species added to solution are seen at 468, 495 and 656 nm. The 468 and 656 nm absorptions are characteristic of the unoxidized 16 π -electron Zn(II) porphyrin while the 495 nm band is associated with the singly oxidized 17 π -electron porphyrin.

Despite the fact that a rapid reduction of the 16 π -electron porphyrin occurs in the PhCN solutions, the desired [(TPTBP)Zn^{II}(H₂O)₂]²⁺•2[SbF₆]⁻ (**5**) could be quantitatively regenerated *in situ* by applying a fixed oxidizing potential of 1.40 V to the thin-layer cell after which conversion to the porphyrin's 17 π and 18 π electron forms could be studied under the application of a fixed reducing potential. The spectral changes associated with the quantitative *in situ* generation of [(TPTBP)Zn^{II}(H₂O)₂]²⁺•2[SbF₆]⁻ in solution are shown in the top illustration of Figure 6-4 where the 468, 495 and 656 nm bands disappear and a new band at 406 nm characteristic of **5** is formed under the application of the fixed oxidizing potential. Having quantitatively generated the 16 π -electron porphyrin, the applied potential was first switched to 0.60 V and then to 0.00 V to stepwise generate the 17 π and 18 π electron compounds respectively. These spectral changes are also shown in Figure 6-4.

A similar sequence of reactions involving a potential-driven interconversion between **4** and **5** is observed in CH₂Cl₂ containing 0.1 or 0.2 M TBAP and examples of the thin-layer spectral changes at specific oxidizing or reducing potentials are shown in Figure 6-3. The UV-visible spectrum of **5** is characterized by a band at 315 and 405 nm but there is also a band at 491 nm associated with some reductions to the 17 π -electron

form of the porphyrin.

6.3 Conclusions

The combined electrochemical and spectroelectrochemical data of the five benzofused metalloporphyrin species are self-consistent and indicate that reversible potential driven interconversions between the 16π , 17π and 18π electron forms of the porphyrins may be accomplished in solutions of CH_2Cl_2 or PhCN without any apparent interference from the supporting electrolyte. Thin-layer spectroelectrochemistry can also be used as an electrosynthetic tool to quantitatively generate the porphyrin in a specifically desired oxidation state prior to *in situ* spectroscopic characterization which might not be otherwise possible in the absence of an applied potential.

6.4 References

1. Mori, S.; Osuka, A., *J. Am. Chem. Soc.* **2005**, *127*, 8030.
2. Mori, S.; Kim, K. S.; Yoon, Z. S.; Noh, S. B.; Kim, D.; Osuka, A., *J. Am. Chem. Soc.* **2007**, *129*, 11344.
3. Suzuki, M.; Osuka, A., *J. Am. Chem. Soc.* **2007**, *129*, 464.
4. Yoon, Z. S.; Cho, S.; Suzuki, M.; Osuka, A.; Kim, D., *J. Am. Chem. Soc.* **2009**, *131*, 7360.
5. Vogel, E.; Grigat, I.; Köcher, M.; Lex, J., *Angew. Chem.* **1989**, *101*, 1687.
6. Setsune, J.; Kashihara, K.; Wada, K.; Shiozaki, H., *Chem. Lett.* **1999**, 847.
7. Liu, C.; Shen, D.-M.; Chen, Q.-Y., *J. Am. Chem. Soc.* **2007**, *129*, 5814.
8. Chen, X.-G.; Liu, C.; Shen, D.-M.; Chen, Q.-Y., *Synthesis* **2009**, 3860.
9. Cissell, J. A.; Vaid, T. P.; Rheingold, A. L., *J. Am. Chem. Soc.* **2005**, *127*, 12212.
10. Song, H.-e.; Cissell, J. A.; Vaid, T. P.; Holten, D. J., *J. Phys. Chem. B* **2007**, *111*, 2138.
11. Weiss, A.; Hodgson, M. C.; Boyd, P. D. W.; Siebert, W.; Brothers, P. J., *Chem. Eur. J.* **2007**, *13*, 5982.
12. Yamamoto, Y.; Yamamoto, A.; Furuta, S.; Horie, M.; Kodama, M.; Sato, W.; Akiba, K.; Tsuzuki, S.; Uchimaru, T.; Hashizume, D.; Iwasaki, F., *J. Am. Chem. Soc.* **2005**, *127*, 14540.
13. Yamamoto, Y.; Hirata, Y.; Kodama, M.; Yamaguchi, T.; Matsukawa, S.; Akiba, K.; Hashizume, D.; Iwasaki, F.; Muranaka, A.; Uchimaru, T.; Chen, P.; Kadish, K. M.; Kobayashi, N., *J. Am. Chem. Soc.* **2010**, *132*, 12627.
14. Kakui, T.; Sugawara, S.; Hirata, Y.; Kojima, S.; Yamamoto, Y., *Chem. Eur. J.* **2011**,

- 17, 7768.
15. Cissell, J. A.; Vaid, T. P.; Yap, G. P. A., *Org. Lett.* **2006**, *8*, 2401.
16. Sugawara, S.; Hirata, Y.; Kojima, S.; Yamamoto, Y.; Miyazaki, E.; Takimiya, K.; Matsukawa, S.; Hashizume, D.; Mack, J.; Kobayashi, N.; Fu, Z.; Kadish, K. M.; Sung, Y. M.; Kim, K. S.; Kim, D., *Chem. Eur. J.* **2012**, *18*, 3566.
17. Renner, M. W.; Cheng, R.-J.; Chang, C. K.; Fajer, J., *J. Phys. Chem.* **1990**, *94*, 8508.

Chapter Seven

Tetra-2,3-pyrazinoporphyrazines with Externally Appended

Thienyl Rings: UV-visible and Electrochemical Behaviors

7.1 Introduction

Porphyrazines, apart from the phthalocyanine family (tetrabenzoporphyrines), have received increasing attention over the last decade.¹⁻³ Our own group has concentrated in part on the synthesis and characterization of (thia/seleno) diazolo porphyrazines,⁴⁻⁷ diazepinoporphyrazines⁸⁻¹⁰ and pyrazinoporphyrazines,¹¹⁻¹⁴ the latter of which is represented by $[\text{Py}_8\text{TPyzPzM}]$ where $\text{Py}_8\text{TPyzPz} =$ the tetrakis-2,3-[5,6-di-(2-pyridyl)-pyrazino]porphyrazino anion and $\text{M} = \text{Mg}^{\text{II}}(\text{H}_2\text{O}), \text{Mn}^{\text{II}}, \text{Co}^{\text{II}}, \text{Cu}^{\text{II}}, \text{Zn}^{\text{II}}, \text{Pd}^{\text{II}}$ or 2H^{I} . All of the studied porphyrazines can be characterized as electron-deficient macrocycles on the basis of their UV-visible spectral features and electrochemical behavior and in the case of pyrazinoporphyrazines (Chart 7-1A), the exocyclic pendant vicinal pyridine rings will strongly influence the electronic structure of the macrocycle, so much so that the compounds become remarkably easier to reduce than their related phthalocyanine analogues,¹¹⁻¹⁶ In nonaqueous media, the electrochemical processes occur via stepwise one-electron additions to give stable species with charges of -1, -2, -3 and -4.

The present chapter have extended our studies to include a related series of pyrazinoporphyrazines. These compounds have the formula $[\text{Th}_8\text{TPyzPzM}]$ where $\text{Th}_8\text{TPyzPz} =$ the tetrakis-2,3-[5,6-di-(2-thienyl)-pyrazino]porphyrazino anion and $\text{M} = (\text{Mg}^{\text{II}}(\text{H}_2\text{O}), \text{Co}^{\text{II}}, \text{Cu}^{\text{II}}, \text{Zn}^{\text{II}}$ or H_2^{I} (Chart 7-1B). The role played by the external thienyl rings in the electronic distribution within the entire molecular framework of the present macrocycles is the target of the present investigation, mainly conducted by UV-visible spectral and electrochemical investigation.

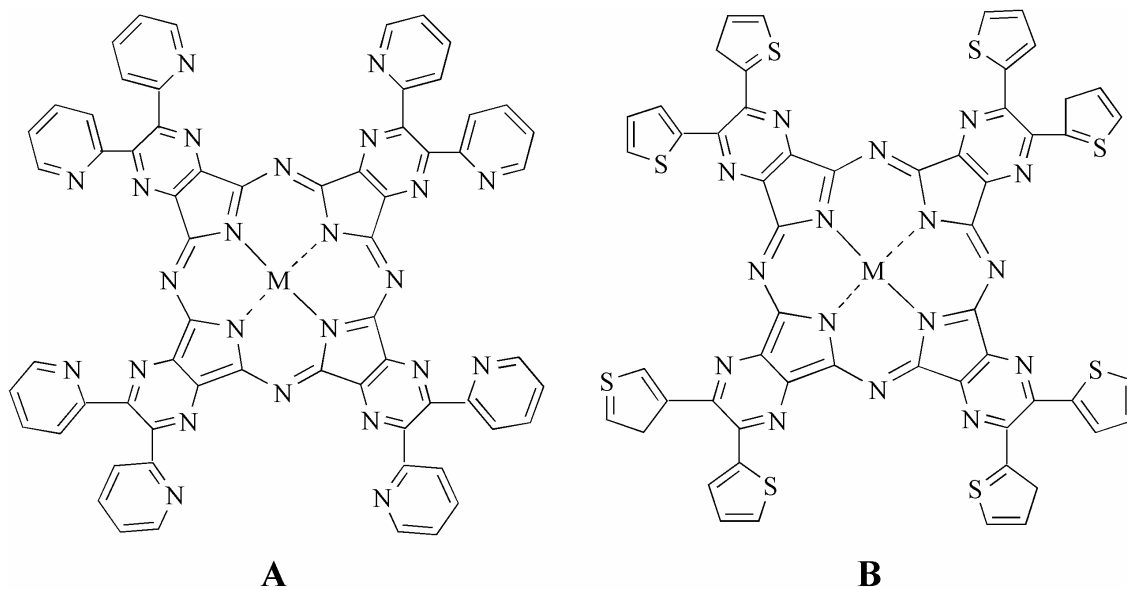


Chart 7-1. Schematic representation of the macrocycles [Py₈TPyzPzM] (A) and [Th₈TPyzPzM] (B) (M = Mg^{II}(H₂O), Zn^{II}, Cu^{II}, Co^{II}, 2H⁺).

7.2 Results and Discussion

7.2.1 Solution UV-visible Spectra.

The examined octathienyl macrocycles are intense dark-blue/green colored amorphous materials which are completely insoluble in water and very poorly soluble in the nonaqueous non-polar solvents CH_2Cl_2 , CHCl_3 and the low-polar benzonitrile, in which, based on UV-visible spectra (broad featureless absorptions of low intensity throughout the explored region), they manifest strong aggregation independent of concentration. Better solubility is obtained in the polar solvents dimethylformamide (DMF), dimethyl sulfoxide (DMSO) and pyridine, in which, especially at the highest possible concentrations (ca. 10^{-4} M) aggregation is also present. This problematic aspect has been successfully overcome for the electrochemical studies, as described in the next section and will be further illustrated below. Nevertheless, for many of the compounds, the monomeric form becomes largely prevalent at concentrations of ca. 10^{-5} M immediately after dissolution of the compounds or after some time so that, as specified in more detail below for each single species, quantitative UV-visible spectra and measurements of quantum yields of singlet oxygen production were made possible.¹⁷

The UV-visible spectral evolution of the Mg^{II} and Zn^{II} complexes in solutions of DMF, DMSO and pyridine as a function of time systematically showed the complete formation of monomers. In these cases, the spectra of monomeric $[\text{Th}_8\text{TPyzPzMg}(\text{H}_2\text{O})]$ and $[\text{Th}_8\text{TPyzPzZn}]$ display absorptions in the Soret (300-450 nm) and Q-band (600-700 nm) regions attributable to intra-ligand HOMO-LUMO π - π^* transitions, which is in line with the normally observed behavior for phthalocyanines and

porphyrazines.¹⁸⁻²⁰ The UV-visible spectra of the Mg^{II} and Zn^{II} complexes are quite similar to each other in terms of the number of absorptions, their wavelength maxima and the relative intensity of the bands (quantitative spectral data are given in Table 7-1). In addition, [Th₈TPyzPzMg(H₂O)] in DMF often exhibited a broad peak of weak intensity in the lower energy region of the spectrum which can be attributed to aggregation. This band is seen at 700-900 nm in Figure 7-1 (dotted line) and disappeared upon heating of the solution to 70 °C for 30 min.

Unlike the Mg^{II} and Zn^{II} complexes, [Th₈TPyzPzCu] and [Th₈TPyzPzCo] remain aggregated in DMF and DMSO solutions after standing, and only qualitative spectra could be obtained (Table 7-1). In addition, [Th₈TPyzPzCo], although it exhibits limited aggregation, tends to undergo a spontaneous one-electron reduction to its corresponding Co^I form which has a completely different UV-visible spectrum from that of the neutral species (see further information on this point in the electrochemical section below).

As to the free-base macrocycle, the initially obtained UV-visible spectrum of [Th₈TPyzPzH₂] in pyridine, DMSO or DMF is characterized by a narrow unsplit Q band (Figure 7-1), indicative for the presence of the species in its deprotonated [Th₈TPyzPz]⁻² dianionic form (D_{4h} symmetry). The octapyridinated analogue [Py₈TPyzPzH₂] behaves differently in that in the same solvents it is initially aggregated. However, it shows a clean spectral evolution with the presence of isosbestic points that can be interpreted in terms of a dimer → monomer (dianionic) conversion.¹²

From the spectral data in Table 7-1, it can be seen that peak maxima of the investigated compounds are practically independent of solvent. The species

Table 7-1. UV-visible Solution Spectra in Pyridine, DMSO and DMF of the Thienyl Compounds [Th₈TPyzPzM]·xH₂O (M = Mg^{II}(H₂O), Zn^{II}, Cu^{II}, Co^{II}, 2H^I) and Related Octapyridino Analogues [Py₈TPyzPzM].

Compound	Solvent	Soret region			Q-band region		Ref.
		λ [nm] (log ε)			λ [nm] (log ε)		
[Th ₈ TPyzPzMg(H ₂ O)]·5H ₂ O	py	387 (4.90)			609 (4.30)	674 (5.04)	tw
	DMSO	394 (4.90)			611 (4.50)	672 (4.90)	tw
	DMF	386 (4.90)			608 (4.30)	672 (5.04)	tw
[Th ₈ TPyzPzZn]·4H ₂ O	py	393 (5.10)			608 (4.60)	674 (5.40)	tw
	DMSO	390 (5.03)			609 (4.41)	672 (5.30)	tw
	DMF	395 (5.09)			609 (4.50)	672 (5.40)	tw
[Th ₈ TPyzPzCu]·3H ₂ O	py ^a	380				672	tw
[Th ₈ TPyzPzCo]·2H ₂ O	DMSO ^b	373	428 sh		656	tw	
[Th ₈ TPyzPz] ²⁻	py	391 (4.80)			614 (4.20)	679 (4.90)	tw
	DMSO	393 (4.86)			614 (4.30)	679 (4.98)	tw
	DMF	389 (4.80)			612 (4.30)	677 (4.90)	tw
[Py ₈ TPyzPzMg(H ₂ O)]	py	375 (5.23)		596 (4.65)	631(4.64)sh	658 (5.54)	15
	DMSO	374 (5.08)	566 (3.96)sh	594 (4.36)	629(4.55)sh	653 (5.34)	15
[Py ₈ TPyzPzZn]	py	378 (4.90)	598 (4.31)		630(4.35)sh	658 (5.18)	15
	DMSO	372 (5.10)	565 (4.54)	592 (4.54)	629(4.61)sh	655 (5.36)	15

Table 7-1 continued

Compound	Solvent	Soret region			Q-band region		Ref.
		λ [nm] (log ϵ)			λ [nm] (log ϵ)		
[Py ₈ TPyzPzCu]	py	379 (4.64)		591 (4.18)		653 (4.93)	15
	DMSO	365 (4.91)		590 (4.44)		648 (5.18)	15
[Py ₈ TPyzPzCo]	py	364 (5.01)	441 (4.40)	575 (4.38)sh		635 (4.94)	15
	DMSO	355 (5.23)	450 (4.65)sh	586 (4.71)sh		634 (5.24)	15
[Py ₈ TPyzPz] ²⁻	py	362 (4.83)	402 sh	605 (4.39)	643 sh	667 (5.06)	12
	DMSO	362	402 sh	607	635 sh	664	12

^a Qualitative spectrum obtained with a sample showing low presence of aggregation.

^b Peak positions of the unreduced compound taken from the spectroelectrochemical data illustrated in Figure 7-7.

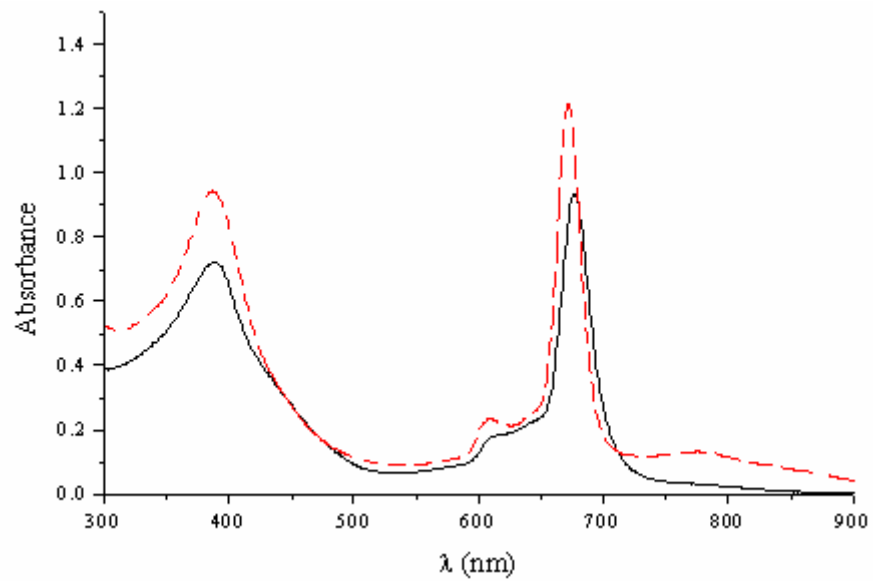


Figure 7-1. UV-visible solution spectra in DMF of $[\text{Th}_8\text{PyzPzH}_2]$ (solid line) and $[\text{Th}_8\text{PyzPzMg}(\text{H}_2\text{O})]$ (dashed line).

[Th₈TPyzPzM] (M = Mg^{II}(H₂O), Zn^{II}, Cu^{II}) and [Th₈TPyzPz]⁻² have Soret and Q bands which vary over a narrow range of 380-395 and 672-679 nm, respectively. The spectrum of the Co^{II} complex [Th₈TPyzPzCo] is distinct from the other porphyrazines in that it exhibits Soret and Q-bands whose peaks are shifted to lower wavelengths by an average of 15-20 and 25 nm, respectively. A comparison between UV-visible spectra of the octathienyl and octapyridinated compounds shows that the Soret and Q-band positions of the thienyl compounds are shifted *bathochromically* by about 20-25 nm for the metal complexes (the Co^{II} derivative included) and by 10-12 nm in the case of the free-base compound. These shifts are in the same direction as observed for the octapyridino species upon quaternization of the external pyridine N atoms to give the cationic species [(2-Mepy)₈TPyzPzM]⁸⁺¹⁵ and [(2-Mepy)₈TPyzPz]⁶⁺¹⁶. The resulting shifts in λ_{max} are also in the same direction as upon formation of the homo- and heteropentametallic derivatives [(PdCl₂)₄Py₈TPyzPzPd]¹³ and [(PdCl₂)₄Py₈TPyzPzM]²¹ where the average range of bathochromic shifts is 5-15 nm. These spectral shifts have been considered in direct relationship to the increased electron-withdrawing properties consequent to charge location or coordination of PdCl₂ on the external pyridine rings. In light of these data, the parallel bathochromic spectral shifts observed for the thienyl compounds with respect to those observed for the series of the octapyridinated analogues can be taken as being directly related to the presence of the external thienyl rings, which evidently behave as strong electron-attracting fragments.

7.2.2 Pretreatment of Sample

Because the investigated [Th₈TPyzPzM] complexes are highly aggregated in

nonaqueous media, no meaningful electrochemistry and spectroelectrochemistry could be carried out on the neutral compounds without first “solubilizing” the material as described earlier for the case of “thiadiazolporphyrazines” [TTDPzM] ($M = \text{Zn}^{\text{II}}$, $\text{Mg}^{\text{II}}(\text{H}_2\text{O})$, Cu^{II} , 2H^{I}).⁶ In the present chapter we first generated the triply reduced $[\text{Th}_8\text{TPyzPzM}]^{3-}$ derivatives which were not aggregated in solution and then examined properties of the trianionic species as well as the singly and doubly reduced species in their monomeric forms. This was accomplished by first scanning to negative potentials to generate the more soluble trianion of each compound and then reversing the potential to 0.0 V to regenerate the neutral compound in its unaggregated form, after which the electrochemistry and UV-visible spectra could be measured. The electrogenerated monomers were moderately stable and the UV-visible properties of each reduced form of the compounds could then be measured in a thin-layer cell in the absence of aggregation (see below).

7.2.3 Electrochemical Measurements

Electrochemical and spectroelectrochemical measurements were carried out in pyridine, DMSO and DMF. Examples of thin-layer cyclic voltammograms are shown in Figures 7-2 and 7-3 which illustrate data for $[\text{Th}_8\text{TPyzPzZn}]$ in DMSO, DMF and pyridine. Aggregation, which dominates the UV-visible spectra at concentrations of ca 10^{-5} M (see the earlier discussion), is even more evident at the concentrations used for electrochemical measurements ($\geq 10^{-4}$ M), and for this reason, a meaningful electrochemical response could not be obtained on the initial potential scan of the aggregated species (see the dashed line in Figure 7-2).

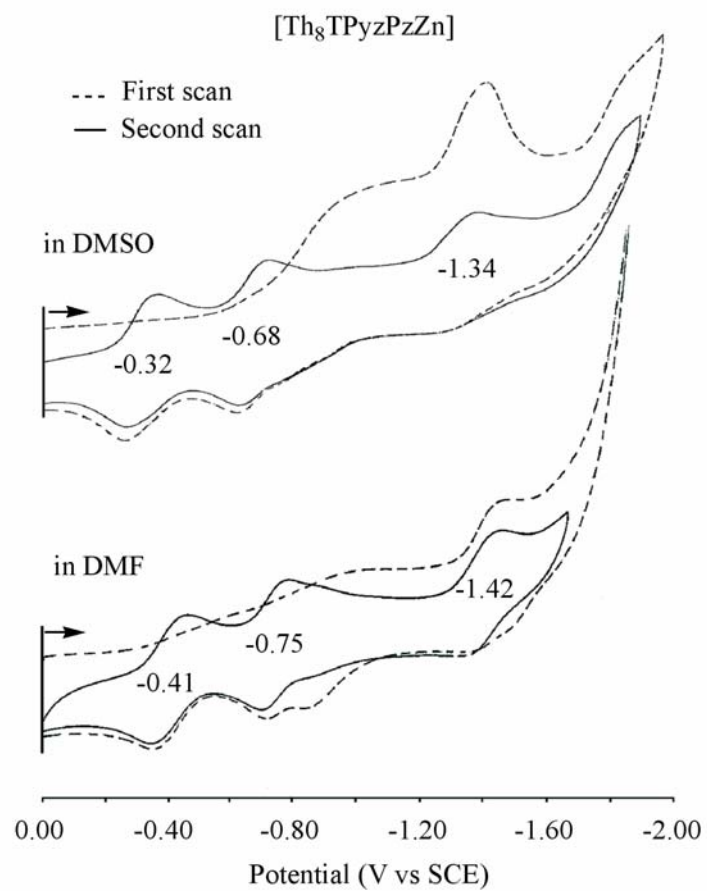


Figure 7-2. First scan (---) and second scan (—) thin-layer cyclic voltammograms of [Th₈TPyzPzZn] in DMSO and DMF, 0.2 M TBAP.

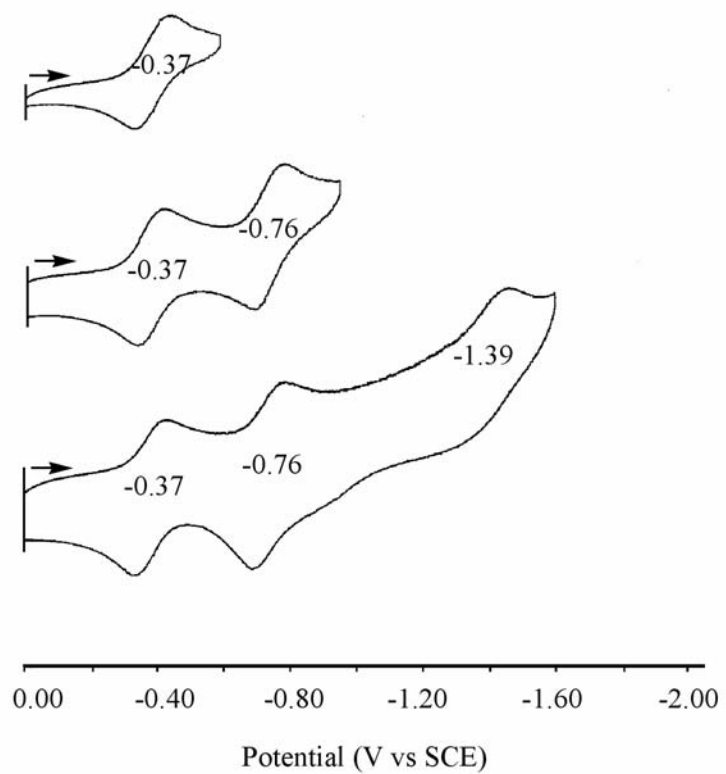


Figure 7-3. Second scan thin-layer cyclic voltammograms of $[\text{Th}_8\text{TPyzPzZn}]$ in pyridine, 0.2 M TBAP.

In contrast to the first negative potential scan from 0.00 to -2.00 V, useful electrochemical data were obtained in all cases on the second potential sweep (solid line in Figures 7-2 and 7-3). Under these experimental conditions, three of the four expected reductions are observed over the investigated potential range, the first of which occurs at $E_{1/2} = -0.32$ to -0.41 V, the second at $E_{1/2} = -0.68$ to -0.76 V and the third at $E_{1/2} = -1.34$ to -1.42 V, all *vs* SCE. Half-wave potentials of the Fc/Fc⁺ couple were measured as 0.47, 0.50 and 0.53 V in DMSO, DMF and pyridine, respectively, and the thermodynamic values of $E_{1/2}$ *vs* Fc/Fc⁺ for the first reduction of [Th₈TPyzPzZn] are then given as -0.79 V (DMSO), -0.91 V (DMF) and -0.90 V (pyridine), respectively. These potentials are also listed in Table 7-2 which summarizes half-wave potentials for each metalated porphyrzine in the three solvents.

Several trends can be seen from the data in Table 7-2, the most evident of which is that the first reduction of the Co^{II} complex [Th₈TPyzPzCo] is substantially easier than for reduction of the Zn^{II}, Mg^{II} and Cu^{II} derivatives under the same solution conditions. At the same time, the second reduction of the cobalt porphyrzine is harder (occurs at a more negative potential) than the other metalated compounds, thus leading to a much larger difference in $E_{1/2}$ ($\Delta E_{\text{avg}} = 650$ mV) between the two processes as compared to the other three compounds where an average $\Delta E_{1/2} = 340$ mV is obtained in the three solvents. As described later in the manuscript, this difference in redox behavior is due to a different site of electron transfer for the two series of compounds.

There is also a marked solvent dependence of the measured $E_{1/2}$ values for all four compounds. The most facile first reduction occurs in DMSO for the M = Zn^{II}, Mg^{II} and Co^{II} derivatives (see $E_{1/2}$ *vs*. Fc/Fc⁺ values listed in Table 7-2) but not for the Cu^{II}

Table 7-2. Half-wave Potentials ($E_{1/2}$, V vs SCE and vs Fc/Fc⁺) for Reduction of [Th₈TPyzPzM] (M = Zn^{II}, Mg^{II}(H₂O), Cu^{II}, Co^{II}) in DMSO, DMF and Pyridine, 0.2 M TBAP.

Metal ion	Solvent	1 st red		2 nd red		3 rd red	
		vs SCE	vs Fc/Fc ⁺	vs SCE	vs Fc/Fc ⁺	vs SCE	vs Fc/Fc ⁺
Zn ^{II}	DMSO	-0.32	-0.79	-0.68	-1.15	-1.34	-1.81
	DMF	-0.41	-0.91	-0.75	-1.25	-1.42	-1.92
	pyridine	-0.37	-0.90	-0.76	-1.29	-1.39	-1.92
Mg ^{II} (H ₂ O) ^a	DMSO	-0.37	-0.84	-0.68	-1.15	-1.40	-1.87
	DMF	-0.43	-0.93	-0.77	-1.27	-1.41	-1.91
	pyridine	-0.46	-0.99	-0.79	-1.32	-1.49	-2.02
Cu ^{II}	DMSO	-0.30	-0.77	-0.67	-1.14	-1.34	-1.81
	DMF	-0.26	-0.76	-0.60	-1.10	-1.24	-1.77
	pyridine	-0.35	-0.88	-0.67	-1.20	-1.36	-1.79
Co ^{II}	DMSO ^b	-0.12	-0.59	-0.78	-1.25	-1.36	-1.83
	DMF	-0.13	-0.63	-0.82	-1.32	-1.36	-1.86
	pyridine	-0.25	-0.78	-0.85	-1.38	-1.35	-1.88

^a Unknown impurity or side reaction seen for Mg^{II} complex at $E_{1/2} = -0.98$ to -1.04 V vs SCE in all solvents. ^b The oxidization of [Th₈TPyzPzCo^{II}] to [Th₈TPyzPzCo^{III}]⁺ occurs at $E_{1/2} = 0.57$ V in DMSO.

complex where almost identical $E_{1/2}$ values of -0.77 and -0.76 V are obtained in DMSO and DMF. In contrast to the easier first reductions in DMSO, a more difficult first reduction is seen in pyridine for three of the four compounds ($M = \text{Mg}^{\text{II}}$, Cu^{II} and Co^{II}) but not for the Zn^{II} porphyrazine where virtually identical $E_{1/2}$ values of -0.90 and -0.91 V are measured in pyridine and in DMF, respectively.

The second reduction of the Zn^{II} complex ranged from $E_{1/2} = -1.15$ to -1.29 V vs Fc/Fc^+ in the three solvents, with a difference of 40 mV between the measured half-wave potentials in DMF and those in pyridine, the easier reduction being in DMF. A 50 mV difference between $E_{1/2}$ in these two solvents is also seen for the Mg^{II} analogue, where an easier reduction again occurs in DMF. The same trend in ease of reduction is seen for the Cu^{II} complex in the same two solvents, but here a larger $\Delta E_{1/2}$ of 100 mV is observed between the two electron transfer processes which occur at $E_{1/2} = -1.10$ and -1.20 V in DMF and pyridine, respectively (see Table 7-2). These differences in solvent effects on redox potentials of the Zn^{II} , Mg^{II} and Cu^{II} derivatives can be related to different interactions between the solvent and the three porphyrazines in their neutral, singly reduced and doubly reduced forms.

Additional examples for thin-layer cyclic voltammograms of the four metalated compounds in pyridine shown in Figures 7-4, while voltammograms for the metalated compounds under “regular” CV conditions are illustrated in Figures 7-5. The measured $E_{1/2}$ values in pyridine, DMSO and DMF are summarized in Table 7-3 and arranged according to solvent to better see how the potentials are shifted with changes in metal ion under each solution condition. As earlier indicated, the half-wave potentials were recorded on the second potential sweep after reductive break up of the aggregates.

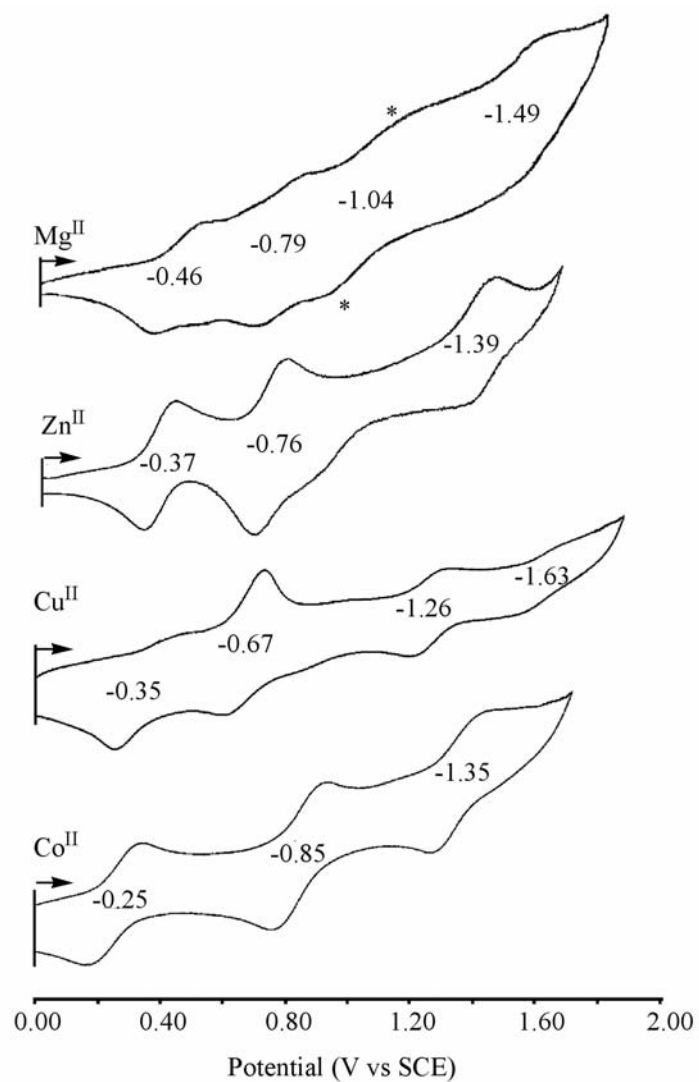


Figure 7-4. Thin-layer cyclic voltammograms obtained on second scan for reduction of $[\text{Th}_8\text{TPyzPzM}]$ ($M = \text{Mg}^{\text{II}}(\text{H}_2\text{O})$, Zn^{II} , Cu^{II} , Co^{II}) in pyridine containing 0.2 M TBAP. Peaks for reduction of unknown trace impurity in the Mg^{II} sample is indicated by an asterisk (*).

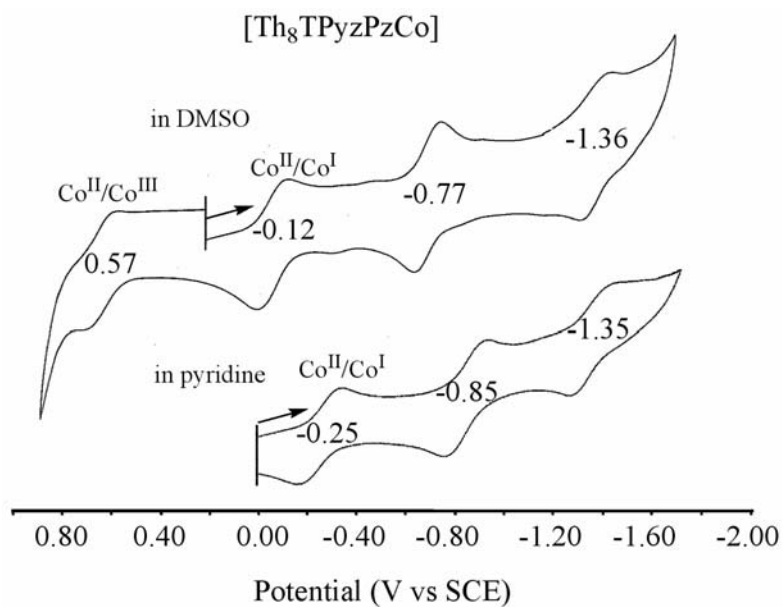


Figure 7-5. Thin-layer cyclic voltammograms of [Th₈TPyzPzCo] in DMSO and pyridine, 0.2 M TBAP.

Table 7-3. Half-wave Potentials Measured by Regular Cyclic Voltammetry ($E_{1/2}$, V vs SCE) for Reductions of [Th₈TPyzPzM] (M = Mg^{II}, Zn^{II}, Cu^{II}, Co^{II}, 2H⁺) and Analogues in Pyridine, DMSO and DMF, 0.1 M TBAP (Scan Rate = 0.1 V/s).

Compound	Solvent	Reduction				Δ_{1-2}	Δ_{2-3}	Δ_{3-4}
		first	second	third	fourth			
[Th ₈ TPyzPzMg(H ₂ O)] ^a	py	-0.49	-0.75	-1.37	-1.65	0.26	0.62	0.28
[Th ₈ TPyzPzZn]		-0.40	-0.70	-1.35	---	0.30	0.65	0.32
[Th ₈ TPyzPzCu]		-0.35	-0.68	-1.28	-1.64	0.32	0.61	0.36
[Th ₈ TPyzPzCo]		-0.27	-0.85	-1.34	---	0.58	0.49	---
[Th ₈ TPyzPzH ₂] ^b		-0.23	-0.47	-0.98	-1.65	0.24	0.51	0.45
[Th ₈ TPyzPzMg(H ₂ O)] ^a	DMSO	-0.37	-0.67	-1.38	---	0.30	0.71	0.29
[Th ₈ TPyzPzZn]		-0.30	-0.64	-1.29	-1.67	0.34	0.65	0.38
[Th ₈ TPyzPzCu]		-0.31	-0.62	-1.17	-1.54	0.31	0.55	0.37
[Th ₈ TPyzPzCo]		-0.13	-0.76	-1.25	-1.72	0.63	0.49	0.47
[Th ₈ TPyzPzH ₂] ^b		-0.16	-0.37	-0.93	-1.79	0.21	0.56	0.63
[Th ₈ TPyzPzMg(H ₂ O)] ^a	DMF	-0.43	-0.74	-1.40	---	0.31	0.66	---
[Th ₈ TPyzPzZn]		-0.39	-0.69	-1.40	-1.64	0.30	0.71	0.24
[Th ₈ TPyzPzCu]		-0.33	-0.60	-1.27	---	0.27	0.67	---
[Th ₈ TPyzPzCo]		-0.14	-0.81	-1.35	-1.81	0.67	0.54	0.46
[Th ₈ TPyzPzH ₂] ^b		-0.16	-0.39	-0.95	-1.64	0.23	0.56	0.39
[Py ₈ TPyzPzMg(H ₂ O)] ^c	py	-0.40	-0.79	-1.43	-1.70	0.39	0.64	0.27
[Py ₈ TPyzPzZn] ^c		-0.34	-0.72	-1.38	-1.66	0.38	0.66	0.28
[Py ₈ TPyzPzCu] ^c		-0.30	-0.68	-1.28	-1.61	0.38	0.61	0.33

^a Unknown impurity or side reaction for the Mg^{II} complex at $E_{1/2} = -0.94$ to -1.04 V vs SCE in all solvents. ^b Additional reductions seen for free base compounds at -1.43 V (pyridine), -1.56 V (DMSO) or -1.34 V (DMF). (0.2 M TBAP in thin-layer experiments and 0.1 M in regular CV). ^c Data from Ref 11.

No exchange of electrons is observed in the positive range of potentials for these compounds, with the exception of the Co^{II} complex which undergoes three one-electron reductions and a single one-electron oxidation which generates $[\text{Th}_8\text{TPyzPzCo}^{\text{III}}]^+$ in DMSO containing 0.1 M TBAP (see Figure 7-5 which also illustrates cyclic voltammograms of the compound in DMSO and pyridine). The observation of a $\text{Co}^{\text{II}}/\text{Co}^{\text{III}}$ process in DMSO but not in pyridine was also reported for $[\text{Py}_8\text{TPyzPzCo}]^{\text{I}5}$ and can be accounted for by a strong binding of one or two py molecules to the Co^{II} form of the compound which shifts $E_{1/2}$ for the metal-centered oxidation in pyridine to a value that is more positive of the solvent potential cutoff limit (about 0.7 to 0.8 V vs SCE). It should be pointed out that $[\text{Py}_8\text{TPyzPzCo}]$ undergoes a $\text{Co}^{\text{II}} \rightarrow \text{Co}^{\text{I}}$ in DMSO, followed by a slow reverse $\text{Co}^{\text{I}} \rightarrow \text{Co}^{\text{II}}$ process, and this reoxidation leads to isolation of the bis-DMSO adduct $[\text{Py}_8\text{TPyzPzCo}(\text{DMSO})_2]$, whose structure was elucidated by single-crystal X-ray work.¹⁴ In the same study,¹⁴ the Co^{I} and Co^{III} species, $\text{Na}[\text{Py}_8\text{TPyzPzCo}^{\text{I}}]$ and $[\text{Py}_8\text{TPyzPzCo}^{\text{III}}](\text{SbCl}_6)$, respectively, were isolated and characterized as solid materials via chemical pathways.

It should also be noted that current-voltage curves for the reduction and oxidation of $[\text{Th}_8\text{TPyzPzCo}]$ are much better defined than for the other metalated compounds. This was true in all three solvents and can be accounted for by a lack of adsorption which seems to be associated with the aggregated π -anion radical in the case of the Zn^{II} , Mg^{II} and Cu^{II} derivatives. The degree of adsorption varies in strength as a function of the specific metal ion, but is maximum for $\text{M} = \text{Cu}^{\text{II}}$ and minimum for $\text{M} = \text{Zn}^{\text{II}}$ as seen in Table 7-2. As described below, a Co^{II} porphyrazine π -anion radical is not generated in first reduction of $[\text{Th}_8\text{TPyzPzCo}^{\text{II}}]$ but rather the first one-electron addition occurs at the

metal center to give a Co^{I} porphyrzine with an unreduced π -ring system. The second reduction of $[\text{Th}_8\text{TPyzPzCo}^{\text{II}}]$ generates a Co^{II} porphyrzine dianion as the final product, and thus no aggregation or adsorption is seen for the cobalt porphyrzine radical form simply because this form of the compound does not exist on any appreciable time scale. This was also the case for the previously examined $[\text{Py}_8\text{TPyzPzCo}]$ (see Figure 4 in Ref. 15).

As seen in Figures 7-3 to 7-4 and Table 7-3, the half-wave potential for the initial one-electron reduction of the $[\text{Th}_8\text{TPyzPzM}]$ compounds moves progressively towards more positive values in the order $\text{Mg}^{\text{II}} \rightarrow \text{Zn}^{\text{II}} \rightarrow \text{Cu}^{\text{II}} \rightarrow \text{Co}^{\text{II}}$, irrespective of the solvent used. The same order in ease of reduction is essentially maintained for the second, third and fourth electron additions, with the exception of the Co^{II} complex which has a different electron transfer mechanism as described below. The $E_{1/2}$ values in the “regular” and thin-layer cyclic voltammograms are almost identical for all of the examined porphyrzines, despite the different concentrations of supporting electrolyte

In summary, up to four stepwise one-electron reductions can be seen for each metalated porphyrzine in the three solvents. Because the Mg^{II} , Zn^{II} and Cu^{II} metal ions are redox inactive, the stepwise reductions must be considered as ring-centered and occur as shown by Eqs. 7-1 to 7-4.



The proposed sequence of reduction steps for the Co^{II} complex is different from that of the other metalated derivatives in that the first one-electron addition occurs at the Co^{II} center to give a Co^I porphyrzine (Eq. 7-5) while the second one-electron reduction occurs at the macrocycle (Eq. 7-6a) and is followed by an internal electron transfer from the metal to the macrocycle (Eq. 7-6b) to give as a final product a Co^{II} porphyrzine with a doubly reduced macrocycle, ie. [Th₈TPyzPzCo^{II}]²⁻. The next two one-electron reductions of [Th₈TPyzPzCo^{II}]²⁻ then proceed as shown in Eqs. 7-3 and 7-4.



A electrochemical reduction mechanism similar to those shown in Eqs. 7-5 and 7-6 was earlier proposed for the Co^{II} octapyridino analogue [Py₈TPyzPzCo]¹⁵ as well as the diazepino compound, [Ph₈DzPzCo].⁹ Evidence for the sequence of steps given by Eqs. 7-5 and 7-6 followed by Eqs. 7-3 and 7-4 in the current study is given in part by the similar spectrum of doubly reduced [Th₈TPyzPzCo^{II}]²⁻ with the other three doubly reduced [Th₈TPyzPzM]²⁻ compounds (see following Spectroelectrochemistry section) as well as by the fact that the third reduction potential of [Th₈TPyzPzCo]²⁻ is quite close to *E*_{1/2} values for the third reduction of [Th₈TPyzPzM]²⁻ where M = Mg^{II} or Zn^{II}, independent of solvent (see Tables 7-2 and 7-3).

The absolute potential separations between each stepwise reduction of the metalated complexes is also given in Tables 7-3 and listed as Δ₁₋₂, Δ₂₋₃ and Δ₃₋₄. These separations vary little with changes in the central metal ion upon going from the

porphyrizine with $M = \text{Mg}^{\text{II}}(\text{H}_2\text{O})$ to Zn^{II} to Cu^{II} and the average $\Delta E_{1/2}$ values are 0.29, 0.63 and 0.32 V, respectively, in pyridine. Comparable average values of $\Delta E_{1/2}$ are seen for the same compounds in the other two solvents.

From the measured $E_{1/2}$ values in Table 7-2 and 7-3, it is clear that the stepwise addition of electrons to the series of $[\text{Th}_8\text{TPyzPzM}]$ compounds takes place at much more positive $E_{1/2}$ values than for the related phthalocyanine analogues,¹ a fact which is attributed to the presence of the strongly electron-withdrawing dithienylpyrazino fragments which replace the benzene rings of the phthalocyanine macrocycle (see Chart 1B). This shift in $E_{1/2}$ towards more positive potentials is a feature shared by the related diazepino-⁹ and thiadiazolporphyrizine⁶ macrocycles, with parallel results also being obtained for related compounds having peripheral dipyridinopyrazine fragments (Chart 7-1A)^{11, 12, 13} as well as for the octacationic^{15, 13} and the homo-¹³ and heteropentametallic²¹ derivatives.

Finally, it should be mentioned that the observed trend of reduction potentials as a function of solvent, metal ion and structure approaches what was earlier reported for related electron-deficient macrocycles, each one of which shares the feature of possessing a five-,⁴⁻⁷ six-,^{11-16, 21} or seven-membered^{8, 10, 22} heterocycle annulated to the four pyrrole rings of the porphyrizine core. A further common feature connecting these related compounds is that the electron deficiency of the macrocycle is associated with a facile redistribution and stabilization of the excess negative charge within the entire framework of the π -conjugated system.

7.2.4 Spectroelectrochemistry

UV-visible spectra for each reduced species were obtained by thin-layer spectroelectrochemistry as described in the Experimental Section and are discussed below in the order $M = \text{Mg}^{\text{II}}$ and Zn^{II} , followed by Co^{II} and then 2H^{I} . Although the cyclic voltammograms of Cu^{II} complex enable $E_{1/2}$ values to be determined (see Figures 7-4 to 7-6), aggregation and adsorption of the neutral and singly reduced complex was too extensive for obtaining meaningful measurements of UV-visible spectral changes after each stepwise one-electron reduction.

$M = \text{Mg}^{\text{II}}$ and Zn^{II} . Figure 7-6 depicts the thin-layer UV-visible spectral changes which occur during the first two reductions of the Mg^{II} and Zn^{II} complexes in DMSO. An example of the thin-layer cyclic voltammogram for $[\text{Th}_8\text{TPyzPzZn}]$ obtained under the same solution conditions as the thin-layer spectroelectrochemistry measurements is shown in Figure 7-2. Similar thin-layer voltammograms were obtained for $[\text{Th}_8\text{TPyzPzMg}(\text{H}_2\text{O})]$ whose half-wave potentials for reduction are listed in Table 7-2.

Each redox process of $[\text{Th}_8\text{TPyzPzZn}]$ and $[\text{Th}_8\text{TPyzPzMg}(\text{H}_2\text{O})]$ is spectrally reversible but, as noted in previous section (7.2.2), it was necessary to first reduce the aggregated compounds to generate the trianion of the M^{II} species in its monomeric form. The applied potential was then set to 0.00 V to obtain the spectrum of the neutral compound in its monomeric form after which the applied potential was shifted to more negative values where the monomeric monoanion and dianion could be electrogenerated and their spectra recorded.

As seen in Figure 7-6, similar spectral changes occur during the first two reductions

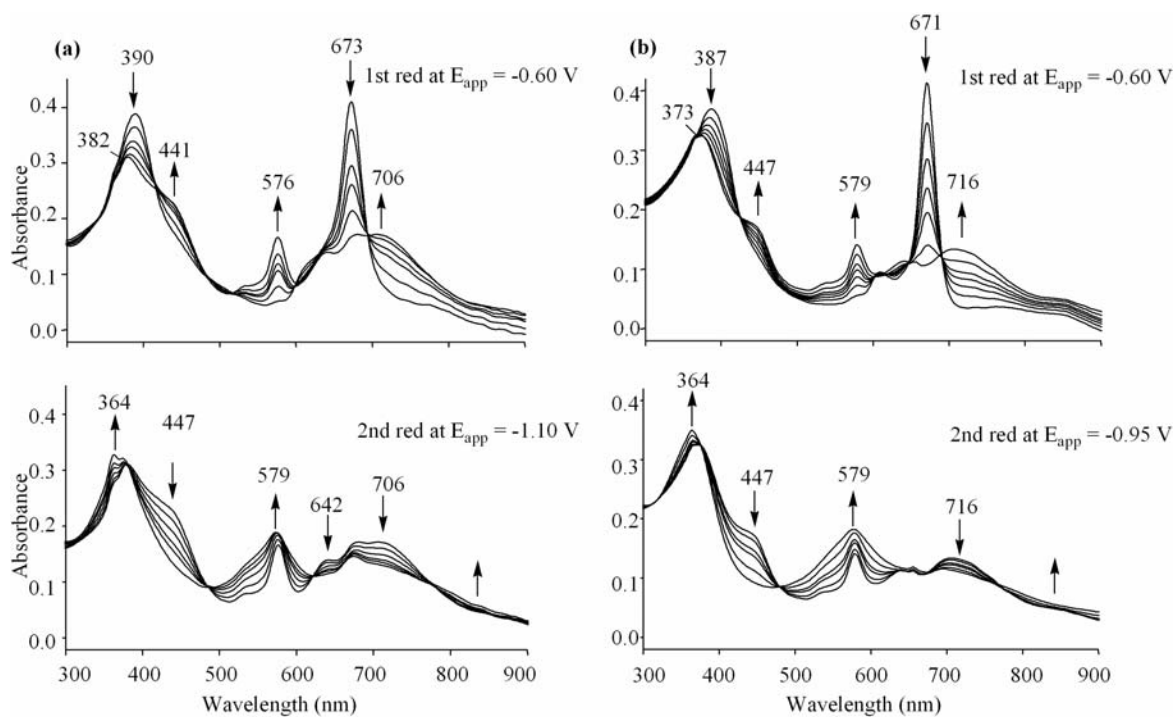


Figure 7-6. UV-visible spectral changes during first and second one-electron reductions of (a) $[\text{Th}_8\text{TPyzPzZn}]$ and (b) $[\text{Th}_8\text{TPyzPzMg}(\text{H}_2\text{O})]$ in DMSO containing 0.2 M TBAP.

of monomeric $[\text{Th}_8\text{TPyzPzZn}]$ and $[\text{Th}_8\text{TPyzPzMg}(\text{H}_2\text{O})]$ in DMSO. The multiple isosbestic points in the Figure 7-6 indicate the absence of any spectrally detectable intermediates in solution during the first two one electron additions. A similarity in spectra before and after electroreduction was earlier reported for the Mg^{II} and Zn^{II} octapyridino analogues¹⁵ as well as for the tetrakis(thiadiazole)porphyrazine macrocycles $[\text{TTDPzM}]$ ($\text{M} = \text{Mg}^{\text{II}}(\text{H}_2\text{O})$ and Zn^{II})⁶ having central the same two metal ions.

In the case of the Zn^{II} and Mg^{II} thienyl porphyrazines, there is a disappearance of the Q band at 671 to 673 nm and the appearance of new absorption bands at ca. 576-579 nm and 706-716 nm as the monoanion is electrogenerated (see top two spectra in Figures 7-6a and 7-6b). The 576-579 nm band further increases in intensity during the second reduction while the 706-716 nm band decreases in intensity (see lower two spectra in Figures 7-6a and 7-6b). An interpretation of these spectral features along with DFT and TDDFT theoretical calculations has been published⁶ for the redox processes $[\text{TTDPzZn}] \rightarrow [\text{TTDPzZn}]^{1-}$ and $[\text{TTDPzZn}]^{1-} \rightarrow [\text{TTDPzZn}]^{2-}$. The Zn^{II} complex was selected in the earlier theoretical study as a representative compound describing the ground and excited-state electronic structures of the entire series of neutral $[\text{TTDPzM}]^5$ and negatively charged $[\text{TTDPzM}]^{n-}$ derivatives ($n = 1-4$; $\text{M} = \text{Zn}^{\text{II}}, \text{Mg}^{\text{II}}(\text{H}_2\text{O}), \text{Cu}^{\text{II}}, 2\text{H}^1$).⁶

$\mathbf{M} = \mathbf{Co}^{\text{II}}$. As indicated in Eqs 7-3 to 7-5, a metal-centered $\text{Co}^{\text{II}}/\text{Co}^{\text{I}}$ process is assigned for the first reduction of $[\text{Th}_8\text{TPyzPzCo}]$ which gives a stable Co^{I} complex. $[\text{Th}_8\text{TPyzPzCo}]^{1-}$ is then further reduced in the second step to a transient $[\text{Th}_8\text{TPyzPzCo}]^{1-2-}$ species (Eq. 7-8a) which undergoes a rapid conversion of Co^{I} to Co^{II} to give as a final product the Co^{II} porphyrazine dianion, $[\text{Th}_8\text{TPyzPzCo}^{\text{II}}]^{2-}$ (Eq. 7-6b).

The spectroelectrochemical data confirms the proposed mechanisms for the

sequence of steps in the first two reductions (Equations 7-5 and 7-6). As seen in Figure 7-7a, the first reduction of $[\text{Th}_8\text{TPyzPzCo}]$ leads to a spectrum of the -1 charged species which exhibits an intense broad peak centered at 581 nm. At the same time the initial Q band at 656 nm is red-shifted to 709 nm and decreases in intensity. The Soret band at 373 nm also decreases in intensity and shifts to 338 nm during this process. The final spectrum after the addition of one electron to give $[\text{Th}_8\text{TPyzPzCo}^{\text{I}}]^-$ is quite different from that of singly reduced $[\text{Th}_8\text{TPyzPzZn}^{\text{II}}]^-$ (Figure 7-7b) where a π anion radical is generated, but the spectra generated upon the second one-electron reduction of the Co^{II} and Zn^{II} porphyrazines are quite similar to each other, both dinegative species having bands at 576-579 nm and 363-364 nm (see lower two spectra in Figure 7-7).

Similar spectral changes occur during reduction of the cobalt porphyrazine in pyridine as in DMSO but in pyridine all three one-electron reductions of $[\text{Th}_8\text{TPyzPzCo}^{\text{II}}]$ could be characterized in the thin-layer cell (Figure 7-8). The spectral evolutions in pyridine are similar to what was reported for the reduction of octapyridino analogue.¹⁵ The broad peak at 584 nm for $[\text{Th}_8\text{TPyzPzCo}^{\text{I}}]^-$ can be considered as a metal-to-ligand charge-transfer band. A similar assignment was made for a bound peak in the spectra of the singly reduced phthalocyanine Co^{II} complex, $[\text{PcCo}]$, in different solvents.^{23,24,25}

In addition to three reversible reductions, the $[\text{Th}_8\text{TPyzPzCo}^{\text{II}}]$ complex also undergoes a reversible one-electron oxidation at $E_{1/2} = 0.57$ V in DMSO, a potential close to that measured for the $\text{Co}^{\text{II}}/\text{Co}^{\text{III}}$ process of the octapyridino analogue in the same solvent (0.67 V).¹⁵ A comparison of the spectral changes for the two compounds is shown in Figure 7-9. The spectrum of $[\text{Th}_8\text{TPyzPzCo}^{\text{III}}]^+$ and $[\text{Py}_8\text{TPyzPzCo}^{\text{III}}]^+$ are quite similar to each other in shape, the main difference between the two being a batho-

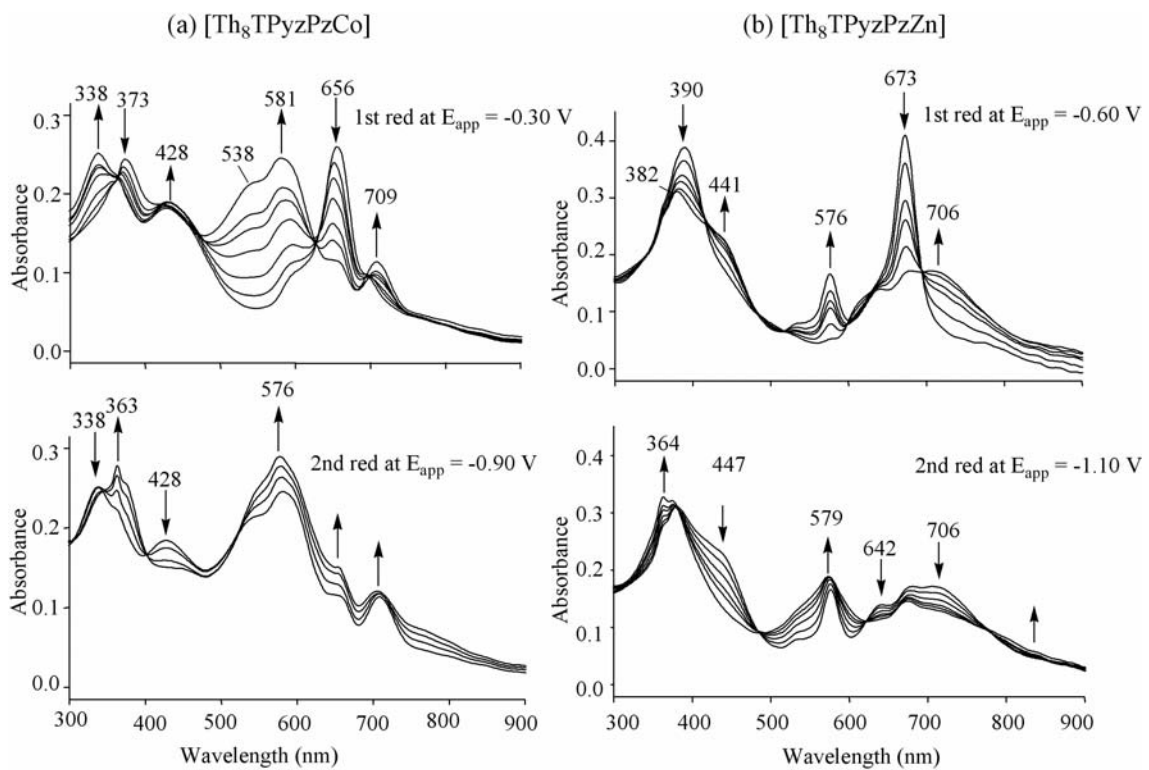


Figure 7-7. UV-visible spectral changes obtained during first and second reductions of (a) [Th₈TPyzPzCo] (b) [Th₈TPyzPzZn] in DMSO containing 0.2 M TBAP.

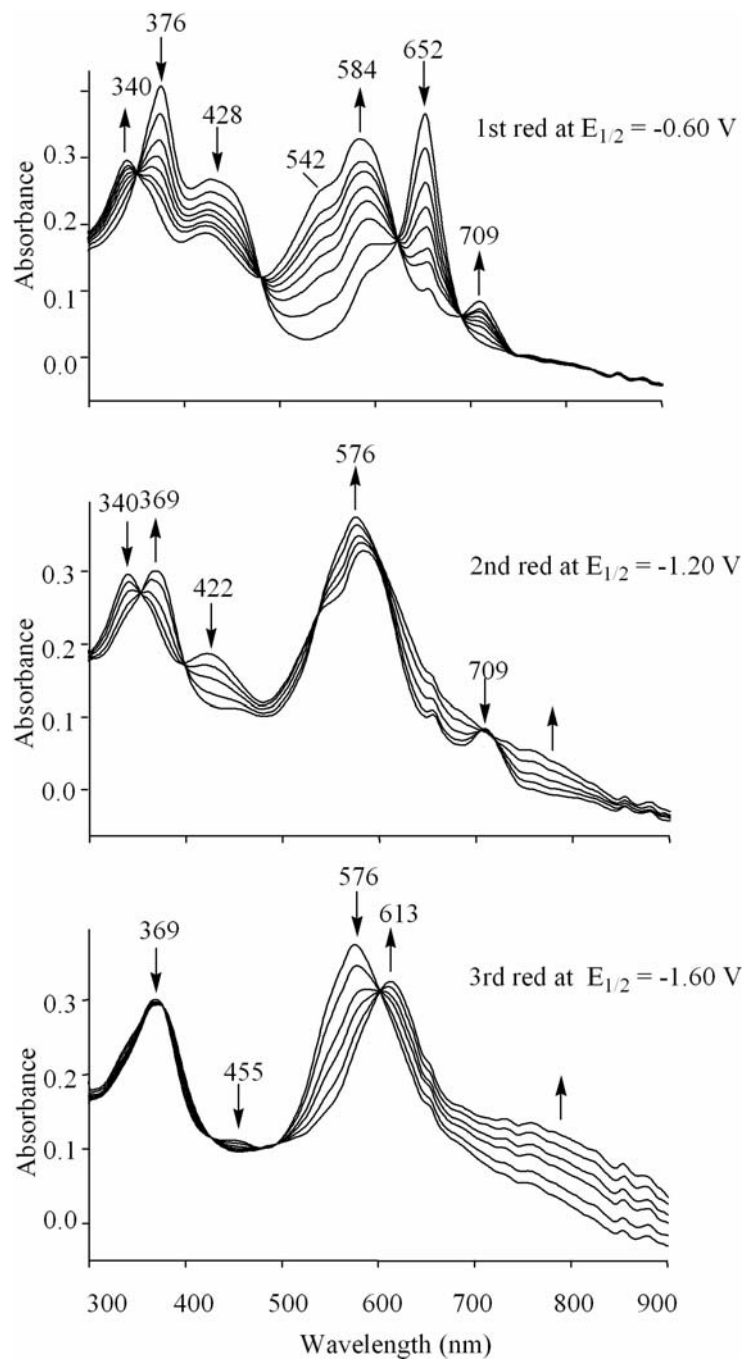


Figure 7-8. UV-visible spectral changes obtained during stepwise reductions of $[Th_8TPyzPzCo^{II}]$ in pyridine containing 0.2 M TBAP.

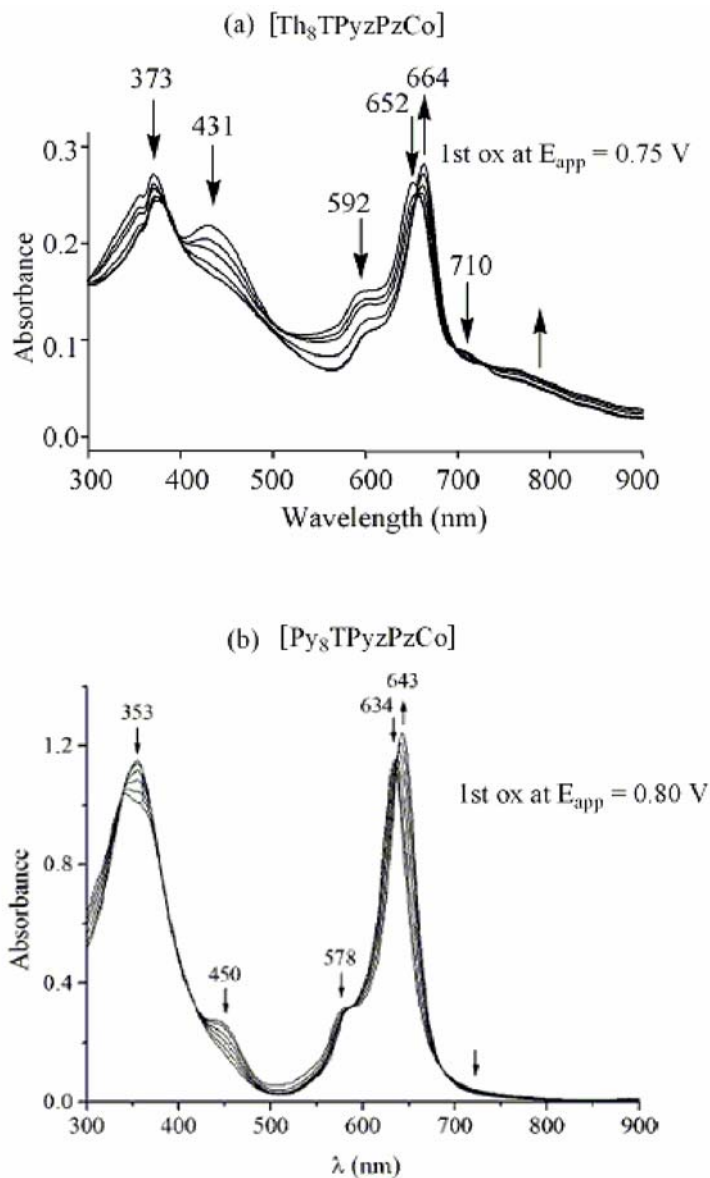


Figure 7-9. UV-visible spectral changes obtained during metal centered $\text{Co}^{\text{II}} \rightarrow \text{Co}^{\text{III}}$ oxidation of (a) $[\text{Th}_8\text{TPyzPzCo}]$ and (b) $[\text{Py}_8\text{TPyzPzCo}]$ in DMSO containing 0.2 M TBAP.

chromic shift of Q bands for the neutral and singly oxidized compounds in the case of Co^{II} complex.

$M = 2H^I$. The free-base porphyrine [Th₈TPyzPzH₂] undergoes five ill-defined reductions in pyridine, DMSO and DMF as seen in Figure 7-10. The third process at $E_p = -1.02$ to -1.07 V for a scan rate of 0.1 V/s, is actually due to a reduction of dianionic [Th₈TPyzPz]²⁻ which is in equilibrium with the neutral form of [Th₈TPyzPzH₂] as shown in Equation 7-7:



In order to further investigate the equilibrium shown in Equation 7-7, cyclic voltammograms were taken of [Th₈TPyzPzH₂] in pyridine containing 0.1 M TBAP and 0.12 M OH⁻ in the form of TBAOH. Under these experimental conditions, the equilibrium in Equation 7-7 is completely shifted to the right, and the first reduction occurs as shown in Equation 7-8.



The fact that two reductions at -0.23 and -0.47 V are no longer seen after adding TBA(OH) to the pyridine solvent containing [Th₈TPyzPzH₂] (Figure 7-11) strengthens the conclusion that these processes are assigned as the first and second reductions of the free-base neutral macrocycle [Th₈TPyzPzH₂]. Figure 7-12 shows the UV-visible spectral changes which occur upon the first and second one-electron reductions of [Th₈TPyzPzH₂] in pyridine, 0.1 M TBAP, to give [Th₈TPyzPzH₂]⁻ in the first step and then [Th₈TPyzPzH₂]²⁻ in the second. A similar series of reductions was earlier reported for [Py₈TPyzPzH₂]¹² and these reactions were not further examined as part of current work.

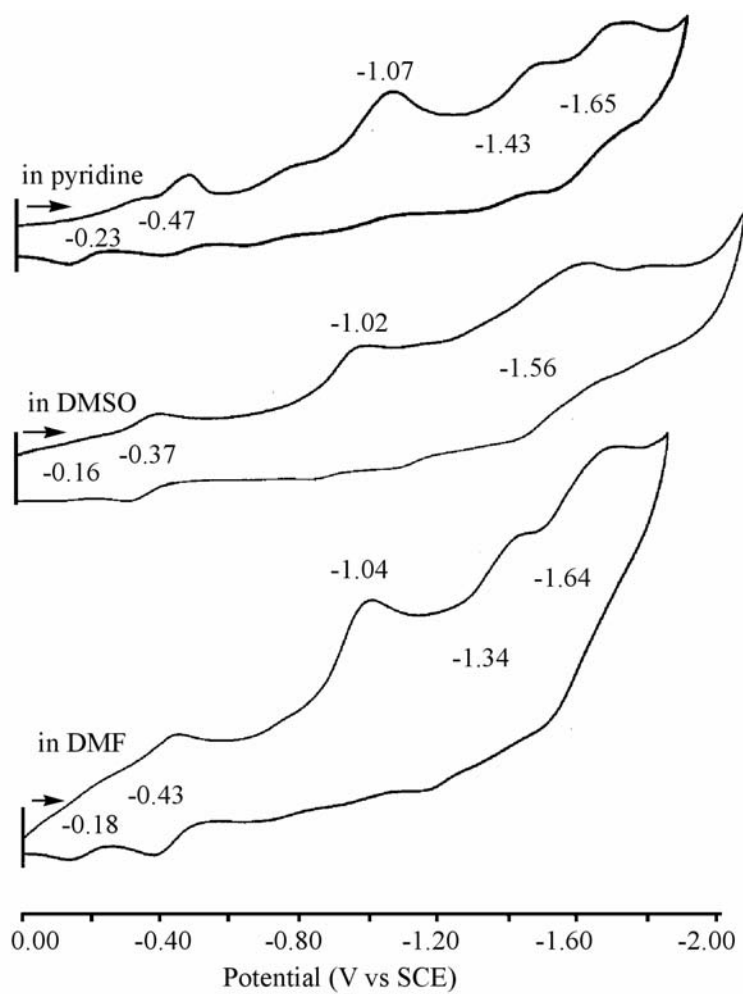


Figure 7-10. Cyclic voltammograms of $[Th_8TPyzPzH_2]$ in pyridine, DMSO and DMF, all containing 0.1 M TBAP. Scan rate = 0.1 V/s.

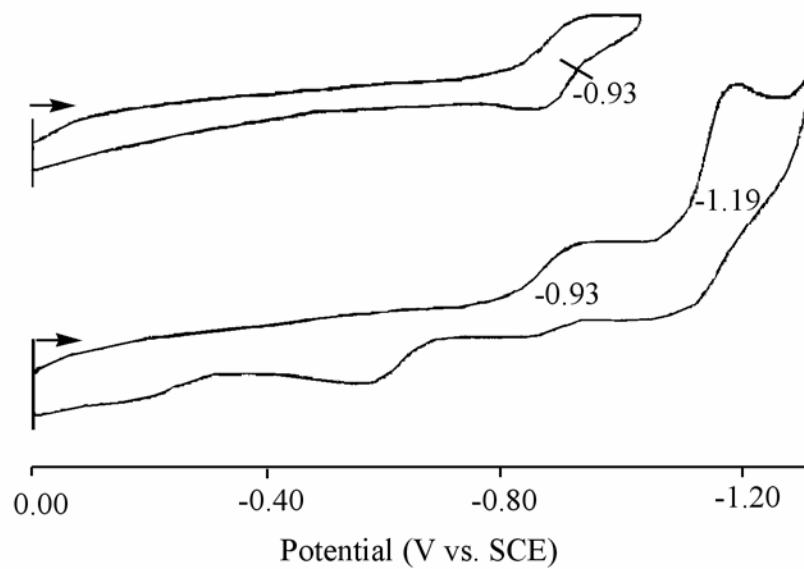


Figure 7-11. Cyclic voltammograms of $[\text{Th}_8\text{TPyzPz}]^{2-}$ in pyridine, 0.1 M TBAP and 0.12 M TBAOH.

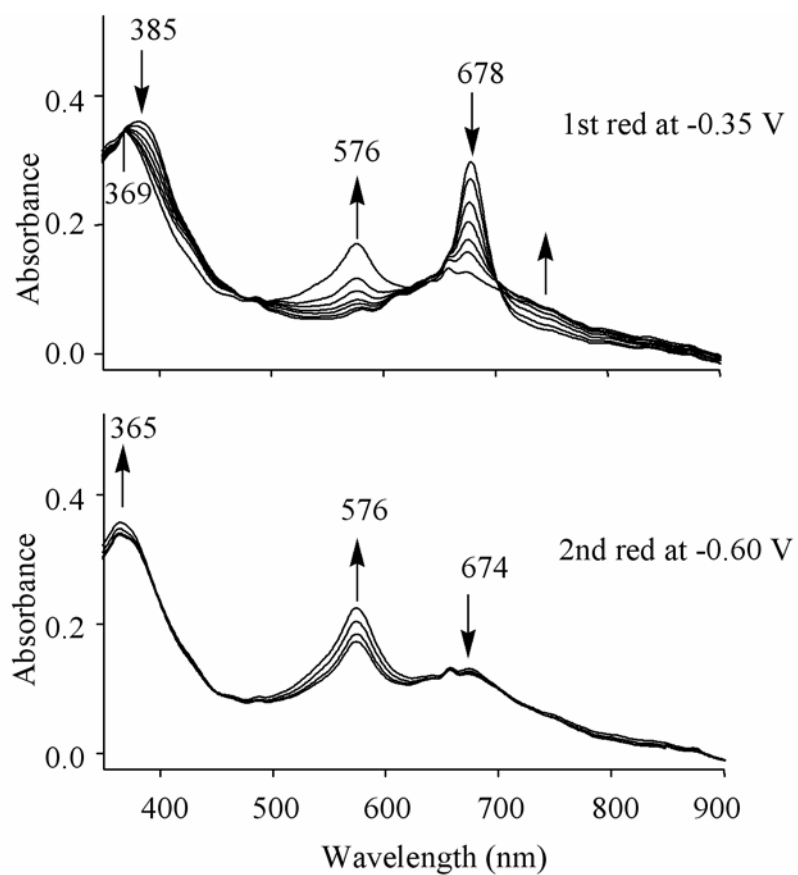


Figure 7-12. UV-vis spectral changes of $[\text{Th}_8\text{TPyzPzH}_2]$ in pyridine containing 0.2 M TBAP during controlled-potential electrolysis.

7.3 Conclusions

UV-visible spectral solution studies carried out in DMF, DMSO and pyridine on a series of pyrazinoporphyrazine macrocycles having the formula $[\text{Th}_8\text{TPyzPzM}]$ ($M = \text{Mg}^{\text{II}}(\text{H}_2\text{O}), \text{Zn}^{\text{II}}, \text{Co}^{\text{II}}, \text{Cu}^{\text{II}}, 2\text{H}^{\text{I}}$) (Chart 7-1B) indicate that all of the compounds behave as highly electron-deficient macrocycles due to the presence of the external electron-withdrawing 2-thienyl rings.

Cyclic voltammetry and spectroelectrochemical measurements show generally clean reversible or quasi-reversible stepwise one-electron reductions leading to the formation of -1, -2, -3, -4 charged species at half-wave potential value markedly less negative than those of the parent phthalocyanine compounds, the behaviour approaching that of the parallel series of octapyridinated analogues.

The uptake of electrons by these compounds induces spectral changes which closely resemble those of the parent octapyridinated analogues. The Co^{II} complex deserves special mention because of its distinct behaviour in the first and second one-electron reductions both metal-centered, implying the sequence $\text{Co}^{\text{II}} \rightarrow \text{Co}^{\text{I}}$ followed by the reverse process $\text{Co}^{\text{I}} \rightarrow \text{Co}^{\text{II}}$ with formation of the species $[\text{Th}_8\text{TPyzPzCo}^{\text{I}}]^-$ and $[\text{Th}_8\text{TPyzPzCo}^{\text{II}}]^{2-}$, respectively. Moreover, the Co^{II} complex is the only one among the examined porphyrazines which undergoes one-electron oxidation in the range of potentials explored (0.00 to 1.6 V vs SCE) leading to formation of the species $[\text{Th}_8\text{TPyzPzCo}^{\text{III}}]^+$.

7.4 References

1. Kudrevich, S. V.; van Lier, J. E., *Coord. Chem. Rev.* **1996**, *156*, 163.
2. Michel S, L. J.; Hoffman, B. M.; Baum, S. M.; Barrett A, G. M., *Progress in Inorganic Chemistry*. J. Wiley & Sons: **2001**; p 473-591.
3. Stuzhin, P. A.; Ercolani, C., The Porphyrin Handbook. In Kadish, K. M.; Smith, K. M.; Guillard, R., Eds. Academic Press: New York, **2003**; Vol. 15, pp 263-364.
4. Donzello, M. P.; Ercolani, C.; Stuzhin, P. A., *Coord. Chem. Rev.* **2006**, *250*, 1530.
5. Donzello, M. P.; Ercolani, C.; Kadish, K. M.; Ricciardi, G.; Rosa, A.; Stuzhin, P. A., *Inorg. Chem.* **2007**, *46*, 4145.
6. Donzello, M. P.; Ercolani, C.; Kadish, K. M.; Ricciardi, G.; Rosa, A., *Inorg. Chem.* **2009**, *48*, 9890.
7. Donzello, M. P.; Fujimori, M.; Miyoshi, Y.; Yoshikawa, H.; Viola, E.; Awaga, K.; Ercolani, C., *J. Porphyrins Phthalocyanines* **2010**, *14*, 343.
8. Donzello, M. P.; Ercolani, C.; Stuzhin, P. A.; Chiesi-Villa, A.; Rizzoli, C., *Inorg. Chem.* **1999**, 2075.
9. Donzello, M. P. D., D.; D'Arcangelo, G.; Zhan, R.; Ou, Z.; Ercolani, C.; Stuzhin, P.A.; Kadish, K. M., *J.Am.Chem.Soc.* **2003**, *125*, 14190.
10. Donzello, M. P.; Ercolani, C.; Mannina, L.; Viola, E.; Bubnova, A.; Khelevina, O. G.; Stuzhin, P. A., *Aus. J. Chem.* **2008**, *61*, 262.
11. Donzello, M. P.; Ou, Z.; Dini, D.; Meneghetti, M.; Ercolani, C.; Kadish, K. M., *Inorg. Chem.* **2004**, *43*, 8637.
12. Donzello, M. P.; Ou, Z.; Monacelli, F.; Ricciardi, G.; Rizzoli, C.; Ercolani, C.; Kadish, K. M., *Inorg. Chem.* **2004**, *43*, 8626.

13. Donzello, M. P.; Viola, E.; Cai, X.; Mannina, L.; Rizzoli, C.; Ricciardi, G.; Ercolani, C.; Kadish, K. M.; Rosa, A., *Inorg. Chem.* **2008**, *47*, 3903.
14. Viola, E.; Donzello, M. P.; Ciattini, S.; Portalone, G.; Ercolani, C., *Eur. J. Inorg. Chem.* **2009**, 1600.
15. Bergami, C.; Donzello, M. P.; Monacelli, F.; Ercolani, C.; Kadish, K. M., *Inorg. Chem.* **2005**, *44*, 9862.
16. Bergami, C. D., M. P.; Ercolani, C.; Monacelli, F.; Rizzoli, C., *Inorg. Chem.* **2005**, *44*, 9852.
17. Mori, G. D.; Fu, Z.; Viola, E.; Cai, X.; Ercolani, C.; Donzello, M. P.; Kadish, K. M., *Inorg. Chem.* **2011**, *50*, 8225.
18. Mack, J.; Stillman, M. J., *The Porphyrin Handbook*. Academic Press: New York, 2003; Vol. 16.
19. Stillman, M. J., *Phthalocyanine: Properties and Applications*. VCH Publisher Inc.: New York, 1989; Vol. 1.
20. Guouterman, M., *The Porphyrins*. Academic Press: New York, 1978; Vol. III, and reference therein.
21. Donzello, M.; Viola, E.; Cai, X.; Mannina, L.; Ercolani, C.; Kadish, K. M., *Inorg. Chem.* **2010**, *49*, 2447.
22. Dozello, M. P.; Dini, D.; D'Arcangelo, G.; Ercolani, C.; Kadish, K. M.; Ou, Z.; Stuzhin, P. A.; Zhan, R., *J. Chem. Soc. A* **2003**, *125*, 14190.
23. Stillman, M. J.; Thomson, A. J., *J. Chem. Soc. Faraday. Trans II* **1974**, *70*, 790.
24. Clack, D. W.; Hush, N. S.; Yandle, J. R., *Inorg. Chem.* **1972**, *11*, 1738.
25. Day, P.; Hill, H. A. O.; Price, M. G., *J. Chem. Soc. A* **1968**, (1), 90.

Chapter Eight

Electrochemistry and Spectroelectrochemistry of

Metal Complexes of

Tetrakis-2,3-[5,6-di(2-pyridyl)pyrazino]porphyrazine

with Exocyclic (Pt^{II}) Metal Ion Binding

8.1 Introduction

The synthesis and characterization of tetrakis-2,3-[5,6-di(2-pyridyl)pyrazino] porphyrazine,¹ [Py₈TPyzPzH₂] and its metallated derivatives,² [Py₈TPyzPzM]·xH₂O, where M = Mg^{II}(H₂O), Mn^{II}, Co^{II}, Cu^{II} or Zn^{II} has been reported (see structure in Chart 8-1a). The four external dipyridinopyrazine fragments on [Py₈TPyzPzM] significantly enhance the overall electron-deficiency of the macrocycle, leading to facile multistep one-electron reductions and also making these compounds easier to reduce than the related phthalocyanine analogues (PcM), whose structure is shown in Figure 1-5d.

Heteropentametallic porphyrazine macrocycles with different central metal ions have also been investigated.^{3,4} The four electroactive PdCl₂ units of [(PdCl₂)₄Py₈TPyzPzZn] (see Chart 8-1c) are coordinated at the pyridine N atoms of the external dipyridinopyrazine fragments (“py-py” coordination) and displaced out the plane of the central pyrazinoporphyrazine macrocycle, as verified by ¹H and ¹³C NMR data.⁴ Each complex can be stepwise reduced via two reversible or quasi-reversible one-electron transfer processes prior to an irreversible electroreduction of the four bound PdCl₂ groups at more negative potentials. The first two one-electron reductions of [(PdCl₂)₄Py₈TPyzPzM] are easier (occur at more positive potentials) than the first two one-electron reductions of the monometallic [Py₈TPyzPzM] derivatives with the same central metal ion.^{3,4} Thus the ease of reduction follows the order [(PdCl₂)₄Py₈TPyzPzM] > [Py₈TPyzPzM] > PcM for compounds with the same central metal ion.

The pyrazinoporphyrazine complexes in Figure 8-1c have also been shown to act as photosensitizers for the production of singlet oxygen,⁵ and are promising materials for use in photodynamic therapy (PDT), a widely expanding anticancer therapeutic

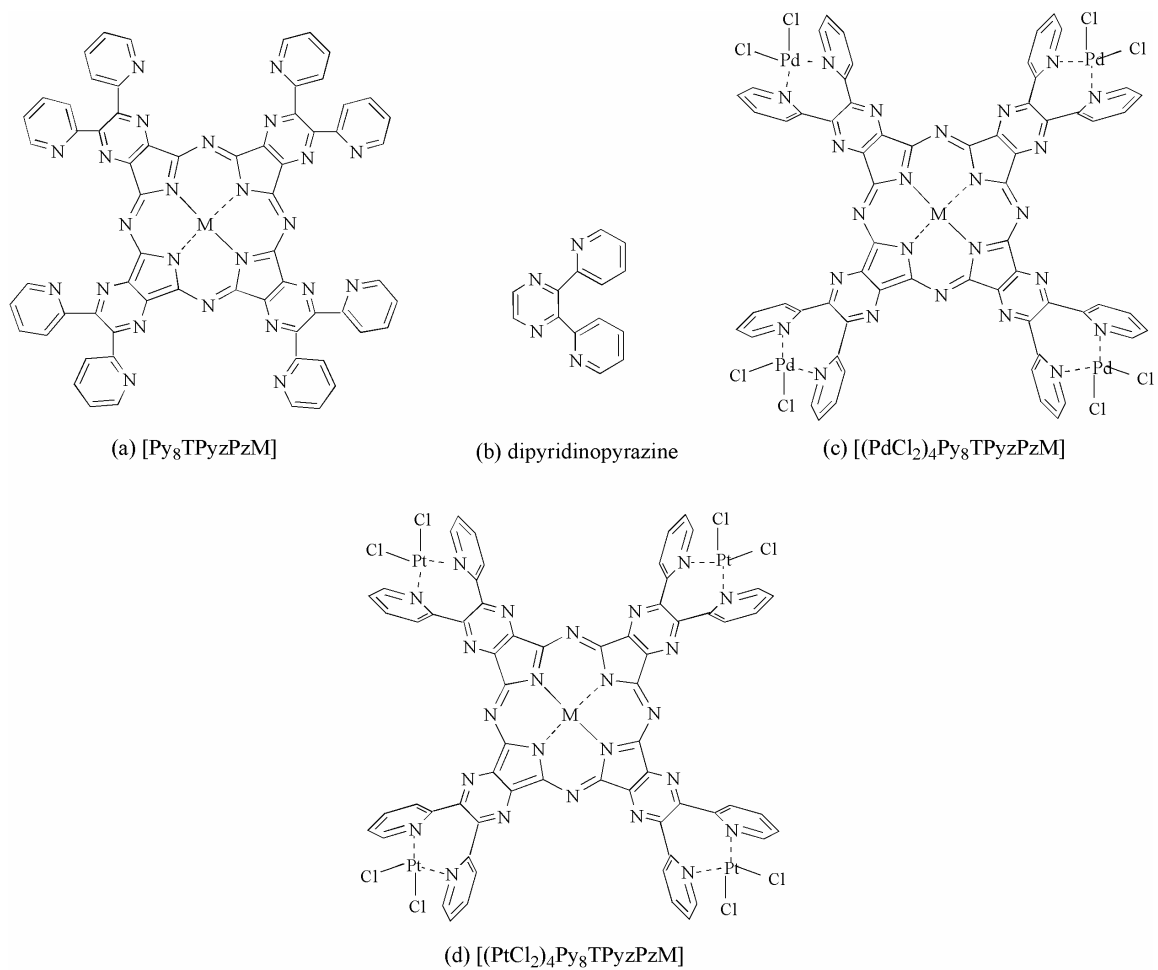


Chart 8-1. Structures of (a) $[\text{Py}_8\text{TPyzPz}\text{M}]$, (b) dipyridinopyrazine, (c) $[(\text{PdCl}_2)_4\text{Py}_8\text{TPyzPz}\text{M}]$ and (d) $[(\text{PtCl}_2)_4\text{Py}_8\text{TPyzPz}\text{M}]$.

modality.⁶⁻¹¹

The work described in the present Chapter reports the spectroscopic and electrochemical behavior of $[(\text{PtCl}_2)_4\text{Py}_8\text{TPyzPzM}]$ (see Chart 8-1d), where $\text{M} = \text{Pd}^{\text{II}}$, Pt^{II} , Cd^{II} , Cu^{II} , Zn^{II} , Mg^{II} . Like in the case of $[(\text{PdCl}_2)_4\text{Py}_8\text{TPyzPzM}]$, the PtCl_2 units in $[(\text{PtCl}_2)_4\text{Py}_8\text{TPyzPzM}]$ are coordinated at the pyridine N atoms of the external dipyridinopyrazine fragments (“py-py” coordination) and are displaced out of the plane of the central pyrazinoporphyrazine macrocycle as confirmed by $^1\text{H}/^{13}\text{C}$ NMR spectra.¹²

8.2 Results and Discussion

8.2.1 Electrochemistry

Cyclic voltammetry and spectroelectrochemistry of $[(\text{PtCl}_2)_4\text{Py}_8\text{TPyzPzM}]$ were carried out in DMSO, DMF and pyridine containing 0.1 or 0.2 M TBAP. At the concentrations used for the electrochemical experiments (ca. 5×10^{-4} M or higher), the Pd^{II} , Zn^{II} and Mg^{II} pentametallc porphyrazines are soluble and exist as monomers. Aggregation is not observed for these three metallomacrocycles in DMSO, DMF and pyridine but extensive aggregation is seen for the Pt^{II} , Cd^{II} and Cu^{II} derivatives, and meaningful measurements could not be made on these compounds without a prior “electrochemical solubilization” of the material. This was accomplished by first scanning to negative potentials to generate the more soluble trianion of each compound and then reversing the potential to 0.2 V to regenerate the neutral porphyrazine which was soluble in its unaggregated form for a sufficient period of time to measure the redox potentials and UV-visible spectra. This technique of measuring spectra and redox potentials for almost totally insoluble porphyrazine compounds has been described in

the literature.¹³

Examples of results on the aggregated Pt, Cd and Cu derivatives in DMSO are shown in Figure 8-1. No reversible reductions are seen on the first negative sweep (dashed line) by four well-defined processes are obtained on the second scan after generation of the monomers. The measured half-wave potentials for these compounds ($E_{1/2}$, V vs SCE) as well as for the other compounds are listed in Table 8-1. This table includes published data on the related $[\text{Py}_8\text{TPyzPzM}]^{14,15}$ and $[(\text{PdCl}_2)\text{Py}_8\text{TPyzPzM}]^{3,4}$. No oxidations were observed for any of the examined tetraplatinated porphyrazines within the positive potential limit of DMSO (~ 1.3 V vs SCE).

Figure 8-2 compares the electrochemistry of PtCl_2 , $[\text{Py}_8\text{TPyzPzM}]$ and $[(\text{PtCl}_2)_4\text{Py}_8\text{TPyzPzM}]$ in DMSO, 0.1 M TBAP. The reduction of PtCl_2 occurs in two steps at, $E_p = -1.20$ and -1.58 V, for a scan rate of 0.1 V/s as described in literature.³ The first two reductions of $[\text{Py}_8\text{TPyzPzM}]$ and $[(\text{PtCl}_2)_4\text{Py}_8\text{TPyzPzM}]$ involve the porphyrazine macrocycle to give a π -anion radical and dianion, respectively. As indicated earlier, the pentametallic compound is easier to reduce than the monometallic derivative with the same Zn(II) central metal ion and $E_{1/2}$ values for the first two reductions are shifted positively by 160 and 220 mV, respectively, as shown in Figure 8-2. Similar positive shifts in $E_{1/2}$ are also seen for the other investigated compounds upon going from $[\text{Py}_8\text{TPyzPzM}]$ to $[(\text{PtCl}_2)_4\text{Py}_8\text{TPyzPzM}]$ whose $\Delta E_{1/2}$ values range from 160 mV for M = Zn(II) to 410 mV for M = Cd(II) (see Table 8-1).

The first two one-electron additions to $[(\text{PtCl}_2)_4\text{Py}_8\text{TPyzPzM}]$ are given by Equations 8-1 to 8-2 and are followed by a two step reduction of the four bound PtCl_2 units at more negative potentials.

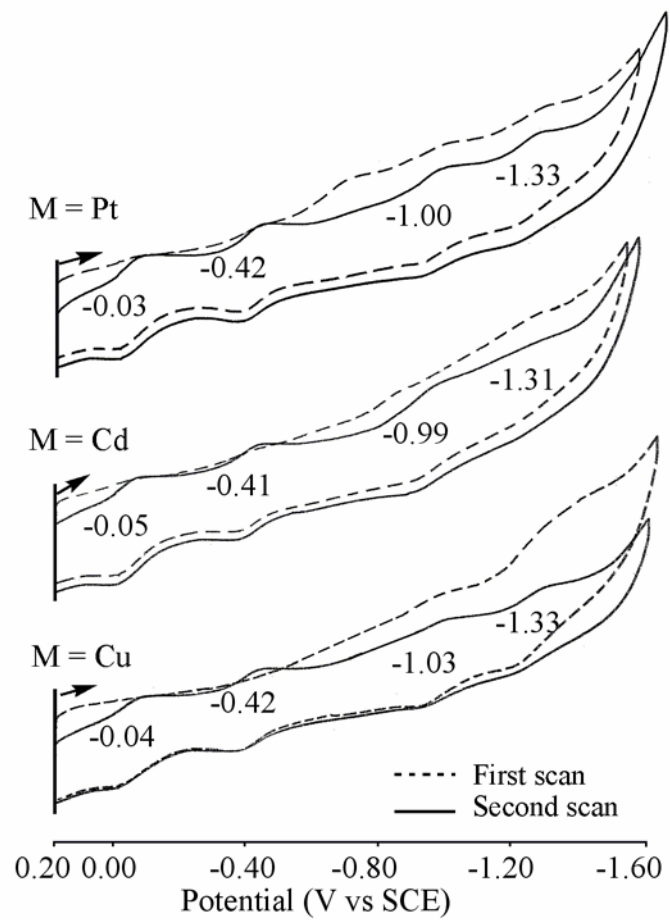


Figure 8-1. Thin-layer cyclic voltammograms of $[Py_8TPyzPzM]$ where $M = Pt, Cd$ and Cu in DMSO, 0.2 M TBAP. Scan rate = 20 mV/s.

Table 8-1. Half-wave Potential ($E_{1/2}$, V vs SCE) of the LM, [(PtCl₂)₄LM] and [(PdCl₂)₄LM] (L = Py₈TPyzPz; M = Zn^{II}, Mg^{II}, Cu^{II}, Cd^{II}, Pd^{II}, Pt^{II}) and Analogues in DMSO, 0.1 M TBAP.

Compound	macrocycle				PtCl ₂ *	Δ_1^b	Δ_2^c	Ref. ^d	
	1st	2nd	3rd	4th					
PtCl ₂					-1.20	-1.58		3	
[LZn]	-0.26	-0.67	-1.38	-1.64				15	
[(PtCl₂)₄LZn]	-0.10	-0.45	-1.10*		-1.36	-1.74	0.16	0.22	tw
[(PdCl ₂) ₄ LZn]	-0.13	-0.54	-1.39	-1.63			0.13	0.13	4
[LMg]	-0.33	-0.70	-1.39	-1.70					15
[(PtCl₂)₄LMg]	-0.15	-0.49	-1.12	-1.33	--	-1.78	0.18	0.21	tw
[(PdCl ₂) ₄ LMg]	-0.15	a	a	a			0.18		4
[LCu]	-0.22	-0.58	-1.22	-1.58					15
[(PtCl₂)₄LCu]	-0.04	-0.41	-0.97	-1.25		-1.65	0.18	0.17	tw
[(PdCl ₂) ₄ LCu]	-0.03	-0.41	-1.24	-1.60			0.19	0.17	4
[LCd]	-0.41	-0.77	-1.39	--					15
[(PtCl₂)₄LCd]	-0.05	-0.43	-0.97		-1.36	-1.69	0.41	0.36	tw
[(PdCl ₂) ₄ LCd]	-0.22	a	a	a		a	0.24		4
[LPd]	-0.26	-0.60	-1.26	-1.61					3
[(PtCl₂)₄LPd]	0.00	-0.35	-0.97		-1.30	-1.78	0.26	0.25	tw
[(PdCl ₂) ₄ LPd]	0.00	-0.37	-1.24	-1.59			0.26	0.23	3
[LPt]	-0.25	-0.61	--	--					tw
[(PtCl₂)₄LPt]	-0.03	-0.39	-0.95		-1.31	-1.78	0.22	0.22	tw

^aComplicated current-voltage curves due to overlapping peaks assigned to the pentapalladated complex present as a transmetalation contaminant. ^b Δ_1 = difference in $E_{1/2}$ between first reduction of [LM] and [(PtCl₂)₄LM] or [(PdCl₂)₄LM]. ^c Δ_2 = difference in $E_{1/2}$ between second reduction of [LM] and [(PtCl₂)₄LM] or [(PdCl₂)₄LM]. ^d tw = This Work. *irreversible peak.

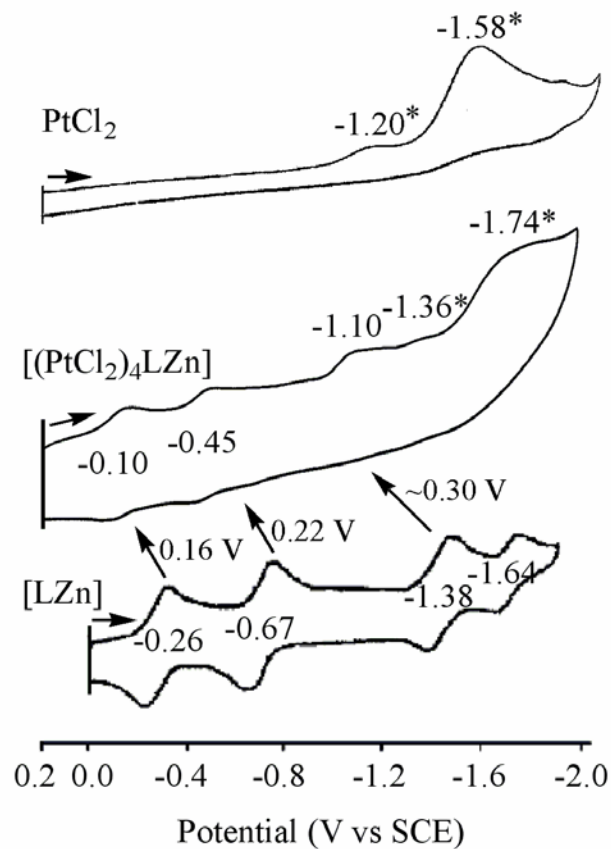
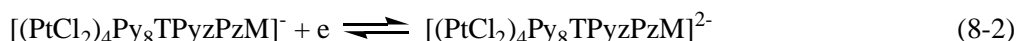
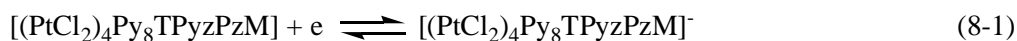


Figure 8-2. Cyclic voltammograms of PtCl₂ (reproduced from ref 3), [LZn] (reproduced from ref ¹⁵) and [(PtCl₂)₄LZn] (L = Py₈TPyzPz) in DMSO, 0.1 M TBAP. The peak marked by an asterisk is associated with reduction of bound PtCl₂. Scan rate = 0.1 V/s.



The electrochemical data in Table 8-1 indicates that the first and second ring-centered reductions of $[(\text{PtCl}_2)_4\text{Py}_8\text{TPyzPzM}]$ are systematically easier by 160 to 260 mV than the first and second ring-centered reductions of $[\text{Py}_8\text{TPyzPzM}]$ with the same central metal ion. A similar trend was earlier reported for $[(\text{PdCl}_2)_4\text{Py}_8\text{TPyzPzM}]$ and $[\text{Py}_8\text{TPyzPzM}]$ which demonstrates that external coordination of PtCl_2 or PdCl_2 units both induces an easier acceptance of excess negative charge within the macrocyclic framework, independent of the central metal atom.

The negative shift in potential for the reduction of PtCl_2 , from $E_p = -1.20$ and -1.58 V in the absence of the macrocycle to $E_p = -1.36$ and -1.70 V when contained within $[(\text{PtCl}_2)_4\text{Py}_8\text{TPyzPzM}]$, is accompanied by a positive shift in $E_{1/2}$ values for the first two reductions of the porphyrazine-centered reductions of the same compound. This is consistent with a redistribution of negative charge density toward the PtCl_2 group and away from the porphyrazine π -ring system.

In the case of $[(\text{PdCl}_2)_4\text{Py}_8\text{TPyzPzM}]$, a loss of the four PdCl_2 groups occurs after reduction to generate Pd^0 and $E_{1/2}$ values for the following reductions were virtually at the same potentials as those for reduction of $[\text{Py}_8\text{TPyzPzM}]$ (see Figure 5 in Ref. 4). This contrasts with what occurs with $[(\text{PtCl}_2)_4\text{Py}_8\text{TPyzPzM}]$ where dissociation does not occur prior to fourth reduction of the macrocycle. The third and fourth reductions are both easier by 250-370 mV than the corresponding reductions of $[\text{Py}_8\text{TPyzPzM}]$ as described in Equations 8-3 and 8-4. This is illustrated in Figure 8-3.

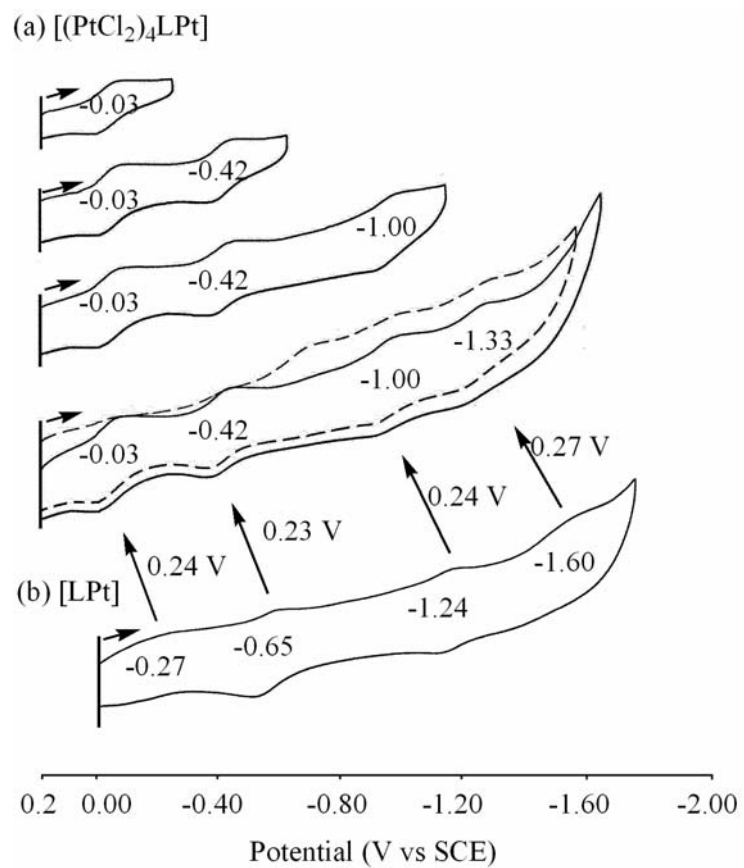
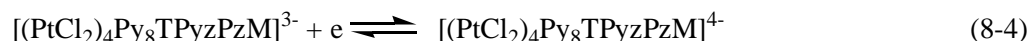
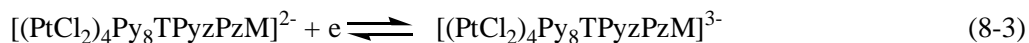


Figure 8-3. Thin-layer cyclic voltammograms of $[(PtCl_2)_4LPt]$ and $[LPt]$ ($L = Py_8TPyzPz$) in DMSO, 0.2 M TBAP.



Despite the narrow range of total potential variation in $E_{1/2}$ for the first reductions of total potential in DMSO (150 mV), there is a systematic shift of the $E_{1/2}$ values toward less negative potentials over the whole series of $[(\text{PtCl}_2)_4\text{Py}_8\text{TPyzPzM}]$ compounds with a more facile reduction occurring in the sequence: Mg^{II} (-0.19 V) \rightarrow Zn^{II} (-0.13 V) \rightarrow Cd^{II} (-0.05 V) \rightarrow Cu^{II} (-0.04 V) \rightarrow Pt^{II} (-0.03 V) \rightarrow Pd^{II} (0.00 V) in thin-layer cell. The corresponding cyclic voltammograms of first two reductions are shown in Figure 8-4. The same trend holds in regular cell, DMSO: Mg^{II} (-0.15 V) \rightarrow Zn^{II} (-0.10 V) \rightarrow Cd^{II} (-0.05 V) \rightarrow Cu^{II} (-0.04 V) \rightarrow Pt^{II} (-0.03 V) \rightarrow Pd^{II} (0.00 V), in DMF: Mg^{II} (-0.17 V) \rightarrow Zn^{II} (-0.15 V) \rightarrow Cd^{II} (-0.05 V) \rightarrow Cu^{II} (-0.03 V) \rightarrow Pt^{II} (-0.02 V) \rightarrow Pd^{II} (0.04 V), and in pyridine: Mg^{II} (-0.20 V) \rightarrow Zn^{II} (-0.18 V) \rightarrow Cd^{II} (-0.07 V) \rightarrow Cu^{II} (-0.06 V) \rightarrow Pt^{II} (-0.05 V) \rightarrow Pd^{II} (-0.02 V).

8.2.2 Spectroelectrochemistry.

UV-visible spectral data for each investigated complexes are summarized in Table 8-2. The neutral $[(\text{PtCl}_2)_4\text{Py}_8\text{TPyzPzM}]$ ($\text{M} = \text{Zn}^{\text{II}}$, Mg^{II} and Pd^{II}) compounds are characterized by a Soret band at 348-392 nm and two visible bands at 567-600 nm and 639-664 nm in DMSO without aggregation. UV-visible spectral changes during first reduction of $[\text{Py}_8\text{TPyzPzPd}]$, $[(\text{PdCl}_2)_4\text{Py}_8\text{TPyzPzPd}]$ (reproduced from ref 3) and $[(\text{PtCl}_2)_4\text{Py}_8\text{TPyzPzPd}]$ in DMSO containing 0.2 M TBAP are illustrated in Figure 8-5, which shows that the spectroelectrochemical features of pentaplatinated species are

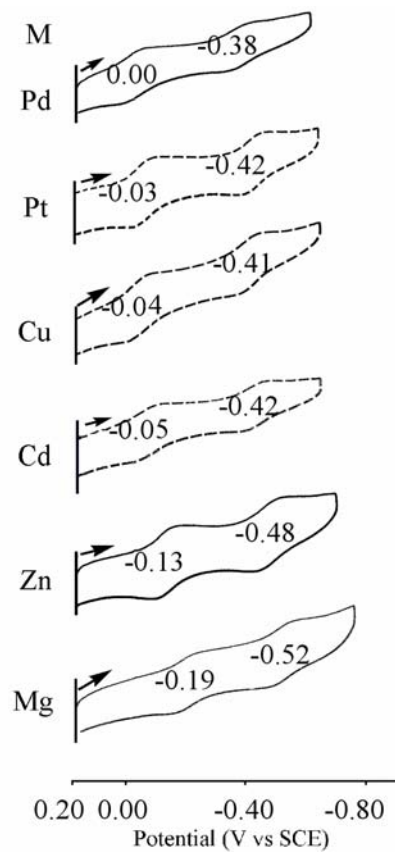


Figure 8-4. Thin-layer cyclic voltammograms with added $E_{1/2}$ values (V vs SCE) of $[(\text{PtCl}_2)_4\text{Py}_8\text{TPyzPzM}]$ in DMSO containing 0.2 M TBAP. Scan rate = 20 mV/s.

Table 8-2. UV-visible Solution Spectra of the [(PtCl₂)LM] (L = Py₈TPyzPz; M = Zn^{II}, Mg^{II}, Cd^{II}, Pd^{II}, Pt^{II}) in DMSO, DMF and Py (0.2 M TBAP).

Compound	Solvent	$\lambda(\text{nm}) (\log\epsilon)$		
		Soret region		Q-band region
[(PtCl ₂) ₄ LZn].15H ₂ O	DMSO	392 (4.75)	600 (4.30)	664 (5.11)
	DMF	394 (4.61)	599 (4.33)	663 (4.94)
	py	395 (4.67)	605 (4.37)	671 (4.93)
[(PtCl ₂) ₄ LMg].13H ₂ O	DMSO	387 (4.74)	597 (4.30)	659 (5.04)
	DMF	385 (4.64)	599 (4.20)	663 (5.00)
	py	385 (4.67)	601 (4.23)	667 (5.03)
[(PtCl ₂) ₄ LCd]. 5 H ₂ O	DMSO	323(4.94) 367(4.96)	568 (4.49)	628 (5.05)
	DMF	321(4.88) 367(4.86)	569(4.51)	625 (5.08)
	py	324(4.91) 367(4.92)	573 (4.44)	634 (5.01)
[(PtCl ₂) ₄ LPd].10H ₂ O	DMSO	348 (4.92)	581 (4.41)	639 (5.03)
	DMF	347 (4.70)	574 (4.33)	636 (4.85)
	py	353 (4.75)	582 (4.36)	642 (4.95)
[(PtCl ₂) ₄ LPt].10H ₂ O	DMSO	323 (4.73) 366 (4.80)	567 (4.31)	625 (4.87)
	py	325 (4.81) 365 (4.84)	572 (4.45)	631 (4.98)

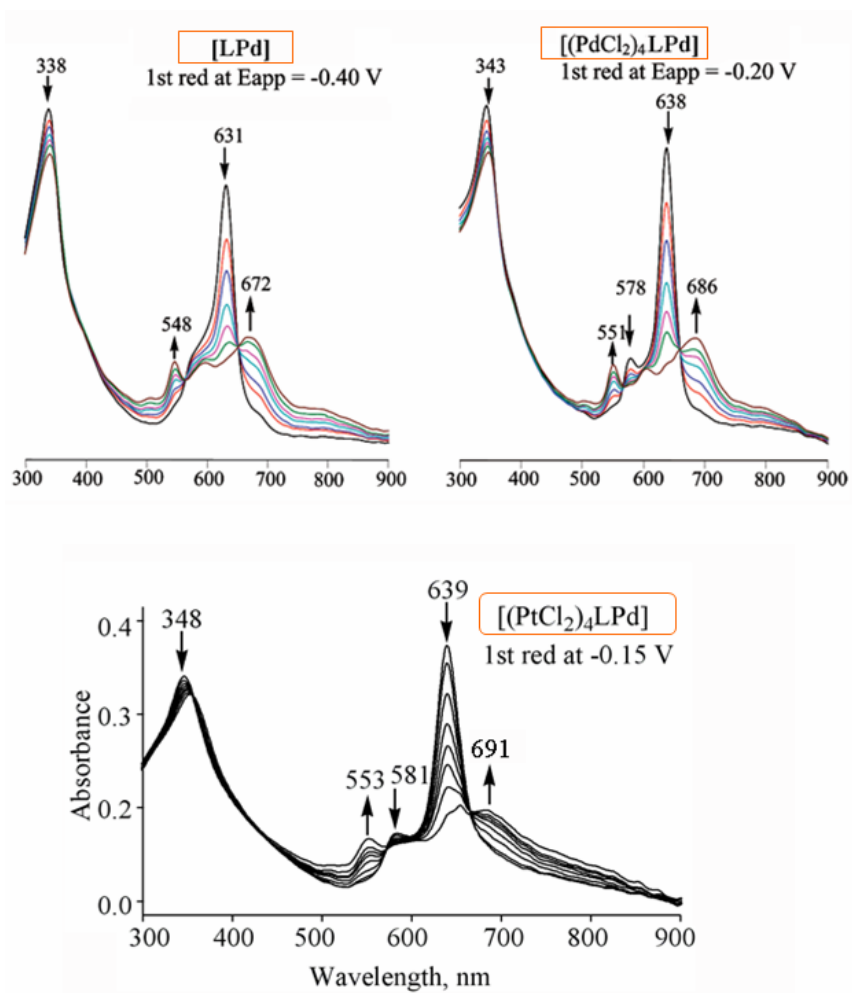


Figure 8-5. UV-visible spectral changes during first reduction of [LPd], [(PdCl₂)₄LPd] (reproduced from ref 3) and [(PtCl₂)₄LPd] (L = Py₈TPyzPz) in DMSO containing 0.2 M TBAP.

common to those of the corresponding species $[(\text{PdCl}_2)_4\text{Py}_8\text{TPyzPzM}]$ and also in general for other $[\text{Py}_8\text{TPyzPzM}]$ species, which are ligand-centered reductions.

The neutral $[(\text{PtCl}_2)_4\text{Py}_8\text{TPyzPzM}]$ ($\text{M} = \text{Cd}^{\text{II}}, \text{Pt}^{\text{II}}$ and Cu^{II}) compounds obtained by pretreating the compounds after an initial reduction at -1.40 V followed by reoxidation at 0.2 V are characterized by two Soret band at 323 and 366-367 nm and two visible bands at 567-568 nm and 625-628 nm in the case of Cd and Pt complexes and one Soret band at 374 nm and two visible bands at 591 and 651 nm in the case of Cu derivative in DMSO.

Figure 8-6a shows the UV-visible spectral changes in DMSO during first two one-electron reductions of $[(\text{PtCl}_2)_4\text{Py}_8\text{TPyzPzZn}]$ and similar changes are obtained for $[(\text{PtCl}_2)_4\text{Py}_8\text{TPyzPzMg}]$ (Figure 8-6b). Figure 8-7 illustrates the case for $[(\text{PdCl}_2)_4\text{Py}_8\text{TPyzPzPt}]$ and $[(\text{PdCl}_2)_4\text{Py}_8\text{TPyzPzCd}]$ in DMSO containing 0.2 M TBAP. The isosbestic points in the spectra in DMSO indicate the lack of detectable intermediates upon going from the neutral form of the complexes $[(\text{PtCl}_2)_4\text{Py}_8\text{TPyzPzZn}]$, $[(\text{PtCl}_2)_4\text{Py}_8\text{TPyzPzMg}]$, $[(\text{PtCl}_2)_4\text{Py}_8\text{TPyzPzPt}]$ and $[(\text{PtCl}_2)_4\text{Py}_8\text{TPyzPzCd}]$ to the corresponding -1 charged species. There is also a common evolution of the spectra expressed by the disappearance of the Q band and the appearance of new bands at about 545-573 nm in addition to a broad absorption in the region 670-730 nm.

The spectral changes of third and fourth reductions of $[(\text{PtCl}_2)_4\text{Py}_8\text{TPyzPzM}]$ could also been observed in thin-layer cell due to the more negative reduction of PtCl_2 than that of PdCl_2 . The example spectral changes of the third and fourth reductions for $[(\text{PtCl}_2)_4\text{Py}_8\text{TPyzPzZn}]$ as illustrated in Figure 8-8. The Q band at 574 nm decreases in

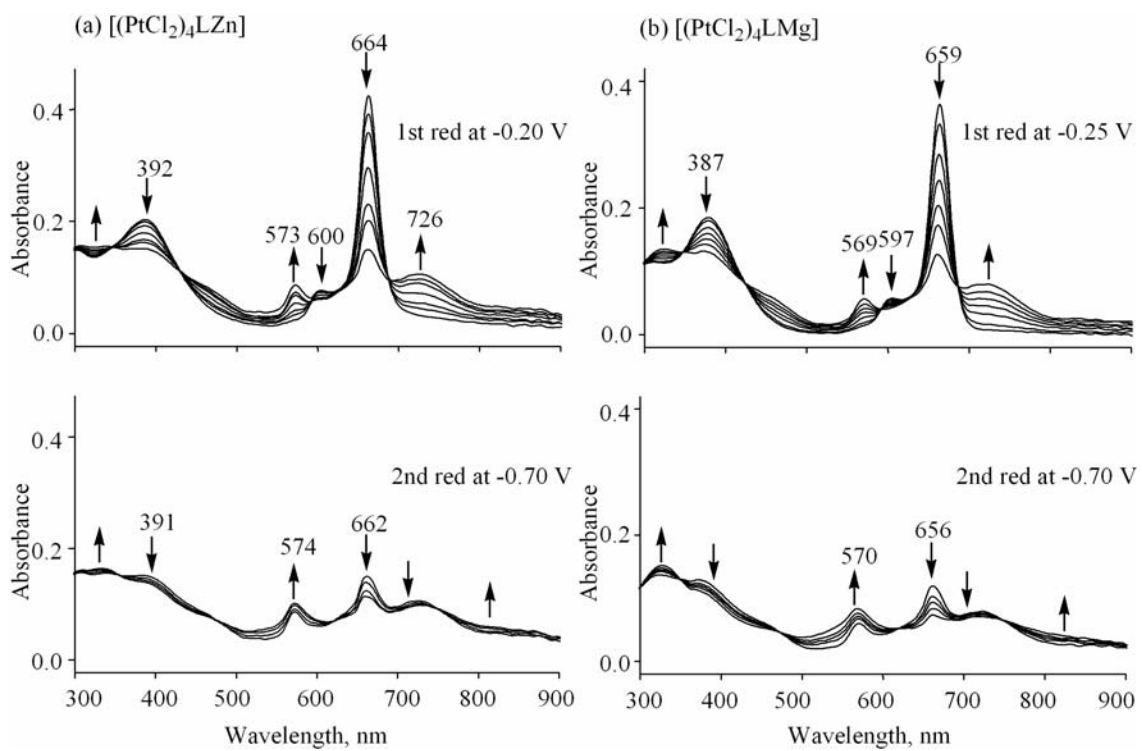


Figure 8-6. UV-visible spectral changes obtained during the first and second reductions of (a) $[(\text{PtCl}_2)_4\text{LZn}]$ and (b) $[(\text{PtCl}_2)_4\text{LMg}]$ ($\text{L} = \text{Py}_8\text{TPyzPz}$) in DMSO containing 0.2 M TBAP.

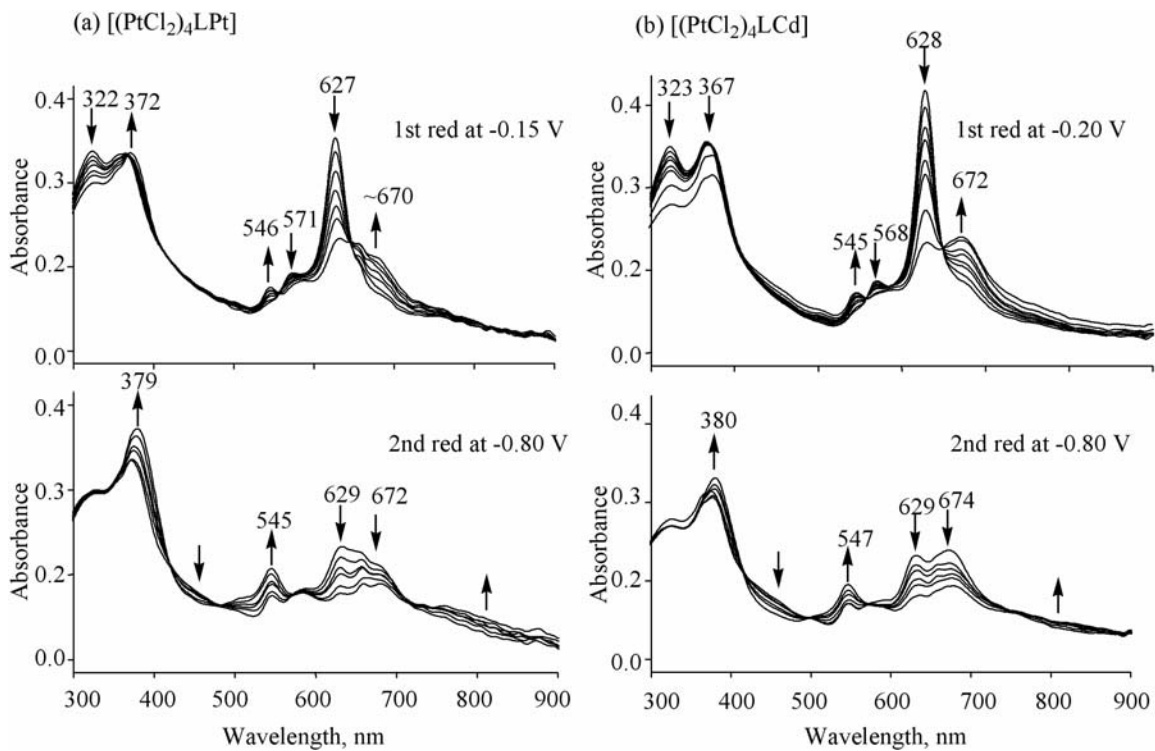


Figure 8-7. UV-visible spectral changes obtained during the first and second reductions of (a) $[(PtCl_2)_4LZn]$ and (b) $[(PtCl_2)_4LMg]$ ($L = Py_8TPyzPz$) in DMSO containing 0.2 M TBAP.

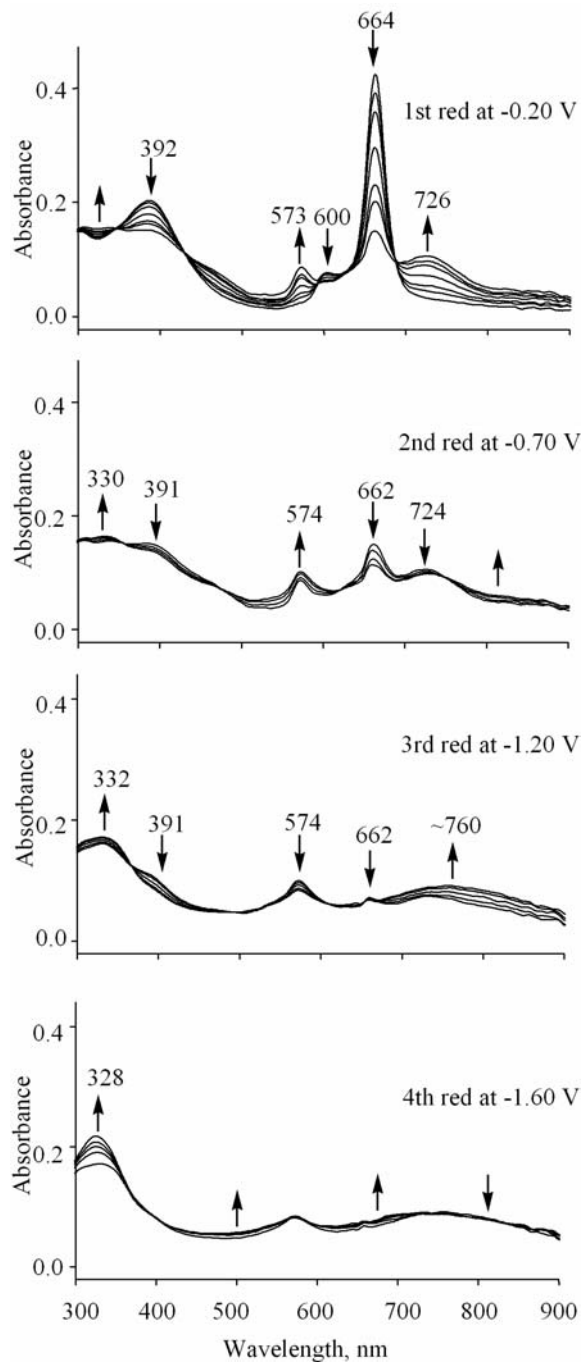


Figure 8-8. UV-visible spectral changes obtained during the first to fourth reductions $[(\text{PtCl}_2)_4\text{Py}_8\text{TPyzPzZn}]$ in DMSO containing 0.2 M TBAP.

intensity while a new broad band at 760 nm appears when potential is applied at -1.20 V and then the broad band decrease in intensity when potential is applied at -1.60 V.

8.3 Conclusions

UV-visible spectral and electrochemical data provide unequivocal evidence that external platination influences the HOMO-LUMO energy gap and makes the macrocycles more easily reduced. This is a direct effect of the enhanced electron withdrawing properties of the peripheral fragments due to platination, in line with similar effects seen for the [Py₈TPyzPzM] species when changed to platination. The spectra of [(PtCl₂)₄Py₈TPyzPzCu], [(PtCl₂)₄Py₈TPyzPzPd] and [(PtCl₂)₄Py₈TPyzPzPt] were recorded after an initial reduction at -1.40 V followed by reoxidation at 0.2 V to generate the monomeric species in solution. Because Pt^{II} convert to Pt⁰ at more negative potential (-1.58 V) compared to Pd^{II}→Pd⁰ (-0.86 V), the third and fourth reductions of [(PtCl₂)₄Py₈TPyzPzM] could be obtained in thin-layer cell. The redistribution of negative charge density is towards the PdCl₂ groups and away from the porphyrazine π -ring system.

8.4 References

1. Donzello, M. P. O., Z.; Meneghetti, M.; Ercolani, C.; Kadish, K. M. *Inorg. Chem.* **2004**, *43*, 8626.
2. Donzello, M. P.; Ou, Z.; Meneghetti, M.; Ercolani, C.; Kadish, K. M. *Inorg. Chem.* **2004**, *43*, 8637.
3. Donzello, M. P.; Viola, E.; Cai, X.; Mannina, L.; Rizzoli, C.; Ricciardi, G.; Ercolani, C.; Kadish, K. M.; Rosa, A. *Inorg. Chem.* **2008**, *47*, 3903.
4. Donzello, M.; Viola, E.; Cai, X.; Mannina, L.; Ercolani, C.; Kadish, K. M. *Inorg. Chem.* **2010**, *49*, 2447.
5. Donzello, M. P.; Viola, E.; Bergami, C.; Dini, D.; Ercolani, C.; Giustini, M.; Kadish, K. M.; Meneghetti, M.; Monacelli, F.; Rosa, A.; Rosa, A.; Ricciardi, G. *Inorg. Chem.* **2008**, *47*, 8757.
6. Redmond, R. W.; Gamlin, J. N. *Photochem. Photobiol.* **1999**, *70*, 391.
7. De Rosa, M. C.; Crutchley, R. J. *J. Coord. Chem. Rev.* **2002**, 233.
8. Detty, M. R.; Gibson, S. L.; Wagner, S. J. *J. Med. Chem.* **2004**, *47*, 3897.
9. Szacilowski, K.; Macyk, W.; Drzewiecka-Matuszek, A.; Brindell, M.; Stochel, G. *Chem. Rev.* **2005**, *105*, 2647.
10. Dougherty, T. J.; Gomer, C. J.; Henderson, B. W.; Jori, G.; Kessel, D.; Korbek, M.; Moan, J.; Peng, Q. *J. Natl. Cancer Inst.* **1998**, *90*, 889.
11. Pandey, R. K.; Zheng, G. In *The Porphyrin Handbook*; Kadish, K. M., Smith, K. M.,

- Guilard, R., Eds.; Academic Press: San Diego, CA, **2000**; Vol. 6, p 157.
12. Donzello, M. P.; Viola, E.; Fu, Z.; C., E.; *J. Porphyrins Phthalocyanines*, **2011**, *15*, 984.
13. Donzello, M. P.; Ercolani, C.; Kadish, K. M.; Ricciardi, G.; Rosa, A. *Inorg. Chem.* **2009**, *48*, 9890.
14. Bergami, C. D., M. P.; Ercolani, C.; Monacelli, F.; Rizzoli, C. *Inorg. Chem.* **2005**, *44*, 9852.
15. Bergami, C.; Donzello, M. P.; Monacelli, F.; Ercolani, C.; Kadish, K. M. *Inorg. Chem.* **2005**, *44*, 9862.